Stress-Strain Behaviour of Confined Rubberised Concrete

A thesis presented for the degree of

Doctor of Philosophy in Civil and Structural Engineering

at The University of Sheffield

By

Zhao Wang

Sheffield

April 2019

Thank you for the little ways that you help me every day.

Abstract

Large reinforced concrete (RC) structures can be subjected to significant lateral loads and deformations. To prevent the development of large moments, highly deformable and high strength elements can be utilised, such as elastomeric bearings. These elements are currently expensive and not as durable as the structure itself. Extensive research carried out at The University of Sheffield propose a novel and cost-effective alternative solution, which is utilising FRP-confined rubberised concrete (CRuC).

Since the determination of deformation in RC depends on knowledge of the stress-strain characteristics, this research aimed to develop a comprehensive understanding of the stress-strain behaviour of CRuC and develop effective modelling methods that can be used for the development of high-strength high-deformability concrete elements.

Notched three-point bending tests are used to characterise the Mode I fracture behaviour of rubberised concrete (RuC). Test result shows that rubber particles enhance energy absorption capacity and ductility of concrete. The tensile stress-strain curves of RuC are obtained through inverse finite element analysis.

The compressive behaviour of CRuC in circular and non-circular sections is examined experimentally under uniaxial compression. Test results show that the confinement effectiveness in RuC elements is better than in regular concrete. An analytical model is proposed based on a new definition of the effective confinement area.

The shear behaviour of CRuC is assessed by axisymmetric four-point bending tests. Test results indicate that CRuC shows ductile and stable performance that allows the development of high shear deformations. By adopting a nonlinear numerical approach for the practical implementation of the smeared, fixed-angle crack approach in finite element analysis, the shear response of CRuC can be correctly predicted.

The experimental results support the idea that CRuC can be effectively used to develop highly ductile RC structural components for deformable elements and structures located in high seismicity regions. The proposed constitutive relations and models provide the necessary information for the development of design tools.

Acknowledgements

感恩我亲爱的妈妈，爱与信任是您给予我最珍贵的礼物！

First and foremost, I would like to thank my supervisor Prof. Kypros Pilakoutas wholeheartedly, not only for offering me the opportunity to carry out this research but also for your patient guidance, encouragement, continuous support throughout my study. It has been an honour to be one of your students.

I would like to extend my deepest gratitude to my co-supervisor Dr. Maurizio Guadagnini for his overwhelming supervision and tremendous academic support at every stage of my research, which have enabled me to complete my thesis.

I am also hugely appreciative to my co-supervisor Dr. Iman Hajirasouliha for his timely help and prompt inspirations with enthusiasm and dynamism.

Again, I am very grateful to my supervisors. Their contribution has raised the quality of thesis and make me better.

My heartfelt thanks to Concrete and Earthquake Engineering family for lending their hands. It is gratifying to work with all of you. Special thanks to David, Reyes, Panos, Harris and to my true friends, Hu Hang, Chen Lin and Chen zhijian.

Thank you to the technicians in the Heavy Structures Laboratory for the assistance. Especially, I like to thank Kieran Nash and Rob Markwell for their continuous support.

Finally, thanks to my family and my friends for always on my side.

Table of Contents

Chapter 1. Introduction

Chapter 2. Literature Review

Chapter 5. Axial Behaviour of FRP-Confined Concrete Columns: A Modelling Investigation

Chapter 6. Shear Behaviour Model for FRP-Confined and Unconfined Rubberised Concrete

Chapter 7. Summary, conclusions and recommendations for future research

Appendices

List of Figures

Chapter 2. Literature Review

Chapter 3. Tensile Stress-Crack Opening Characteristics of Rubberised Concrete

Chapter 4. Axial Behaviour of FRP-Confined Concrete Columns: An Experimental Investigation

List of Tables

List of Acronyms

AAE	average absolute error;
AFRP	aramid fibre reinforced polymer;
CDP	concrete damage plasticity;
CFRP	carbon fibre reinforced polymer;
CFT	compression field theory;
CMOD	crack mouth opening displacement;
CRC	FRP-confined regular concrete;
CRuC	FRP-confined rubberised concrete;
FA-STM	fixed-angle softened truss model;
FEA	finite element analysis
FRP	fibre reinforced polymer;
LVDT	linear variable differential transducers;
MSE	mean square error;
RA-STM	rotating-angle softened truss model;
RC	reinforced concrete;
RuC	rubberised concrete;
SD	standard deviation;
TPB	three-point bending;
UMAT	user defined material subroutine.

List of Symbols

Chapter 3. Tensile Stress-Crack Opening Characteristics of Rubberised Concrete

a = effective depth of prisms;

b = width of prisms;

d = depth of the prism;

d_a = maximum aggregate size;

d_{agg} = unit weight of mineral aggregates;

d_c = compressive damage variable;

d_{cy} = diameter of cylinder;

d_{RuC} = unit weight of RuC;

d_t = tensile damage variable;

f_{bo} = biaxial compressive strength;

f_{co} = compressive strength;

f_{cr} = cracking stress;

f_{ct} = tensile strength of RuC;

$f_{ct,sp}$ = splitting tensile strength;

$f_{ctm,fl}$ = flexural tensile strength;

g = gravity acceleration;

h_e = element mesh size;

l = span of the specimens;

m_1 = mass of the beam between supports;

m_2 = mass of the loading apparatus;

t = width of the loading area;

w = crack opening;

w_1 = ratio of G_F/f_{ct};

w_2 = ratio of $5G_F/f_{ct}$;

w_c = mean crack opening;

$w_{c,ult}$ = ultimate mean crack opening;

w_{cb}	=	crack band width;
w_{ult}	=	ultimate crack mouth opening;
A_e	=	element area;
A_f	=	area of the fracture surface;
E_c	=	elastic modulus of RuC;
E_d	=	slope of descending branch of load-deflection curve;
K_{fm}	=	flexural modulus of elasticity;
G_F	=	fracture energy of regular concrete;
$G_{F,RuC}$	=	fracture energy of RuC;
I	=	second moment of area of the middle cross-section;
K_c	=	shape parameter of yield surface;
N	=	total number of collection data;
P_{max}	=	maximum load of splitting tests;
R_c	=	size of round corner of rectangular section;
U_s	=	total fracture work in three-point bending tests;
W_0	=	energy absorption capacity;
γ_t	=	shape factor;
δ	=	deflection at mid-span;
δ_0	=	maximum deflection at mid-span;
ε_{ck}	=	tensile strain;
ρ_{vr}	=	rubber volume replacement ratio;
σ_t	=	tensile stress;
$(\chi)^{anal}$	=	predicted values;
$(\chi)^{exp}$	=	experimental values;
ψ	=	dilation angle;

Chapter 4. Axial Behaviour of FRP-Confined Concrete Columns: An Experimental Investigation

a	=	width of square section;

b	=	width of rectangular section;
f_{co}	=	uniaxial compressive strength of RuC;
f_{cc}	=	ultimate compressive strength of CRuC;
f_{cr}	=	critical stress;
f_f	=	tensile strength of FRP;
$k_{\varepsilon f}$	=	FRP efficiency factor;
n_f	=	number of FRP layers;
t_f	=	thickness of FRP jacket;
v	=	Poisson's ratio;
A_c	=	area of expansion of circumference;
A_f	=	expansion fan-shaped area;
D	=	diameter of cylinder;
D_{eq}	=	diameter of equivalent circular section;
E_f	=	elastic modulus of FRP;
K_j	=	normalised confinement stiffness;
R_c	=	size of round corner of rectangular section;
ε_c	=	uniaxial compressive strain;
ε_{co}	=	compressive strain at peak load of RuC;
ε_A	=	area strain;
ε_{au}	=	ultimate area strain of CRuC;
ε_{cu}	=	ultimate compressive strain of CRuC;
ε_{fu}	=	failure tensile strain of FRP;
$\varepsilon_{h,rup}$	=	actual hoop rupture strain of FRP;
ε_r	=	radius strain;
ε_h	=	hoop strain;
ε_V	=	volumetric strain;
ρ_{vr}	=	rubber volume replacement ratio;

Chapter 5. Axial Behaviour of FRP-Confined Concrete Columns: A Modelling Investigation

a	=	distance between applied load and support;
a_n	=	the elongation of the flat side;
b	=	width of rectangular section;
d_t	=	damage variable;
h_f	=	deformation of the flat side;
f_{co}	=	uniaxial compressive strength of RuC;
f_{cb}	=	strength of concrete under biaxial compression;
f_{cc}	=	ultimate compressive strength of CRuC;
f_{cr}	=	critical stress;
f_{ct}	=	tensile strength of RuC;
f_{tr}	=	axial stress at the transition point;
f_{frp}	=	tensile strength of FRP;
$f_{l,a}$	=	actual lateral confinement pressure;
f_i	=	confining stress;
k_{s1}	=	shape factor for strength enhancement;
k_{s2}	=	shape factor for strain enhancement;
$k_{\varepsilon f}$	=	FRP efficiency factor;
n_f	=	number of FRP layers;
t_f	=	thickness of one layer of carbon − FRP jacket;
v	=	Poisson's ratio;
A_c	=	area of expansion of circumference;
A_f	=	expansion fan-shaped area;
D	=	diameter of cylinder;
D_{eq}	=	diameter of equivalent circular cylinders;
E_c	=	elastic modulus of RuC;
E_f	=	tensile elastic modulus of FRP;
E_2	=	slope of straight second portion;
K_c	=	normalised confinement stiffness;
Kj	=	normalised confinement stiffness;

I_1 = first deviatoric;

J_2 = second deviatoric;

J_3 = third deviatoric;

R_c = size of round corner of rectangular section;

R_i = radius of equivalent circular cylinders;

γ_t = tensile shape factor;

$\varepsilon_{a,eq}$ = equivalent lateral strain;

ε_c = uniaxial compressive strain;

ε_{co} = compressive strain at peak load of RuC;

ε_{cu} = ultimate compressive strain of CRuC;

ε_{fu} = failure tensile strain of FRP;

$\varepsilon_{h,rup}$ = actual hoop rupture strain of FRP;

ε_h = hoop strain;

ε_p = strain at maximum stress of concrete under biaxial compression;

ε_r = radius strain;

ε_t = uniaxial tensile strain;

ε_{tr} = axial strain at the transition point;

ε_A = area strain;

ε_{Au} = ultimate area strain of CRuC;

ε_V = volumetric strain;

θ = chord length;

ρ_{vr} = rubber volume replacement ratio;

σ_c = uniaxial compressive stress;

σ_{ct} = uniaxial tensile stress;

φ = loading stress ratio;

Chapter 6. Shear Behaviour Model for FRP-Confined and Unconfined Rubberised Concrete

a = distance between applied load and support;

b = width of rectangular section;

d	=	depth of specimen;
d_t	=	damage variable;
f'_{co}	=	uniaxial cylindrical compressive strength of RuC;
$f'_{c,max}$	=	strength of inclined concrete strut;
f'_{cc}	=	ultimate compressive strength of CRuC;
f_{ct}	=	tensile strength of RuC;
f_{frp}	=	tensile strength of FRP;
$f_{l,a}$	=	actual lateral confinement pressure;
h	=	depth of rectangular section;
k_{s1}	=	shape factor for strength enhancement;
k_{s2}	=	shape factor for strain enhancement;
k_{ε}	=	FRP efficiency factor;
n_f	=	number of FRP layers;
t_f	=	thickness of one layer of carbon − FRP jacket;
w	=	crack width;
w_{cb}	=	crack band width;
w_{ult}	=	ultimate crack mouth opening;
A_c	=	total area of concrete;
A_e	=	effective confinement area;
A_g	=	gross area of column section with rounded corner;
A_0	=	facture surface area;
D	=	diameter of cylinder;
D_{eq}	=	diameter of equivalent circular section;
E_c	=	elastic modulus of RuC;
E_f	=	tensile elastic modulus of FRP;
E_2	=	slope of straight second portion;
G_F	=	fracture energy;
G_p	=	secant shear modulus at shear strength;
G_t	=	tangent shear modulus;

$G_{0,CRuC}$ = initial shear modulus of CRuC;

$G_{0,RuC}$ = initial shear modulus of RuC;

G_2 = gradient of shear hardening of CRuC;

I_1 = first stress invariant;

J_2 = second deviatoric stress invariant;

J_3 = third deviatoric stress invariant;

R_c = size of round corner of rectangular section;

U_s = total fracture work in three-point bending tests;

W_s = energy per unit volume;

α = rotating angle between *d*-axis and *l*-axis;

α_2 = fixed angle between *2*-axis and *l*-axis;

β = deviating angle between principal *2*-axis and *d*-axis;

$\gamma_{cr,CRuC}$ = cracking shear strain of CRuC;

$\gamma_{cr,RuC}$ = cracking shear strain of RuC;

γ_{cu} = ultimate shar strain of CRuC;

γ_{lt} = average shear strain in *l-t* coordinate;

γ_{nm} = average shear strain in *n-m* coordinate;

γ_p = shear strain at peak load;

γ_t = transition shear strain of CRuC;

ε_c = uniaxial compressive strain;

ε_{co} = compressive strain at peak load of RuC;

ε_{cr} = cracking strain in tension;

ε_{ct} = uniaxial tensile strain;

ε_{cu} = ultimate compressive strain of CRuC;

ε_f = direct uniaxial tensile strain of FRP;

$\varepsilon_{h,rup}$ = actual hoop rupture strain of FRP;

ε_{tr} = uniaxial compressive strain at transition point;

ε_{ult} = ultimate tensile strain;

$\varepsilon_d, \varepsilon_r$ = average normal strains in *d*- and *r*-directions, respectively;

$\varepsilon_l, \varepsilon_t$ = average normal strains in *l*- and *t*-directions, respectively;

$\varepsilon_n, \varepsilon_m$ = average normal strains in *n*- and *m*-directions, respectively;

$\varepsilon_2, \varepsilon_1$ = average normal strains in *2*- and *1*-directions, respectively;

$\varepsilon_{1p}, \varepsilon_{2p}$ = principal compressive and tensile strains in asymmetric shear tests, respectively;

ζ = compressive capacity reduction factor;

θ_c = angle between *d*-axis and *l*-axis;

θ_f = angle of inclined strut;

θ_p = principal angle between *2*-axis and *l*-axis;

ρ_{sc} = reinforcement ratio;

ρ_t = FRP ratio in *t*-direction;

σ_c = uniaxial compressive stress;

σ_{ct} = uniaxial tensile stress;

σ_d, σ_r = average normal stresses of concrete in the *d*- and *r*-directions, respectively;

σ_l, σ_t = average normal stresses in *l*- and *t*-directions, respectively;

σ_n^c, σ_m^c = average normal stresses of concrete in the *n*- and *m*-directions, respectively;

σ_2^c, σ_1^c = average normal stresses of concrete in *2*-and *1*-directions, respectively;

τ_{cc} = shear strength of CRuC;

$\tau_{cr,CRuC}$ = cracking shear strength of CRuC;

$\tau_{cr,RuC}$ = cracking shear strength of RuC;

τ_{lt} = applied shear stress in *l,t*-coordinate;

τ_{nm}^c = average shear stress in *n,m*-coordinate;

τ_p = shear strength of RuC;

τ_t = transition shear stress of CRuC;

φ = loading stress ratio;

Γ_{CRuC} = energy dissipated per unit volume of CRuC during shearing;

Γ_{RuC} = energy dissipated per unit volume of RuC during shearing.

Chapter 1

Introduction

1.1 RESEARCH MOTIVATION

In EU countries, more than 3 million tonnes of tyres reach the end of their lives each year [1] and worldwide 17 million tonnes [2]. Waste tyres are often disposed of in landfills, leading to significant threats to the environment and public health in particular developing countries [3]. The European Landfill Directive (Council Directives 1991/31/EC) prohibits the disposal of waste tyre products in landfills, whilst the Council Directive 2008/98/EC favours reusing or recycling scrap tyre components.

Tyres are made of high-quality vulcanised rubber belts, placed in several layers, many of which are structurally reinforced with corded steel wire or polymer textiles (see Fig. 1 – 1). The recycled rubber particles (see Fig. 1 - 2) can be extracted from car (sizes up to 10 mm) and truck (sizes in the range of 10–20 mm) end-of-life tyres, through a variety of chemical and mechanical means (e.g. shredding and granulating). These rubber particles are highly durable, and it has good strength, flexibility and a remarkable ability to maintain its volume under stress. As a result, there is a drive for finding new applications for recycled rubber, particularly in construction. This is due to the construction industry consumes more than 25 gigatons concrete per annum [1]. As a result, utilising recycled tyre compotes in concrete can create a significant impact on this worldwide problem.

In the past few decades, the feasibility of using recycled rubber in the concrete application has been assessed by many studies [2-5]. The use of rubber in concrete is mainly applied for non-structural applications [6, 7] (e.g. crash barriers[8-11], flowable fill [12], pavement [13-17], blast panels [18, 19] and acoustic or thermal insulation units [20, 21]). This is attributed to the characteristics of rubberised concrete (e.g. low strength and stiffness [22, 23], high toughness and impact resistance and good thermal and sound insulation [24-29]). More recently, researchers have found that the inclusion of rubber in concrete can enhance lateral strain of concrete under axial loading [22, 30], thus led researchers to confine rubberised concrete (RuC) in an attempt to improve axial strength and strain capacity [30]. The hypothesis is that confined RuC could be

used in the regions with high deformation demands. The research at The University of Sheffield, within the EU funded "Anagennisi" project [31], proved that fibre reinforced polymer (FRP) Confined Rubberised Concrete (CRuC) with up to 60% total aggregate replacement is able to withstand high levels of stress (up to 90 MPa) at large levels of deformation (up to 6%) [23, 30, 32-35]. Moreover, the experimental study within "Anagennisi" project examined the long-term performance and durability of RuC exposed to various environments (e.g. water or saltwater, normal (20 $^{\circ}$C) and high temperature (40 $^{\circ}$C)) for different exposure periods (100 h and 1000 h). Compared with the compressive strength of unconditioned specimens, the performance of conditioned RuC specimens was found slightly enhanced after a long exposure period [36]. The durability of FRP jackets has also been proved to be durable enough when exposed to water or alkaline environments up to 40 $^{\circ}$C, comprising only a small portion of their tensile strength. Hence, CRuC is proposed for use in structural applications, such as base isolation columns and bridge bearings, where high-strength and high-deformability are needed.
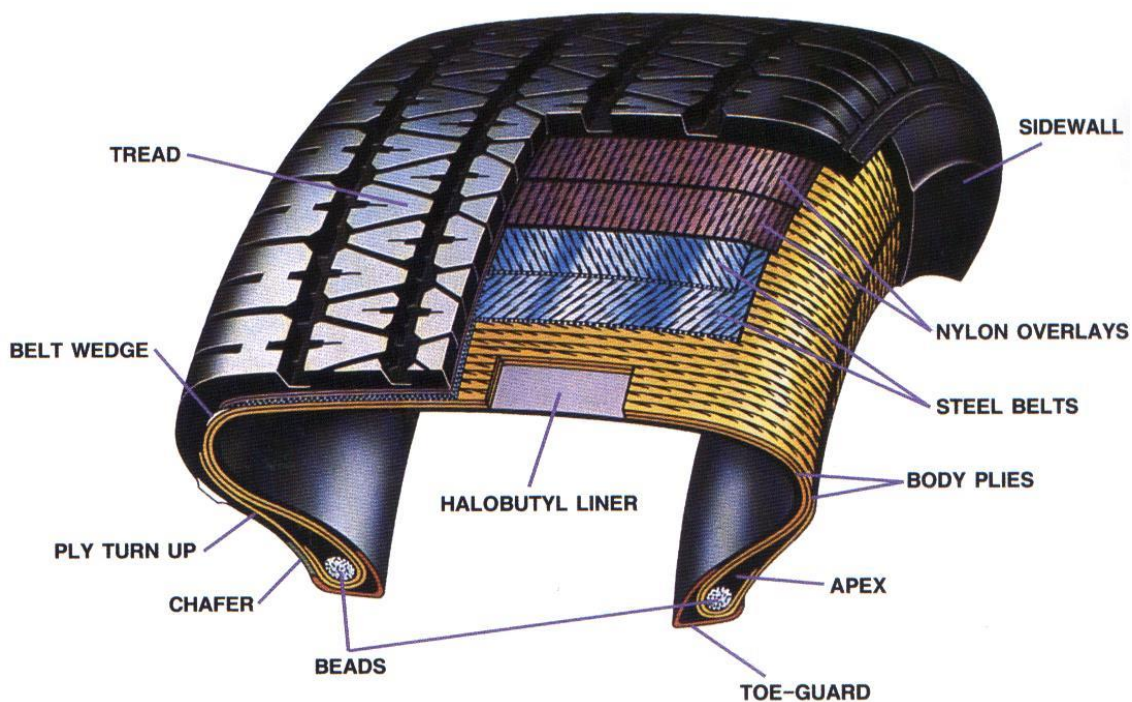
Fig. 1 - 1. Cross-section of the tyre, reproduced from [37].

Fig. 1 - 2. Rubber particles used in the concrete mix to replace sand (size:0-4 mm) and gravel (sizes: 4-10 mm and 10-20 mm).

Elements of large reinforced concrete (RC) structures can be subjected to significant lateral loads and or deformations either due to shrinkage and thermal moments or accidental actions, such as arising from the differential settlement or seismic motion. To prevent the development of large moments, highly deformable component, often made with elastomeric materials, are utilised, such as rubber bridge bearings or base isolation elements. Such components are required to carry high axial loads and at the same time be sufficiently flexible to allow large deformations. These components are, in general, not as durable as the structure itself and, hence, require inspection and regular replacement, adding costs and service disruption. Furthermore, forming plastic hinge zones at beams and columns to develop large inelastic deformations plays an important role in enhancing the ductility and deformation capacity of RC structures under extreme events. It is normally required to carefully design and detail the reinforcement to achieve ductility. However, due to the quasi-brittle behaviour of concrete, the potential deformation capacity of RC elements is still limited unless a massive amount of confinement provided. CRuC elements can potentially result in more deformable and resilient structural systems and improve the integrity of structures, which will have a big impact on RC structural design.

1.2   AIM AND OBJECTIVES

The aim of this research is to understand the mechanical characteristics of FRP-confined and unconfined rubberised concrete and propose effective modelling methods that can be used for the development of high-strength high-deformability concrete elements.

To achieve this aim, experimental and numerical work was performed. The list of the main objectives of this research is given below:

1. Examine the tensile characteristics of rubberised concrete using three-point bending beam tests along with splitting test and propose tensile stress-crack opening relations for rubberised concrete.

2. Assess the accuracy of propose relations through finite element (FE) modelling of three-point bending beam tests and compare to the performance of Model code relations.

3. Examine the compressive behaviour of FRP-confined and unconfined columns using uniaxial compressive test and assess the applicability of existing constitutive models for conventional confined concrete in the case of FRP-confined rubberised concrete.

4. Develop an analytical model for FRP-confined rubberised concrete.

5. Examine the shear behaviour of FRP-confined and unconfined rubberised concrete using asymmetric shear test and assess the capability of existing shear behaviour models for conventional reinforced concrete to describe the behaviour of FRP-confined rubberised concrete.

6. Propose a shear behaviour model by incorporating the developed tensile and compressive relations.

7. Implement the shear behaviour model in a FE analysis program.

1.3   METHODOLOGY

The research methodology includes experimental programme and numerical investigation. The experimental studies were performed to determine fundamental material properties and essential

behaviours. The experimental data will be analysis then used to calibrate the numerical model or develop the modelling tools. Fig. 1 – 4 shows the main stages of this study.

1.3.1 Experimental methods

Two rubberised concrete mixes and a reference regular concrete mix were adopted in this research to manufacturing all the specimens for different tests (Fig. 1 - 3).

To achieve objective 1, the following tests were performed:

- (a) Three-point bending beam test

  This test is developed to examine Mode I fracture of rubberised and regular concrete and determine the corresponding fracture energy, as well as complete load-deflection curve. The test results along with the determined tensile splitting strength are utilised to drive tensile stress-crack opening relations that can be implemented in finite element analysis.

- (b) Cylindrical splitting test

  This test is used to obtain the splitting tensile strength of rubberised and regular concrete.

To achieve objective 3, the following test was conducted:

- (c) Uniaxial compressive test

  This test is designed to assess the uniaxial compressive behaviour of unconfined and confined rubberised and regular concrete. The stress-strain behaviours (axial and lateral), as well as dilation behaviour, were investigated.

To achieve objective 5, the following experimental test was conducted:

- (d) Asymmetric shear test

This test is selected to study the shear behaviour of unconfined and confined rubberised concrete, as well as used to assess the feasibility of using CRuC to develop high-shear strength high-deformability elements suitable for structural applications.
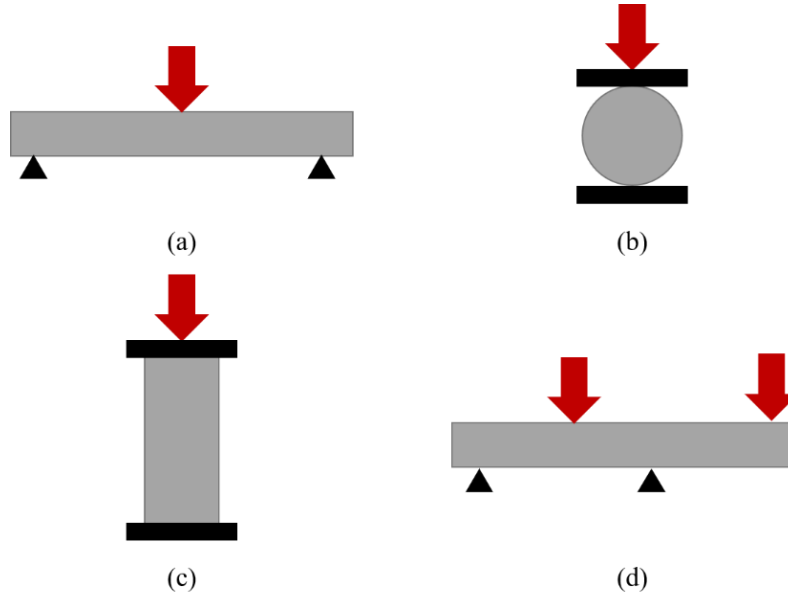
Fig. 1 - 3. Schematic of selected experimental set-up: a) Three-point bending beam test; b) Cylindrical splitting test; c) Uniaxial compressive test; and d) Asymmetric shear test)

1.3.2 Numerical Methods

Two parts of FE analyses are conducted. The first part built FE models in ABAQUS to assess the behaviours (flexural, compression and shear) of unconfined and FRP-confined rubberised concrete. Based on the FE results, objective 2 can be achieved. In the second part, two different types of material model are established:

To achieve objective 4,

- An analytical stress-strain model is programmed using MATLAB based on a new definition of an effective confinement area and considers the properties of both RC and RuC based on a series of experimentally determined relationships and the stress-strain behaviours.

To achieve objectives 6 and 7,

- A shear behaviour model of CRuC and RuC is programmed using FORTRAN and implemented in Abaqus/Standard finite element software package using the user-defined material subroutine.
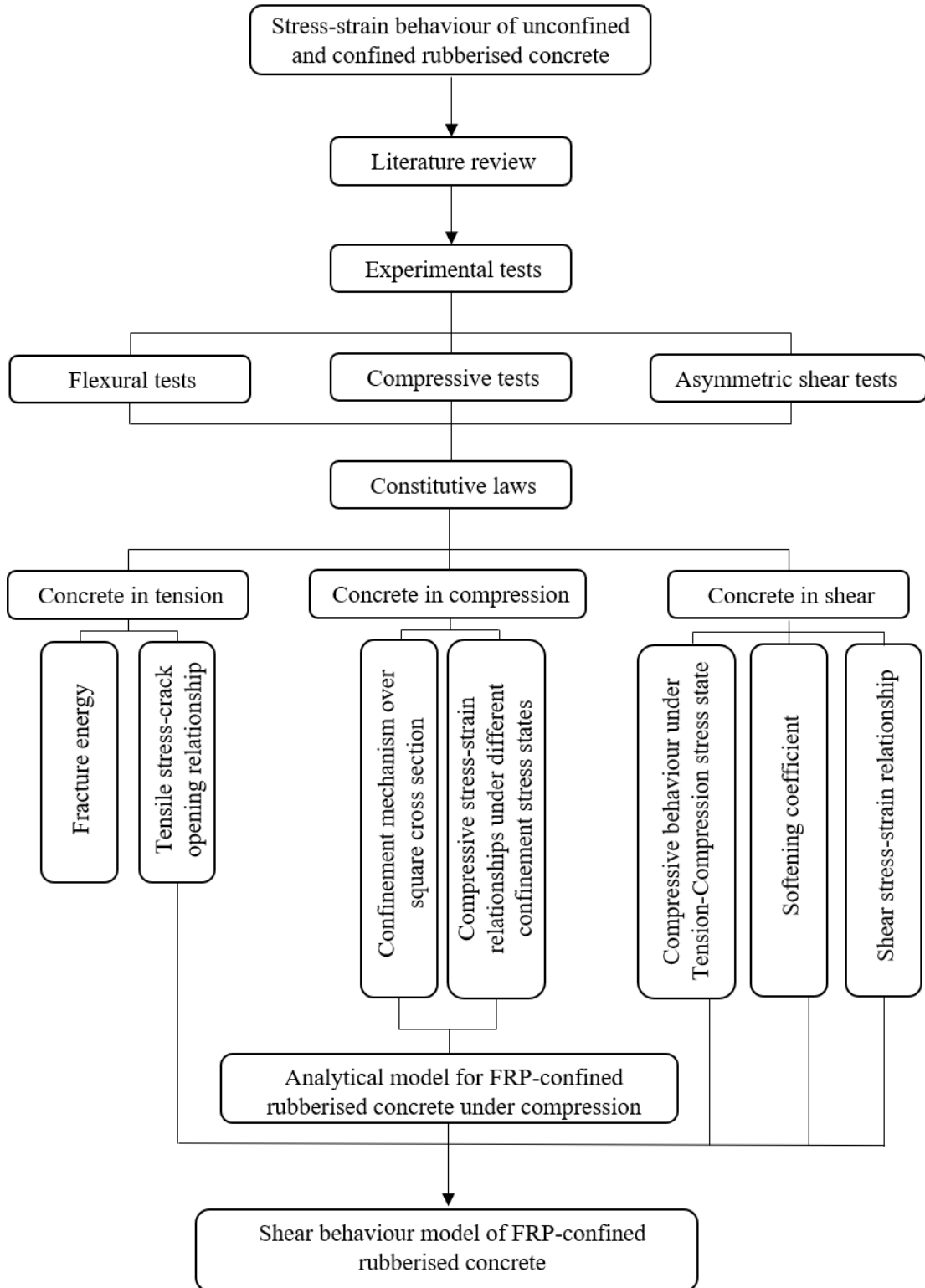
Fig. 1 - 4. Outlines of research

1.4 THESIS LAYOUT

This thesis will be presented in seven chapters and three appendices. A brief description of the thesis chapters and how they contribute to the objectives is provided as follows:

Chapter Two presents the review of the state-of-the-art in research on current study of CRuC structural application and mechanical behaviour of unconfined and confined RuC.

Chapter Three addresses objectives 1-2 and comprise an experimental investigation on the Mode I fracture behaviour of concrete incorporating different volumes of rubber particles obtained from recycled end-of-life tyres. Tensile stress-crack opening relation for RuC is proposed based on the modification of relation for conventional concrete. The performance of the proposed relation is then compared with Model Code 2010 through the general FEA package ABAQUS.

Chapter Four addresses objective 3. 128 samples, including cylinders and square columns, cast by regular concrete and rubberised concrete, are tested in axial compression. The stress-strain and dilation behaviours are examined to develop a deep understanding of the confinement mechanism over the non-circular section.

Chapter Five addresses objective 4. The effectiveness of Lam and Teng's model for FRP-confined rectangular columns and Concrete Damage Plasticity Model is assessed. An analysis-oriented model for FRP-confined concrete (RC or RuC) in the circular and non-circular section is proposed based on a new understanding of effective confinement area and volumetric strain-to-axial stress relationship.

Chapter Six is based on Wang et al. [38] and addresses objectives 5-7. It includes experimental and numerical investigations on shear behaviour of FRP-confined and unconfined RuC. It examines the suitability of existing shear behaviour models for reinforced concrete and assesses their potential use for modelling FRP-confined RuC. It proposes a shear behaviour model for

FRP-confined and unconfined RuC, which is implemented in Abaqus/Standard finite element software package using the user-defined material subroutine.

Chapter Seven comprises concluding remarks based on Chapters 3-6. Additional comments and recommendations for future work are also provided.

Appendix A includes detailed information on all experiments (A1. Flexural tests; A2. Compressive tests and A3. Asymmetric shear tests).

Appendix B provides established finite element models for the experiments reported in Appendix A.

Appendix C shows the developed code for the implantation in the FEA package ABAQUS (C1. Shear behaviour model of FRP-confined and unconfined RuC and C2. Compressive behaviour model of FRP-confined concrete columns).

1.5 REFERENCES

1.   Gursel, A.P., et al., *Life-cycle inventory analysis of concrete production: A critical review.* Cement and Concrete Composites, 2014. **51**: p. 38-48.
2.   Eldin, N.N. and A.B. Senouci, *Rubber-tire particles as concrete aggregate.* Journal of materials in civil engineering, 1993. **5**(4): p. 478-496.
3.   Topcu, I.B., *The properties of rubberized concretes.* Cement and Concrete Research, 1995. **25**(2): p. 304-310.
4.   Siddique, R. and T.R. Naik, *Properties of concrete containing scrap-tire rubber– an overview.* Waste Management, 2004. **24**(6): p. 563-569.
5.   Khatib, Z.K. and F.M. Bayomy, *Rubberized Portland cement concrete.* Journal of materials in civil engineering, 1999. **11**(3): p. 206-213.
6.   Freakley, P.K. and A.R. Payne, *Theory and practice of engineering with rubber.* 1978: Applied Science Publishers.
7.   Sienkiewicz, M., et al., *Progress in used tyres management in the European Union: a review.* Waste Management, 2012. **32**(10): p. 1742-1751.
8.   Toutanji, H.A., *The use of rubber tire particles in concrete to replace mineral aggregates.* Cement and Concrete Composites, 1996. **18**(2): p. 135-139.
9.   Reda Taha, M.M., et al., *Mechanical, fracture, and microstructural investigations of rubber concrete.* Journal of materials in civil engineering, 2008. **20**(10): p. 640-649.
10. Atahan, A.O. and A.Ö. Yücel, *Crumb rubber in concrete: static and dynamic evaluation.* Construction and Building Materials, 2012. **36**: p. 617-622.
11. Najim, K.B. and M.R. Hall, *Workability and mechanical properties of crumb-rubber concrete.* Proceedings of the Institution of Civil Engineers-Construction Materials, 2012. **166**(1): p. 7-17.
12. Pierce, C. and M. Blackwell, *Potential of scrap tire rubber as lightweight aggregate in flowable fill.* Waste Management, 2003. **23**(3): p. 197-208.
13. da Silva, F.M., et al., *Investigation on the properties of concrete tactile paving blocks made with recycled tire rubber.* Construction and Building Materials, 2015. **91**: p. 71-79.
14. Cairns, R., H. Kew, and M. Kenny. *The use of recycled rubber tyres in concrete construction.* in *Sustainable Waste Management and Recycling: Used/Post-Consumer Tyres. Proceedings of the International Conference of the Concrete and Masonry Research Group 2004.* 2004.
15. Najim, K. and M. Hall, *A review of the fresh/hardened properties and applications for plain-(PRC) and self-compacting rubberised concrete (SCRC).* Construction and building materials, 2010. **24**(11): p. 2043-2051.
16. Kardos, A.J. and S.A. Durham, *Strength, durability, and environmental properties of concrete utilizing recycled tire particles for pavement applications.* Construction and Building Materials, 2015. **98**: p. 832-845.
17. Hesami, S., I.S. Hikouei, and S.A.A. Emadi, *Mechanical behavior of self-compacting concrete pavements incorporating recycled tire rubber crumb and reinforced with polypropylene fiber.* Journal of cleaner production, 2016. **133**: p. 228-234.
18. Naito, C., et al., *Crumb rubber concrete performance under near-field blast and ballistic demands.* Journal of Materials in Civil Engineering, 2013. **26**(9): p. 04014062.

19.   Naito, C., et al., *Assessment of crumb rubber concrete for flexural structural members.* Journal of Materials in Civil Engineering, 2013. **26**(10): p. 04014075.

20.   Sukontasukkul, P., *Use of crumb rubber to improve thermal and sound properties of pre-cast concrete panel.* Construction and Building Materials, 2009. **23**(2): p. 1084-1092.

21.   Holmes, N., A. Browne, and C. Montague, *Acoustic properties of concrete panels with crumb rubber as a fine aggregate replacement.* Construction and Building Materials, 2014. **73**: p. 195-204.

22.   Bompa, D., et al., *Experimental assessment and constitutive modelling of rubberised concrete materials.* Construction and Building Materials, 2017. **137**: p. 246-260.

23.   Raffoul, S., et al., *Optimisation of rubberised concrete with high rubber content: an experimental investigation.* Construction and Building Materials, 2016. **124**: p. 391-404.

24.   Medina, N.F., D. Flores-Medina, and F. Hernández-Olivares, *Influence of fibers partially coated with rubber from tire recycling as aggregate on the acoustical properties of rubberized concrete.* Construction and building Materials, 2016. **129**: p. 25-36.

25.   Ghizdăveț, Z., et al., *Sound absorbing materials made by embedding crumb rubber waste in a concrete matrix.* Construction and Building Materials, 2016. **124**: p. 755-763.

26.   Marie, I., *Thermal conductivity of hybrid recycled aggregate–Rubberized concrete.* Construction and Building Materials, 2017. **133**: p. 516-524.

27.   Dehdezi, P.K., S. Erdem, and M.A. Blankson, *Physico-mechanical, microstructural and dynamic properties of newly developed artificial fly ash based lightweight aggregate–Rubber concrete composite.* Composites Part B: Engineering, 2015. **79**: p. 451-455.

28.   Liu, F., et al., *Dynamic mechanical behaviour of recycled crumb rubber concrete materials subjected to repeated impact.* Materials Research Innovations, 2015. **19**(sup8): p. S8-496-S8-501.

29.   Guo, Y.-c., et al., *Compressive behaviour of concrete structures incorporating recycled concrete aggregates, rubber crumb and reinforced with steel fibre, subjected to elevated temperatures.* Journal of cleaner production, 2014. **72**: p. 193-203.

30.   Raffoul, S., et al., *Behaviour of unconfined and FRP-confined rubberised concrete in axial compression.* Construction and Building Materials, 2017. **147**: p. 388-397.

31.   Pilakoutas, K., et al. *Innovative reuse of all tyre components in concrete: the Anagennisi project.* in *Proc. of the International Conference on Sustainable Structural Concrete.* 2015.

32.   ABAQUS, V., *6.14 documentation.* Dassault Systemes Simulia Corporation, 2014.

33.   Papastergiou, P., *A confinement model for concrete wrapped of pretensioned with frp.* 2010, The University of Sheffield.

34.   Youssf, O., M.A. ElGawady, and J.E. Mills. *Experimental investigation of crumb rubber concrete columns under seismic loading.* in *Structures.* 2015. Elsevier.

35.   Son, K.S., I. Hajirasouliha, and K. Pilakoutas, *Strength and deformability of waste tyre rubber-filled reinforced concrete columns.* Construction and building materials, 2011. **25**(1): p. 218-226.

36.   Abdulaziz Alsaif, H.F., Andreea Serbescu, Lampros Koutas, and P. Papastergiou, *D2.4 - Technical report on long-term performance of modified rubberised concrete elements (unconfined and confined)*, in *Innovative Reuse of all Tyre Components in Concrete*. 2014.

37.   Tyre, E. and R.M. Association, *Reinforcing Fillers in the Rubber Industry-- Assessment as potential nanomaterials with focus on tyres*. 2010.

38.   Wang, Z., et al., *Shear Behavior Model for FRP-Confined and Unconfined Rubberized Concrete*. Journal of Composites for Construction, 2019. **23**(5): p. 04019039.

Chapter 2

Literature Review

2.1   STRUCTURAL APPLICATIONS OF FRP-CONFINED RuC

In recent years, researchers investigate the feasibility of utilising FRP-confined RuC to develop high strength and high deformable elements that can be used in high-value structural applications:

1) Coupling beam

Coupling beams (Fig. 2 - 1) in the couple wall system, which often implemented in medium to high rise buildings to enhance structure performance under large lateral loads or seismic. The coupling beam requires to transfer high shear forces and develop large shear deformations, must have excellent ductility and not progressively loss strength under cyclic load [1]. The investigations on the coupling beam are mainly focused on developing an appropriate reinforcement detailing to improve the strength and ductility [2, 3]. However, its performance is limited by the brittle behaviour of concrete. Furthermore, the complicated reinforcement detailing (Fig. 2 - 2) developed by Paulay at el. [4] and adopted by current codes (EC8 [5] and ACI 318-14 [6]) is difficult to assemble and requires a significant amount of reinforcement.

Recently, researchers at the University of Sheffield have developed a highly deformable concrete (HDC) by replacing the mineral coarse and fine aggregates in concrete with rubber particles external bonded by FRP. The proof-of-concept study (Fig. 2 - 3) to use HDC in the coupling beam has been studied by [7]. The results in Fig. 2 - 4 confirm that confining RuC with CFRP jackets can lead to highly deformable elements under shear conditions and increase the strength of RuC to levels required from structural elements, hence opening the possibility of using CRuC in applications where large strength and shear deformation are required.

Based on the promising results found on the pilot study, large scale experimental study (Fig. 2 - 5) were conducted by Escolano-Margarit et al. [8] to assess the feasibility of using HDC in the coupling beam. Four coupling beams were tested under cyclic displacement reversal. The experimental results showed the HDC could develop a high level of shear stress (4 MPa), which was 1.5 times higher than required in current codes. Furthermore, HDC coupling beam

demonstrated a very stable hysteresis response with minimum pinching and maximum energy dissipation among those four beams (see Fig. 2 - 6). Moreover, HDC coupling beam showed a gradual failure behaviour with an ultimate rotation up to 8%, which resulted in a value of ductility up to 6.
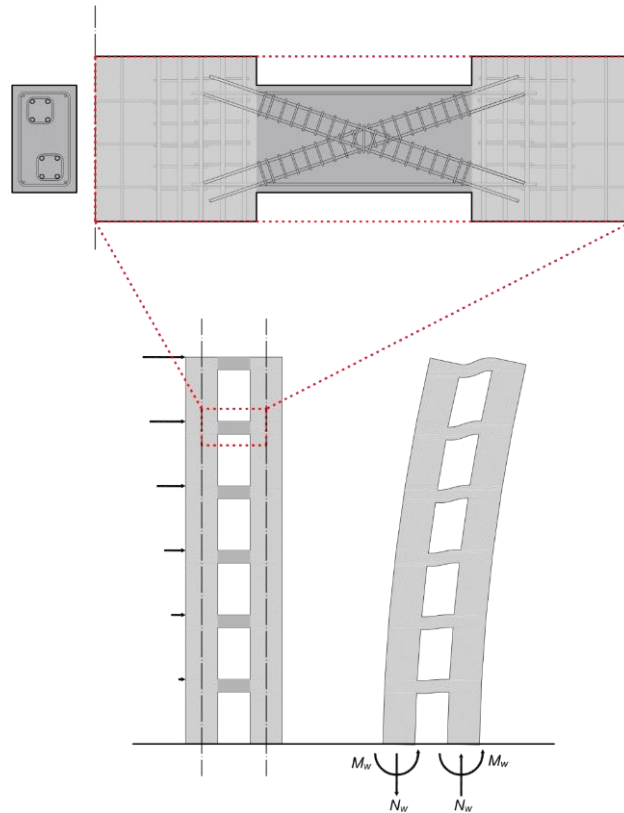
Fig. 2 - 1. Reinforced Concrete structural coupled walls adopted from [8].
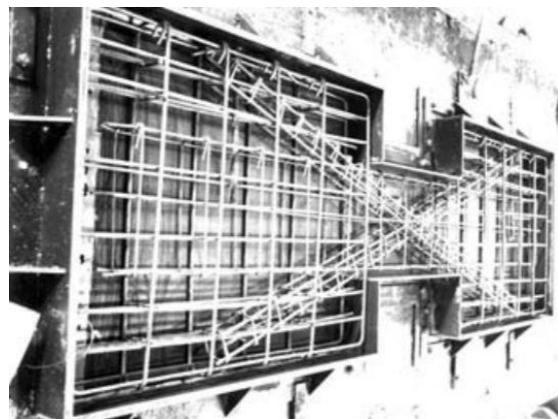
Fig. 2 - 2. Reinforcement detailing of coupling beam, adopted from [4].
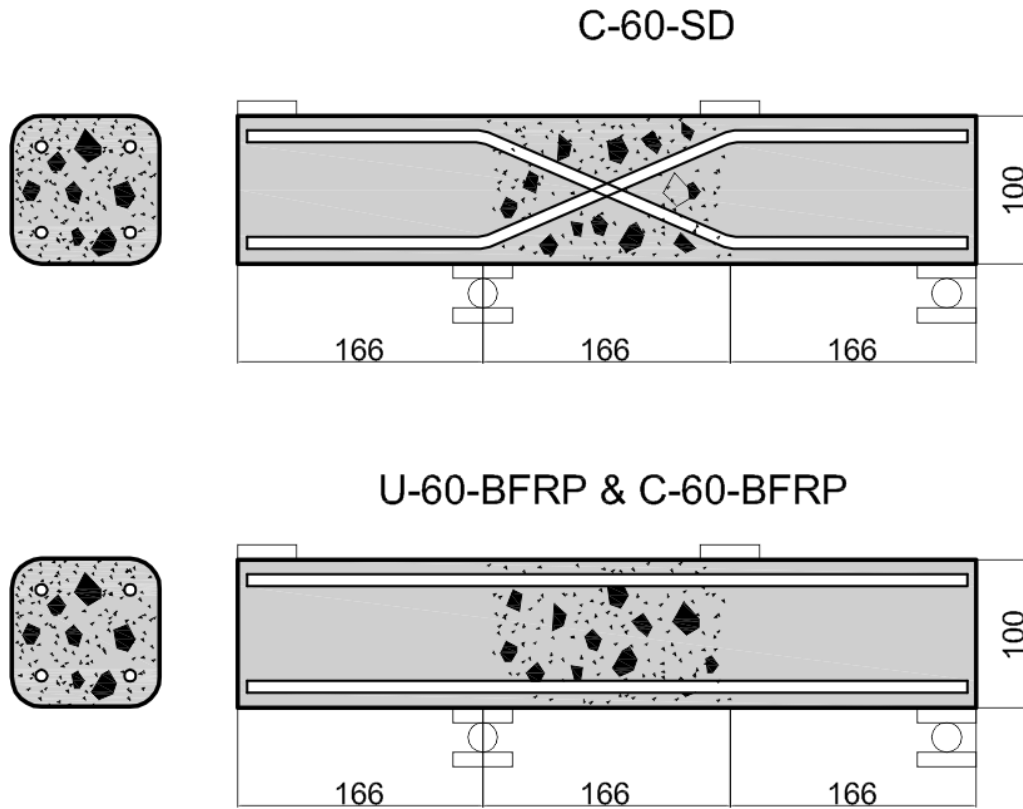
Fig. 2 - 3. Specimen dimensions and reinforcement layout.
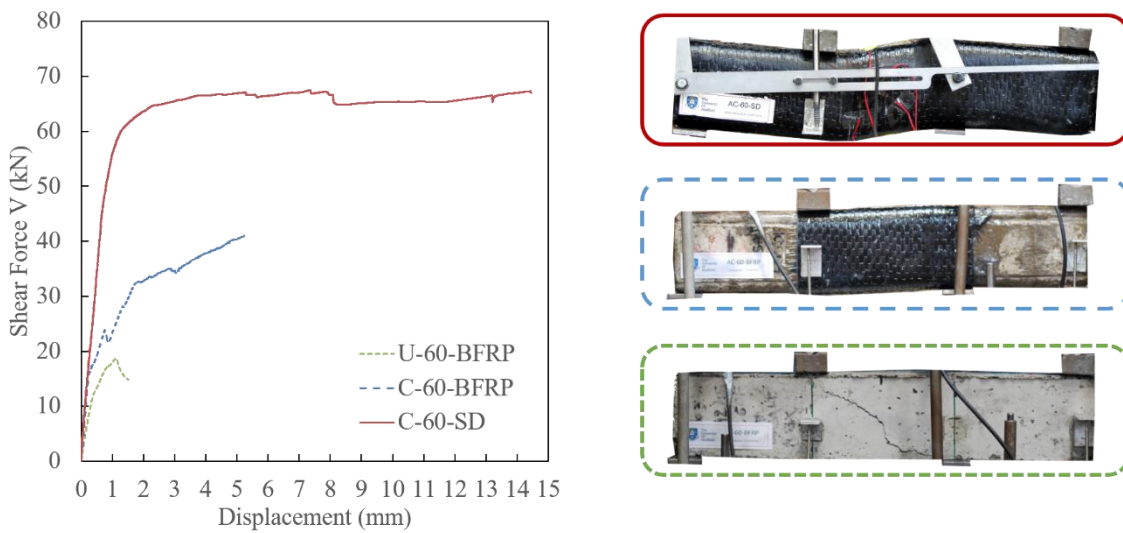
Fig. 2 - 4. Shear Force VS Deflection and failure modes.

Fig. 2 - 5. Test setup of large scale coupling beam test, adopted from [8].
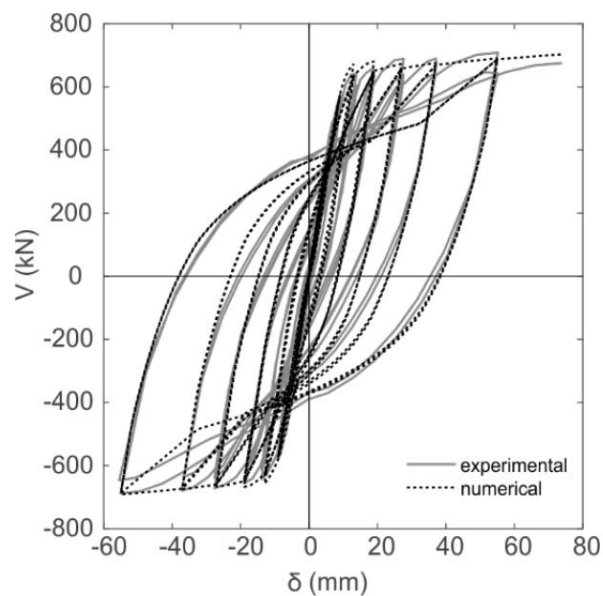
Fig. 2 - 6. Shear force vs displacement hysteretic curve, adopted from [8].

2) High deformable short columns

Son et al. [9] assessed the pure axial compressive behaviour of rectangular reinforced RuC columns in terms of compressive strength and deformation capacity. To avoid excessive strength degradation, only 15 % of rubber replacement volume of fine aggregates was used. As expected, the load-carrying capacity of the column specimens decreased with increasing the rubber content. However, the reinforced RuC columns achieved twice larger lateral deformations when compared

to regular concrete columns. This lead to a much higher energy dissipation capacity and ductility, which are two key parameters in seismic considerations.

Youssf et al. [9] examined the behaviour of FRP-confined reinforced RuC circular columns under a combination of axial and incrementally increasing reversed cyclic loads. The RuC manufactured the specimens with 20 % rubber replacement by volume of fine aggregates. Damping, snap-back tests and cyclic test were carried out. Compared with reinforced regular concrete columns, the FRP-confined reinforced RuC column exhibit larger hysteric damping ratio (+13%) and energy dissipation capacity (+150%) (Fig. 2 - 7). The longitudinal reinforcement strains recorded in FRP-confined reinforced RuC were higher than those in the regular concrete column, making better use of reinforcement.
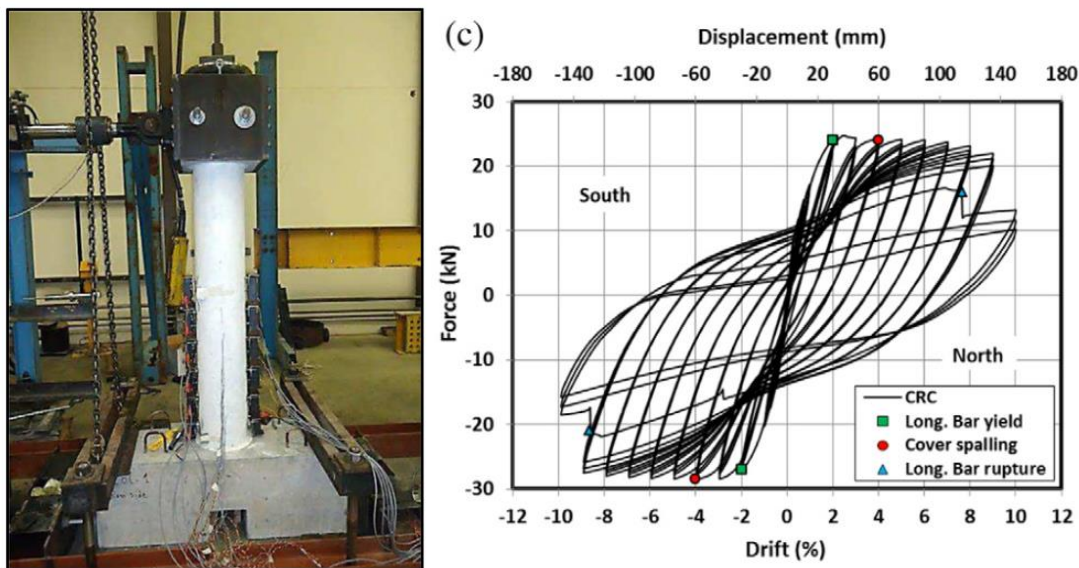
Fig. 2 - 7. Hysteretic behaviour of FRP-confined reinforced RuC column, adopted from [9].

Elghazouli et al. [10] investigate the cyclic performance of reinforced rubberised concrete (up 60 % rubber replacement by volume of fine and coarse aggregates) circular columns (see Fig. 2 - 8) with and without external FRP confinement. The investigation found reinforced RuC columns have a soft crushing behaviour resulting in a preferable energy dissipation and ductility properties. The test results indicate the reinforced RuC columns able to achieve a better balance between ductility and bending capacity compared with their regular concrete counterparts, especially

subject to low axial load. Particularly, the reinforced RuC columns strengthened by AFRP shows a recovered high axial strength and provides a more stable hysteretic response than regular concrete columns (see Fig. 2 - 9).

Fig. 2 - 8. Specimen details: reinforced rubberised concrete column (left) and AFRP-confined reinforced rubberised concrete column (right), adopted from [10].
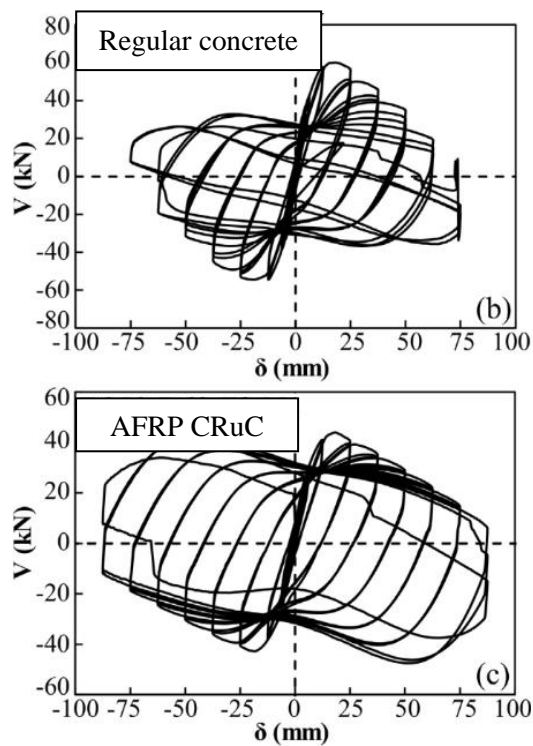
Fig. 2 - 9. Load-deformation (V-δ) response for regular concrete columns (top) and AFRP-confined rubberised concrete column (bottom), adopted from [10].

2.2 MIX DESIGN OF RuC

Table 2 – 1 summarises the mix proportions for RuC adopted from a detailed mix optimisation study conducted by Raffoul et al.[11], in which acceptable strength loss and desirable workability were achieved. The RuC mix was developed on the basis of a reference regular concrete mix (ρ_{vr} = 0), which is typically used in bridge piers design with target 28-day compressive strength of 60 MPa. In the RuC mixes, 20% of the cement (CEM II - 52.5N) was replaced by 50% fly ash [12] and 50% silica fume [13]. Silica fume and fly ash were added to increase flowability and strength and to improve particles packing. In this study, two RuC mixes were used with 30% and 60% of rubber contents, respectively. The specific gravity of mineral aggregates was considered to be 2.65, and that of rubber was 0.8 [11]. The quantities of rubber particles consumed in the mixes were 165 kg/m^3 and 330 kg/m^3, respectively.

Table 2 - 1. Mix proportions for optimised mix used in this study.

ρ_{vr}	CEM II - 52.5 (MPa)	Silica Fume	Pulverized Fuel Ash	Aggregates			Rubber Particles			Plasticizer	Superplasticizer	Water	Designed density
				0/5 mm	5/10 mm	10/20 mm	0/4 mm	4/10 mm	10/20 mm				
	kg/m^3									L/m^3			kg/m^3
0	340	42.5	42.5	820	364	637	-	-	-	2.5	5.1	150	2396
30%	340	42.5	42.5	574	255	456	74	17	75	2.5	5.1	150	2026
60%	340	42.5	42.5	328	146	255	149	33	148	2.5	5.1	150	1634

2.3 TENSILE BEHAVIOUR OF RuC

To date, there are still no standardised test procedures to obtain the direct tensile strength of concrete [14], owing to local stress concentration. However, the tensile strength of concrete is crucial to determine the cracking resistance and one of the essential properties of concrete in design and research. The tensile characteristics of RuC are even more difficult to obtain from direct tensile tests as the uneven distribution of rubber particles, means that the tensile strength, even of a small linear element, is non-uniform [15]. Hence, the tensile performance of RuC is normally derived from splitting or flexural tensile tests [16-18]. Experimental evidence [11, 15, 19] has shown that the tensile strength (splitting or flexural) of RuC decreases with increasing of

rubber content. Furthermore, the tensile strength values obtained from the two types of tests are not equivalent [14]. The maximum strength derived from flexural tests is governed by the concrete strength on the tension surface of the beam and can be calculated according to the formulas in ASTM C 293 and ASTM C 78, which assume concrete is a linear elastic material throughout the loading history. This assumption is not correct when specimens are approaching failure and lead to higher failure stress. However, the influence of this assumption has been proven not significant compared with concrete variability. The flexural strength can be affected more pronounced by other several factors, such as specimen dimensions and size, coarse aggregate size, loading rate and moisture conditions [20]. The flexural strength decreases with increasing specimens size, depth of beam and size of coarse aggregate size, but increases with increasing loading rate [21-24]. The moisture condition has a significant effect on flexural strength. The flexural strength obtained in a saturated condition has been found higher than the strength determined in a drying condition (up to 33 % [25]) [26-28]. This is due to the drying shrinkage induces cracks, which act as stress concentrators and minimise the effective cross-section of the specimens. Thus the specimens should be cured under the same condition as the concrete structure but tested in a saturated condition [14]. Furthermore, for a certain beam size, the flexural strengths determined by four-point bending tests are lower than those determined by three-point bending tests (differences should under 15%) [22-24]. The three-point bending tests are recommended by RILEM to measure the fracture energy of motor and concrete [29]. In the case of the splitting test, the majority of the concrete perpendicular to the loading direction is under constant tensile stress, thus the splitting tensile strength is closer to the strength determined from direct tensile tests and much less affected by specimen length and moisture condition [30], but this test does not provide much information in the σ-ε characteristics. On the other hand, flexural tests produce a more stable load-deflection curve than splitting tests and can demonstrate the ability of RuC in energy dissipation after cracking [15]. Such test results prove that the flexural post-cracking performance of RuC is enhanced by the replacement of aggregates with rubber particles [31]. This can be explained by the ability of rubber particles to store elastic energy and dissipate it through pull-

out. Since both indirect tensile tests do not provide a direct measure of the tensile stress-strain or stress-crack opening relations, there is a lack of a tensile constitutive model for this novel material. This limits the development of numerical models that could demonstrate the applicability of RuC in structural applications.

The Concrete Damage Plasticity (CDP) model is widely used to simulate the failure behaviour of concrete in finite element analysis [32, 33]. The CDP treats cracked concrete as a continuum and cracks are represented by cracking strains smeared over a certain width of fracture zone, or the width of a finite element. Thus the constitutive behaviour of cracked concrete is modelled using the stress-strain relations combined with a damage parameter [34]. The successful finite element modelling of RuC using CDP also requires the complete uniaxial tensile stress-strain or stress-crack opening relationships. Although these relationships cannot be obtained from direct tensile tests, it is possible to obtain indirectly using flexural test result. In addition, if a softening material model is only described on the basis of stress-strain relationships, strain-softening can lead to spurious sensitivity with respect to the size of elements due to the localisation of deformation [35, 36]. Mesh refinement leads to a smaller strain localisation band width and reduces global energy dissipation. One remedy for this spurious mesh sensitivity issue is to use the crack band technique [37], in which the crack opening displacement distribute within crack band with (the effective width of the fracture zone) or characteristics length of the element in FE analysis. This ensures that different size elements dissipate identical fracture energies [38].

2.4 COMPRESSIVE BEHAVIOUR OF UNCONFINED AND FRP-CONFINED RuC

External confinement by FRP jacketing provides an efficient method to increase the load and deformation capacities of RC elements. Extensive studies were conducted to examine the compressive behaviour of FRP-confined regular concrete (CRC) in both circular and non-circular sections and evaluate the confinement effectiveness of FRP jackets [39-44]. For circular sections,

the effect of FRP jacketing in the stress-strain behaviour is well understood as the concrete is uniformly confined, leading to the same stress-state over the section. On the contrary, for non-circular sections, the concrete is non-uniformly confined, which results in variations in stress-state in different parts of the section. This is due to variable confinement pressure with higher pressure at the corners and practically no pressure at the central part of the flat sides. Thus the confinement action depends mainly on the curvature of the corner and tests reported in the literature show that corner radius can also significantly affect the eventual confinement effectiveness [45-47]. Rounding the corners of the cross-section is typically recommended to improve confinement effectiveness and reduce the detrimental effect of sharp corner on the rupture strength of FRP due to biaxial stresses.

Raffoul et al. [41] showed that for CRuC specimens, the confinement provided by FRP jacket is activated earlier than in normal concrete and results in a more uniform FRP strain distribution. By utilising these advantages, the confinement effectiveness in CRuC in circular sections has been observed to be higher than that in CRC. Therefore, it is expected that the effectiveness of confinement for RuC elements in non-circular cross-section would be considerably higher than CRC elements. However, this enhancement has not been assessed experimentally.

Since the determination of the moment-curvature of reinforced concrete elements depends on knowledge of accurate stress-strain relationship for the FRP-confined concrete, extensive studies have been carried out and many stress-strain models have been developed. Although the behaviour of FRP-confined circular columns can be closely predicted by several models [48-51], many stress-strain models have been proposed for FRP-confined columns. this is not the case for FRP-confined non-circular columns. Researchers normally relate the behaviour of rectangular columns to that of circular columns through the use of a geometrically defined shape factor (e.g. Lam and Teng's model [40]). This shape factor is based on the assumption that the rectangular cross-section can be sub-divided into an unconfined and a confined area (see Fig. 2 - 10). However, this assumption does not reflect the actual stress distribution over the section [52]. Moreover, the FRP rupture strain in FRP-confined columns is always lower than the FRP failure

tensile strain from direct coupon tests, and it is affected by the presence of sharp corners. This detrimental effect is usually considered by an empirically determined reduction factor instead of through the mechanical properties of concrete and FRP.

Several researchers attempted to gain a better understanding of the confinement mechanism through finite element analysis using concrete damaged plasticity model (CDPM) [42, 44, 53, 54]. It was found that an accurate lateral strain-to-axial strain relationship is crucial to yield a reliable prediction for FRP-confined concrete and that the dilation angle is the main influencing parameter. Moreover, the CDPM cannot predict the behaviour of heavily confined concrete [44, 53]. That implies that the CDPM may not be successfully used for FRP-confined RuC (CRuC). Therefore, the feasibility of using CDPM to predict the behaviour of CRuC need to be verified.
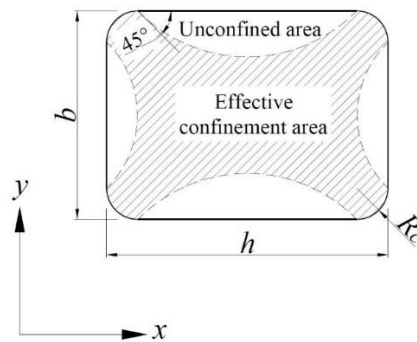
Fig. 2 - 10. Effective confinement area for rectangular section reproduced from Lam and Teng [40].

2.5   SHEAR BEHAVIOUR OF UNCONFINED AND FRP-CONFINED RuC

In the past century, the understanding of the structural performance of concrete in shear has grown significantly around the concept of the truss analogy. A significant step forward was the development of softened concrete struts by Robinson and Demorieux [55], which have reduced compressive strength in the presence of principal tensile stress. Various rational softened truss models have been proposed on the basis of the smeared-crack concept. Vecchio and Collins [56] proposed the compression field theory (CFT) to predict the non-linear behaviour of reinforced

concrete (RC) elements by implementing softened stress-strain characteristics for concrete in compression. This was the first attempt to quantify the softening parameter as a function of the two principal strains. The rotating-angle softened truss model (RA-STM) was generalized by Hsu and his co-workers [57, 58] for shear and torsion of RC members. This model considered both concrete compression softening and tension stiffening effect. It assumed cracks will develop in a direction perpendicular to the principal tensile stress and "rotate" to follow the changing principal stress during loading. Since the crack angle assumed coincides with the principal stress direction, neither the CFT nor the RA-STM can adequately represent shear behaviour, as concrete shear resistance cannot be developed along the principal direction. In contrast, the fixed-angle softened truss model (FA-STM) [59, 60] assumes cracks to be oriented in the direction of the applied principal compressive stresses and are fixed at this angle thereafter. As shear stresses can develop along the crack direction, the FA-STM can account for the concrete contribution in shear resistance. The predictions of these rational shear models are in good agreement with various types of conventional RC structures subjected to shear or torsion.

In the past two decades, engineers started to use more advanced materials to strengthen reinforced concrete, such as FRP [61-64], owing to its superiority, such as corrosion-resistant properties, high strength-to-weight ratio and excellent thermo-mechanical. The FRP strengthened reinforced concrete structures exhibit a more ductile behaviour and can develop larger deformations compare to conventional structures. In addition, there are several implementation methods of FRP sheets for shear strengthening, which shown in Fig. 2 - 11. Thus the shear resistance mechanism in FRP strengthened elements is different from that in conventional concrete [62, 65, 66] and expected to be more complicated. Several analytical models [67] were proposed to consider shear contribution of FRP. However, the prediction of those models shows a large scatter compared to experimental data. This is attributed to the total shear capacity of FRP strengthened RC members is the sum of shear contribution of each component (V_c for concrete, V_s for steel and V_{FRP} for FRP sheets) [68]. However, there is a certain level of interaction exist between these components. For example, tension stiffening can be observed for the concrete in RC members and the steel reinforcement in

FRP strengthened RC members may not reach the yielding point [69]. Hence, a rational shear model for FRP strengthened RC members should consider the constitutive models of each material as well as the interactions between each component. Until now, no study on shear behaviour of CRuC has been reported and the applicability of the shear theories for conventional concrete has not been assessed for CRuC. It is clear that there is lack of knowledge on the material properties of CRuC and an absence of the numerical analytical models that can be used to analyse structures and imposes a barrier for the use of CRuC in structural applications.

    a) Fully wrap   b) U-wrap   c) Side bonding
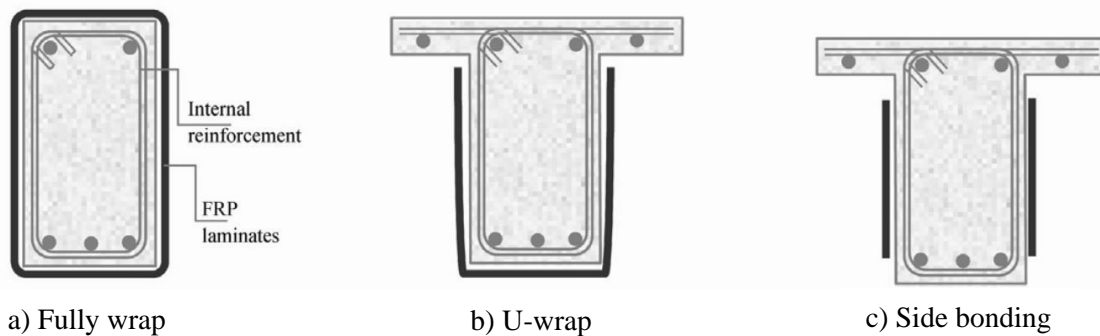
Fig. 2 - 11. Implementation methods for FRP shear strengthening, picture adopted from [70].

2.6 STATE OF THE ART ON MATERIAL SHEAR TEST

Similar to direct tensile test, there is no standard shear test and procedures for determining the shear strength of concrete, owing to its complexity [71, 72]. Several shear testing methods have been proposed to determine the shear characteristic of concrete. Therefore, a finite element analysis has been performed to provide evidence to chose the most suitable test. Fig. 2 - 12 shows the damage (a) and stress contours (b) of the double shear test. Fig. 2 - 13 shows the stress state of the midpoint at the shear plane. As can be seen, the double shear test has a relatively simple geometry that allows fairly easy to carry out. However, the stress state of the midpoint at the shear plane is a combination of high normal and shear stress, thus results in the shear strength obtained from this test is higher than the other test, occupying 17%-25% of cubic compressive strength [73].

(a) Crack pattern

(b) Shear stress
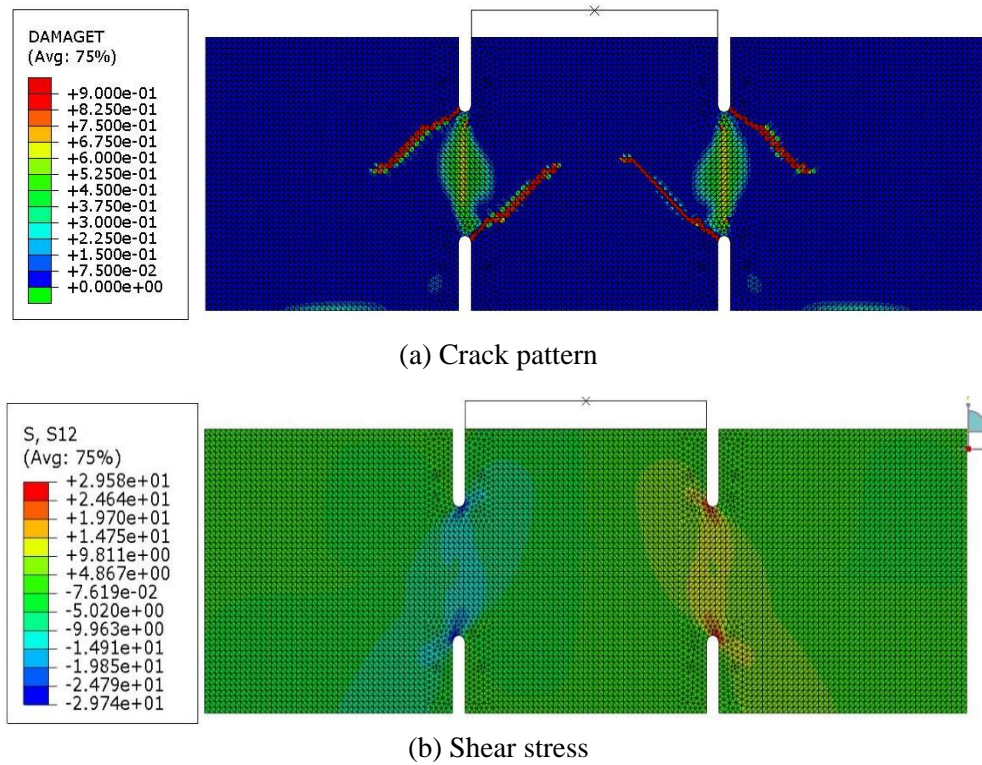
Fig. 2 - 12. FE analysis of the double shear test.
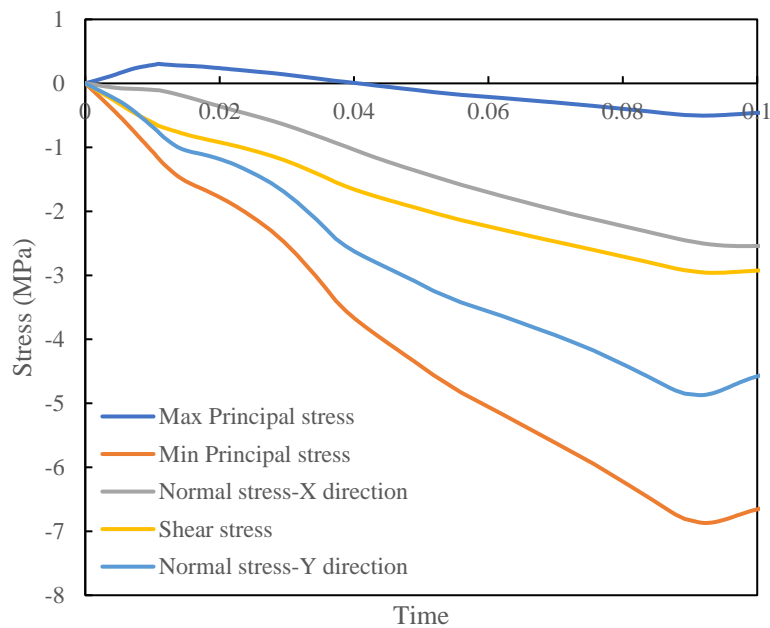
Fig. 2 - 13. Stress state of the mid-point at shear plane of the double shear test.

The "Z" push-off shear test can be processed with simple preparation, but FE analyses (see Fig. 2 - 14 and 15) have shown that the specimens have tensile stress exist at the crack tips, which is a mixed stress condition causes mixed-mode failure [74]. Due to high normal stresses exist on

the. The finite element analyses by the author have shown that the push-off specimen has tensile stresses at the crack tips, which is a mixed stress condition[74].

(a) Crack pattern   (b) Shear stress
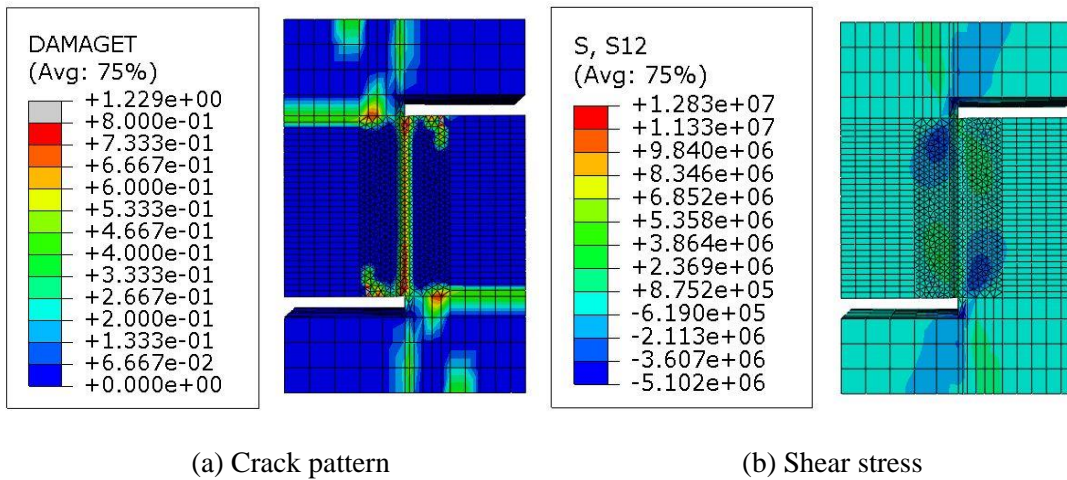
Fig. 2 - 14. FE analysis of the "Z" push-off shear test.
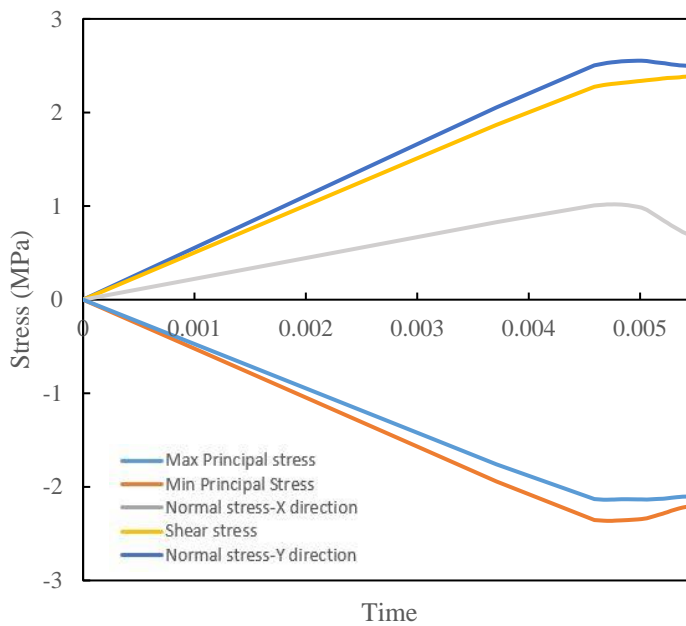
Fig. 2 - 15. Stress state of the mid-point at the shear plane of the "Z" push-off shear test.

Fig. 2 – 16 and 17 show the numerical modelling of axisymmetric shear test with 90-degree notches. This loading configuration was initially proposed by Iosipescu [75] and very attractive. However, due to the stress concentration at the notch, crack normally starts from the tip of the notch, are not at the position where has maximum shear stress. Some researchers [76-78] found

the failure of this test is governed by mode I fracture. It worth to be noticed that the stress state of the mid-pint at shear span shows a pure shear stress state (see Fig. 2 – 17). Thus indicates the loading configuration of this test is suitable for determining pure shear strength.

(a) Crack pattern

(b) Shear stress
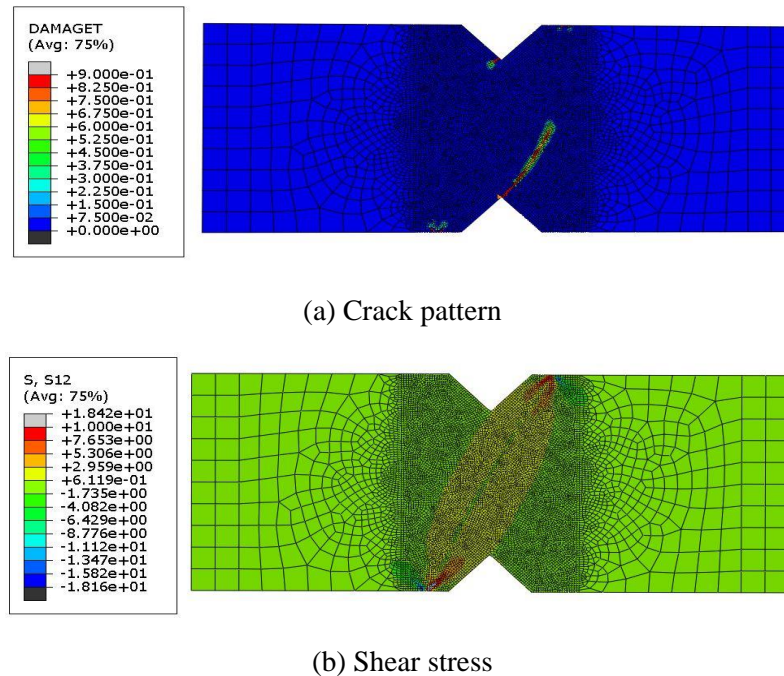
Fig. 2 - 16. FE analysis of the axisymmetric shear test with 90-degree notches.
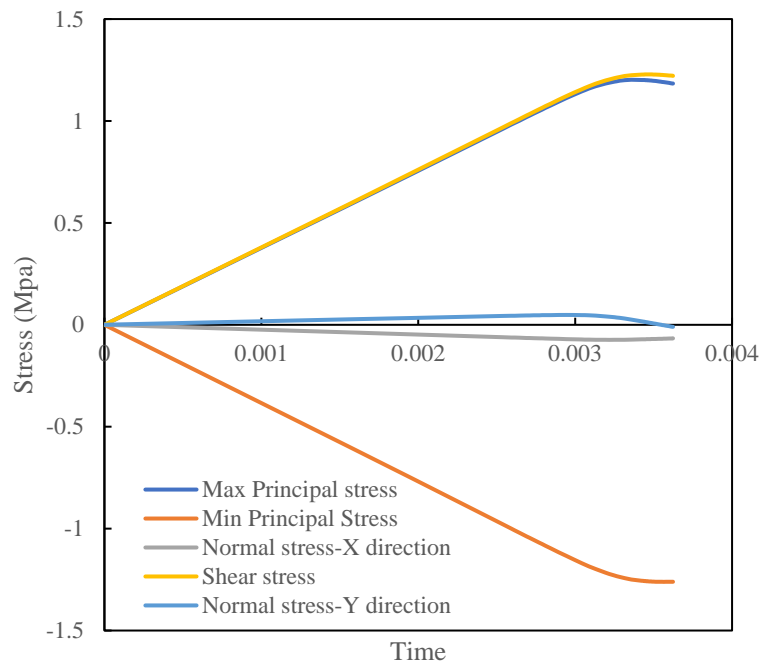
Fig. 2 - 17. Stress state of the mid-point at shear plane of the axisymmetric shear test with 90-degree notches.

In Fig. 2 – 18 and 19, a modified axisymmetric shear test by replacing notches with reduced width in mid-span has been studied, which was proposed by [79]. This test set-up is especially suitable to characterise the shear strength of concrete as the stress state in the mid-span section approaches pure shear stress, with a uniformly distributed shear stress and low normal stress in both X and Y direction. Therefore, the shear strength obtained from this test can be trusted with comparatively accurate.
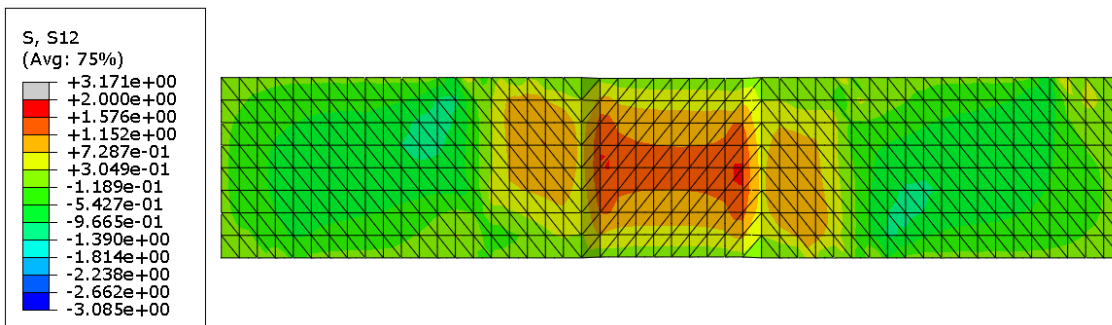
Fig. 2 - 18. FE analysis of the axisymmetric shear test with reduced width in mid-span
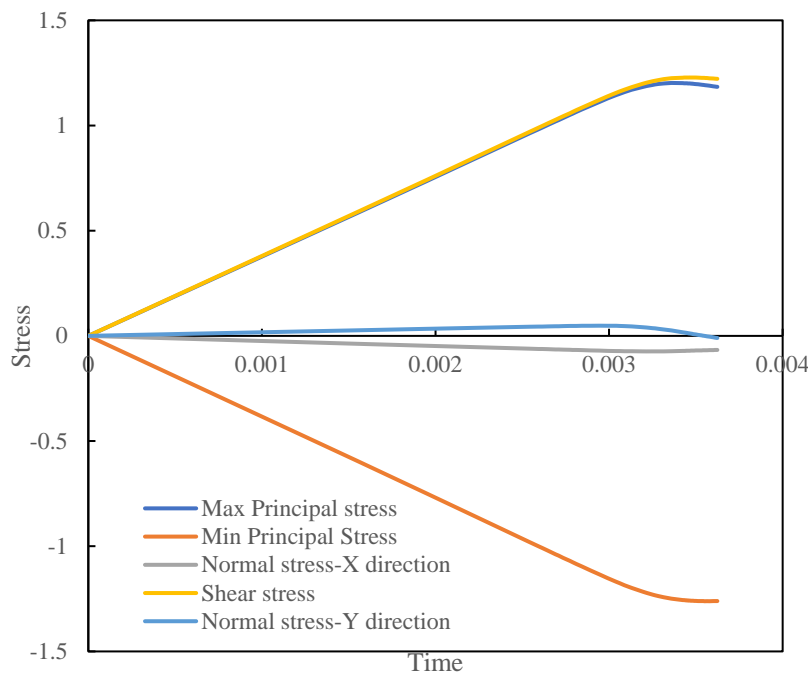
Fig. 2 - 19. Stress state of the mid-point at the shear plane of the axisymmetric shear test with reduced width in mid-span

2.7 DISCUSSION AND CONCLUSION

➤ Need for constitutive laws for unconfined and FRP-confined RuC

The current experimental studies mainly forced on the compressive performance of RuC and CRuC in circular cross-section, but there is little work on the tensile and shear behaviours of this flexible concrete, as well as its compressive behaviour in non-circular section. Thus corresponding experimental programmes present in chapter 1, section 1.3.1 need to be carried out to achieve objectives 1, 3 and 5.

➤ Need for effective numerical models for unconfined and FRP-confined RuC

i) RuC demonstrate a much softer post-cracking behaviour than regular concrete, thus indicating the tensile constitutive model for conventional concrete no longer be able to apply in the case of RuC directly. Therefore, a new tensile constitutive law for RuC is necessary to achieve objective 2.

ii) Rectangular or square cross-sections are very common shapes can be observed in structures. Due to the confinement mechanism in the non-circular cross-section differs from that in the circular section, a robust model is needed to predict the behaviour of FRP-confined non-circular columns (to achieve objective 4).

iii) One of the main functions of FRP-confined RuC is sustaining the larger lateral load. To predict the response of RuC under such loading condition, an accurate shear behaviour model is required to achieve objective 6 and 7.

2.8 REFERENCES

1. Elghazouli, A., *Seismic design of buildings to Eurocode 8*. 2016: CRC Press.
2. Tassios, T.P., M. Moretti, and A. Bezas, *On the behavior and ductility of reinforced concrete coupling beams of shear walls*. Structural Journal, 1996. **93**(6): p. 711-720.
3. Galano, L. and A. Vignoli, *Seismic behavior of short coupling beams with different reinforcement layouts*. Structural Journal, 2000. **97**(6): p. 876-885.
4. Paulay, T. and J. Binney, *Diagonally reinforced coupling beams of shear walls*. Special Publication, 1974. **42**: p. 579-598.
5. Standardization, E.C.f., *Design of structures for earthquake resistance. Part 1: General rules, seismic actions and rules for buildings*. Eurocode 8, 2004.
6. Committee, A. and I.O.f. Standardization. *Building code requirements for structural concrete (ACI 318-08) and commentary*. 2008. American Concrete Institute.
7. David Escolano-Margarit, Z.W., Maurizio Guadagnini, Kypros and K. Pilakoutas, *Proof-of-concept Testing of FRP Confined Rubberised Concrete Coupling Beams*, in *Proceedings of Advanced Composites in Construction*. 2017: Sheffield, UK.
8. D Escolano-Margarit, R.G., S Raffoul, M Di Benedetti, Iman Hajirasouliha, M Guadagnini, K Pilakoutas, *SEISMIC PERFORMANCE EVALUATION OF COUPLED WALLS USING INNOVATIVE HIGHLY DEFORMABLE COUPLING BEAMS*, in *16th World Conference on Earthquake Engineering, 16WCEE 2017*. 2017: Santiago Chile.
9. Son, K.S., I. Hajirasouliha, and K. Pilakoutas, *Strength and deformability of waste tyre rubber-filled reinforced concrete columns*. Construction and building materials, 2011. **25**(1): p. 218-226.
10. Elghazouli, A., et al., *Performance of rubberised reinforced concrete members under cyclic loading*. Engineering Structures, 2018. **166**: p. 526-545.
11. Raffoul, S., et al., *Optimisation of rubberised concrete with high rubber content: an experimental investigation*. Construction and Building Materials, 2016. **124**: p. 391-404.
12. Standardization), C.E.C.f., *EN 450-1:2012 Fly ash for concrete – Part 1: definition, specifications and conformity criteria*. 2012, CEN: Brussels (Belgium).
13. ELKEM. *Elkem Microsilica Grade 940 for Concrete*. Available from: https://www.elkem.com/ silicon-materials/high-performance-concrete/microsilica-concrete-grades/ microsilica-grade-940-construction/.
14. Ozyildirim, C. and N.J. Carino, *Concrete strength testing*, in *Significance of Tests and Properties of Concrete and Concrete-Making Materials*. 2006, ASTM International.
15. Eldin, N.N. and A.B. Senouci, *Rubber-tire particles as concrete aggregate*. Journal of materials in civil engineering, 1993. **5**(4): p. 478-496.
16. ASTM, C. *Standard test method for flexural strength of concrete (using simple beam with third-point loading)*. in *American society for testing and materials*. 2010.
17. ASTM, *Standard test method for flexural strength of concrete (using simple beam with center-point loading)*. 2010.
18. ASTM, C., *Standard test method for splitting tensile strength of cylindrical concrete specimens*. 2011.

19.   Bompa, D., et al., *Experimental assessment and constitutive modelling of rubberised concrete materials.* Construction and Building Materials, 2017. **137**: p. 246-260.

20.   Medina, N.F., et al., *Composites with recycled rubber aggregates: Properties and opportunities in construction.* Construction and Building Materials, 2018. **188**: p. 884-897.

21.   Reagel, F. and T. Willis, *The effect of dimensions of test specimens on the flexural strength of concrete.* Public roads, 1931. **12**(2): p. 37-46.

22.   Kellerman, W., *Effect of size of specimen, size of aggregate, and method of loading upon the uniformity of flexural strength tests.* Public roads, 1933. **13**(11): p. 177-184.

23.   Wright, P. and F. Garwood, *The effect of the method of test on the flexural strength of concrete.* Magazine of Concrete Research, 1952. **4**(11): p. 67-76.

24.   Carrasquillo, P. and R. Carrasquillo, *Improved Concrete Quality Control Procedures Using Third Point Loading.* 1987, CTR Project.

25.   Nielsen, K.E., *Effect of various factors on the flexural strength of concrete test beams.* Magazine of Concrete Research, 1954. **5**(15): p. 105-114.

26.   Neville, A.M., *Properties of concrete.* Vol. 4. 1995: Longman London.

27.   Mindess, S., J.F. Young, and D. Darwin, *Concrete Prentice-Hall.* Englewood Cliffs, NJ, 1981. **481**.

28.   Johnston, C. and E. Sidwell. *Influence of drying on strength of concrete specimens.* in *Journal Proceedings.* 1969.

29.   Elices, M., G. Guinea, and J. Planas, *On the measurement of concrete fracture energy using three-point bend tests.* Materials and structures, 1997. **30**(6): p. 375-376.

30.   EN, B., *Fly ash for concrete-Part 1: Defination, specifications and conformity criteria (BS EN 405-1).* British European Standards Specifications, 2005.

31.   ELKEM, E.M.G., *940 for Concrete.*

32.   Rocco, C., et al., *Size effect and boundary conditions in the Brazilian test: experimental verification.* Materials and Structures, 1999. **32**(3): p. 210.

33.   Bažant, Z.P., *Size effect in blunt fracture: concrete, rock, metal.* Journal of engineering mechanics, 1984. **110**(4): p. 518-535.

34.   EN14651, B.S., *Test method for metallic fibre concrete. Measuring the flexural tensile strength (limit of proportionality (LOP), residual).* 2005, London: BSI.

35.   Banthia, N. and J.-F. Trottier, *Test methods for fexural toughness characterization of fiber reinforced concrete: Some concerns and a proposition.* Materials Journal, 1995. **92**(1): p. 48-57.

36.   Institution, B.S., *Fly ash for concrete—Part 1: Definition, specifications and conformity criteria.* 2005, BSI London.

37.   Barr, B., et al., *Round-robin analysis of the RILEM TC 162-TDF beam-bending test: part 1—test method evaluation.* Materials and Structures, 2003. **36**(9): p. 609-620.

38.   Recommendation, R.D., *Determination of the fracture energy of mortar and concrete by means of three-point bend tests on notched beams.* Materials and structures, 1985. **18**(106): p. 285-290.

39.   Alecci, V., S.B. Bati, and G. Ranocchiai, *Concrete columns confined with CFRP wraps.* Materials and Structures, 2014. **47**(3): p. 397-410.

40.   Lam, L. and J. Teng, *Design-oriented stress-strain model for FRP-confined concrete in rectangular columns.* Journal of Reinforced Plastics and Composites, 2003. **22**(13): p. 1149-1186.

41.   Raffoul, S., et al., *Behaviour of unconfined and FRP-confined rubberised concrete in axial compression.* Construction and Building Materials, 2017. **147**: p. 388-397.

42.   Rousakis, T.C., et al., *Analytical modelling of plastic behaviour of uniformly FRP confined concrete members.* Composites Part B: Engineering, 2008. **39**(7-8): p. 1104-1113.

43.   Teng, J., et al., *Theoretical model for fiber-reinforced polymer-confined concrete.* Journal of Composites for Construction, 2007. **11**(2): p. 201-210.

44.   Yu, T., et al., *Finite element modeling of confined concrete-I: Drucker–Prager type plasticity model.* Engineering structures, 2010. **32**(3): p. 665-679.

45.   Wang, L.-M. and Y.-F. Wu, *Effect of corner radius on the performance of CFRP-confined square concrete columns: Test.* Engineering structures, 2008. **30**(2): p. 493-505.

46.   Mirmiran, A., et al., *Effect of column parameters on FRP-confined concrete.* Journal of Composites for Construction, 1998. **2**(4): p. 175-185.

47.   Rochette, P. and P. Labossiere, *Axial testing of rectangular column models confined with composites.* Journal of Composites for Construction, 2000. **4**(3): p. 129-136.

48.   Jiang, T. and J. Teng, *Analysis-oriented stress–strain models for FRP–confined concrete.* Engineering structures, 2007. **29**(11): p. 2968-2986.

49.   Lim, J.C. and T. Ozbakkaloglu, *Lateral strain-to-axial strain relationship of confined concrete.* Journal of Structural Engineering, 2014. **141**(5): p. 04014141.

50.   Raffoul, S., et al., *Constitutive model for rubberized concrete passively confined with FRP laminates.* Journal of Composites for Construction, 2019. **accepted for publication**.

51.   Lam, L. and J. Teng, *Design-oriented stress–strain model for FRP-confined concrete.* Construction and Building Materials, 2003. **17**(6-7): p. 471-489.

52.   Lin, G. and J. Teng. *FRP-confined concrete in square columns: an advanced stress-strain model based on a new approach.* in *Fourth Asia-Pacific Conference on FRP in Structures (APFIS 2013).* 2013.

53.   Hany, N.F., E.G. Hantouche, and M.H. Harajli, *Finite element modeling of FRP-confined concrete using modified concrete damaged plasticity.* Engineering structures, 2016. **125**: p. 1-14.

54.   Eid, R. and P. Paultre, *Plasticity-based model for circular concrete columns confined with fibre-composite sheets.* Engineering structures, 2007. **29**(12): p. 3301-3311.

55.   Robinson, J. and J. Demorieux, *Essais de traction, compression sur modèles d'âme de poutre en béton armé: compte rendu partiel.* 1968.

56.   Vecchio, F.J. and M.P. Collins. *The modified compression-field theory for reinforced concrete elements subjected to shear.* in *Journal Proceedings.* 1986.

57.   Hsu, T.T., *Softened truss model theory for shear and torsion.* Structural Journal, 1988. **85**(6): p. 624-635.

58.   Pang, X.-B.D. and T.T. Hsu, *Behavior of reinforced concrete membrane elements in shear.* ACI Structural Journal, 1995. **92**(6): p. 665-679.

59.   Pang, X.-B. and T.T. Hsu, *Fixed angle softened truss model for reinforced concrete.* ACI Structural Journal, 1996. **93**(2): p. 197-207.

60.   Zhu, R.R., T.T. Hsu, and J.-Y. Lee, *Rational shear modulus for smeared-crack analysis of reinforced concrete.* Structural Journal, 2001. **98**(4): p. 443-450.

61.   Teng, J., et al., *FRP: strengthened RC structures.* Frontiers in Physics, 2002: p. 266.

62.   Chen, J. and J. Teng, *Shear capacity of fiber-reinforced polymer-strengthened reinforced concrete beams: Fiber reinforced polymer rupture.* Journal of Structural Engineering, 2003. **129**(5): p. 615-625.

63.   李荣, 滕锦光, and 岳清瑞, *FRP 材料加固混凝土结构应用的新领域——嵌入式 (NSM) 加固法.* 2004.

64.   Teng, J., L. Lam, and J. Chen, *Shear strengthening of RC beams with FRP composites.* Progress in Structural Engineering and Materials, 2004. **6**(3): p. 173-184.

65.   Chen, J.-F. and J. Teng, *Shear capacity of FRP-strengthened RC beams: FRP debonding.* Construction and Building Materials, 2003. **17**(1): p. 27-41.

66.   Chen, J., G. Chen, and J. Teng, *Shear resistance of FRP-strengthened RC beams: interaction between internal steel stirrups and external FRP strips.* 2006.

67.   Triantafillou, T.C., *Shear strengthening of reinforced concrete beams using epoxy-bonded FRP composites.* ACI structural journal, 1998. **95**: p. 107-115.

68.   Bousselham, A. and O. Chaallal, *Mechanisms of shear resistance of concrete beams strengthened in shear with externally bonded FRP.* Journal of Composites for Construction, 2008. **12**(5): p. 499-512.

69.   Chen, G., et al., *Interaction between steel stirrups and shear-strengthening FRP strips in RC beams.* Journal of Composites for Construction, 2010. **14**(5): p. 498-509.

70.   Belarbi, A., *Design of FRP systems for strengthening concrete girders in shear.* Vol. 678. 2011: Transportation Research Board.

71.   Chen, W.-F. and B. Trumbauer, *Double-punch test and tensile strength of concrete.* Journal of Materials, 1972. **7**(2).

72.   Tuan, H.-N., *A study on shear strength of concrete under direct shear test.* コンクリート工学年次論文集, 2006. **28**(1): p. 1529-1534.

73.   Bažant, Z. and P. Pfeiffer, *Shear fracture tests of concrete.* Materials and Structures, 1986. **19**(2): p. 111-121.

74.   Di Prisco, M., et al., *Mixed mode fracture in plain and reinforced concrete: some results on benchmark tests.* International journal of fracture, 2000. **103**(2): p. 127-148.

75.   Iosipescu, N. and A. Negoita, *A new method for determining the pure shearing strength of concrete.* Concrete (London), 1969.

76.   Bažant, Z. and P. Pfeiffer, *Shear fracture tests of concrete.* Materials and structures, 1986. **19**(2): p. 111.

77.   Rots, J.G. and R. De Borst, *Analysis of mixed-mode fracture in concrete.* Journal of Engineering Mechanics, 1987. **113**(11): p. 1739-1758.

78.   Schlangen, E., *Experimental and numerical analysis of fracture processes in concrete.* 1995.

79.   Qi, Z. and G. Zhenhai, *Investigation on shear strength and shear strain of concrete.* Journal of Building Structures, 1992. **13**(5): p. 17-24.

Chapter 3

Tensile Stress-Crack Opening Characteristics of Rubberised Concrete

3.1 INTRODUCTION

In this chapter, notched three-point bending tests are used to characterise Mode I fracture behaviour of concrete incorporating high volume of rubber particles obtained from post-consumer tyres. A new tensile constitutive model for rubberised concrete (RuC) is proposed and implemented in the ABAQUS concrete damaged plasticity model (CDPM) to predict the flexural behaviour of RuC. The chapter initially describes an experimental program on which three-point bending (TPB) and splitting tensile tests are utilised to determine the tensile characteristics of RuC. The next sections describe the methodology applied for the determination of tensile stress-crack opening displacement relationships. The key material parameters introduced in the constitutive model are tensile strength and fracture energy. Finally, to demonstrate the efficiency of the proposed model, the predicted mechanical response using the proposed tensile σ-w relationships and relationships obtained from Model Code 2010 are compared. This work will lead to a better understanding of the behaviour of RuC, and the relationship can be used for improved FE simulation of the behaviour of the rubberised concrete elements and structures.

3.2 EXPERIMENTAL PROGRAM

45 samples consisting of 36 cylindrical specimens (Ø100×200 mm) and 9 prisms (L500×W150×H150 mm) were manufactured to examine the compressive and tensile characteristics. All the samples were divided into three sets by rubber contents ($\rho_{vr} = 0\%$, 30% and 60%) and labelled as R0, R30 and R60, respectively. The rubber content ρ_{vr} is defined as the volume of mineral aggregates in the reference regular concrete mix replaced by rubber [1, 2]. The detail of RuC mix and incorporated rubber particles can be found in Chapter 1.

3.2.1 Test procedure and methodology

3.2.1.1 Compressive and splitting tests

The compressive (see Fig. 3 - 1a) and splitting tests (see Fig. 3 - 1b) on cylindrical specimens were carried out under load control using a 3000 kN cube crusher. The loading rate was 0.4 MPa/s [3] and 0.01 MPa/s [4] for the two types of tests, respectively. For the compressive tests, three laser sensors (an accuracy of 0.005 mm) were used to measure global axial displacement. The sensors were mounted radially at 120° on two aluminium rings with 100 mm gauge length. Local axial strains were measured by using strain gauges placed at mid-height of the specimen. The possible initial rotations were accommodated by a top loading plate fitted with a hinge. The dimensions of each specimen were measured before testing. The specimen ends were strengthened with pre-tensioned metal straps with a thickness of 0.8 mm and a width of 25 mm to avoid local failure.
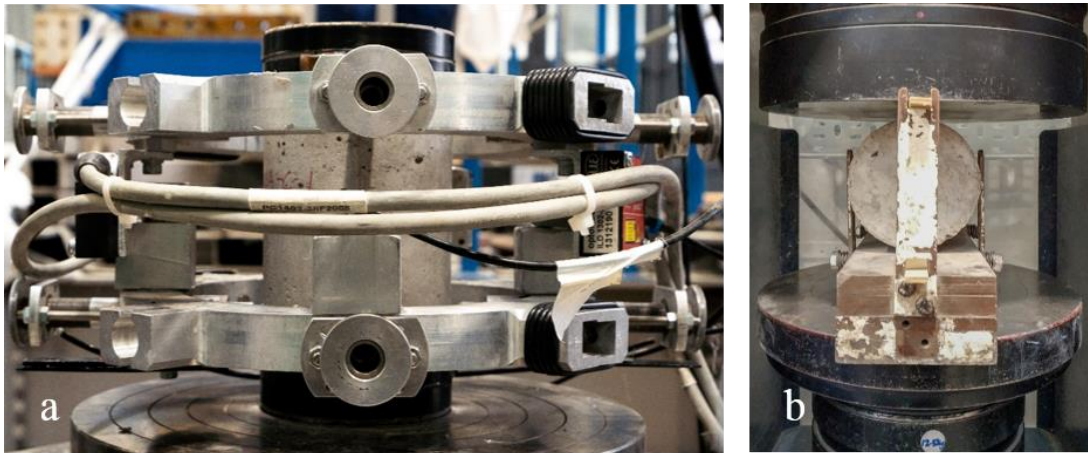
Fig. 3 - 1. View of testing for a) Compression tests and b) Splitting tests.

The splitting tensile strength ($f_{ct,sp}$) can be calculated by Eq. (1) using the maximum load (P_{max}) [4]:

$$f_{ct,sp} = \frac{2P_{max}}{\pi l d} \tag{1}$$

where L is the length of the specimen, d_{cy} is the diameter of the cylinder.

The load in Eq. (1) is assumed to be concentrated along a line. However, the load is practically applied on a sheet of plywood or compact cardboard. Rocco et al. [5] showed that the loading area width (*t*) can affect the tensile strength of the cylinders up to 25%. Tang et al. [6] proposed the following equation to consider the effect of the loading area width on the splitting tensile strength.

$$f_{ct,sp} = \frac{2P_{max}}{\pi l d}\left(1-\left(\frac{2t}{d}\right)^2\right)^{1.5} \tag{2}$$

Bompa et al. [2] proposed Eqs. (3) to predict the splitting tensile strength ($f_{ct,sp}$), tensile strength (f_{ct}) and elastic modulus (E_c) as a function of the compressive strength (f_{co}) of RuC. These equations will be evaluated by comparing with test data in this study.

$$f_{ct,sp} = 0.26 f_{co}^{2/3}; \; f_{ct} = 0.24 f_{co}^{2/3}; \; \varepsilon_{cr} = f_{ct}/E_c; \; E_c = 12\left(\frac{f_{co}}{10}\right)^{2/3} \tag{3}$$

3.2.1.2 Three-point bending tests

Before testing, the geometrical dimensions of each specimen were measured and a 5mm wide and 25 mm deep notch was sawn at mid-span of the prisms and perpendicular to the cast surface using a diamond impregnated rotating [7]. All specimens were tested subject to a TPB loading arrangement using a 300 kN electromagnetic testing machine (see Fig. 3 - 2). Two Linear Variable Differential Transducers (LVDTs) were mounted on an aluminium yoke to measure central deflections [8] and a clip gauge was mounted on either side at the notch to obtain the crack mouth opening displacement (CMOD) [9]. In order to achieve a stable result, the tests were CMOD-controlled at a constant rate of 0.02 mm/min [10]. The load, central deflection and CMOD were recorded throughout loading history.
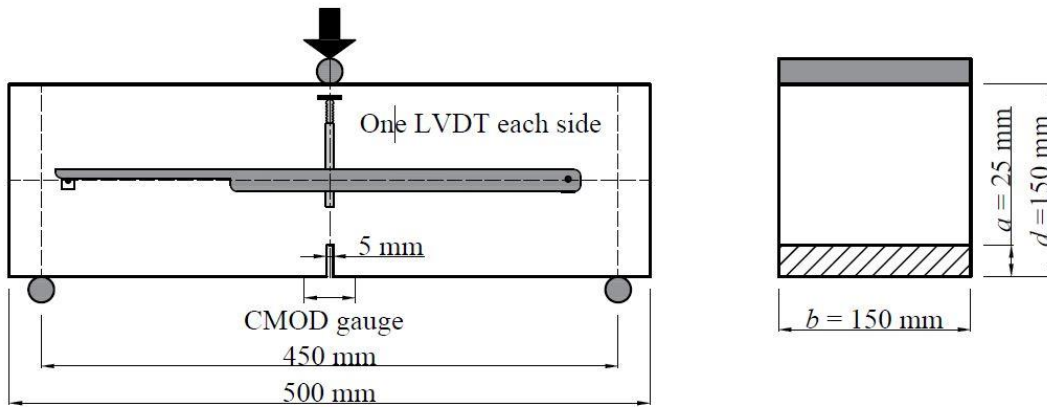
Fig. 3 - 2. Set-up of the three-point bending tests.

The flexural tensile strength ($f_{ctm,fl}$) can be determined as the equivalent elastic tensile flexural stress corresponding to the maximum load recorded, as:

$$f_{ctm,fl} = \frac{3P_{max}l}{2b(d-a)^2} \tag{4}$$

where l is the span of the prism, b is the width of the prism, d is the depth of the prism, and a is the effective depth of the notch.

The flexural modulus of elasticity (K_{fm}) is determined by using the elastic flexural deformations, as given below:

$$K_{fm} = \frac{l^3 P}{48 I \delta} \tag{5}$$

where P/δ (N/mm) is the slope of the load-deflection curve at 40% of the peak load and $I = b(d-a)^3/12$ (mm⁴) is the second moment of area of the mid-span cross-section.

3.2.1.3 Total fracture energy from the work-of-fracture method

Hillerborg's work-of-fracture method assumes that the energy required for crack formation is equivalent to the work of the external load. Thus the complete load-deflection curve of the specimen is necessary to estimate the work of the external load, which can be represented as the

area under the load-deflection curve. The fracture energy (G_F) can be then calculated using the following equation [11]:

$$G_F = \frac{W_0 + \left(m_1 \dfrac{S}{L} + 2m_2 \right) g \delta_0}{A_{lig}}$$

(6)

where W_0 is deformation energy capacity, which represents the area under the load-deflection curve during the bending test; m_1 is the mass of the beam between supports; m_2 is the mass of the unattached loading apparatus; L and l are the length and span of the specimen, respectively; g is the gravity acceleration; δ_0 represents the maximum recorded deflection; and $A_f = (d - a)b$ denotes the area of the fracture surface.

3.2.2 Experimental results

3.2.2.1 Changes in unit weight

As a result of the low unit weight of rubber particles, the unit weight of rubberised concrete reduces by increasing the rubber content. Fig. 3 - 3 shows the expected linear relationship between unit weight (d_{RuC}) and rubber contents (ρ_{vr}). Compared with the unit weight of concrete mixes without rubber, the average unit weight of the concrete mix with a rubber content of 30% and 60% decreased by 15.4% and 31.8%, respectively.

$$d_{RuC} = 2396 - 0.7\rho_{vr} \times d_{agg}$$

$$d_{agg} = 1820 \text{ kg/m}^3$$
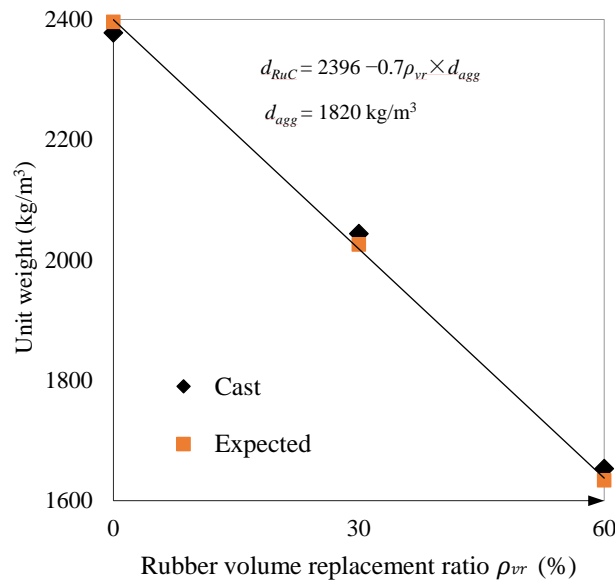
Fig. 3 - 3. Unit weight of RuC with different rubber volume replacement ratio ρ_{vr}.

3.2.2.2 Compressive and splitting tensile strength

The compressive test results are summarised in Table 3 - 1. The mean cylindrical compressive strengths (f_{co}) of R30 and R60 were about 29% and 10% of that of regular concrete R0 (75 MPa), respectively. The compressive stress-strain curves are shown in Fig. 3 - 5. The elastic modulus (E_c) of R30 and R60 was 41% and 21% of that of R0 (41 GPa), respectively. The post-peak behaviour was also strongly influenced by the percentage of rubber replacement of the mineral aggregates. The compressive failure patterns of cylinders are shown in Fig. 3 - 6a. As expected, all plain ($\rho_{vr} = 0\%$) specimens failed suddenly in a brittle manner. The failure of RuC cylinders with $\rho_{vr} = 30\%$ and 60% was more gradual as the cylinders developed a large number of macro-cracks and bulging at mid-height prior to failure. Rubber particles have high level of lateral strain at lower displacements than mineral aggregates due to their low modulus of elasticity and high Poisson's ratio. This dilation helps produce internal splitting tensile stresses that are perpendicular to the loading direction. This causes the concrete to fail at an earlier stage.

Table 3 - 1. Experimental results of examined concrete mixes

ρ_{vr}	f_{co} MPa	E_c GPa	$f_{ct,sp}$ MPa	$f_{ctm,fl}$ MPa	K_{fm} GPa	G_F N/mm
0	75 (5.6)	41 (2.3)	4.1 (0.82)	5.9 (0.5)	44 (9)	0.12 (0.02)
30	21.9 (3.6)	17 (3.5)	1.8 (1.29)	3.9 (1.86)	20 (8)	0.46 (0.14)
60	7.7 (0.3)	8.5 (1.2)	0.9 (0.52)	2.1 (0.22)	10 (0.3)	0.93 (0.06)

Note: Standard Deviation is presented in brackets.
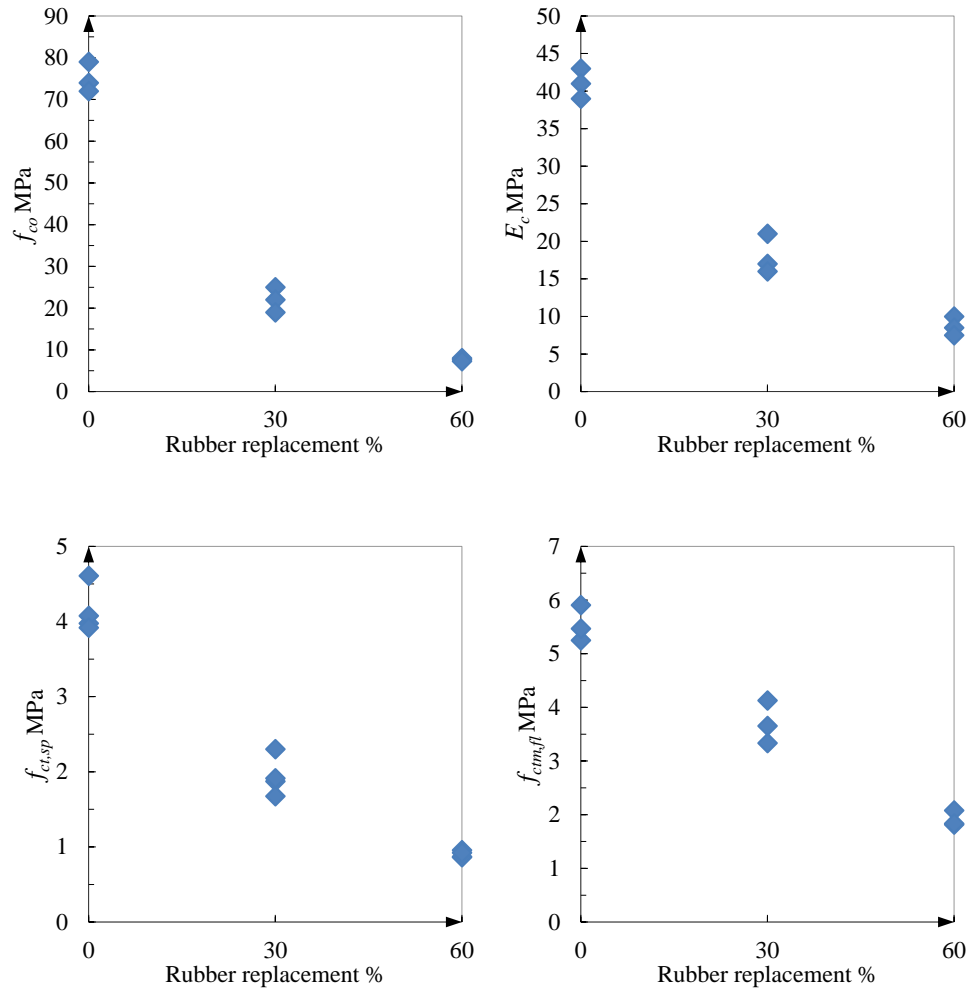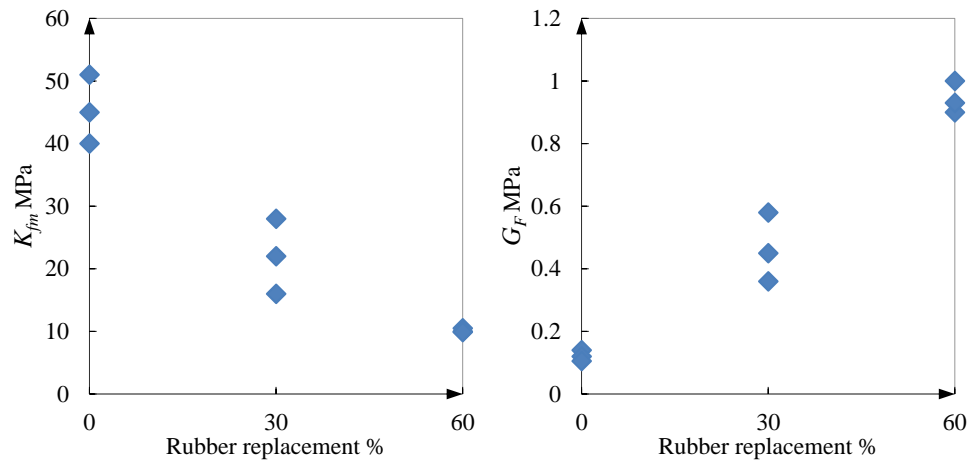
Fig. 3 - 4. Detail test results reported in Table 3 - 1.
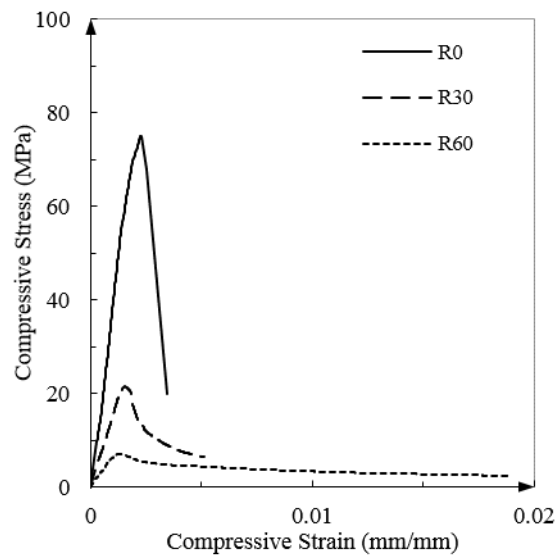
Fig. 3 - 5. Compressive stress-strain curves of R0, R30 and R60.
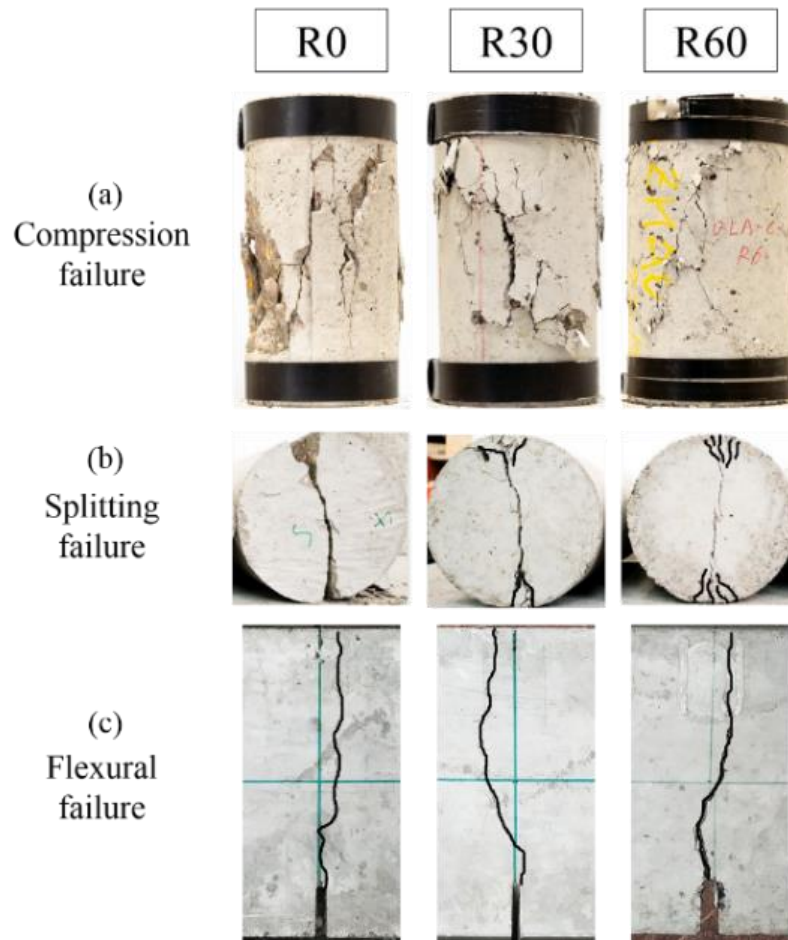
Fig. 3 - 6. Typical failure modes for a) Compression; b) Splitting tension and c) Flexural.

During the splitting tests, as expected all samples failed due to wedge formation and splitting as shown in Fig. 3 - 6b. Compared to the brittle failure mode of plain concrete, the RuC samples exhibited a slower axial splitting process and higher capacity in absorbing plastic energy. The regular concrete specimens split into two halves immediately upon reaching their ultimate load capacity, while the RuC specimens were capable of withstanding at least 80% of the ultimate load for about 30 seconds (R30) and 55 seconds (R60) after splitting. The RuC specimens underwent large displacements before the loading stopped, and the deformation was partially recovered upon unloading. All the RuC specimens maintained their integrity even for highly cracked specimens. The splitting tensile strength ($f_{ct,sp}$) results are reported in Table 3 - 1, which shows a clear degradation in tensile strength with increasing rubber content. However, the trend

in tensile strength loss is less severe than in compressive strength. The splitting tensile strengths of R30 and R60 were 44% and 22% of that of R0 (4.1 MPa), respectively.

3.2.2.3 Three-point bending tests

The flexural failure patterns of all specimens are shown in Fig. 3 - 6c. The average flexural strength ($f_{ctm,fl}$) and modulus (K_{fm}) of three replicates are listed in Table 3 - 1. Fig. 3 - 7 shows the photos of typical sections obtained after the bending test (upper row for each mix) as well as the pictures obtained by digital image processing techniques (lower row) to examine rubber particle distribution along the casting direction. The images show that the rubber tended to float towards the cast face (left in the pictures) during vibration of the fresh concrete leading to an agglomeration of rubber particles. However, this tendency is less obvious at the rubber content of $\rho_{vr} = 60\%$.
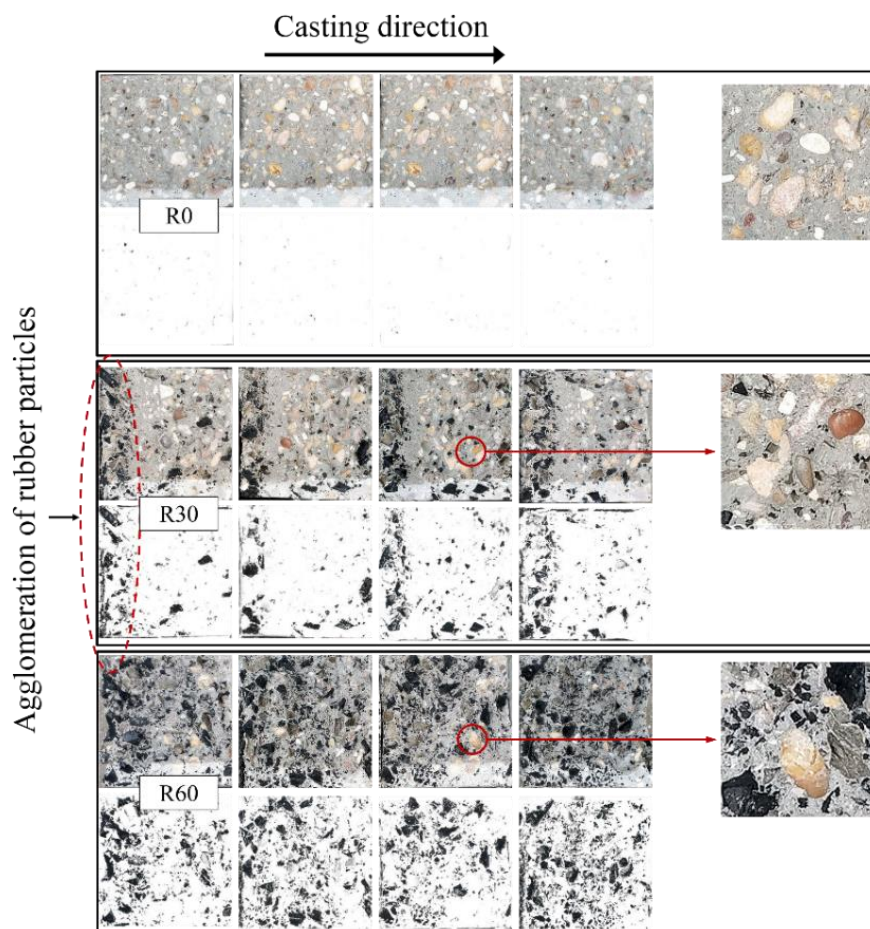
Fig. 3 - 7. The fracture surface of three-point bending tests.

Fig. 3 - 8 shows the individual and average $P - \delta$ curves from three TPB specimens for each of the ρ_{vr} tested. The mid-span deflection of each beam was derived by averaging the deflection values measured by the two LVDTs. The response of the TPB test can be described by three typical phases: 1) an elastic phase up to cracking; 2) a short flexural hardening response up to the maximum flexural capacity; and 3) a reduction of the load with increasing CMOD/deflection. The comparative assessment of load-deflection curves from Fig. 3 - 8 shows a significant reduction in flexural strength and stiffness with increasing rubber content. The flexural strengths ($f_{ctm,fl}$) of concrete with ρ_{vr} = 30% and 60% are 66% and 35.6% of the reference concrete, respectively. The flexural modulus (K_{fm}) of R30 and R60 were reduced to 45% and 20% of that of R0, respectively. However, the ratio of cracking stress to flexural strength ($f_{cr}/f_{ctm,fl}$) are 54%, 68% and 72% for R0, R30 and R60, respectively. Around the peak, RuC specimens showed a stable transition from the pre- to post-cracking regimes, while the reference (plain concrete) beams showed a brittle behaviour after the maximum capacity was reached. Beyond the peak, the descending branch showed reducing gradients ($E_{d,R0}$ = −143, $E_{d,R30}$ = −24 and $E_{d,R60}$ = −7 MPa) and increasing fracture energy ($G_{F,R0}$ = 0.15, $G_{F,R30}$ = 0.51 and $G_{F,R60}$ = 0.93 N/mm^2) as the rubber content increased (see Fig. 3 - 9). This enhancement indicates that the capability of rubberised concrete in deformation energy is significantly better than regular concrete beam as more than 20 times deflection developed. The higher deformability of rubberised concrete elements can potentially result in more resilient structural systems and improve the integrity of the structure under extreme load conditions.
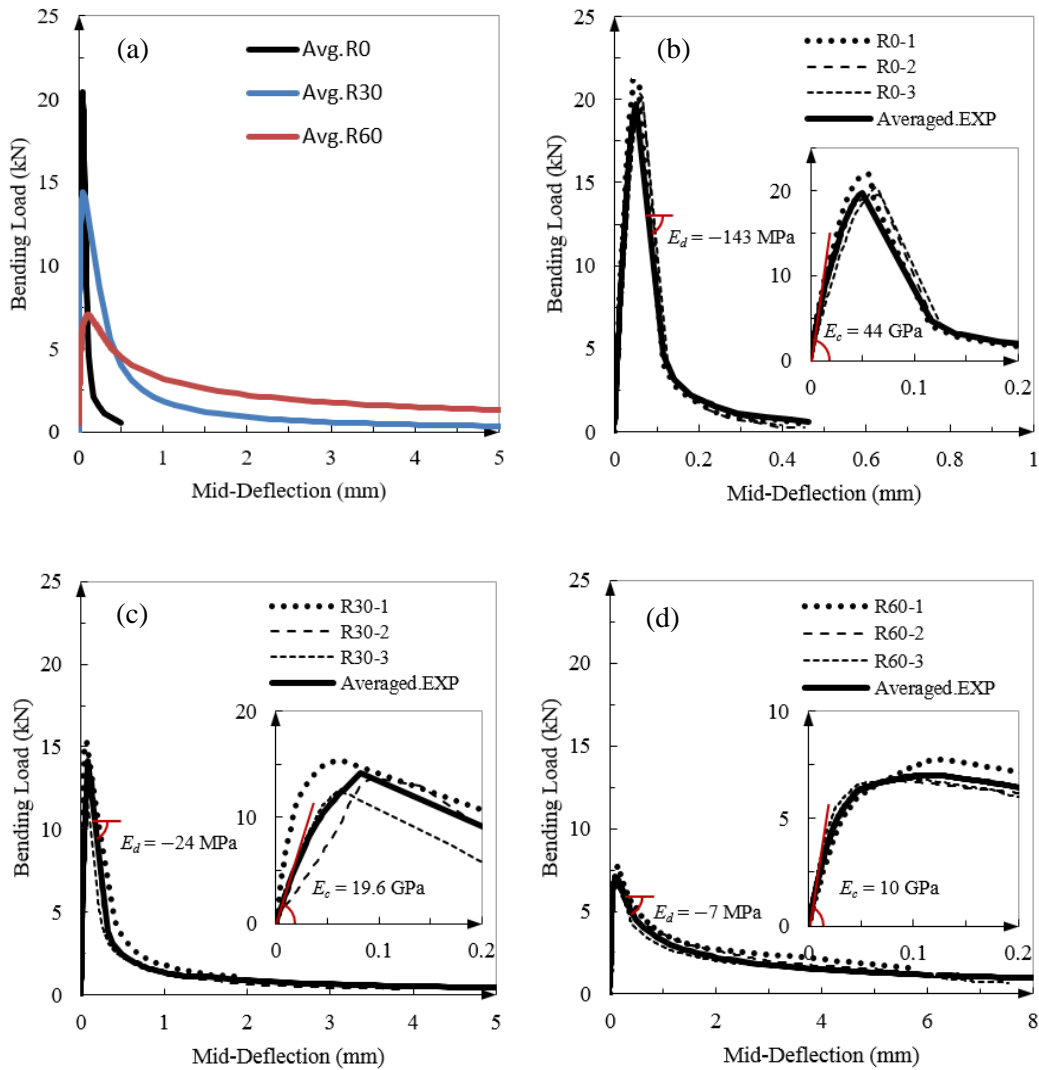
Fig. 3 - 8. Load-deflection of TPB specimens: (a) average stress-deflection curves, (b) R0, (c) R30 and (d) R60.

The fracture energy (G_F) in N/mm^2 for regular concrete can be determined using the CEB-FIB Model Code 2010 [12]:

$$G_F = 0.073 \times f_{co}^{0.18} \tag{7}$$

Using the results of this study, a parametric equation is developed to calculate the fracture energy ($G_{F,RuC}$) of RuC based on Eq. (7). The rubber volume replacement ratio (ρ_{vr}) is incorporated in Eq. (8) and results shown in Fig. 3 - 9:

$$G_{F,RuC} = (1+10.8\rho_{vr}) \cdot G_F \tag{8}$$
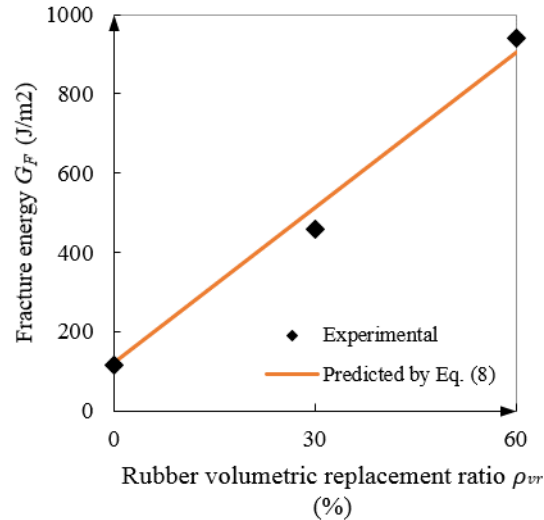
Fig. 3 - 9. Fracture energy with different rubber content.

Further inspection of the fractured surfaces revealed a different degree of roughness depending on the percentage of rubber volume replacement. At 60% rubber replacement, no broken mineral aggregates were found on the fracture surface. At 30% rubber replacement, the majority of mineral aggregates were found broken on the fracture surface. At 0% rubber replacement, almost all the aggregates were found broken. The flexural failure mode of RuC can be explained as follows. When a tension crack propagates to a rubber particle, it keeps its direction instead of bypassing the aggregate as the rubber has the ability to withstand large elastic deformation under small tensile stress. As rubber can withstand much higher tensile stress and strain until failure than cement and mineral aggregates, the primary failure mechanism of rubber particles is pull-out. This failure mechanism results in the energy dissipation enhancement discussed above.

3.3 TENSILE STRESS-CRACK OPENING RELATIONSHIP

In order to obtain the tensile stress-crack opening curves of RuC using the TPB experimental results, the following assumptions are used, the first three proposed by Uchida et al. [13]

i. A single main crack exists through a fracture area (see Fig. 3 - 10). A rotational axis exists on the top of the fracture area. The distribution of the crack opening is linear.

ii. The mean crack opening ($w_{t,m}$) at the fracture area is represented by half of the crack mouth opening displacement (CMOD) at the notch. This opening can be smeared over a crack band width (w_{cb}) to obtain cracking strain (ε_{ck}) [14]. The crack band width (w_{cb}) indicates the effective width of the strain-softening damage zone. In FE analysis, crack band width refers to the characteristic length of an element [15, 16].

iii. The externally applied energy is equivalent to the energy needed for crack development.

iv. The shape of the tensile stress-crack opening curve of concrete is exponential, and the function proposed by Hordijk [17] can be adopted (Eq. (9)). The efficiency of this relationship has been evaluated by Tao and Chen [15].

$$\frac{\sigma_t}{f_{ct}} = \left[1 + \left(c_1 \frac{w_t}{w_{cr}}\right)^3\right] e^{\left(-c_2 \frac{w_t}{w_{cr}}\right)} - \frac{w_t}{w_{cr}}\left(1 + c_1^3\right) e^{-c_2} \qquad (9)$$

$$w_{cr} = \begin{cases} 5.14 \dfrac{G_F}{f_{ct}} & \text{for regular concrete} \\[3mm] 7.21 \dfrac{G_{F,RuC}}{f_{ct}} & \text{for rubberised concrete} \end{cases} \qquad (10)$$

where w_t and w_{cr} are crack opening and ultimate crack opening, respectively; σ_t is tensile stress; f_{ct} is and tensile strength and can be determined by Eqs. (3); G_F and $G_{F,RuC}$ are the fracture enegry of rugular concrete and rubebrised concrete, which can be calculated by Eq. (7) and Eq. (8), respectively; $c_1 = 3.0$ and $c_2 = 6.93$ for rugular concrete are recommended by [15] and $c_1 = 2.6$ and $c_2 = 4.7$ have been found for rubberised concrete.
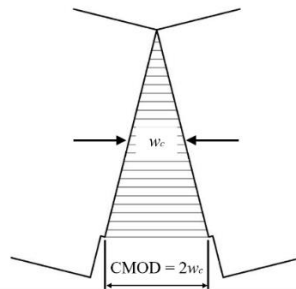
Fig. 3 - 10. Model of fracture area reproduced from Uchida et al. [33]

3.4   NUMERICAL MODELLING

A finite element model has been developed using Abaqus/Standard finite element software package [18]. The "Concrete Damaged Plasticity (CDP)" [19] developed by Lubliner et al. [20] and elaborated by Lee and Fenves [21] is adopted as it allows the use of a custom tensile characteristic for concrete in tension. CDP uses the modified Drucker-Prager criterion and the yield surface F in the deviatoric plane and assumes isotropic damage d. The details can be found in [22].

The CDP model requires the following material functions and parameters:

- Stress-strain relation for uniaxial behaviour in compression and stress-crack opening relation for tension. The compressive stress-strain relations proposed by Bompa et al. [2] are adopted in this study, and the tensile stress-crack opening relations obtained by proposed relation and the relation recommended by Model code 2010 are used (see Fig. 3 - 11).
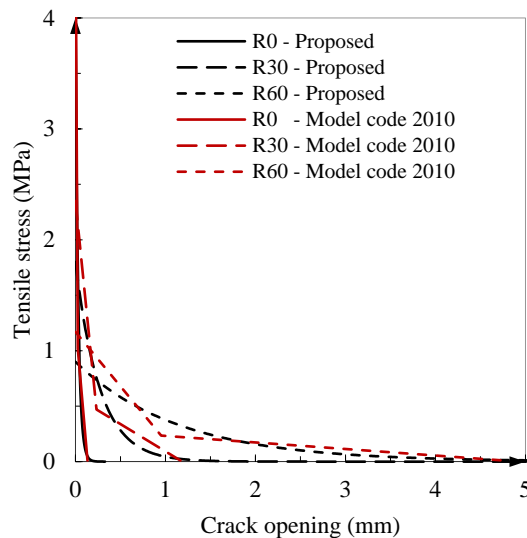
Fig. 3 - 11. Comparison of stress-crack opening curves for Model Code 2010 and proposed model.

- The damage variables d_c and d_t represent the portion of normalised energy dissipation for damage in compression and tension, respectively [20]. The values of d_c and d_t are

determined using Eqs. (11), and the curves of d_t vs w_t are shown in Fig. 3 - 12 (zero means no damage and one means fully damaged).

$$d_c = \int_0^{\varepsilon_{ch}} \sigma_c d\varepsilon_{ch} / g_c ; d_t = \int_0^{w_t} \sigma_t dw_t / G_F \qquad (11)$$

- The CDP model assumes non-associated plastic flow with a default eccentricity $\epsilon = 0.1$. The yield surface is controlled by a shape parameter K_c and the ratio between the biaxial and uniaxial compressive strength f_{b0}/f_{c0}, which were taken as the recommended default values of 2/3 and 1.16, respectively [18]. A low viscosity parameter of 2×10^{-6} was chosen to avoid convergence problems. It should be noted that the non-associative plastic volume deformation of the concrete is controlled by the dilation angle ψ, while the lateral dilation of concrete increases with increasing ψ. As replacing the mineral aggregates with rubber particles can dramatically increase the lateral dilation of RuC by up to 300% over the plain concrete [23], a relatively high dilation angle $\psi = 40°$ was chosen for RuC [24, 25].
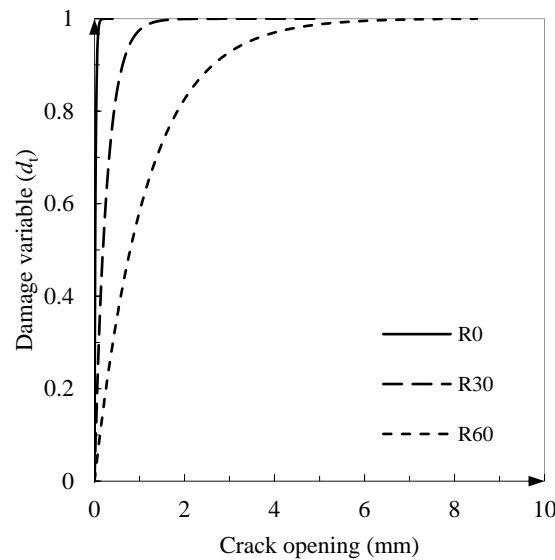
Fig. 3 - 12. Tensile damage variables (d_t) vs crack opening (w_t).

3.4.1 Verification of the material model

3.4.1.1 Splitting tests

The finite element modelling of splitting tests was performed to examine whether Eq. (3) can provide a reasonable prediction of the splitting tensile strength. The diametric compression load was applied experimentally through a plywood strip (width: 10 mm and thickness: 3 mm); and therefore, numerically the load was applied directly on the surface of the cylinder across the same area of the plywood strip. Since maximum capacity is mesh-independent, an arbitrary mesh size of 15 mm was chosen [26]. Fig. 3 - 13 shows the comparison between numerical and experimental results, which confirms the effectiveness of Eq. (3).
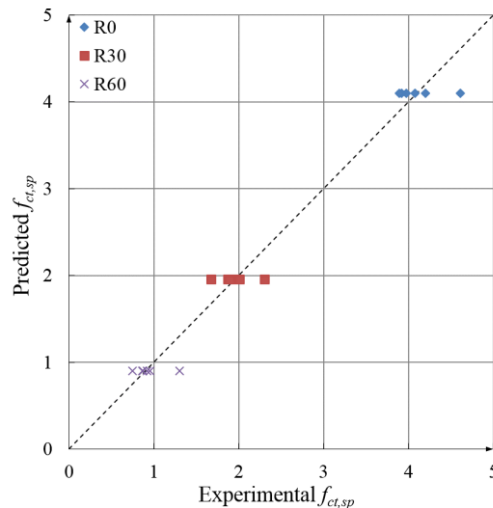
Fig. 3 - 13. Comparison of the predicted splitting tensile strength with experimental results.

3.4.1.2 TPB tests

The finite element meshes shown in Fig. 3 – 14 are used to model the beams failing in bending. In the TPB tests, the load was applied via a steel roller in displacement control. In the numerical study, the steel roller was modelled as a rigid body and a displacement was applied at the relative reference point. A frictionless surface-to-surface interaction was assigned to the steel roller-concrete interface.
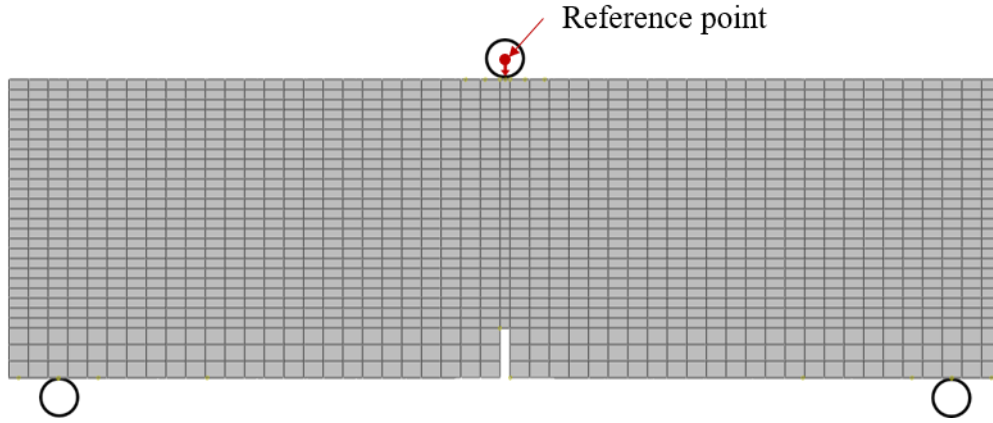
Fig. 3 - 14. Discretisation of the three-point bending beam.

For each rubber volumetric replacement ratio, the load-deflection curves were calculated by using the bilinear stress-crack opening relations suggested by Model Code 2010 [27] (Eqs. (12)) and the proposed relations (Eq. (9)).

$$\sigma_t = f_{ct} \cdot (1.0 - 0.8 \cdot \frac{w}{w_1}) \qquad \text{for } w \leq w_1$$

$$\sigma_t = f_{ct} \cdot (0.25 - 0.05 \cdot \frac{w}{w_1}) \quad \text{for } w_1 < w \leq w_c \tag{12}$$

where $w_1 = G_F/f_{ct}$ is the crack opening at $\sigma_t = 0.2 f_{ct}$; $w_2 = 5 G_F/f_{ct}$ is the crack opening at $\sigma_t = 0$ and $f_{ct} = 0.3 (f_{ct})^{2/3}$.

The accuracy of the two models was evaluated by the errors in the FE predictions for peak load and deformation energy capacity as well as the Mean Square Error (MSE) between the predicted load-deflection behaviour over the entire loading range and the corresponding experimental results (average of three tests).

$$MSE = \frac{\sum_{i=1}^{N} [(\chi)_i^{anal} - (\chi)_i^{\exp}]^2}{N} \tag{13}$$

where $(\chi)_i^{anal}$ represents the predicted values of flexural load $(f_{ctm,fl})$, $(\chi)_i^{exp}$ shows the corresponding experimental values and N is the total number of collection data.

The comparisons between the average experimental and numerical load-deflection curves of all tested TPB specimens are shown in Fig. 3 – 15. It can be seen that the numerical curves using

the proposed relations show a considerably better agreement with the experimental data for both normal and rubberised concrete (RuC) specimens. For better comparison, the calculated errors are also summarised in Table 3 - 2. The results indicate that the Model Code stress-strain relation led to, on average, 32% and 63 % overestimation of the peak flexural load and the deformation energycapacity, respectively. It should be mentioned that similar observations were reported in [28, 29]. However, by using the proposed relation, the average errors reduced to 3% and 11% for peak flexural load and the deformation energy capacity, respectively. The MSE results also confirm that the proposed relation is capable of proving accurate simulation of the flexural behaviour of concrete over the entire loading range.

Fig. 3 - 15 demonstrates that the bilinear relation of the Model Code model provides less detailed softening behaviour compared to the proposed exponential relations, and can considerably overestimate the coefficients g_t.

Fig. 3 - 16 displays the tensile damage variables (d_t) vs CMOD plots obtained from R0, R30 and R60. The d_t of reference concrete R0 remains at low level until the CMOD reaches 0.11 mm and increases rapidly in a narrow CMOD range due to its relative tougher and higher brittleness. The d_t of RuC (R30 and R60) starts to increase once the crack is developed. However, the severity of crack development decreases with increasing rubber content. The rubber particles enable the concrete to behave in a ductile manner by controlling the crack development and increasing the ultimate CMOD.

In general, the results of this study indicate that the proposed tensile stress-crack opening relation can provide considerably better accuracy compared to conventional models, and therefore, should prove useful for finite element modelling and design of rubberised concrete elements and structures.
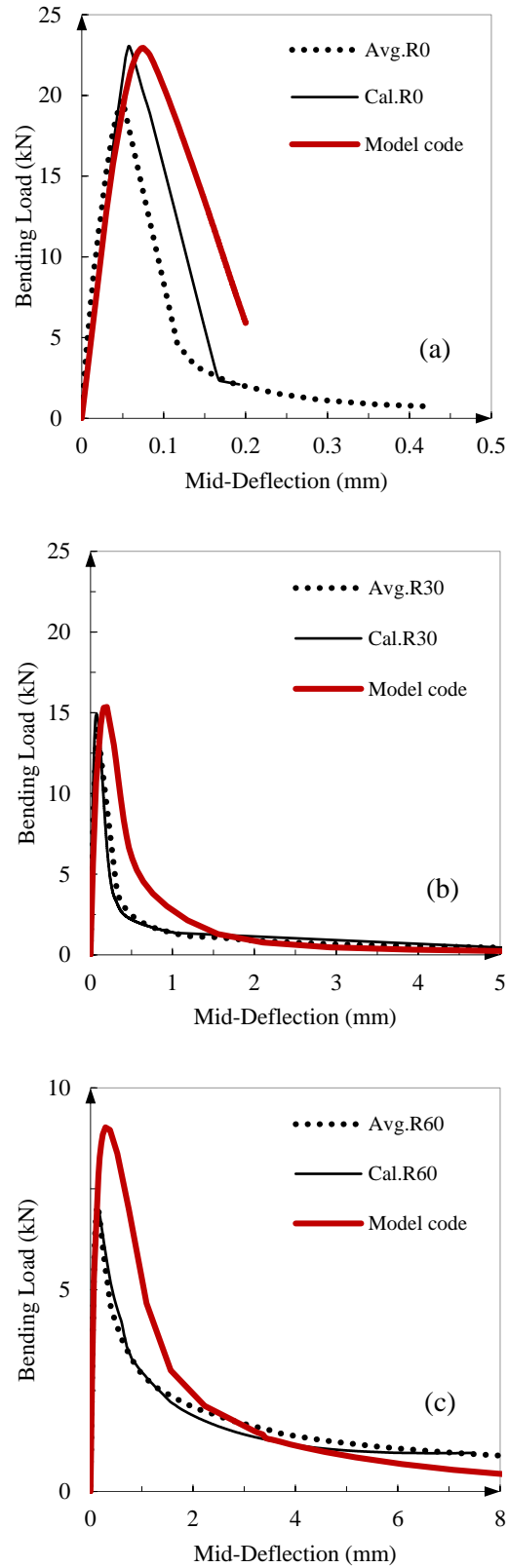
Fig. 3 - 15. Comparison of the load-deflection curves using proposed relations and Model code 2010 relations ((a) regular concrete, (b) RuC with 30 % rubber replacement ratio and (c) RuC with 60 % rubber replacement ratio).

Table 3 - 2. Errors in predicting peak load, deformation energy and load-deflection response.

ρ_{vr} (%)	Error in peak load		Error in energy absorption		MSE of load-deflection response	
	MC 2010	Proposed	MC 2010	Proposed	MC 2010	Proposed
R0	26%	2.6%	70%	10%	78%	5.1%
R30	25%	5.6%	58%	17%	21%	7.4%
R60	49%	0.2%	50%	16%	9%	4.8%
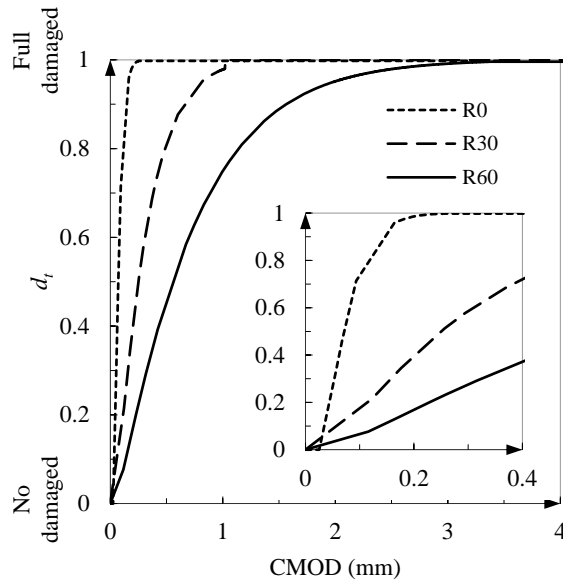
Fig. 3 - 16. Evolution of damage variable d_t.

3.5 CONCLUSIONS

In this chapter, the fracture energy of the rubberised concrete incorporating rubber particles recycled from end-of-life tyres has been investigated by conducting three-point bending tests. The primary parameter investigated was the rubber volume replacement ratio of fine and coarse mineral aggregates. The experimental results showed that replacing mineral aggregates with rubber particles leads to an apparent reduction in strength (compressive, tensile and flexural) and elastic modulus. However, a less serve reduction was observed in the tensile and flexural properties. Replacing aggregates with rubber also enhanced the fracture energy and deformation energy capacity and led to a more ductile post-cracking behaviour. The test results enabled the development of an fracture energy-based method to indirectly obtain the tensile stress-crack

opening relation of rubberised concrete. The proposed material laws were implemented in the concrete damage plasticity model in ABAQUS to analyse the tensile strain-softening behaviour numerically. It was shown that the proposed relations can provide significantly more accurate predictions compared to Model Code 2010 in terms of the peak load, deformation energy capacity and load-deflection response over the loading range.

3.6 REFERENCES

1.   Raffoul, S., et al., *Optimisation of rubberised concrete with high rubber content: an experimental investigation.* Construction and Building Materials, 2016. **124**: p. 391-404.
2.   Bompa, D., et al., *Experimental assessment and constitutive modelling of rubberised concrete materials.* Construction and Building Materials, 2017. **137**: p. 246-260.
3.   International, A., *C39/C39M - 15 Standard Test Method for Compressive Strength of Cylindrical Concrete Specimens.* 2015, West Conshohocken (USA).
4.   International, A., *C496/C496M - 11 Standard Test Method for Splitting Tensile Strength of Cylindrical Concrete Specimens.* 2011, West Conshohocken (USA).
5.   Rocco, C., et al., *Size effect and boundary conditions in the Brazilian test: experimental verification.* Materials and Structures, 1999. **32**(3): p. 210.
6.   Tang, T., S.P. Shah, and C. Ouyang, *Fracture mechanics and size effect of concrete in tension.* Journal of Structural Engineering, 1992. **118**(11): p. 3169-3185.
7.   Institution, B.S., *Test Method for Metallic Fibre Concrete: Measuring the Flexural Tensile Strength (limit of Proportionality (LOP), Residual).* 2008: BSI.
8.   Banthia, N. and J.-F. Trottier, *Test methods for flexural toughness characterization of fiber reinforced concrete: some concerns and a proposition.* ACI Materials Journal, 1995. **92**: p. 48-48.
9.   Standardization), C.E.C.f., *EN 450-1:2012 Fly ash for concrete – Part 1: definition, specifications and conformity criteria.* 2012, CEN, Brussels (Belgium).
10.   Barr, B., et al., *Round-robin analysis of the RILEM TC 162-TDF beam-bending test: part 1—test method evaluation.* Materials and Structures, 2003. **36**(9): p. 609-620.
11.   Recommendation, R.D., *Determination of the fracture energy of mortar and concrete by means of three-point bend tests on notched beams.* Materials and structures, 1985. **18**(106): p. 285-290.
12.   Concrete, I.F.f.S., *CEB-FIP Model Code 2010.* 2010.
13.   UCHIDA, Y., K. ROKUGO, and W. KOYANAGI. *Determination of tension softening curves of concrete by means of bending tests.* in *ECF8, Torino 1990.*
14.   Bažant, Z.P. and B.H. Oh, *Crack band theory for fracture of concrete.* Matériaux et construction, 1983. **16**(3): p. 155-177.
15.   Tao, Y. and J.-F. Chen, *Concrete damage plasticity model for modeling FRP-to-concrete bond behavior.* Journal of Composites for Construction, 2014. **19**(1): p. 04014026.
16.   Rots, J.G., et al., *Smeared crack approach and fracture localization in concrete.* 1985.
17.   Hordijk, D.A., *Local approach to fatigue of concrete.* 1993.
18.   Systèmes, D., *Abaqus analysis user's manual.* Simulia Corp. Providence, RI, USA, 2007.
19.   Abaqus, *Abaqus user manual (version 6.14).* 2014.
20.   Lubliner, J., et al., *A plastic-damage model for concrete.* International Journal of solids and structures, 1989. **25**(3): p. 299-326.
21.   Lee, J. and G.L. Fenves, *Plastic-damage model for cyclic loading of concrete structures.* Journal of engineering mechanics, 1998. **124**(8): p. 892-900.
22.   Systèmes, D., *Abaqus 6.14–Analysis Users's Guide: Volume IV: Elements.* Providence, Rhode Island, 2013.
23.   Raffoul, S., et al., *Behaviour of unconfined and FRP-confined rubberised concrete in axial compression.* Construction and Building Materials, 2017. **147**: p. 388-397.
24.   Youssf, O., et al., *An experimental investigation of crumb rubber concrete confined by fibre reinforced polymer tubes.* Construction and Building Materials, 2014. **53**: p. 522-532.
25.   Duarte, A., et al., *Mechanical characterization of rubberized concrete using an image-processing/XFEM coupled procedure.* Composites Part B: Engineering, 2015. **78**: p. 214-226.

26.   Rots, J.G., *Computational modeling of concrete fracture.* 1988.
27.   Walraven, J., *fib Model Code for Concrete Structures 2010: mastering challenges and encountering new ones.* Structural Concrete, 2013. **14**(1): p. 3-9.
28.   Hu, H., et al., *Mechanical properties of SFRC using blended manufactured and recycled tyre steel fibres.* Construction and Building Materials, 2018. **163**: p. 376-389.
29.   Tlemat, H., K. Pilakoutas, and K. Neocleous, *Modelling of SFRC using inverse finite element analysis.* Materials and Structures, 2006. **39**(2): p. 221-233.

Chapter 4

Axial Behaviour of FRP-Confined Concrete Columns: An Experimental Investigation

4.1 INTRODUCTION

This chapter investigates the axial behaviour of square and circular concrete columns confined by externally bonded Fibre Reinforced Polymer (FRP) jackets. This paper first introduces the details of the comprehensive experimental programme. Axial compression tests were performed on 128 regular and rubberised concrete specimens. The parameters considered were rubber volumetric replacement ratio (0% and 60%), section shape (circular and square), FRP type (Carbon or Aramid) and the number of FRP layers (1, 2 and 3). Next, a discussion is carried out on the experimental behaviour in terms of stress-strain and dilation. The behaviour of the specimens in both axial and lateral directions, as well as their dilation characteristics, were investigated. Then the influence of various parameters on the confinement effectiveness is examined. The test results indicate that the confinement effectiveness of Aramid-FRP is better than that of Carbon-FRP. It is also shown that the detrimental effect of sharp corner on confinement effectiveness is less critical when using high rubber contents as the element can develop large lateral expansion at unprecedented axial deformation. Finally, the ability of selected design-oriented stress-strain models to capture the behaviour of for rubberised concrete square columns is assessed and found that existing design-oriented models fail to predict the behaviour of confined rubberised concrete, indicating the need for developing more refined confinement models.

4.2 EXPERIMENTAL PROGRAMME

One hundred and twenty-eight samples, including cylinders (Ø100mm × 200mm) and square columns (100 × 100mm in cross-section by 200mm in height), were manufactured using regular and rubberised concrete. Only one size of specimens was adopted owing to the fact that the size has negligible effects on the confinement effectiveness as long as similar confining pressure provided [1] (i.e. 2L FRP-confined cylinder with a dimension of Ø100mm × 200mm have same confining pressures as 3L FRP-confined cylinder with a dimension of Ø150mm × 300mm). To assess the compressive characteristics, a minimum of three replicates were tested for each of the examined parameters. The main parameters investigated were:

1) The radius of the corner (12mm and 50mm) (see Fig. 4 - 1);

2) Rubber volume replacement ratio ($\rho_{vr} = 0$ and 60%). This is defined as the ratio of the volume of mineral aggregates replaced by rubber to the total volume of mineral aggregates in the reference regular concrete mix;

3) The type of FRP fibre (Carbon or Aramid FRP) and confinement pressure (number of FRP layers).
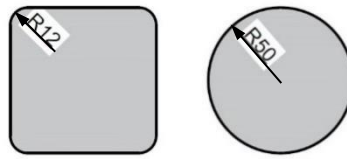
Fig. 4 - 1. Cross-sections of samples.

4.2.1   Fibre reinforced polymer jacket

Before applying the FRP confinement, the corners of the square specimens were ground to ensure a smooth transition with the flat sides and to improve adherence with the FRP jacket. The specimens were externally confined with one, two or three layers of Carbon FRP (CFRP) or Aramid FRP (AFRP) sheets using the wet lay-up technique. The unidirectional fabrics were oriented in the hoop direction and overlapped by a length of 100mm. The mean mechanical properties of the unidirectional FRP sheets shown in Table 4 – 2 were obtained using direct tensile tests on 12 FRP coupons.

Table 4 - 1. Material properties of FRP

	1-layer thickness (t_f)	Tensile strength (f_f)	Ultimate Strain (ε_{fu})	Modulus of Elasticity (E_f)
	mm	MPa	%	GPa
Aramid-FRP	0.185	2400 (24*)	2.06 (0.07*)	122 (25*)
Carbon-FRP	0.15	2040 (39*)	0.90 (0.05*)	225 (17*)

*Standard Deviation

4.2.2 Test setup and instrumentation

All samples were subjected to axial compressive load using a servo controlled ESH Universal Testing Machine. The test rig (see Fig. 4 - 3) was designed to measure global axial displacement using three laser sensors (LS) with an accuracy of 0.005 mm, placed radially at 120 degrees and 100 mm gauge length. The global lateral deformations of the cylindrical specimens were measured using three Linear Variable Differential Transformers (LVDTs), placed radially around the specimens (120 apart, see Fig. 4 – 3 (a)). Local axial strains (V1 and V2) and local lateral strains (H1, H2 and H3) were also measured by using strain gauges placed at mid-height of the specimen (see Fig. 4 – 3 (b)). The lateral expansion at mid-height of the square column specimens was measured with four LVDTs mounted on an aluminium frame (see Fig. 4 – 3 (c)). The transverse strains were measured at the centre of two opposite faces (LVDT1 and LVDT3) and at two opposite corners of the section (LVDT2 and LVDT4). Local axial strains (V1 and V2), local flat side lateral strain (H1, H2, H3 and H4) and local corner lateral strain (CH1, CH2 and CH3) were also measured using strain gauges placed at mid-height of the specimen (see Fig. 4 – 3 (d)). The lateral strain in the overlap area was not measured during the tests. To prevent possible local failure the specimen ends were confined using high strength high ductility post-tensioned metal straps of thickness 0.8 mm and width 25 mm [2]. The specimens were tested in displacement control at a rate of 0.5 mm/min up to failure [3].
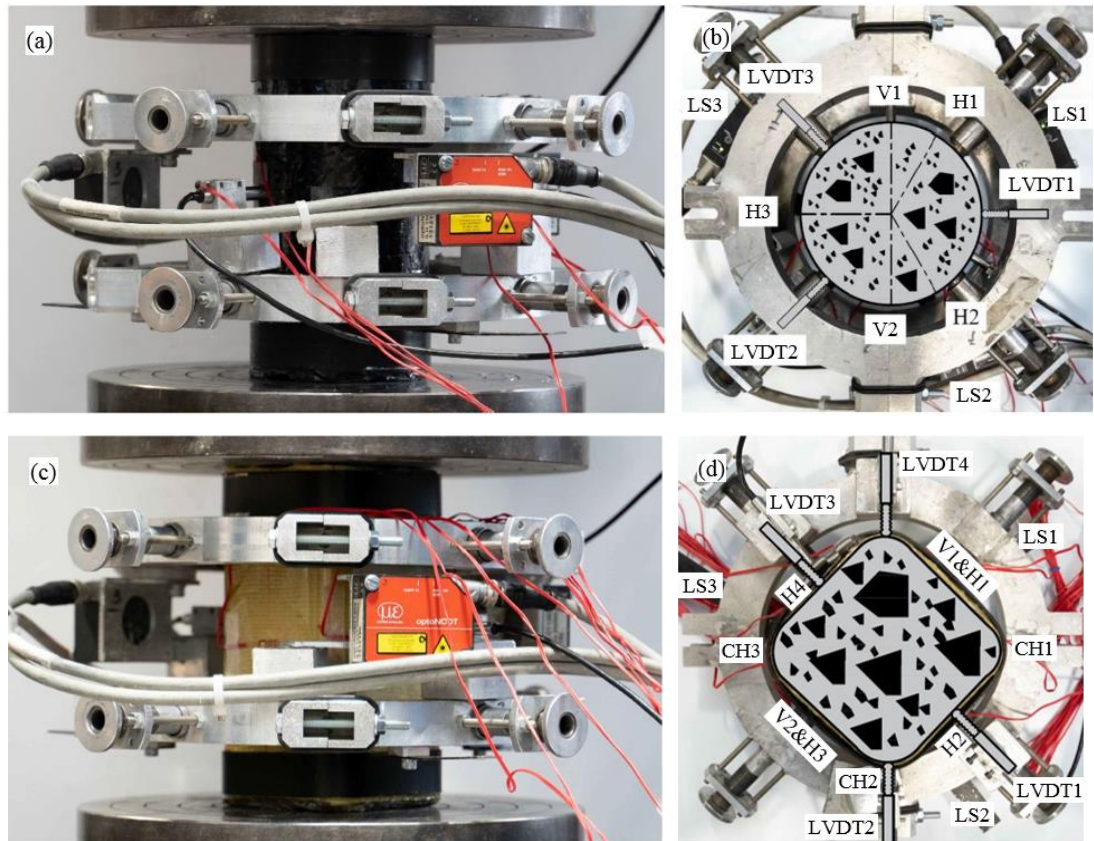
Fig. 4 - 2. Set-up of compressive tests: (a) front view and (b) top view of cylinder compressive tests,; (c) front view and (d) top view of square column compressive tests.

4.3   EXPERIMENTAL RESULTS

Table 4 - 3 summarises the mean-values of the compression test results of the FRP-confined specimens. The specimens are separated into two groups by rubber volumetric replacement ratios of ρ_{vr} = 0% (regular concrete) and 60% (rubberised concrete) and labelled as R0 and R60, respectively. In each group, the samples are identified according to the number of confining layers (1L, 2L or 3L), confining material (A=AFRP or C=CFRP) and shape of the cross-section (C=circular or S=square). For example, 2LA-S-R60 stands for rubberised concrete square column wrapped with two layers of AFRP.

Table 4 - 3 lists the material properties of FRP jacket (fabric thickness (t_f) , elastic modulus (E_f) and average hoop rupture strain ($\varepsilon_{h,rup}$)), confining jacket stiffness (K_j) (see Eq. (1)), critical stress (f_{cr}), ultimate compressive strength (f_{cc}), ultimate axial strain (ε_{cu}), ultimate area strains (ε_{au}),

confinement effectiveness (f_{cc}/f_{co}), ductility ($\varepsilon_{cu}/\varepsilon_{co}$) and crushing energy ($g_c$) obtained from the experimental tests. Critical stress (f_{cr}) is defined as the stress at which the secant modulus (E_{sec}) drops to around 70% of the concrete initial stiffness (E_c). f_{cc}/f_{co} and $\varepsilon_{cu}/\varepsilon_{co}$ were calculated as the ratio of the ultimate stress and strain of the FRP-confined specimens to the average peak stress and peak strain of the unconfined specimens, respectively. The average peak stress (f_{co}) and peak strain (ε_{co}) of the unconfined regular concrete (RC) specimen were 74.5 MPa and 0.225%, respectively; while the f_{co} and ε_{co} of the unconfined RuC specimen were 7.9 MPa and 0.133%, respectively. g_c is the area under the uniaxial compressive stress-strain curves. Fig. 4 – 4 shows the aforementioned parameters schematically.

$$K_j = \frac{2nt_f E_f}{Df_{co}}; K_j = \frac{2nt_f E_f}{D_{eq}f_{co}} \tag{1}$$

where D is the diameter of the circular section and $D_{eq} = \sqrt{2}a - (\sqrt{2}-1)2R_c$ is the equivalent circular diameter for the square section (a is the side length of square section and R_c is the size of the corner).
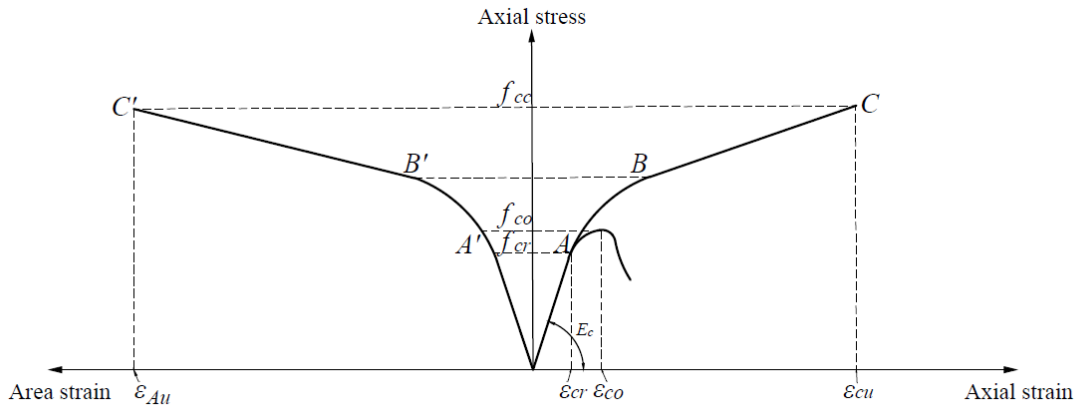
Fig. 4 - 3. Schematic representation of typical stress-strain behaviour of FRP-confined concrete.

In Fig. 4 - 4, the vertical strain gauges readings (V1 and V2) were used to determine the axial strains within the elastic region (O-A) and the axial strains beyond the critical stress (f_{cr}) (A-C) were derived from the laser sensors readings (LS1-LS3). This was due to the excessive localised bulging on the FRP jacket, which led to spurious strain gauge readings after f_{cr} (point A). In order

to directly compare the stress-strain behaviour of FRP-confined cylinders with that of FRP-confined square columns, the area strain was analysed instead of lateral strain and the value was calculated as following:

For circular cross-sections, the area strain with in region O-A and A-C can be determined by Eq. (2) and (3), respectively.

Using strain gauge measurements:

$$\varepsilon_h = \frac{\Delta L_c}{L_c} = \frac{2\pi r(1 + \varepsilon_r) - 2\pi r}{2\pi r} = \varepsilon_r$$

$$\varepsilon_A = 2\varepsilon_r = 2\varepsilon_h$$

(2)

Using LVDT measurements:

$$\varepsilon_A = \frac{\Delta A}{A} = \frac{\pi(r + \Delta r)^2 - \pi r^2}{\pi r^2} = (1 + \varepsilon_r)^2 - 1 = 2\varepsilon_r + \varepsilon_r^2 \approx 2\varepsilon_r$$

(3)

For square cross-sections, the expansion of the cross-section can be divided into two parts: A_c and A_f. A_c stands for the expansion of the circumference and A_f indicates the expansion of the fan-shaped area (see Fig. 4 - **Error! Reference source not found.**). Therefore, the total area expansion of square cross-section is $A_c + 4A_f$. The value of ε_A can be obtained using measurements recorded by strain gauge (Eq. (4)) and LVDTs (Eq. (5)), respectively. Eq. (6) can be used to calculate the value of A_f.
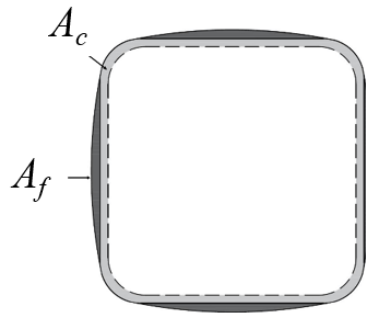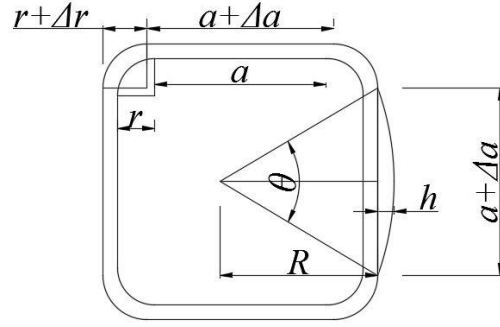
Fig. 4 - 4. Schematic representation of deformation for the square cross-section.

Using strain gauge measurements

$$
\begin{aligned}
\varepsilon_A = \frac{\Delta A}{A} &= \frac{A + A_c + 4A_f - A}{A} \\
&= \frac{\left[a^2 \left(1 + \varepsilon_a\right)^2 + 4ar\left(1 + \varepsilon_a\right)\left(1 + \varepsilon_r\right) + \pi r\left(1 + \varepsilon_r\right)^2 \right] - \left(a^2 + 4ar + \pi r^2\right) + 4A_f}{a^2 + 4ar + \pi r^2} \\
&\approx \frac{\left[2a^2\varepsilon_a + 4ar\left(\varepsilon_a + \varepsilon_r\right) + 2\pi r\varepsilon_r \right] + 4A_f}{a^2 + 4ar + \pi r^2}
\end{aligned} \tag{4}
$$

Using LVDT measurements

$$
\begin{aligned}
\varepsilon_A = \frac{\Delta A}{A} &= \frac{A + A_c + 4A_f - A}{A} \\
&= \frac{\left[\left(a + \Delta a\right)^2 + 4\left(a + \Delta a\right)\left(r + \Delta r\right) + \pi\left(r + \Delta r\right)^2 \right] + 4A_f - \left(a^2 + 4ar + \pi r^2\right)}{a^2 + 4ar + \pi r^2}
\end{aligned} \tag{5}
$$

where the value of fan-shaped area A_f can be determined as follows:

$$
A_f = \frac{1}{2}R^2\theta - \frac{1}{2}b\sqrt{R^2 - \left(\frac{a_n}{2}\right)^2} \quad (\theta \text{ in rad})
$$

$$
a_n = a + \Delta a, \ R = \frac{a_n^2 + 4h^2}{8h} \quad \text{and} \quad \theta = \arctan\frac{2h}{a_n}
$$

(6)

Table 4 - 2. Mean-values of experimental results.

ρ_{vr}	Specimen	D or D_{eq} mm	t_f mm	E_f GPa	$\varepsilon_{h,rup}$ %	K_j	f_{cr} MPa	f_{cc} MPa	ε_{cu} %	ε_{au} %	f_{cc}/f_{co}	$\varepsilon_{cu}/\varepsilon_{co}$	g_c N/mm^2
R0	1LA-C	100	0.185	122	1.515	6.06	59.5	85	1.48	3.03	1.14	6.58	1.07
	2LA-C	100	0.37	122	1.505	12.12	79.8	114	1.66	3.01	1.53	7.38	1.45
	3LA-C	100	0.555	122	1.575	18.18	98.14	140.2	2.07	3.15	1.88	9.2	2.15
	1LA-S	129	0.185	122	0.772	4.7	43.575	62.25	0.76	1.83	1	3.38	0.46
	2LA-S	129	0.37	122	0.896	9.39	67.9	75	1.26	2.52	1.06	5.6	0.96
	3LA-S	129	0.555	122	1.007	14.09	69.79	99.7	1.73	3.03	1.34	7.69	1.42
	1LC-C	100	0.15	225	0.69	9.06	56.7	81	0.8	1.32	1.09	3.56	0.62
	2LC-C	100	0.3	225	0.72	18.12	77	110	1.1	1.44	1.48	4.89	0.92
	3LC-C	100	0.45	225	0.74	27.18	91	130	1.29	1.52	1.74	5.73	1.27
	1LC-S	129	0.15	225	0.382	7.02	48.65	69.5	0.5	0.91	1	2.22	0.31
	2LC-S	129	0.3	225	0.414	14.05	58.8	84	0.67	1	1.13	2.98	0.46
	3LC-S	129	0.45	225	0.483	21.07	67.2	96	0.79	1.2	1.29	3.51	0.52
R60	1LA-C	100	0.185	122	1.68	50.72	19.18	27.4	3.12	3.03	3.08	23.46	0.85
	2LA-C	100	0.37	122	1.785	101.44	29.4	42	3.81	3.31	4.72	28.65	1.04
	3LA-C	100	0.555	122	1.798	152.16	42.35	60.5	4.89	3.38	6.8	36.77	1.59
	1LA-S	129	0.185	122	1.281	39.32	14.42	20.6	3.76	3.61	2.58	27.14	0.71
	2LA-S	129	0.37	122	1.496	78.63	24.43	32.2	4.95	4.45	4.03	33.46	1.26
	3LA-S	129	0.555	122	1.632	117.95	35.7	47	5.71	5.06	5.88	38.05	2.14
	1LC-C	100	0.15	225	0.78	75.84	16.59	23.7	1.52	1.43	2.66	11.43	0.26
	2LC-C	100	0.3	225	0.805	151.69	25.13	35.9	1.84	1.63	4.03	13.83	0.44
	3LC-C	100	0.45	225	0.795	227.53	33.11	47.3	2.05	1.59	5.31	15.41	0.6
	1LC-S	129	0.15	225	0.619	58.79	10.15	14.5	1.32	1.08	1.63	8.35	0.12
	2LC-S	129	0.3	225	0.741	117.59	14.35	20.5	1.67	1.45	2.3	12.56	0.26
	3LC-S	129	0.45	225	0.811	176.38	19.95	28.5	2.1	1.63	3.2	15.79	0.41

4.3.1   Failure mode and ultimate condition

All FRP-confined specimens failed abruptly by tensile rupture of the FRP jackets (see Fig. 4 - 6). In the case of CRC, the rupture of both Aramid and Carbon FRP always happened in the corner region. However, in the case of CRuC, rupture of the Carbon-FRP rupture was observed at either the corner or flat region, while rupture of the Aramid-FRP always occurred at the flat side. This will be discussed in more detail in the following sections.

Fig. 4 - 5. Failure modes of square columns.

Fig. 4 - 7 shows that for both CRC and CRuC specimens, the average FRP hoop rupture strain ($\varepsilon_{h,rup}$) is below the failure tensile strain of the FRP coupons (ε_{fu}) (i.e. ε_{fu} = 2.06% and 0.9% for aramid and carbon, respectively). This premature rupture was also reported in many other studies [4-9] and can be attributed to several factors (e.g. non-homogeneous deformations of the cracked concrete that lead to stress concentrations in the FRP, triaxial stress states of FRP during loading, geometrical imperfections, and nonuniform supports in test setup, as well as fibre misalignment and overlap length). Chen et al. [8] have discussed in detail about the failure models of and defined 17 contributory factors fall into 5 categories. Nevertheless, these factors may interact with each other and lead to a more complicated mechanism and there is still no available rational model can be used to predict this phenomenon.

It can be seen from Fig. 4 - 7 that the $\varepsilon_{h,rup}$ of CRuC specimens was higher than that of CRC specimens. More specifically, CFRP CRC and CRuC cylinders failed at around 75-80% and 80-90% of ε_{fu}, respectively. AFRP CRC and CRuC cylinders failed at around 70-80% and 85-90% of ε_{fu}, respectively. This phenomenon is more pronounced in square columns, in which the $\varepsilon_{h,rup}$ of CRuC was up to 1.8 times higher than that of CRC. It is worth noting that the $\varepsilon_{h,rup}$ of the three-layer CRuC square columns nearly reached the value developed in cylinder columns. This confirms that replacing mineral aggregates with rubber particles can lead to an enhancement in

FRP efficiency. For circular columns, the $\varepsilon_{h,rup}$ was found to be independent of the number of FRP

layers, whilst for square columns, it increases with an increasing number of FRP layers.
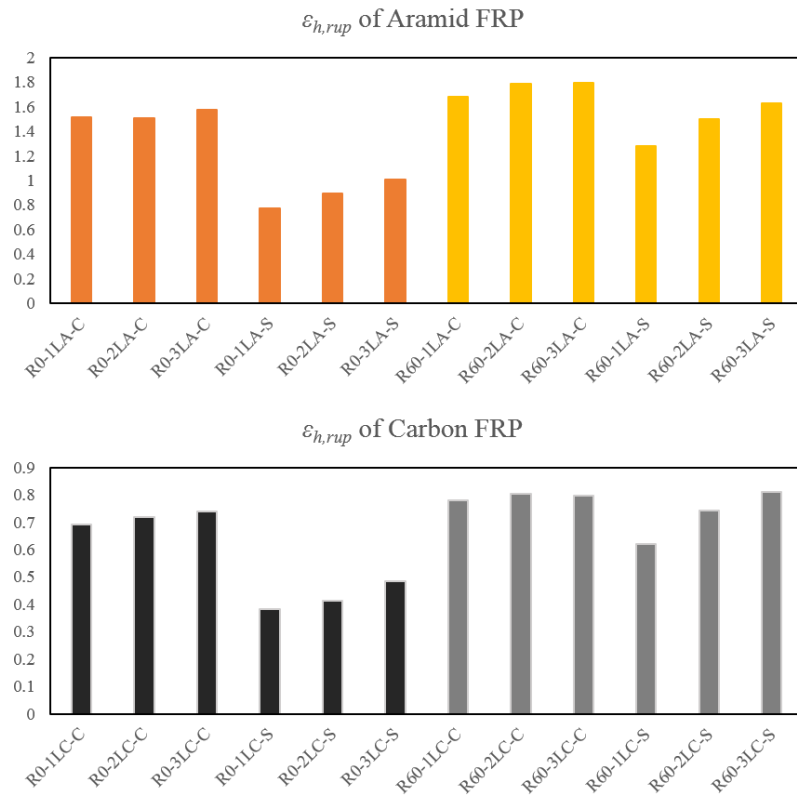
Fig. 4 - 6. The average FRP hoop rupture strains

4.3.2 Hoop strain at corner vs flat side

Fig. 4 - 8 shows the mean value of the FRP hoop strain on the flat side (ε_{h_F}) and in the corner

region (ε_{h_C}), as determined by the strain gauge readings H1-H4 and CH1-CH3, respectively. The

significant difference between these two hoop strains indicates high variability in strain

distribution along the circumference of the jacket. The strain distribution in CRC shows higher

values of ε_{h_C}, while higher values of ε_{h_F} are typically seen in CRuC. This confirms that the FRP

hoop strain is considerably influenced by location and concrete type. The development of higher

ε_{h_C} in CRC can be attributed to the arch effect in the confined section, as the concrete in the

diagonal direction is under significantly higher confinement pressure than the concrete close to

the flat side. The difference between ε_{h,rup_F} and ε_{h,rup_C} decreases with increasing number of FRP

layers, as a higher expansion of the flat side is developed. In the CFRP CRuC specimens, the difference between ε_{h,rup_F} and ε_{h,rup_C} is smaller when compared to CFRP CRC. This indicates that CFRP CRuC deformed more uniformly than CFRP CRC. However, a more non-uniform strain distribution was unexpectedly observed in AFRP CRuC specimens. In these specimens, the ε_{h_C} is significantly lower than ε_{h_F} and slightly decreases with increasing number of FRP layers. This may be the result of considerable lateral expansion of the flat side of AFRP CRuC specimens (up to 6 mm), which creates opposite curvature and reduces the relative bending strain at the corner. It is worth noting that if $\varepsilon_{h,rup}$ was determined by readings H1-H4, its value would reach ε_{fu}; if $\varepsilon_{h,rup}$ was determined through readings CH1-CH3, the value would only be 48% of ε_{fu}.
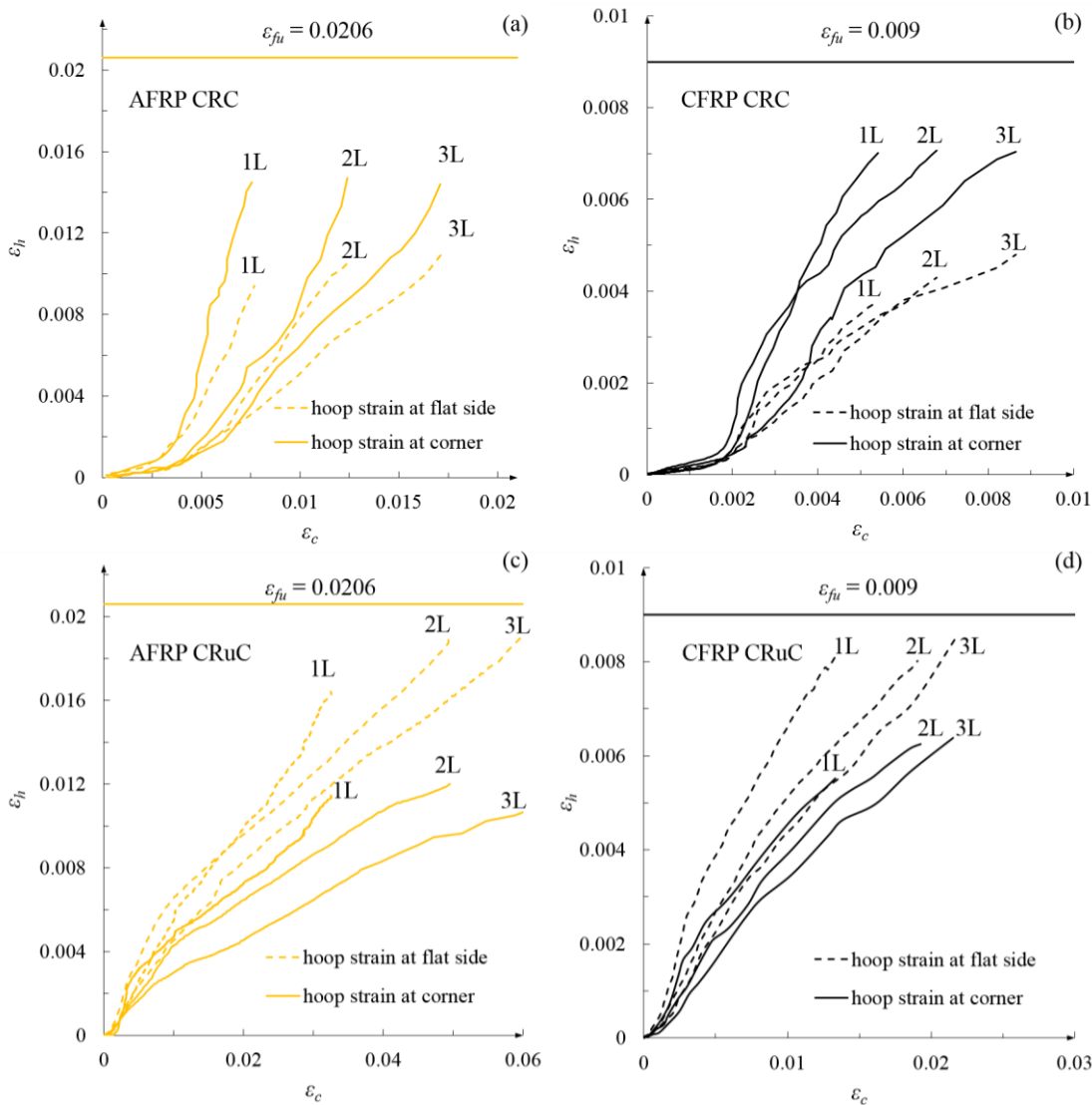
Fig. 4 - 7. Comparison between the average FRP hoop rupture strains at the flat side and the corner of square columns.

In most existing stress-strain models, failure is controlled by $\varepsilon_{h,rup}$, which is normally related to ε_{fu} through an FRP strain reduction factor ($k_{\varepsilon f}$). For CRC, a value of $k_{\varepsilon f}$ should be determined from the hoop rupture strain at the round corner, rather than the strain measured on the flat side [10]. However, in CRuC, this will lead to a significant underestimation of strength and ultimate strain capacity. Hence, a more rational way to calculate the value of $k_{\varepsilon f}$ is needed.

4.4 KEY RESPONSE PARAMETERS

4.4.1 Stress-strain behaviour

Fig. 4 - 8 and 3 - 9 present the average experimental stress-strain behaviour of CRC and CRuC in circular and square cross-sections, respectively. Yellow lines and black lines indicate AFRP-confined and CFRP-confined specimens, respectively. Solid lines and dashed lines represent cylinders and square columns, respectively. The axial compressive stress f_{cc} was determined by normalising the compressive force with respect to the cross-sectional area at mid-height of the specimen. The axial strain (ε_c) is shown on the right of the figure (positive side), and the area strain (ε_A) is shown on the left (negative side). A detailed discussion of these results is presented in the following sections.
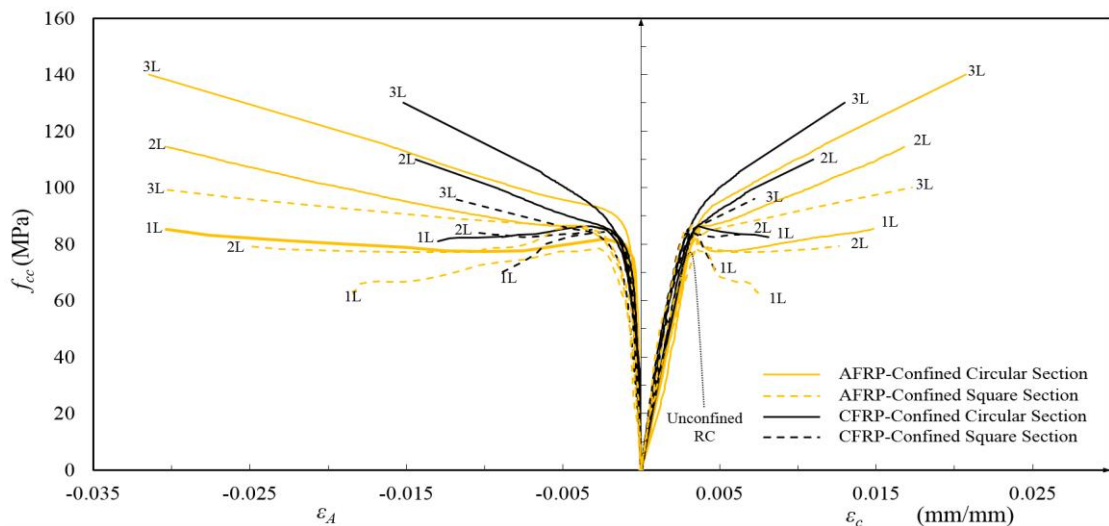
Fig. 4 - 8. Stress-strain curves of CRC in circular and square sections.
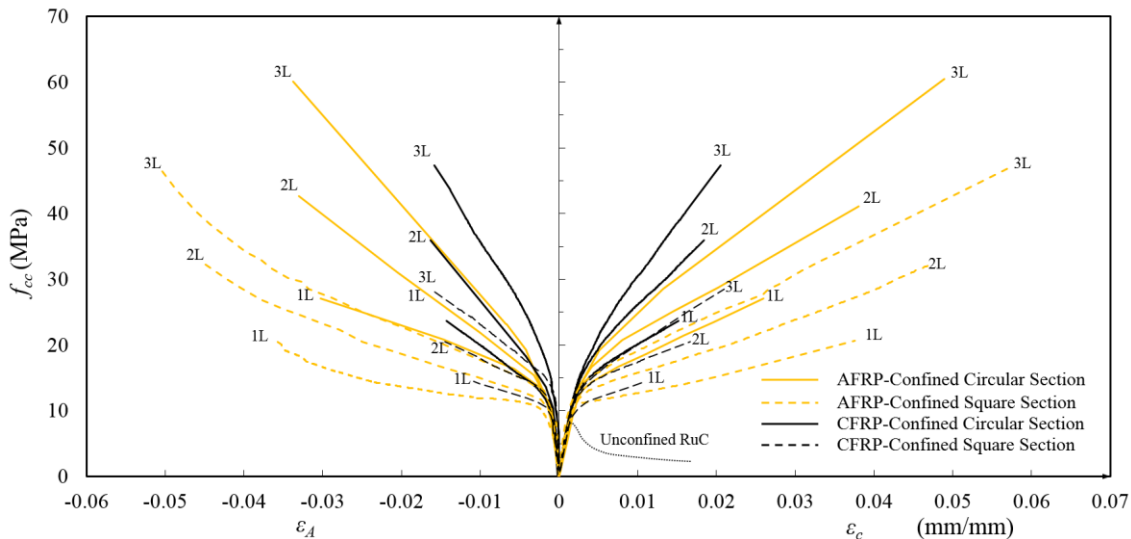
Fig. 4 - 9. Stress-strain curves of CRuC in circular and square sections.

4.4.2 CRC vs CRuC

In Fig. 4 - 8 and 9, two types of behaviour can be identified. Some CRC specimens (1LA-C-R0, 1LC-C-R0, 1/2LC-S-R0 and 1/2LA-S-R0) show a strain-softening behaviour, which indicates insufficient confinement. The remaining CRC specimens and all CRuC specimens show strain-hardening. Although the strength of unconfined RuC was only 10% of that of the unconfined RC, the use of FRP confinement led to an increase in strength up to 51% of the strength of the corresponding CRC specimens.

Table 4 – 3 indicates that the influence of confinement stiffness on the behaviour of CRuC is more pronounced than CRC. For example, compared with the 3-layer AFRP CRC square columns, the corresponding CRuC columns show 250% and 170% increases in axial and area strain, respectively. The maximum ratio of f_{cc}/f_{co} of CRC is 1.88, while the CRuC reaches 6.8. More importantly, the maximum ratio of $\varepsilon_{cu}/\varepsilon_{co}$ of CRC is 9.2, while it reaches 38 for CRuC. These improvements result in greater crushing energy for CRuC specimens as measured by the area under the axial stress-strain curve. For instance, the crushing energy of 3-layer AFRP CRC square column is 1.42×10^{-3} J, while the corresponding CRuC column dissipates a total of 2.14×10^{-3} J. This greater crushing energy can be exploited, for example, in seismic applications.

4.4.3   CFRP vs AFRP confinement

Fig. 4 - 8 and 9 indicate that the use of the same number of carbon or aramid FRP layers, which means that CFRP jacket stiffness is about 1.5 times higher than an AFRP jacket (see Table 4 – 3)), leads to a stiffer hardening response for CFRP (about 1.8 times higher). However, due to the higher rupture strain of aramid, the AFRP-confined specimens show higher ultimate compressive stress and strain. As a result, the confinement effectiveness of AFRP is significantly higher than that of CFRP.

Despite the fact that the CRC specimens confined with AFRP or CFRP have similar strengths (f_{cc}/f_{co}), the specimens confined with AFRP exhibit much higher axial deformability ($\varepsilon_{cu}/\varepsilon_{co}$). On the contrary, the CRuC specimens confined with AFRP are considerably stronger, as well as being more deformable than CFRP-confined specimens, especially in square columns. For example, the f_{cc}/f_{co} of 3-layer AFRP CRuC square columns is almost 2 times that of the corresponding CFRP specimens. Although superior confinement effectiveness of AFRP in terms of $\varepsilon_{cu}/\varepsilon_{co}$ has also been reported in the literature [19, 25, 26], the improvement in f_{cc}/f_{co} was only observed before in CRuC [5]. This may be attributed to the very high axial deformability of CRuC, which results in large axial loads being transferred to the CFRP jacket, which loses strength under the biaxial stress-state (compression-tension). This shows that aramid, which is more tolerant to biaxial stresses, is more suitable when developing high-strength high-deformability elements for structural applications.

4.4.4   Circular vs Square section

As expected the confinement effectiveness of FRP on square columns is less than on circular sections (see Fig. 4 - 8 and 9). In the case of CRC, the increase in confinement stiffness produces less improvement in the strength and deformability of square columns than the corresponding cylinders. In the case of CRuC, thus reduction of confinement effectiveness is also observed, but unlike CRC, the deformability of CFRP CRuC is less affected by the section shape. The AFRP CRuC exhibit even better deformability in square sections than circular sections, as a larger area

strain develops. A recovery in confinement effectiveness is also observed at large deformation levels, which indicates that the confined shape is becoming more efficient.

4.4.5 Area strain vs Axial strain

In general, the curves of area strain-to-axial strain can be characterised by three phases (see Fig. 4 – 11): I) an initial elastic phase up to the axial compressive strain of around 0.6-0.8 of the peak strain of unconfined concrete; II) a transition phase where the stiffness drops and then stabilises or slightly increases; and III) a linear phase until the hoop rupture strain is reached. In Phase I, the initial slope is in agreement with Poisson's ratio of concrete within its elastic range. At the axial strain of 0.001, the area strain of RuC (6.4×10^{-4}) was higher than that of RC (3.5×10^{-4}), confirming that the use of high rubber contents in concrete can increase lateral expansion. In Phase II, the unstable microcrack propagation occurs and leads to a rapid increase in the lateral strain and results in the loss of cohesion with the concrete. In Phase III, the gradient of the slope depends on the confinement stiffness. However, this effect reduces at high strain levels for CRuC square columns. Furthermore, based on the results shown in Fig. 4 - 12 (a-d), the ultimate area strain of FRP-confined cylinder does not appear to be greatly affected by the number of FRP layers and the strength of the concrete. However, the ultimate area strain of FRP-confined square columns increases with increasing confinement level (see Fig. 4 - 12 (e-h)).
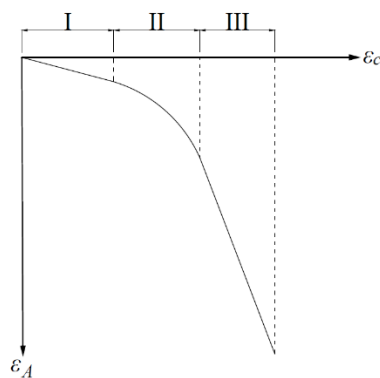
Fig. 4 - 10. Schematic representation of a typical curve of area strain-to-axial strain.

(a) AFRC CRC Cylinder

(b) CFRC CRC Cylinder

(c) AFRP CRuC Cylinder

(d) CFRP CRuC Cylinder

(e) AFRP CRC Square Columns

(f) CFRP CRC Square Columns
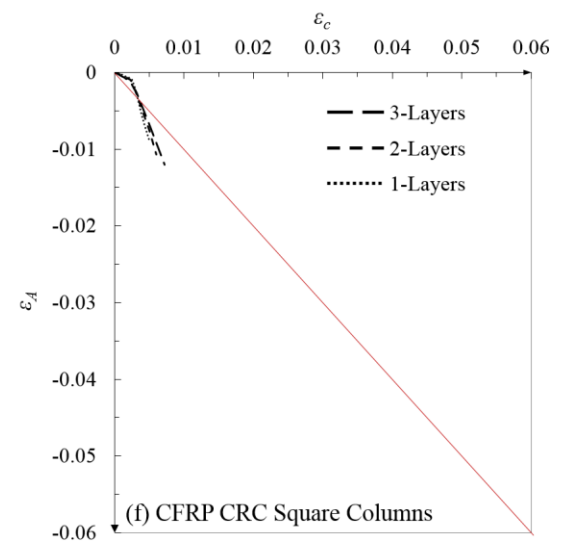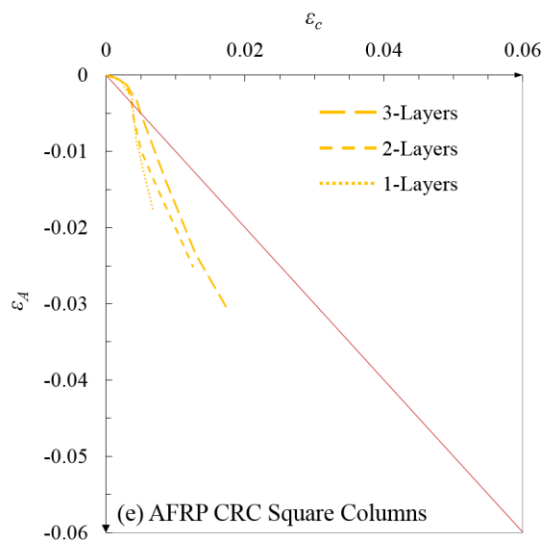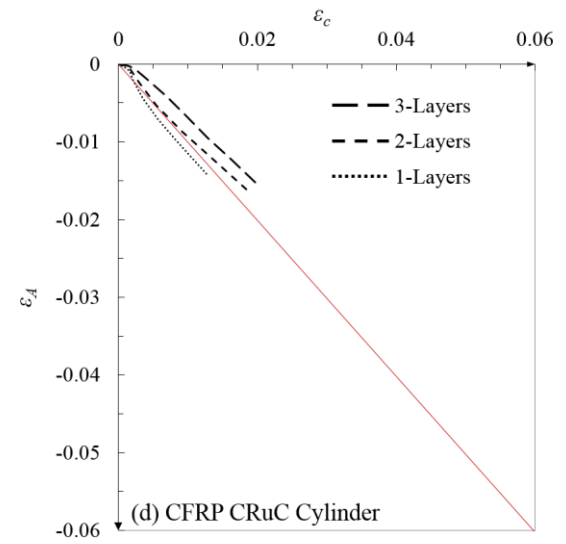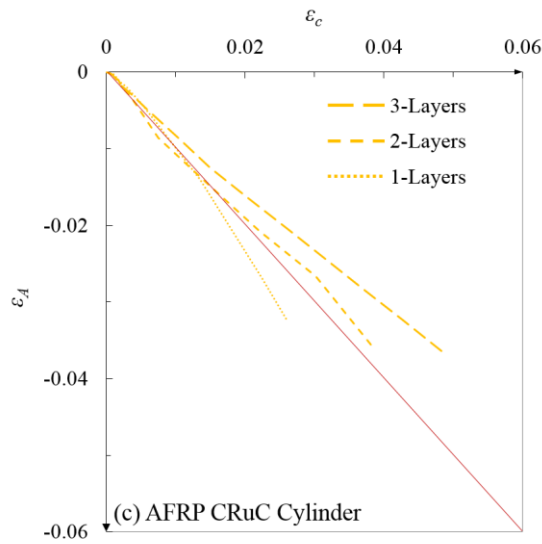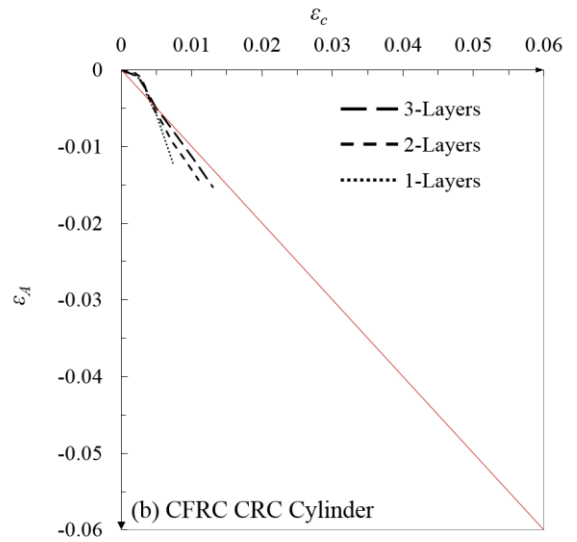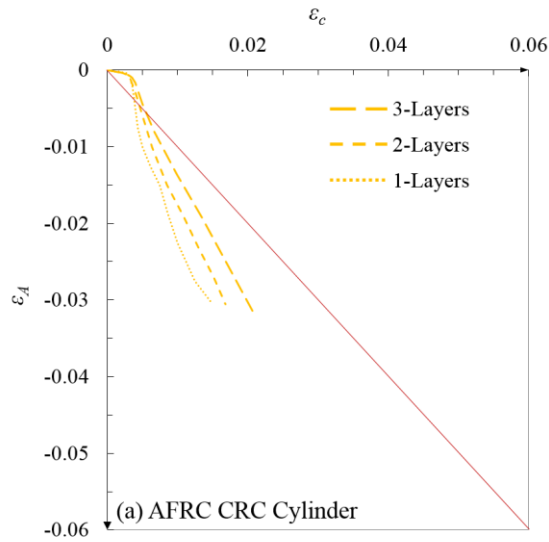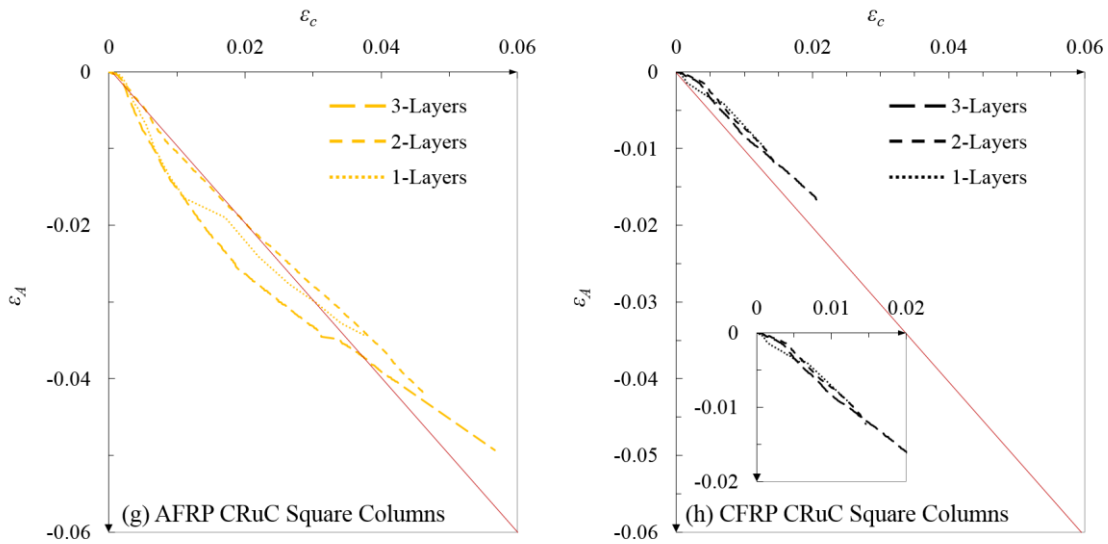
Fig. 4 - 11. Axial strain vs area strain of FRP-confined concrete.

4.4.6 Volumetric behaviour and Poisson's ratio

To provide further insight into the mechanical behaviour of regular and rubberised concrete under passive FRP confinement, the volumetric behaviour and Poisson's ratio v of the tested specimens are examined in this section. Fig. 4 - 12 compares the average axial stress of FRP-confined specimens and their corresponding volumetric strains (ε_V), which are calculated as:

$$\varepsilon_V = \varepsilon_A - \varepsilon_c \qquad (7)$$

where ε_A and ε_c are the absolute values of area and axial strains measured during the test, respectively. In Eq. (7), negative ε_V values denote volumetric contraction, whilst positive values indicate volumetric expansion.
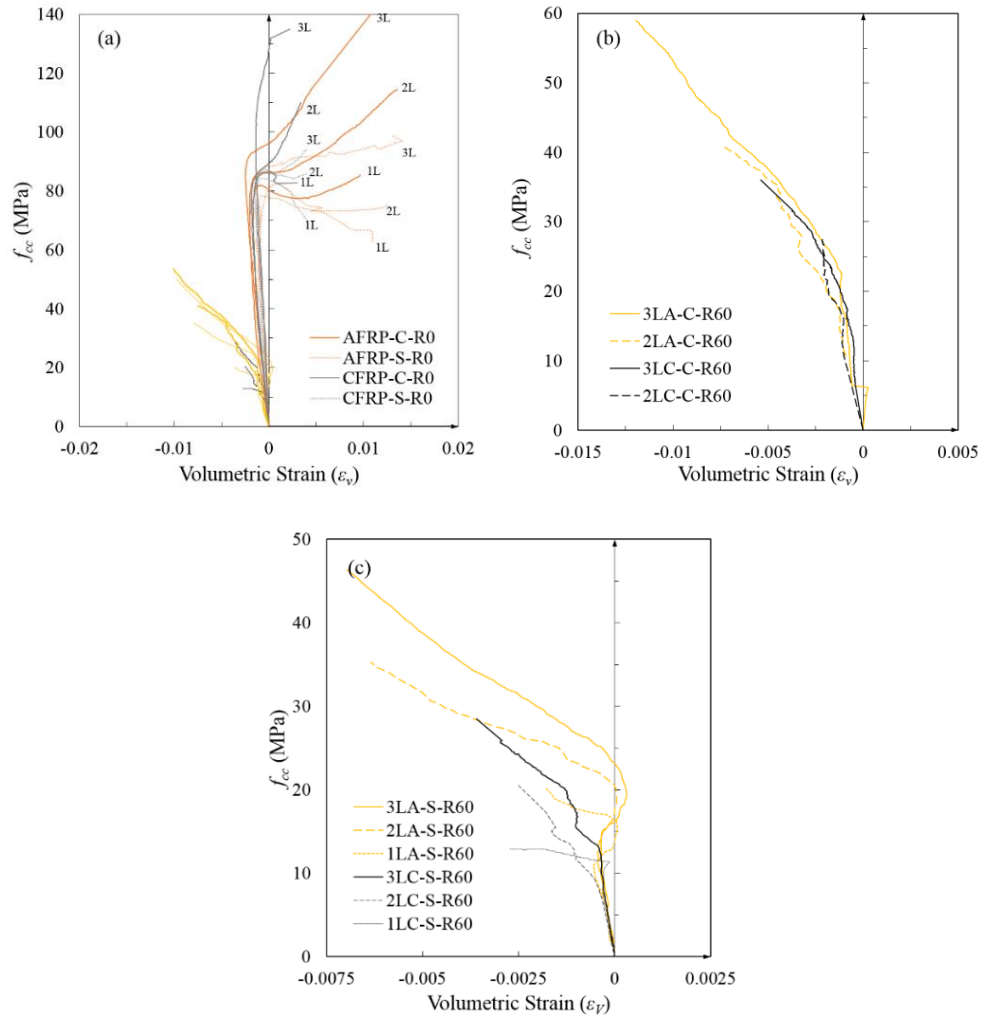
Fig. 4 - 12. Volumatic strain vs Axial stress: (a) CRC; (b) CRuC cylinders and (c)FRP-confined square columns.

Fig. 4 - 12 indicates that all FRP-confined specimens exhibit volumetric contraction at the initial elastic stage up to the critical stress f_{cr} with a similar rate to the bulk modulus of the unconfined concrete. For CRuC, f_{cr} increases with increasing confinement level, while the critical stress f_{cr} of CRC is equal to around 95% of the strength of the unconfined RC. During this stage, the Poisson's ratio v remains in the range of 0.15-0.25 for RC and 0.22-0.35 for RuC. Beyond this stage, the volumetric strain of CRC increases and becomes zero at axial stress 20 % higher than the compressive strength of unconfined concrete. This dilation behaviour continues to increase until failure. This dilatancy phenomenon appears to be affected by the level of confining pressure, thus the higher FRP confinement, the less volumetric expansion. When compared with the behaviour of CRC, CRuC shows entirely different behaviour. Apart from AFRP CRuC square columns, for

which initial contraction is followed by a temporary expansion, all the CRuC samples contract continuously. This contraction behaviour may be attributed to the "fluidity" of rubber particles, which possibly fill in the voids left by the crushed concrete. Similar behaviour was observed in the literature [12]. This double volumetric reversal has also been reported in the literature [11, 12], for regular concrete confined by very large amounts of FRP (e.g. 10 layers and 14 layers FRP). Therefore, volumetric behaviour is also strongly influenced by the confinement stiffness (K_j). However, due to the limited test data, the critical confinement stiffness (K_j) that leads to zero volume change cannot be determined accurately.

Fig. 4 – 14 compares the secant dilation ratio against axial strain. The secant dilation ratio is calculated by:

$$v = -\frac{\varepsilon_h}{\varepsilon_c} \tag{8}$$

Fig. 4 - 13a shows that the secant dilation ratio of CRC starts at 0.18 at low axial strain and increases rapidly beyond 1.0 with increasing axial strain, which indicates that the concrete experiences significant volume expansion due to unstable crack propagation. The secant dilation ratio then tends to stabilise once the FRP jacket is fully activated. In the case of CRuC, the secant dilation ratio starts around 0.2 and increases to around 0.4, then stabilises at an asymptotic value in the range of 0.35 to 0.4 (see Fig. 4 - 13b). This unique behaviour indicates that CRuC stops dilating due to cracking and behaves almost like a hydrostatic material. The high and constant value of secant dilation ratio results in a low and constant shear modulus, which can lead to high shear deformability. This was investigated in a previous numerical and experimental study by the authors [13].
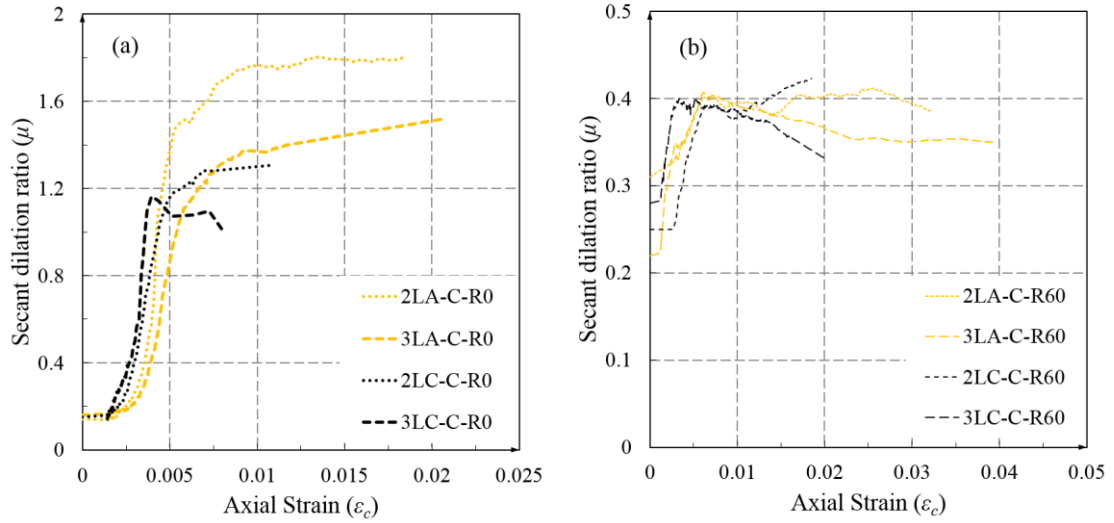
Fig. 4 - 13. Secant dilation ratio of CRC (a) and CRuC (b).

4.5 ASSESSMENT OF EXISTING DESIGN-ORIENTED MODELS FOR CRC RECTANGULAR COLUMNS

In the literature, many stress-strain models have been developed for CRC and can be classified into two categories: 1) analysis-oriented models and 2) design-oriented models [14]. Analysis-oriented models are generally more versatile as they consider the interaction between concrete and confining device. The accuracy of prediction highly relies on the accurate dilation characteristic of FRP-confined concrete (i.e. lateral strain to axial strain relationship). However, due to non-uniform strain distribution around the perimeter of the rectangular cross-sections, there is no available model that can describe the dilation behaviour of FRP-confined rectangular columns. Design-oriented models consider the FRP-confined concrete as a uniform material and only require several experimental-determined material properties (e.g. FRP properties (thickness (t_f), tensile stress (f_f) and elastic modulus (E_f)) and concrete properties (compressive strength (f_{co}) and corresponding strain (ε_{co})). The majority of design-oriented models focus on relating the compressive behaviour of FRP-confined rectangular columns to that of circular columns through a geometrically defined efficiency factor. This allows the use of a unified approach based on the simple and robust formulations of σ-ε developed for circular sections. The selected designed-

oriented stress-strain models for rectangular columns are summarised in Table 4 - 4 [6, 15-18]. The main difference between those models revolves around the definitions of diameter (D_{eq}) of an equivalent circular column and an FRP strain reduction factor ($k_{\varepsilon f}$). For example, according to ACI 440 [15] and Youssef et al. [6], D_{eq} can be calculated as $2bh/(b+h)$, while Lam and Teng use $D_{eq} = \sqrt{b^2 + h^2}$. In this study, the accuracy of the models was evaluated using three statistical indicators ((1) Mean Square Error (MSE), (2) Average Absolute Error (AAE) and (3) Standard Deviation (SD)), as determined by Eqs. (9)-(11).

$$\omega_w = \frac{4n_f t_f E_f \varepsilon_{h,rup}}{D_{eq} f_{co}} \tag{9}$$

$$MSE = \frac{\sum_{i=1}^{N} [\frac{pre_i - exp_i}{exp_i}]^2}{N} \tag{10}$$

$$AAE = \frac{\sum_{i=1}^{N} \left| \frac{pre_i - exp_i}{exp_i} \right|}{N} \tag{11}$$

$$SD = \sqrt{\frac{\sum_{1}^{N} \left(\frac{pre_i}{exp_i} - \frac{pre_{avg}}{exp_{avg}} \right)^2}{N}} \tag{12}$$

where pre and exp represent the predicted and experimental values of f_{cc}/f_{co} or $\varepsilon_{cu}/\varepsilon_{co}$, respectively; the subscript avg indicates the average value and N is the total number of the tests data.

Figs. 3 - 15 and 3 - 16 show the performance of selected models through comparing the test results (summarised in Table 4 - 5) of CRC and CRuC square columns to the theoretical predictions in terms of f_{cc}/f_{co} and $\varepsilon_{cu}/\varepsilon_{co}$, respectively; while the error indicators of the models are presented in Figs. 17 and 18.

In general, all selected models successfully predict an increase in strength gained with increasing confinement. The selected models provide better predictions for the ultimate strength and strain of CRC compared to that of CRuC specimens and better performance can be observed in CFRP confined specimens rather than AFRP confined specimens. As can be seen in Figs. 15 and 16, the

ACI 440.2R significantly underestimates the confinement effectiveness of CRuC (up to 2 times in strength and 16 times in strain). Due to the limitation of k ($0 \leq k \leq 0.8\%$), the model proposed by Chaallal et al. [16] cannot be applied to CRuC, but a good correlation has been found for one layer confined CRC. The model of Youssef et al. [6] shows a close prediction with the ultimate strain of CFRP CRC and tends to underestimate the ultimate strength of CRC and CRuC. Lam and Teng [17] and Wang and Restrepo [18] offer the best agreement with test results for CFRP CRC and can predict the f_{cc}/f_{co} ratio for CFRP CRuC with acceptable accuracy. However, both of them dramatically underestimate the ultimate strength and strain of AFRP confined specimens, especially for AFRP CRuC. By evaluating the error indicators (MSE, AAE and SD) of each model (see Fig. 17 and 18), it is shown that Lam and Teng' model [17] produces the most accurate prediction among these five selected models. Therefore, its performance in terms of stress-strain history will be evaluated in the next section.

Table 4 - 3. Selected designed-oriented stress-strain models for FRP-confined rectangular columns

Youssef et al. [6]	$$\frac{f_{cc}}{f_{co}} = 0.5 + 1.225\left(\frac{f_{l,a}}{f_{co}}\right)^{0.6}$$ $$\frac{\varepsilon_{cu}}{\varepsilon_{co}} = 0.004325 + 0.2625\left(\frac{f_{l,a}}{f_{co}}\right)\left(\frac{\varepsilon_{h,rup}}{E_f}\right)^{0.5}$$ $$k_e = 1 - \frac{\left[(h-2R_c)^2 + (h-2R_c)^2\right]}{3hb}$$
Lam and Teng [17]	$$\frac{f_{cc}}{f_{co}} = 1 + 3.3\cdot\left(\frac{b}{h}\right)^2 \frac{A_e}{A_c}\frac{f_{l,a}}{f_{co}}$$ $$\frac{\varepsilon_{cu}}{\varepsilon_{co}} = 1.75 + 12\cdot\left(\frac{b}{h}\right)^{0.5}\left(\frac{A_e}{A_c}\right)\left(\frac{f_{l,a}}{f_{co}}\right)\left(\frac{\varepsilon_{h,rup}}{\varepsilon_{co}}\right)^{0.45}$$ $$\frac{A_e}{A_c} = 1 - \frac{\left[\left(\frac{b}{h}\right)(h-2R_c)^2 + \left(\frac{h}{b}\right)(h-2R_c)^2\right]}{3A_g}$$
Wang and Restrepo [18]	$$\frac{f_{cc}}{f_{co}} = k_c = \alpha_1\alpha_2$$

	$\alpha_1 = 1.25 \left(1.8 \sqrt{1 + 7.94 \dfrac{f_{l,j1}}{f_{co}}} - 1.6 \dfrac{f_{l,j1}}{f_{co}} - 1 \right)$ $\alpha_2 = \left[1.4 \dfrac{f_{l,j2}}{f_{l,j1}} - 0.6 \left(\dfrac{f_{l,j2}}{f_{l,j1}} \right)^2 - 0.8 \right] \sqrt{\dfrac{f_{l,j1}}{f_{co}}} + 1$ $\dfrac{\varepsilon_{cu}}{\varepsilon_{co}} = 1 + 5 \left(\dfrac{f_{cc}}{f_{cu}} - 1 \right)$ $f_{l,j1} = \dfrac{2nt}{b} k_s f_j ; f_{l,j2} = \dfrac{2nt}{h} k_s f_j$ $k_s = 1 - \dfrac{(b-2r)^2 + (h-2r)^2}{3bh(1-A_s)}$
Chaallal et al[16]	$\dfrac{f_{cc}}{f_{co}} = 1 + \dfrac{4.12 \times 10^5}{f_{co}} k$ $\dfrac{\varepsilon_{cu}}{\varepsilon_{co}} = 1 + \dfrac{10^3 (3k - 150k^2)}{f_{co} \cdot \varepsilon_{co}}$ $k = \dfrac{E_f A_f}{E_c A_c} \quad (0 \le k \le 0.8\%)$
ACI 440.2R [15]	$\dfrac{f_{cc}}{f_{co}} = 2.25 \sqrt{1 + 7.9 \dfrac{f_l}{f_{co}}} - 2 \dfrac{f_l}{f_{co}} - 1.25$ $\dfrac{\varepsilon_{cu}}{\varepsilon_{co}} = \dfrac{1.71 (5 f_{cc} - 4 f_{co})}{E_c \varepsilon_{co}}$ $k_s = 1 - \dfrac{(b-2r)^2 + (h-2r)^2}{3bh(1-A_s)}$
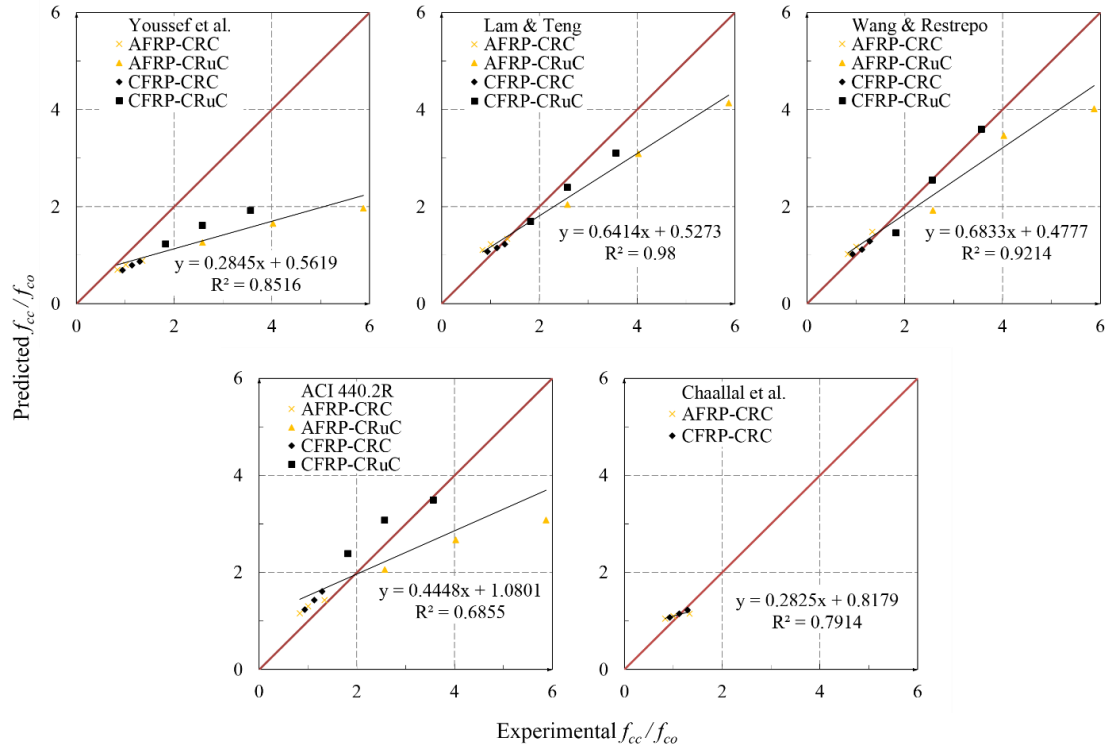
Fig. 4 - 14. Experimental results vs existing model predictions in terms of fcc/fco.
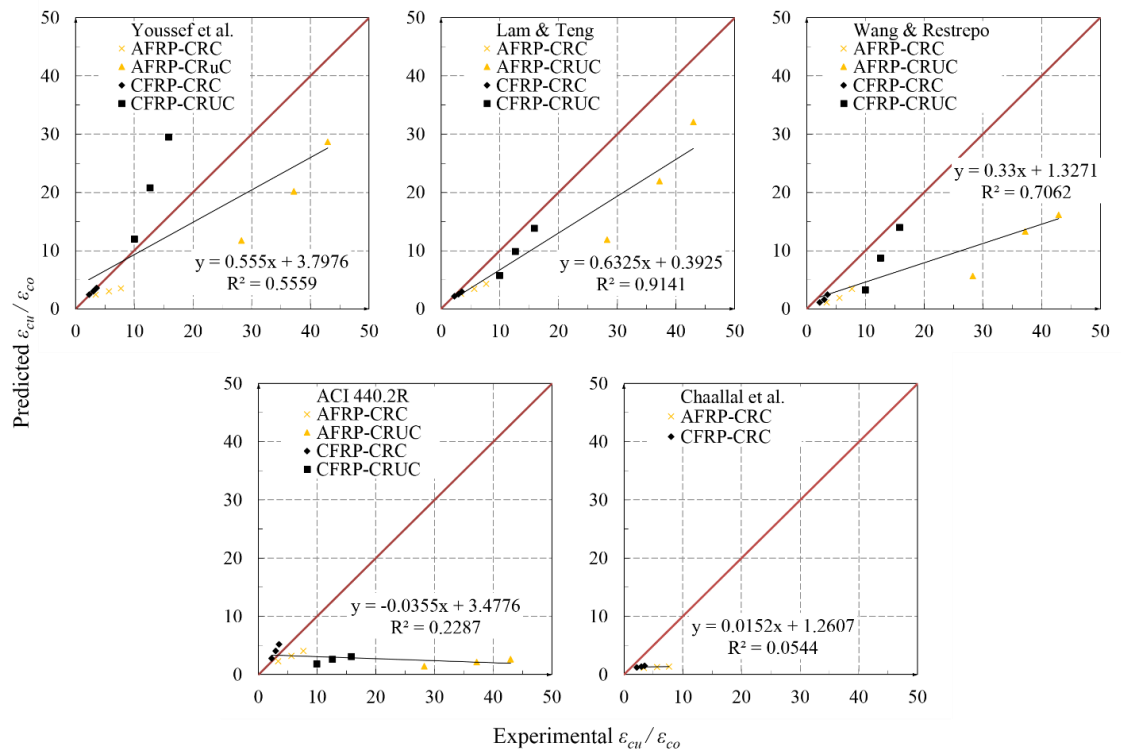
Fig. 4 - 15. Experimental results vs existing model predictions in terms of $\varepsilon_{cu}/\varepsilon_{co}$.
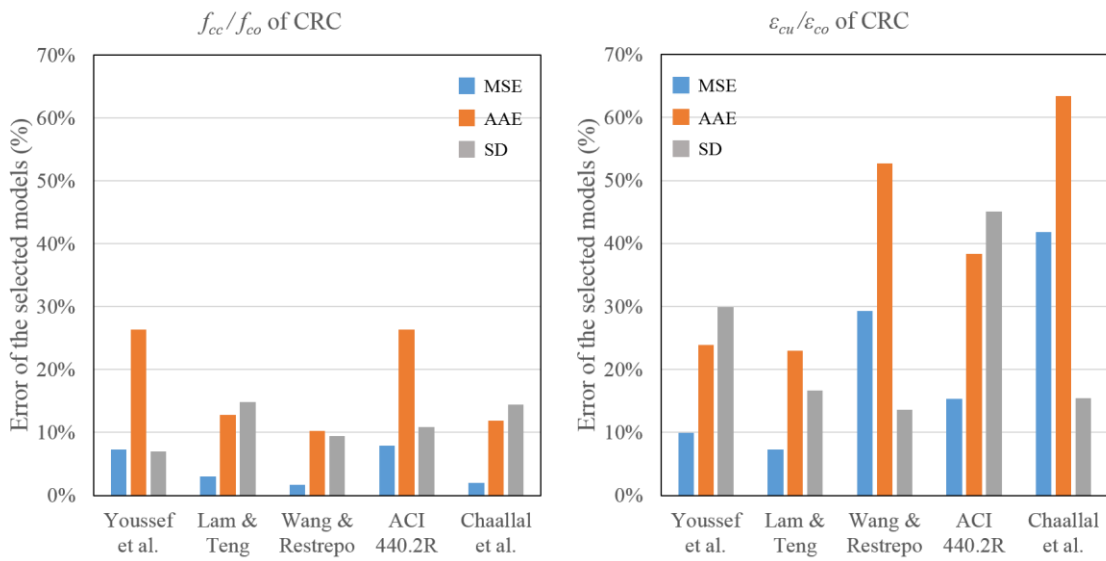
Fig. 4 - 16. Accuracy of the selected models for CRC.
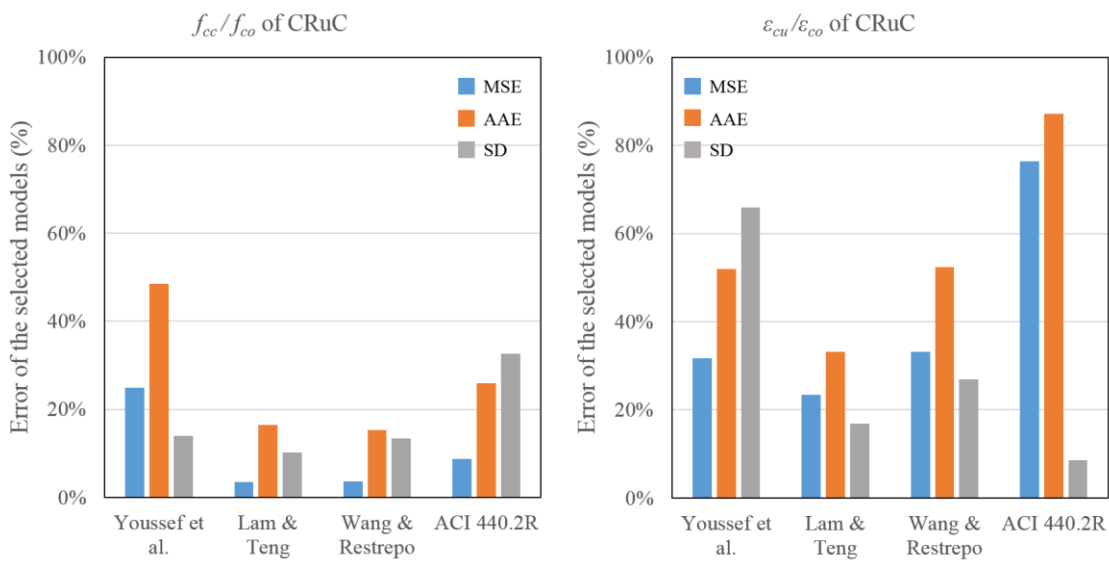
Fig. 4 - 17. Accuracy of the selected models for CRuC.

Table 4 - 4. Performance of selected models.

		Youssef et al.	Lam & Teng	Wang & Restrepo	ACI 440.2R	Chaallal et al.
f_{cc}/f_{co} of CRC	MSE	7.34%	3.04%	1.70%	7.92%	2.01%
	AAE	26.34%	12.84%	10.22%	26.39%	11.86%
	SD	6.98%	14.82%	9.43%	10.81%	14.47%
$\varepsilon_{cu}/\varepsilon_{co}$ of CRC	MSE	9.93%	7.26%	29.26%	15.35%	41.85%
	AAE	23.92%	22.97%	52.67%	38.30%	63.37%
	SD	29.93%	16.69%	13.64%	45.08%	15.38%
f_{cc}/f_{co} of CRuC	MSE	24.97%	3.47%	3.67%	8.72%	-
	AAE	48.50%	16.41%	15.24%	25.89%	-
	SD	13.94%	10.15%	13.37%	32.64%	-
$\varepsilon_{cu}/\varepsilon_{co}$ of CRuC	MSE	31.66%	23.36%	33.17%	76.41%	-
	AAE	51.93%	33.20%	52.44%	87.12%	-
	SD	65.95%	16.84%	26.86%	8.64%	-

4.6 CONCLUSION

This chapter examined the axial behaviour of FRP-confined circular and square rubberised concrete columns, using rubber particles obtained from recycled end-of-life tyres. In total 128 uniaxial compression tests were conducted to investigate the effects of a range of design parameters, including rubber volumetric replacement ratio, section shape, FRP type and number of FRP layers. The experimental results were then used to assess the efficiency of existing confinement models. On the basis of the discussion presented above, the following conclusions can be drawn:

- The ultimate confinement condition of CRC is governed by the corner hoop rupture strain, whilst for CRuC the flat side hoop rupture strain dominates its behaviour.

- The confinement effectiveness of CRuC is higher than that of CRC in both circular and square sections. The effect of the corner geometry on the effectiveness of confinement in CRuC is less severe than in CRC.

- Rubber aggregates significantly reduce concrete strength, but a large amount of strength is recovered with FRP-confinement. CRuC specimens exhibit significantly higher deformability (ultimate axial strains up to 5.7%) and absorb more energy than CRC specimens.

- Unlike confined regular concrete, CRuC exhibits volumetric contraction throughout the loading history.

- The confinement effectiveness of CFRP is lower than that of AFRP. Furthermore, for the same FRP confinement level, the AFRP CRuC square sections show higher deformability (up to 19%) than the circular sections with an acceptable sacrifice in strength (less than 20%).

- The secant dilation ratio of CRuC stabilises at around 0.4, which makes this material suitable for the development of high-strength highly-deformability elements under shear.

- Existing prediction models for conventional concrete are highly inaccurate (up to 85% error) in the prediction of the behaviour of CRuC, which indicate the need for further model development.

4.7 REFERENCES

1. Raffoul, S., et al., *Constitutive Model for Rubberized Concrete Passively Confined with FRP Laminates.* Journal of Composites for Construction, 2019. **23**(6): p. 04019044.
2. Garcia, R., et al., *Seismic retrofitting of RC buildings using CFRP and post-tensioned metal straps: shake table tests.* Bulletin of Earthquake Engineering, 2017. **15**(8): p. 3321-3347.
3. International, A., *C39/C39M - 15 Standard Test Method for Compressive Strength of Cylindrical Concrete Specimens.* 2015, West Conshohocken (USA).
4. Alecci, V., S.B. Bati, and G. Ranocchiai, *Concrete columns confined with CFRP wraps.* Materials and Structures, 2014. **47**(3): p. 397-410.
5. Raffoul, S., et al., *Behaviour of unconfined and FRP-confined rubberised concrete in axial compression.* Construction and Building Materials, 2017. **147**: p. 388-397.
6. Youssef, M.N., M.Q. Feng, and A.S. Mosallam, *Stress–strain model for concrete confined by FRP composites.* Composites Part B: Engineering, 2007. **38**(5-6): p. 614-628.
7. Ozbakkaloglu, T., J.C. Lim, and T. Vincent, *FRP-confined concrete in circular sections: Review and assessment of stress–strain models.* Engineering structures, 2013. **49**: p. 1068-1088.
8. Chen, J., S. Li, and L. Bisby, *Factors affecting the ultimate condition of FRP-wrapped concrete columns.* Journal of Composites for Construction, 2012. **17**(1): p. 67-78.
9. Lam, L. and J. Teng, *Ultimate condition of fiber reinforced polymer-confined concrete.* Journal of Composites for Construction, 2004. **8**(6): p. 539-548.
10. Lin, G. and J. Teng. *FRP-confined concrete in square columns: an advanced stress-strain model based on a new approach.* in *Fourth Asia-Pacific Conference on FRP in Structures (APFIS 2013).* 2013.
11. Lam, L. and J. Teng, *Design-oriented stress–strain model for FRP-confined concrete.* Construction and Building Materials, 2003. **17**(6-7): p. 471-489.
12. Mirmiran, A. and M. Shahawy, *Dilation characteristics of confined concrete.* Mechanics of Cohesive‐frictional Materials: An International Journal on Experiments, Modelling and Computation of Materials and Structures, 1997. **2**(3): p. 237-249.
13. Wang, Z., et al., *Shear Behavior Model for FRP-Confined and Unconfined Rubberized Concrete.* Journal of Composites for Construction, 2019. **23**(5): p. 04019039.
14. Lam, L. and J. Teng, *Design-oriented stress–strain model for FRP-confined concrete.* Construction and Building Materials, 2003. **17**(6): p. 471-489.
15. 440, A.C. *Guide for the design and construction of externally bonded FRP systems for strengthening concrete structures.* 2008. American Concrete Institute.
16. Chaallal, O., M. Hassan, and M. Shahawy, *Confinement model for axially loaded short rectangular columns strengthened with fiber-reinforced polymer wrapping.* Structural Journal, 2003. **100**(2): p. 215-221.
17. Lam, L. and J. Teng, *Design-oriented stress-strain model for FRP-confined concrete in rectangular columns.* Journal of Reinforced Plastics and Composites, 2003. **22**(13): p. 1149-1186.
18. Wang, Y.C. and J.I. Restrepo, *Investigation of concentrically loaded reinforced concrete columns confined with glass fiber-reinforced polymer jackets.* Structural Journal, 2001. **98**(3): p. 377-385.

Chapter 5

Axial Behaviour of FRP-Confined Concrete Columns: A Modelling Investigation

5.1 INTRODUCTION

This chapter presents an investigation on the axial behaviour of regular concrete (RC) and rubberised concrete (RuC) columns in circular and non-circular sections confined with fibre reinforced polymer (FRP) composites. The efficiency of two of the most widely used models a) Lam and Teng's model for FRP-confined rectangular columns and b) concrete damage plasticity model (CDPM) are assessed. It was found that existing designed-oriented stress-strain model and concrete damage plasticity model cannot accurately predict the behaviour of FRP-confined RuC, due to its unique behaviour (high deformation, constant Poisson's ratio and volumetric contraction). Hence, an analysis-oriented model for circular and non-circular sections FRP-confined concrete (RC or RuC) is proposed based on a new understanding of effective confinement area and volumetric strain to axial stress relationship. The model includes the properties of both RC and RuC through a series of relationships developed from experimental data and the fundamental stress-strain behaviours. Confining stiffness plays a critical role in the development of the model. The performance of the proposed model is validated against the experimental data reported in Chapter 3, as well as the published experimental results [1, 2]. This work will enable a deeper understanding of the behaviour of FRP-confined elements and will assist in developing applications for highly deformable elements.

5.2 DISCUSSION ON LAM AND TENG'S MODEL FOR FRP-CONFINED RECTANGULAR COLUMNS

Lam and Teng's model [2] is selected as a representative design-oriented stress-strain model for FRP-Confined regular concrete (CRC) in rectangular sections according to the evaluation results reported in Chapter 3 and used to assess its applicability in CRuC. The stress-strain curves of Lam and Teng's model consist of two smoothly connected parts: 1) a parabolic ascending part and a straight-line ascending part [2] (see Fig. 5 – 2).
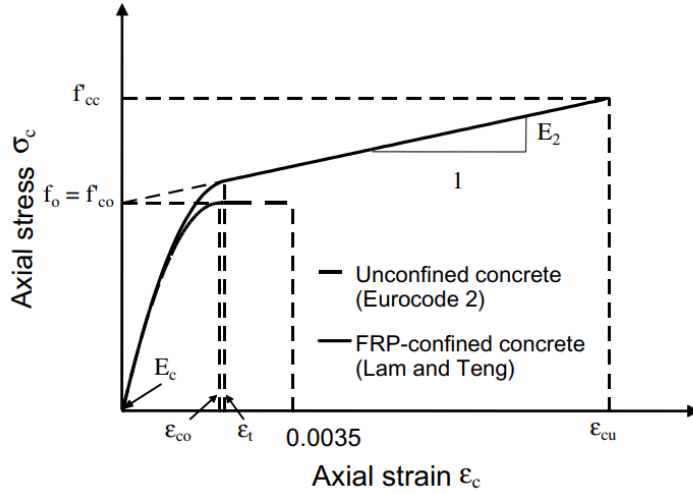
Fig. 5 - 1. Lam and Teng's stress-strain model for FRP-confined concrete [2].

The initial slope of the parabolic part is determined by the modulus of elasticity of unconfined concrete (E_c). The slope of the linear part (E_2) is used to reflect different FRP confinement levels and ends at a point where the ultimate states (ε_{cu} and f_{cc}) are reached. The intercept stress (f_{tr}) is defined as the stress where the linear hardening branch intercept with the stress axis and its value is considered independent from the confinement ratios and equal to f_{co} for simplicity. The expressions of the model are given in Eq. (1 – 5):

$$\sigma_c = E_c \varepsilon_c - \frac{(E_c - E_2)^2}{4 f_{co}} \varepsilon_c^2 \quad (0 \le \varepsilon_c \le \varepsilon_{tr})$$

$$\sigma_c = f_{co} + E_2 \varepsilon_c \qquad\qquad (\varepsilon_{tr} \le \varepsilon_c \le \varepsilon_{cu}) \tag{1}$$

where σ_c and ε_c are the axials tress and axial strain of confined concrete, respectively; $\varepsilon_{tr} = 2 f_{co} / (E_c - E_2)$ is the axial strain at the transition point; $E_2 = (f_{cc} - f_{co}) / \varepsilon_{cu}$ is the slope of the straight second portion.

$$\frac{f_{cc}}{f_{co}} = 1 + 3.3 \cdot k_{s1} \frac{f_{l,a}}{f_{co}} \tag{2}$$

$$\frac{\varepsilon_{cu}}{\varepsilon_{co}} = 1.75 + 12 \cdot k_{s2} \left(\frac{f_{l,a}}{f_{co}} \right) \left(\frac{\varepsilon_{h,rup}}{\varepsilon_{co}} \right)^{0.45} \tag{3}$$

where $f_{l,a} = 2E_f t_f \varepsilon_{h,rup}/D_{eq}$ is the actual confining pressure; $D_{eq} = \sqrt{b^2 + h^2}$ is the diameter of equivalent circular section; k_{s1} and k_{s2} are the shape factors for strength enhancement and strain enhancement, respectively, defined as follows:

$$k_{s1} = \left(\frac{b}{h}\right)^2 \frac{A_e}{A_c}; k_{s2} = \left(\frac{b}{h}\right)^{0.5} \frac{A_e}{A_c} \tag{4}$$

$$\frac{A_e}{A_c} = 1 - \frac{\left[\left(\frac{b}{h}\right)(h - 2R_c)^2 + \left(\frac{h}{b}\right)(h - 2R_c)^2\right]}{3A_g} \tag{5}$$

where A_e/A_c is the ratio of effective confined area to total cross-sectional area.

As can be seen in Fig. 5 - 2 (a and b), the Lam and Teng's model provide a reasonable prediction for CFRP CRC but much less accuracy is observed for AFRP CRC. Moreover, it cannot predict the behaviour of low confinement columns, in which concrete has a softening branch.

For FRP confined RuC, Fig. 5 - 2 (c and d) shows that the model underestimates massively the ultimate stress and strain. Furthermore, the use of a constant value of f_{tr} means that the model cannot capture the transition between the initial linear behaviour and the stage at which confinement becomes fully active. The use of critical stress (f_{cr}) as proposed by Raffoul et al. [3] appear to be more rational for use in CRuC modelling. This can be attributed to the volumetric behaviour of CRuC is completed different from that of CRC. After the critical stress (f_{cr}), CRC exhibit a volumetric expansion behaviour, while CRuC experience a volumetric contraction behaviour. Therefore, at the same level of axial strain, CRuC develops larger lateral strain than CRC, which results in higher confining pressure. This behaviour has been discussed in chapter 3, as well as the experimental study by Raffoul et al. [4].
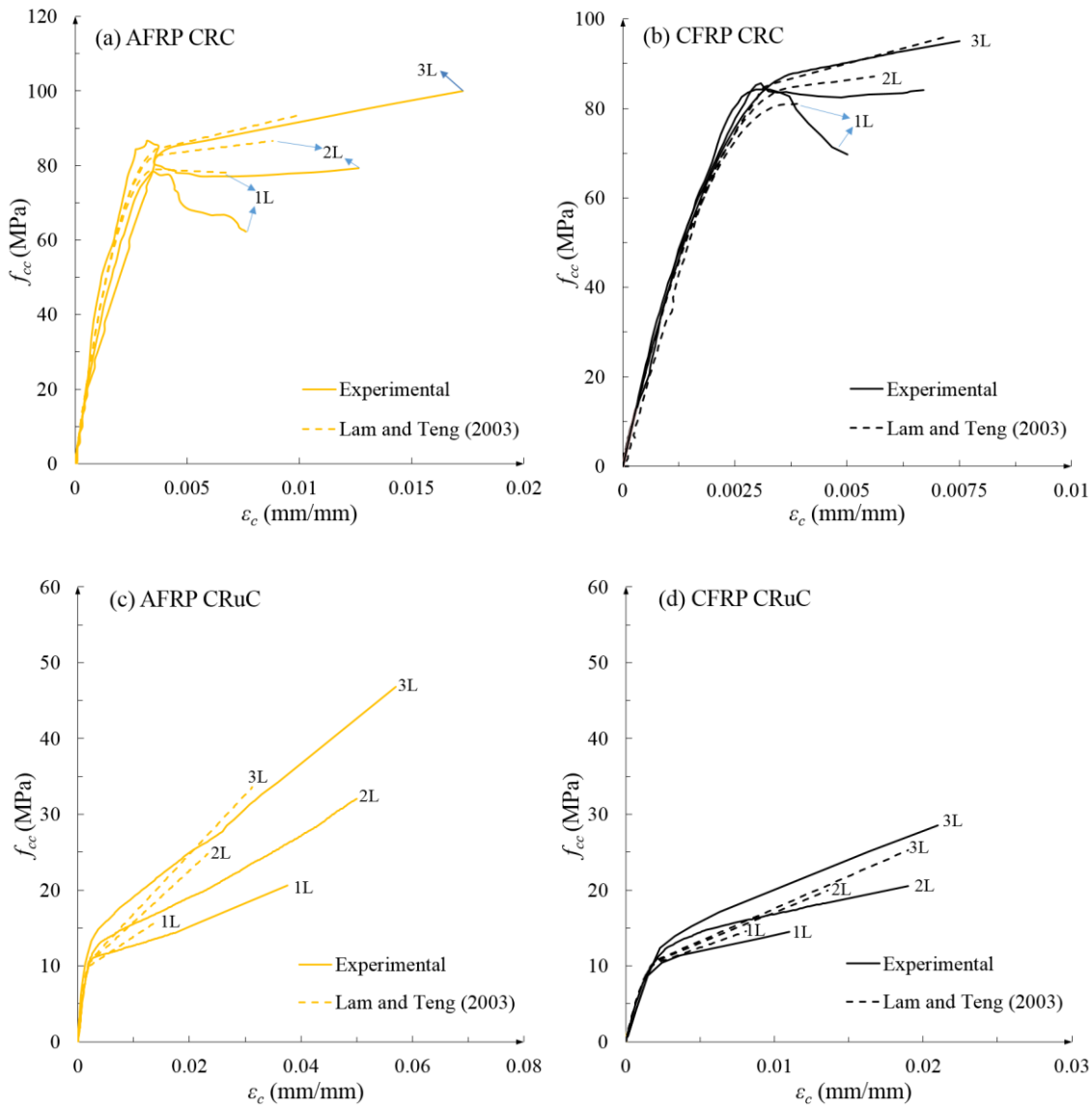
Fig. 5 - 2. Performance of Lam and Teng's model for FRP-confined square columns.

5.3   NUMERICAL   MODELLING   OF   FRP-CONFINED   RUBBERISED

CONCRETE

The Concrete damaged plasticity model (CDPM) available in the finite element software package ABAQUS has been widely used to model CRC under axial load. In this section, a numerical model has been developed to assess if the CPDM can be used in the case of CRuC. The results of finite element analysis are compared with experimental data and used to inspect the stress-state over the square section.

5.3.1 Concrete Damaged Plasticity Model (CDPM)

The CDPM uses the modified Drucker-Prager criterion and the yield surface F in the deviatoric plane and assumes isotropic damage. The details can be found in ABAQUS Analysis User's Guide (6.14) [5]. The parameters needed to define the yield function F are K_c, φ, ϵ, f_{cb}/f_{co} and viscosity.

The eccentricity (ϵ) and a small enough value of viscosity have a negligible influence on the prediction accuracy [6-8]. Therefore, the default value of $\epsilon = 0.1$ is assigned and a value of 2×10^{-6} was chosen for viscosity to avoid convergence problems.

The parameter K_c controls the slope of the yield surface in the deviatoric plane and affects the behaviour of concrete under non-uniform biaxial confinement. The value of K_c is related to f_{cb}/f_{co} and can be determined by the following equation [7, 9]:

$$K_c = \frac{5.5 f_{cb}}{3 f_{co} + 5 f_{cb}} \left(\text{in MPa} \right) \tag{6}$$

where f_{co} the unconfined concrete strength and f_{cb} is the strength of concrete under biaxial compression. The ratio of f_{cb}/f_{co} was determined empirically by Papanikolaou and Kappos [10]:

$$\frac{f_{cb}}{f_{co}} = 1.5 \left(f_{co} \right)^{-0.075} \tag{7}$$

The non-associative plastic volumetric deformation of the material is controlled by the dilation angle φ [7, 11-13]. The dilation angle φ influences the tangent slope of the lateral strain-axial strain curve of concrete (i.e. the lateral dilation of FRP-confined concrete increases with increasing φ). The traditional CDPM shows some limitations when applied to passive confined concrete as it uses a constant dilation angle. That results in almost the same lateral strain-to-axial strain curve for FRP jacket of different stiffness, which is inconsistent with experimental observations where the increase in the FRP stiffness results in a reduction of the lateral strain. The value of the dilation angle could be defined as a function of the ratio of FRP jacket stiffness

to concrete strength ($K_j = \dfrac{2nt_f E_f}{Df_{co}}$) [8, 9, 12]. For circular sections, a reasonable estimate

of the dilation angle can be calculated by the simple equation suggested by Hany et al. [8] (

$\varphi = -1.43K_j + 57.3$). The non-uniform distribution of confinement pressure over rectangular

sections makes the definition of dilation angle more complex. The dilation angle of each

element in the cross-section should be determined as a function of the elements' stress state [7].

Furthermore, the value of K_j = 40 corresponds to the minimum dilation angle (0.1°) allowed in

Abaqus (0° to 56°) [5]. Since the unconfined strength of RuC is significantly less than that of

RC, the ratio of K_j is normally larger than 40 (e.g., one-layer AFRP CRuC, K_j = 60) and the

minimum value of φ = 0.1° is used to perform the FE analysis.

5.3.2 FE modelling

Full-scale specimens wrapped with Aramid-FRP are modelled in ABAQUS. The concrete was

modelled using 8-node solid elements (C3D8R) while the FRP jacket was modelled with 4-node

shell elements (S4R) and attached to the solid elements in the circumferences (see Fig. 5 - 3a).

The mesh displayed in Fig. 5 - 3 was selected after a mesh-sensitivity study was conducted to

achieve an accurate solution with reasonably short analysis time as well as prevent any

discontinuity in the stresses and strains distribution (see Appendix). A uniform displacement

was imposed on the top surface of the specimen and a fixed boundary condition was assigned to

the bottom surface (see Fig. 5 - 3b). A tie constraint was assigned to the concrete-FRP jacket

interface under the assumption that perfect bond developed between the FRP and the concrete

and thus the nodes on both surfaces have the same displacement [7]. A local coordinate system

was assigned to the FRP jacket and the hoop direction and the axial direction were adopted as

the 1-principal and 2-principal material orientations, respectively (see Fig. 5 - 3b).
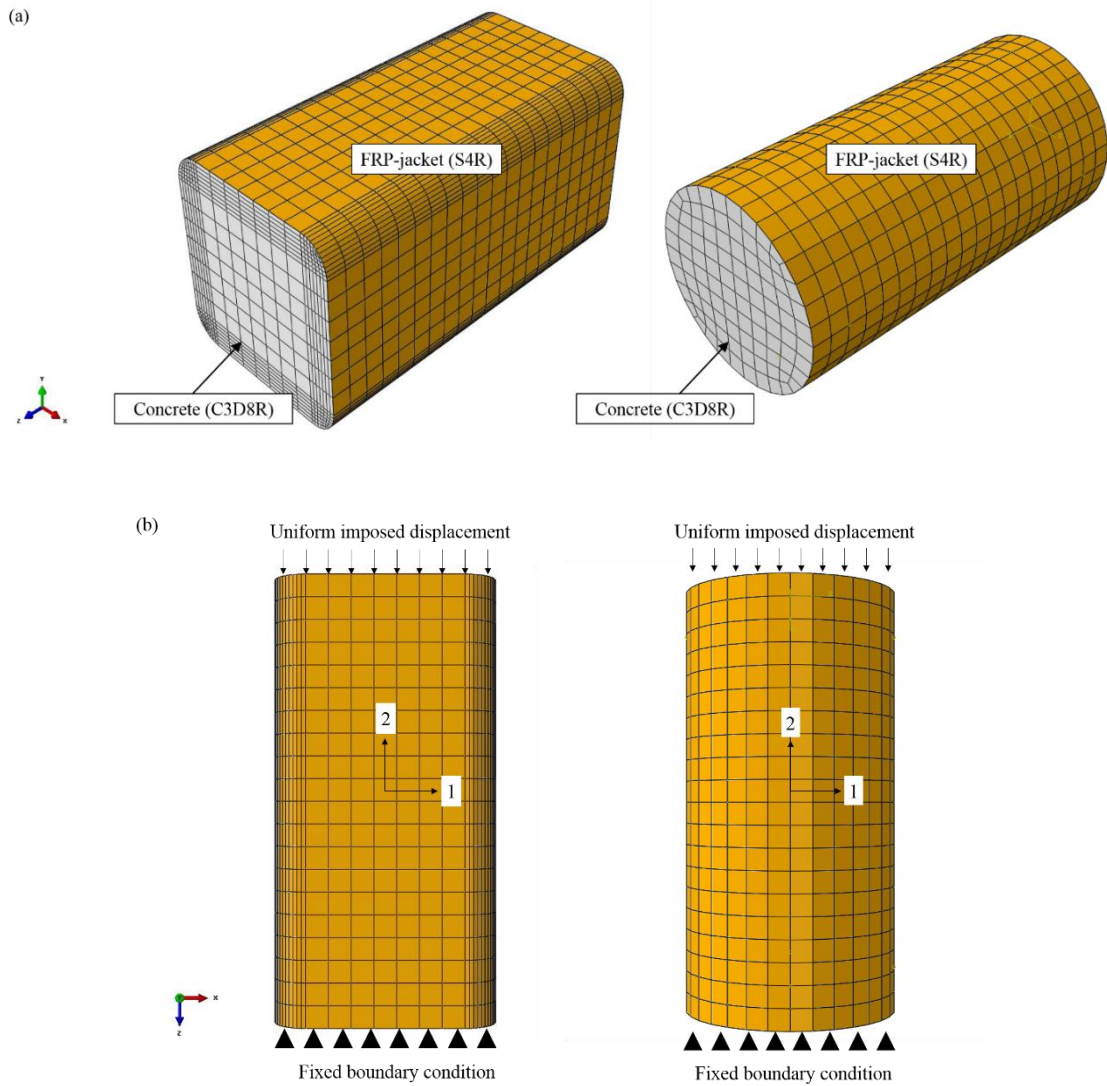
Fig. 5 - 3. FE models of the square and circular confined specimens tests (a) Mesh geometry for concrete and FRP and (b) Boundary and loading conditions.

5.3.3 Material properties

5.3.3.1 FRP jacket

The FRP is modelled as a linear elastic material before brittle rupture. The stiffness of FRP in the transverse direction (i.e., the loading direction) is negligible. The stiffness of FRP in the hoop direction was obtained from direct tensile coupon tests. The actual rupture strains of FRP in the compressive test (presented in chapter 4) are used to determine the ultimate condition of simulation. The elastic behaviour of the FRP jacket was modelled using the elastic lamina

option in ABAQUS, which is used to model isotropic elastic materials. The modulus of elasticity E_1 in the hoop direction was obtained from direct tensile coupon tests (see Chapter 3), while E_2, G_{12}, G_{13} and G_{23} are negligible and were assigned small values. The "no compression" option of elastic material was activated, so the jacket does not carry any of the axial load.

5.3.3.2 Concrete

The compressive strength (f_{co}), tensile strength (f_{ct}) and elastic modulus (E_c) of rubberised concrete with different rubber contents can be calculated by Eqs. (8) [14], which were found to provide a reasonable prediction of the test results presented in Chapter 3.

$$f_{co,RuC} = \frac{1}{1+2\left(\dfrac{8.7\rho_{vr}}{2}\right)^{3/2}} f_{co,RC}$$

$$f_{ct} = 0.26 f_{co}^{2/3}$$

$$E_{cr} = 12\left(\frac{f_{co}}{10}\right)^{2/3} \text{ in GPa}$$

(8)

Uniaxial stress-strain relationship:

The compressive stress-strain relations of RuC suggested by Bompa et al. [14] (see Eq. (9)) and the cracking stress-strain relation in tension proposed by Wang et al. [15] (see Eq. (10)) are used to perform the numerical analysis.

$$\sigma = \begin{cases} E_c \varepsilon_{cr1} & \varepsilon_{cr1} \in \left(0, \varepsilon_{cr1,el}\right) \\[2ex] f_{cr}\left[\dfrac{5}{3}\left(\dfrac{\varepsilon_{cr1} - \varepsilon_{cr1,el}}{\varepsilon_{cr1,1}}\right) - \left(\dfrac{\varepsilon_{cr1} - \varepsilon_{cr1,el}}{\varepsilon_{cr1,1}}\right)^2\right] + \dfrac{0.3 f_{cr}}{f_{cr}} & \varepsilon_{cr1} \in \left[\varepsilon_{cr1,el}, \varepsilon_{cr1,1}\right) \\[2ex] f_{cr}\left[\dfrac{1}{8}\left(\dfrac{f_{cr}}{g_{c,2}} - 1\right)^2 \left(\dfrac{\varepsilon_{cr1} - \varepsilon_{cr1,2}}{\varepsilon_{cr1,1}}\right)^2 - \dfrac{6}{8}\left(\dfrac{f_{cr}}{g_{c,2}} - 1\right)\left(\dfrac{\varepsilon_{cr1} - \varepsilon_{cr1,2}}{\varepsilon_{cr1,1}}\right) + \dfrac{f_{cr,2}}{f_{cr}}\right] & \varepsilon_{cr1} \in \left[\varepsilon_{cr1,1}, \infty\right) \end{cases}$$

(9)

$$\sigma_t = \begin{cases} E_{co}\varepsilon_t & \varepsilon_t \in (0, \varepsilon_{cr}) \\[2ex] f_{ct} e^{-\frac{\varepsilon_t}{\gamma_t}} & \varepsilon_t \in (\varepsilon_{cr}, \infty) \end{cases}$$

(10)

where $\gamma_t = \dfrac{g_t}{f_{ct}} - \dfrac{1}{2}\dfrac{f_{ct}}{E_c}$, The coefficient g_t is equal to the area under $\sigma - \varepsilon^p$ curves in uniaxial tension.

5.3.4 FE modelling vs Experimental results

Fig. 5 - 4 indicates that the CDPM cannot give an accurate prediction for AFRP CRuC in either circular or square sections in terms of overall stress-strain response. The prediction of ultimate strength capacity is 15% higher than the experimental results, while the axial strain capacity is dramatically underestimated. Fig. 5 - 5 shows a comparison between experimental and numerical area strain-to-axials strain of AFRP CRuC cylinders. It can be seen that the slope of the numerical curve is much steeper than the experimental one. This is caused by the fact that the theoretical lateral dilation cannot be predicted accurately for high levels of confinement (K_j >40). This was also reported by other researchers [7, 8, 12] Moreover, the inflexion of the numerical area strain-to-axials strain curves happens at a much lower level of the axial strain than seen experimentally, which also results in an unrealistic volumetric behaviour of CRuC (see Fig. 5 - 6). This is due to the volumetric behaviour of CRuC being completely different from that of CRC.
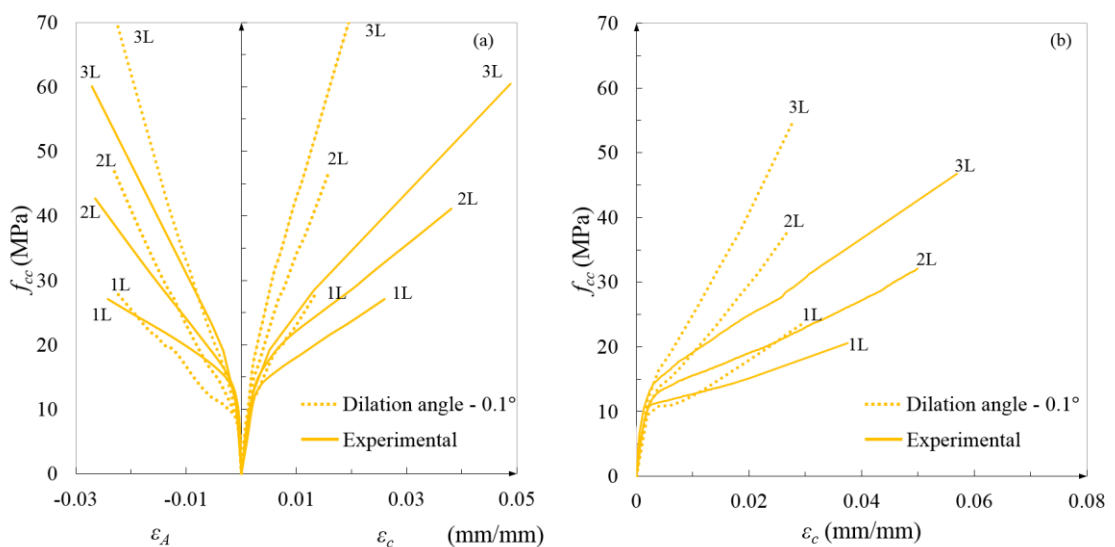
Fig. 5 - 4. FE results vs experimental results of stress-strain curves of AFRP CRuC in the circular sections (a) and rectangular sections (b).
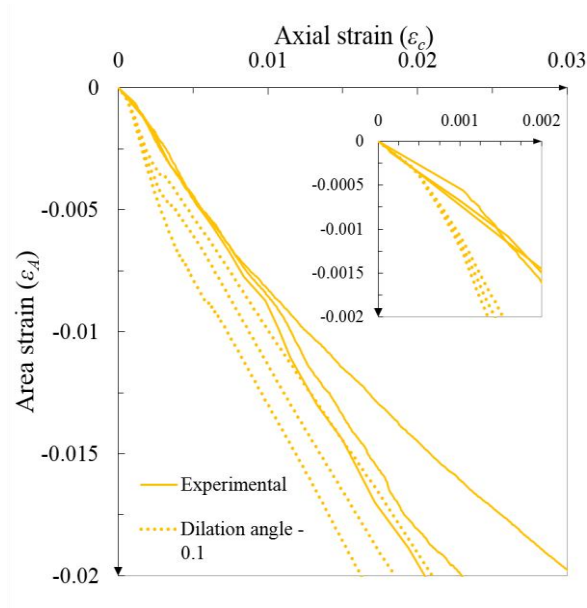
Fig. 5 - 5. FE results vs. experimental results of area strain-to-axial strain curves of AFRP CRuC in the circular sections.
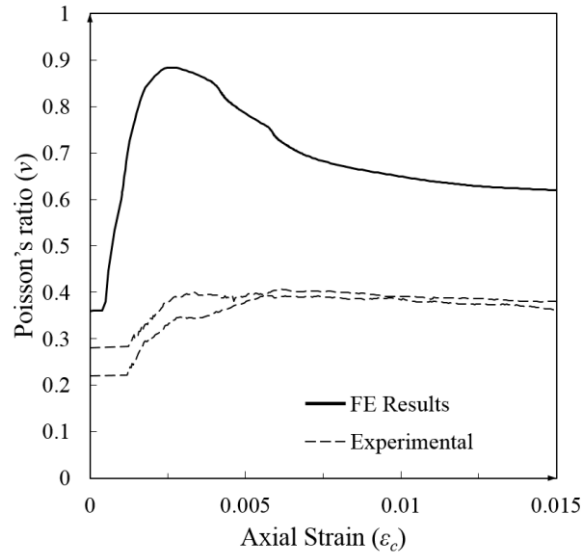
Fig. 5 - 6. FE results vs. experimental results of Poisson's ratio v of AFRP CRuC.

5.3.5 Evaluation of stress states over the square cross-sections

Although CDPM is unable to trace the experimental behaviour of CRuC, it proved its capability in predicting the response of CRC. Moreover, the FE model can capture the increasing gradient

in the stress-strain curve of the AFRP CRuC square column and provide an insight into the stress states of square columns.

Fig. 5 - 7 shows a typical stress-strain response of FRP-confined concrete. Stage 1 indicates the end of elastic behaviour and Stage 2 represents the failure of the specimens. Fig. 5 – 8 shows the distribution of minimum principal stresses (compressive stress) obtained from the FE model in Stage 1 and 2. As expected, in the elastic stage (Stage 1), the whole cross section experiences an almost uniform compressive stress distribution. At failure (Stage 2), the corner and the centre of the section exhibit the highest compressive stresses.
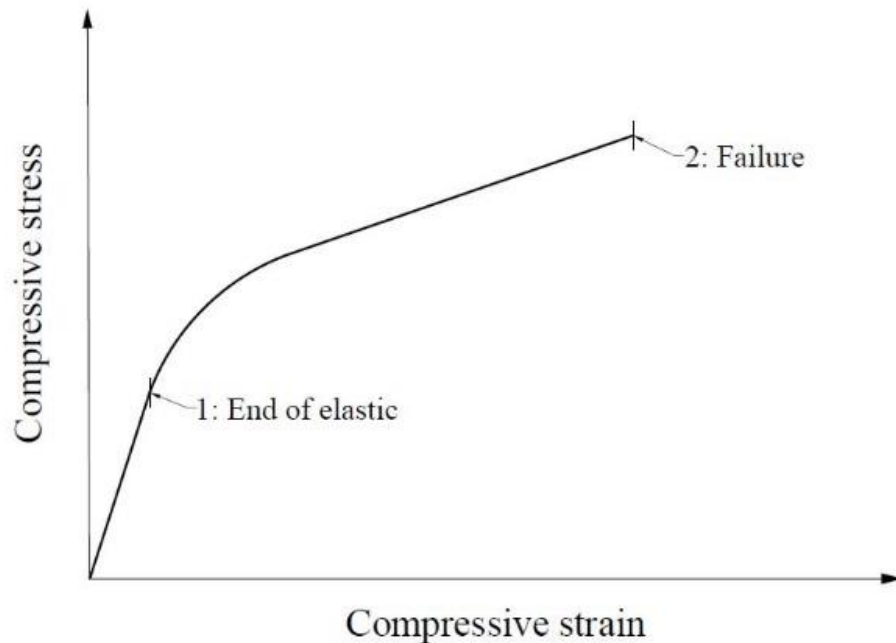
Fig. 5 - 7. Typical stress-strain response of FRP-confined concrete.
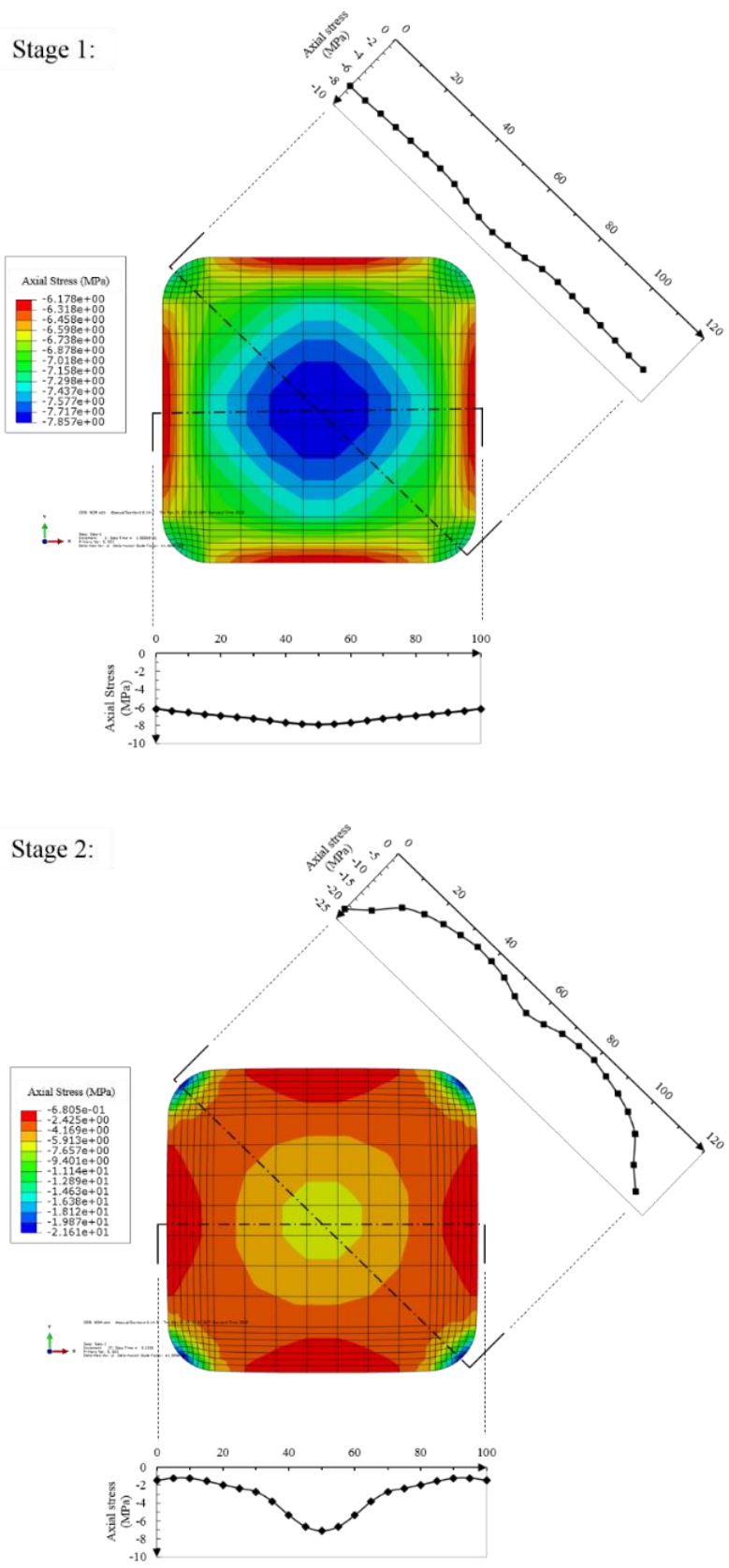
Fig. 5 - 8. Axial stress distribution of the cross-section at the mid-height of the column.

To further investigate the confinement mechanism, the principal stresses were obtained from the marked red elements in Fig. 5 - 9 and plotted to quantify the local confinement. Fig. 5 - 9 indicates that the confining stresses are not distributed uniformly across the section. The elements located at the corner and centre of the section are subjected to uniform bi-directional confining pressure. From corner to centre, the confining pressures in the direction of the diagonal of the cross-section is significantly higher than the confining pressure perpendicular to this direction. For the elements from the flat side to the centre, the confining pressures along the direction parallel to the flat side are significantly higher than the confining pressure in the perpendicular direction.

stress-states in every point of the square section:
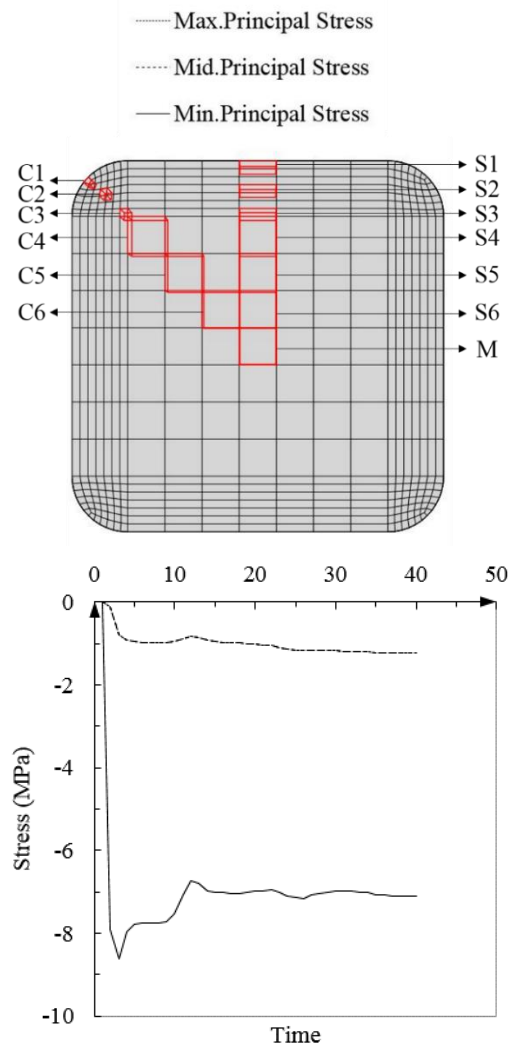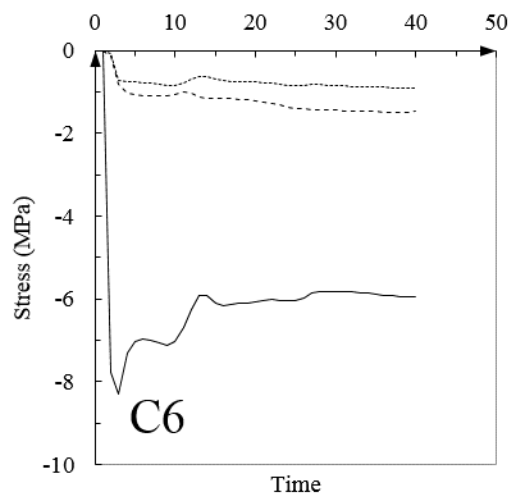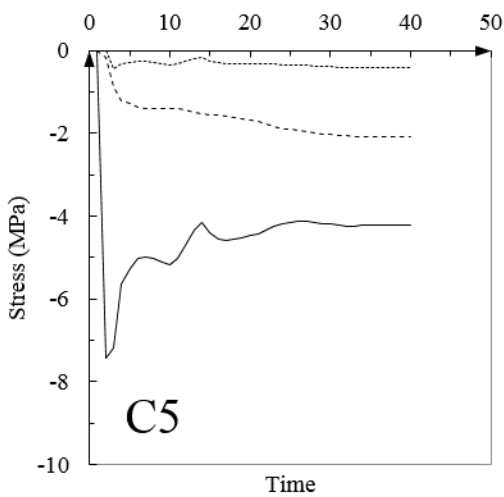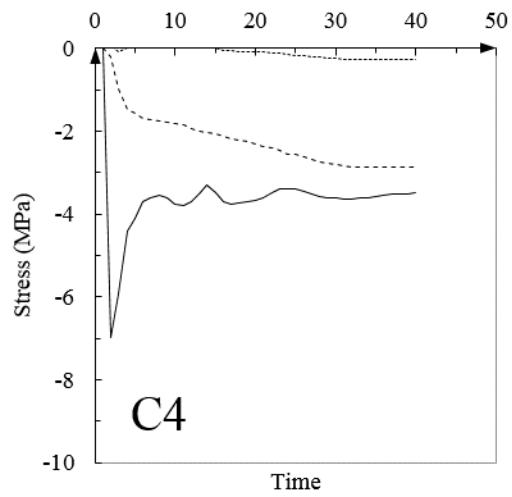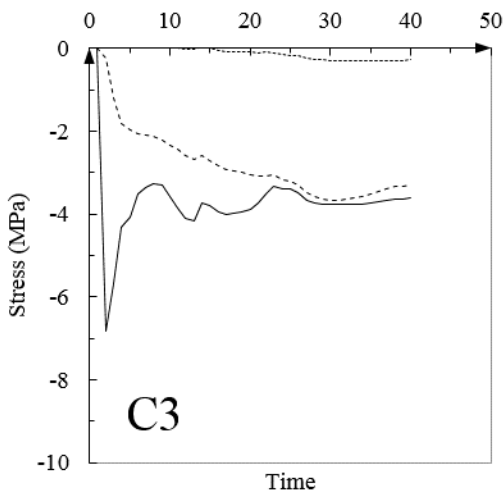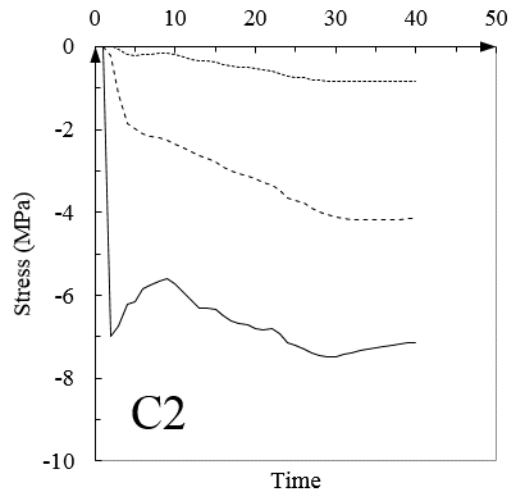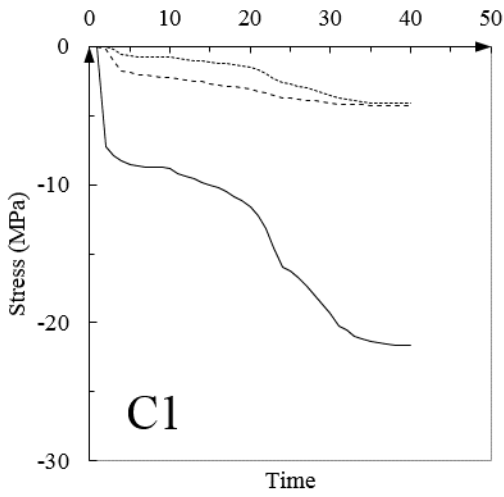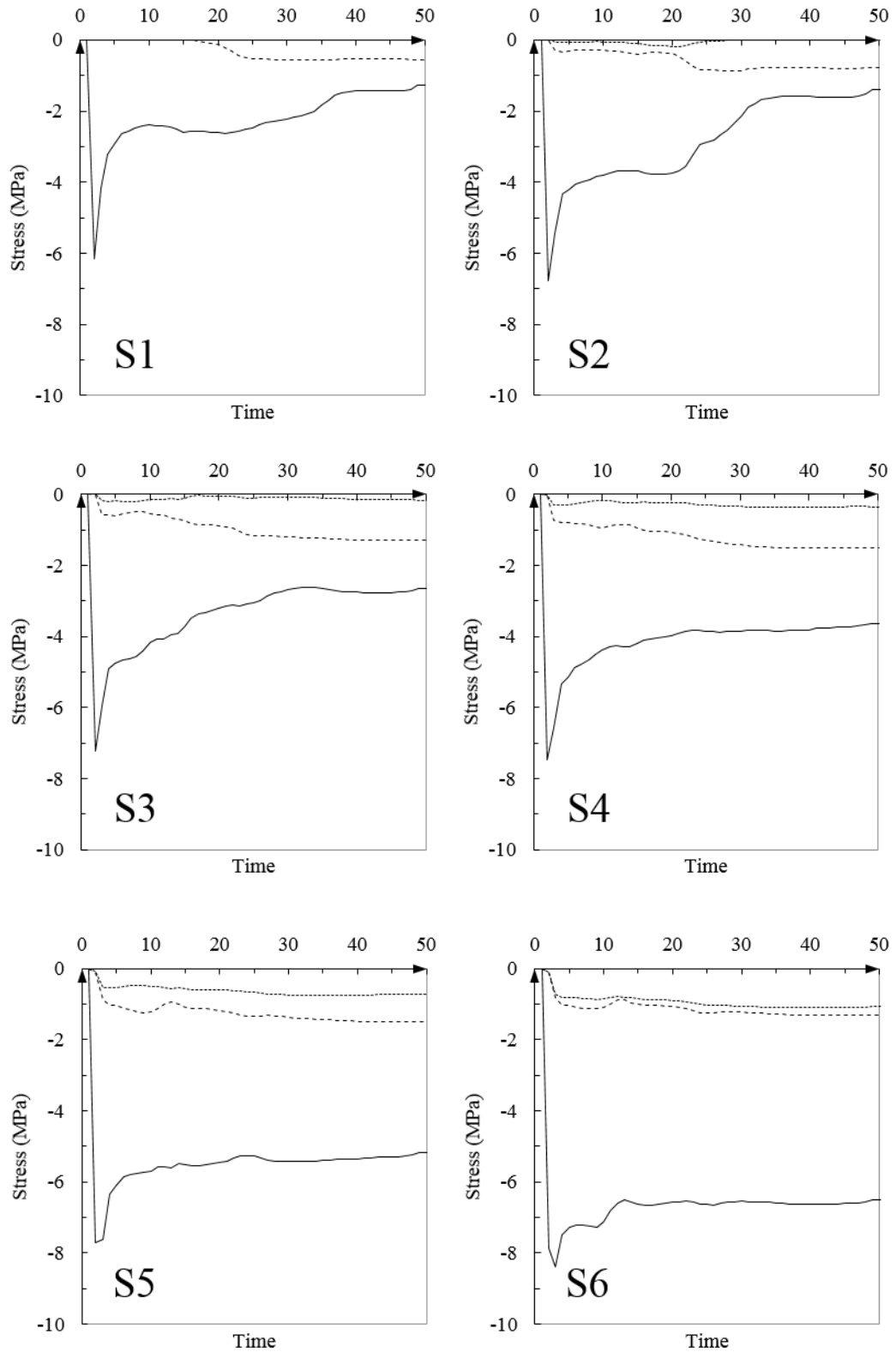
Fig. 5 - 9. Stress states of selected elements.

Table 5 - 1. Summary of the stress states of the elements highlight in Fig. 5 - 9.

	Stage 1			Stage 2		
	Max.Principal Stress	Mid.Principal Stress	Stress state	Max.Principal Stress	Mid.Principal Stress	Stress state
	MPa			MPa		
C1	-0.019	-0.190	BC	-4.125	-4.277	BC
C2	0.041	-0.222	UC	-0.824	-4.156	BC
C3	0.082	-0.231	UC	-0.284	-3.305	BC
C4	0.068	-0.197	UC	-0.269	-2.859	BC
C5	0.009	-0.165	UC	-0.427	-2.084	BC
C6	-0.073	-0.130	BC	-0.904	-1.480	BC
M	-0.110	-0.110	BC	-1.231	-1.231	BC
S1	0.164	0.011	UN	0.091	-0.531	UC
S2	0.083	-0.004	UC	0.065	-0.780	UC
S3	0.021	-0.011	UC	-0.135	-1.283	BC
S4	-0.027	-0.031	BC	-0.364	-1.512	BC
S5	-0.068	-0.094	BC	-0.74726	-1.48085	BC
S6	-0.098	-0.109	BC	-1.09813	-1.31179	BC

Note: + means tensile stress; - means compressive stress; UN means unconfined; UC means uniaxial confinement; BC means biaxial confinement.

5.4 MODELLING OF FRP-CONFINED CONCRETE IN SQUARE SECTIONS

According to the results of the numerical study, the stress distribution within the cross-section is more complex than the simple division of the section into a confined and an unconfined section (see Fig. 5 – 1). Therefore, in order to accurately model the compressive behaviour of FRP-confined concrete square sections, the whole section is divided into four regions, as shown in Fig. 5 - 10. For the rectangular section, the same partition is applied, except the shape of Region-2 is replaced by an ellipse. For each region, an equivalent circular cylinder is assigned to reflect the state of confinement (see Fig. 5 - 11). The equivalent circular cylinders have been used by Mirmiran et al. [16] and Al-Salloum [17] to calculate the equivalent confining pressure in a square or a rectangular section.
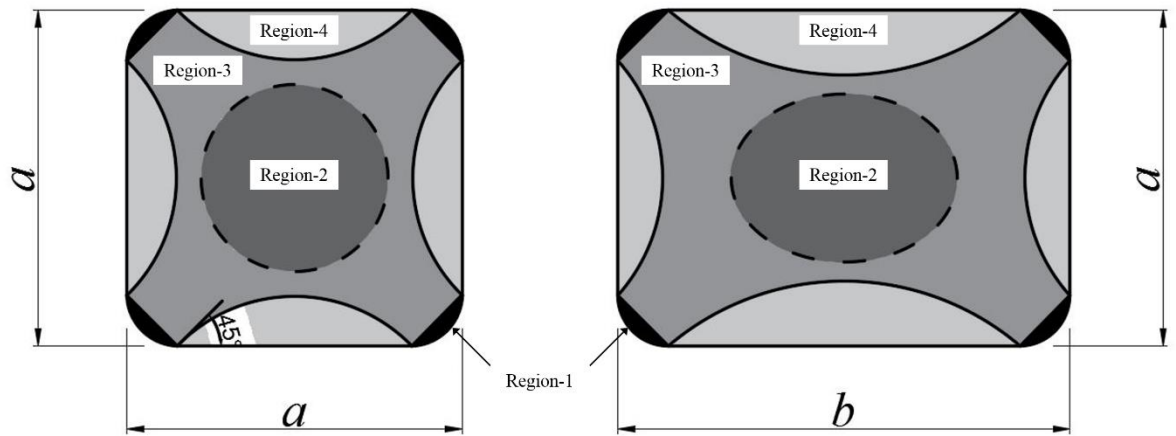
Fig. 5 - 10. Defining the different regions in the section.
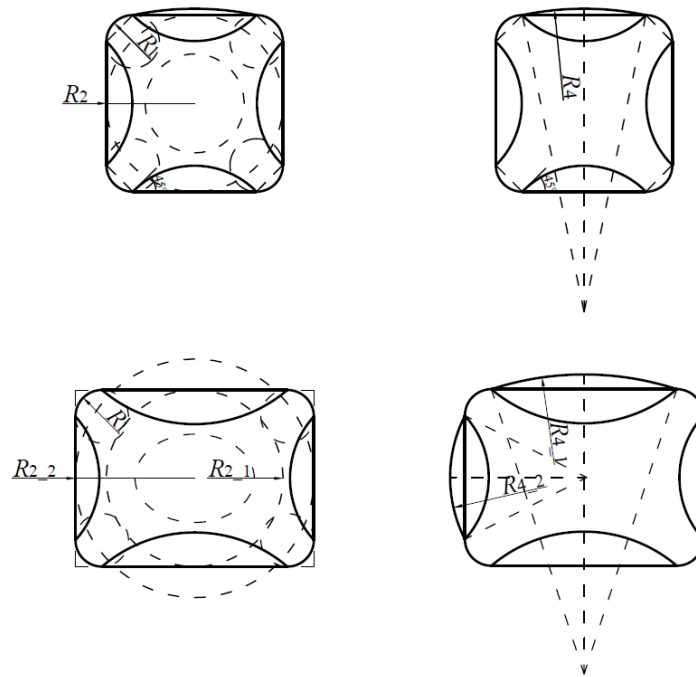
Fig. 5 - 11. Equivalent circular cylinders.

5.4.1 Calculation of equivalent lateral strain ($\varepsilon_{a,eq}$) for non-circular sections

In order to simplify the problem caused by the nonuniform distribution of FRP hoop strain, a uniform area expansion is assumed (see Fig. 5 - 12) and the equivalent lateral strain ($\varepsilon_{a,eq}$) can be calculated by Eq. (11).
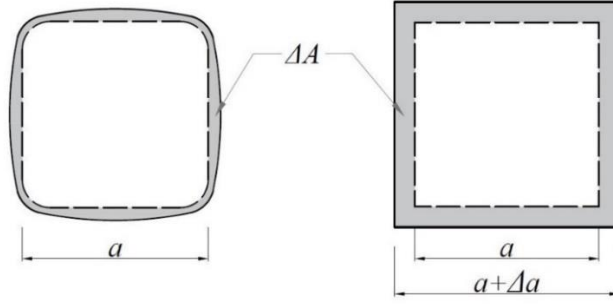
Fig. 5 - 12. Schematic representation of equivalent area expansion.

$$\varepsilon_A = \frac{\Delta A}{A} = \frac{(a + \Delta a)^2 - a^2}{a^2} = \frac{(a + a\varepsilon_{a,eq})^2 - a^2}{a^2} = (1 + \varepsilon_{a,eq})^2 - 1$$

$$\varepsilon_{a,eq} = \sqrt{\varepsilon_A + 1} - 1$$

(11)

5.4.2 Definition of different regions:

Region 1: This is the most effectively confined zone with the highest axial stresses. This region is considered under triaxial stress state (biaxial confinement) and the confining pressures (f_1) along the two directions are considered identical and calculated by Eq. (12). The area of this region can be determined by Eq. (13).
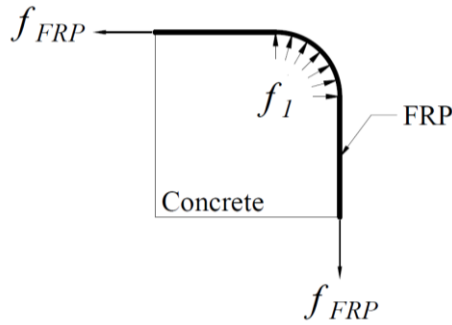
Fig. 5 - 13. Force equilibrium in Region 1.

$$f_1 = \frac{\sqrt{2} f_{FRP}}{R_1} = \frac{\sqrt{2} n_f t_f E_f \varepsilon_{a,eq}}{R_1}$$

(12)

$$A_1 = (\pi - 2) R_1^2$$

(13)

Region 2: This is the central portion of the cross-section. This region has equivalent biaxial confining stresses that lead to the second highest axial stresses. For the square section, the

confining pressures (f_2) in the two directions are considered to be identical and can be calculated by Eq. (14) using an equivalent radius, $R_2 = a/4$. For the rectangular section, the confining pressures (f_{2_1} and f_{2_2}) in the two directions are different and can be calculated using the corresponding equivalent radii R_{2_1} and R_{2_2}, respectively (see Eq. (14)). The corresponding area A_2 is calculated by Eq. (15).

$$f_2 = \frac{n_f t_f E_f \varepsilon_{a,eq}}{R_2} \qquad \text{for square section}$$

$$f_{2\_1} = \frac{n_f t_f E_f \varepsilon_{a,eq}}{R_{2\_1}} \text{ and } f_{2\_2} = \frac{n_f t_f E_f \varepsilon_{a,eq}}{R_{2\_2}} \quad \text{for rectangular section} \tag{14}$$

$$R_2 = \frac{a}{4} \qquad\qquad A_2 = \frac{\pi a^2}{16} \quad \text{for square section}$$

$$R_{2\_1} = \frac{a}{4} ; R_{2\_2} = \frac{b}{4} \quad A_2 = \pi \frac{ab}{16} \quad \text{for rectangular section} \tag{15}$$

Region 3: within this region, confinement along the diagonal direction of the cross-section is significantly higher than the perpendicular direction, and post-peak descending behaviour is expected. Hence, this region is considered to be subjected only to one-directional confinement. The confining pressure (f_3) in this region is calculated by Eq. (16). The corresponding area A_3 is calculated by Eq. (17).
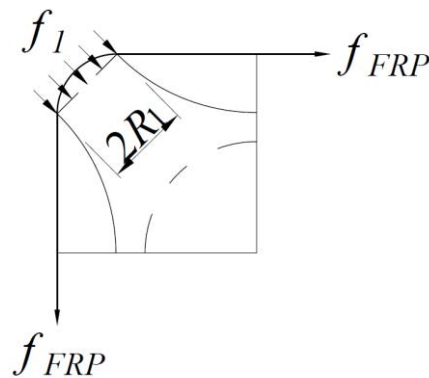
Fig. 5 - 14. Schematic representation of confining pressure in Region 3.

$$f_3 = \frac{f_1}{2R_1} \tag{16}$$

$$A_3 = A_g - \frac{\left[(a - 2R_1)^2 + (b - 2R_1)^2 \right]}{3} - A_2 - A_1 \tag{17}$$

Region 4: confinement is dominated by the deformation of the flat sides and can be determined as a function of the radii of the relevant circumscribed circles, R_4 for a square section or R_{4_1} and R_{4_2} for a rectangular section. The confining pressure (f_4) and the area of this region can be calculated by Eq. (18) and (19), respectively.

$$f_4 = \frac{n_f t_f E_f \varepsilon_{a,eq}}{R_4} \qquad \text{for square section}$$

$$f_{4\_1} = \frac{n_f t_f E_f \varepsilon_{a,eq}}{R_{4\_1}} \text{ and } f_{4\_2} = \frac{n_f t_f E_f \varepsilon_{a,eq}}{R_{4\_2}} \quad \text{for rectangular section} \tag{18}$$

$$A_4 = \frac{\left[(b - 2R_c)^2 + (h - 2R_c)^2 \right]}{3} + 4A_f \tag{19}$$

where A_f is the fan-shaped area (Eq. (20)) representing the area expansion of the cross-sections.

$$A_f = \frac{1}{2} R^2 \theta - \frac{1}{2} b \sqrt{R^2 - \left(\frac{a_n}{2} \right)^2} \quad (\theta \text{ in rad})$$

$$a_n = a + \Delta a = a(1 + \varepsilon_{a,eq})$$

$$R = \frac{a_n^2 + 4h_f^2}{8h} \tag{20}$$

$$\theta = \arctan \frac{2h_f}{a_n}$$

where a_n is the elongation of the flat side, R is the equivalent circular radius of Region 4 and θ is the chord length.

Based on the experimental work conducted as part of this research, the deformation of the flat side (h_f) varies linearly with the area strain (ε_A) and can be described by Eq. (21).

$$h_f = k \varepsilon_A \quad \begin{cases} k = 50 & \text{for Regualr concrete} \\ k = 110 & \text{for Rubbeirsed concrete} \end{cases} \tag{21}$$

5.4.3 The relationship of volumetric strain-to-axial stress

The model proposed by Pantazopoulou and Mills [18] to describe concrete dilation shown

below has been taken as a basis for this study as it considers progress damage to the material:

$$
\begin{aligned}
\varepsilon_V &= (1-2v)\varepsilon_c & \text{for } \varepsilon_c \leq \varepsilon_c^{\lim} = \frac{\varepsilon_{cr}}{v} \\
\varepsilon_V &= (1-2v)\varepsilon_c^* \left[\frac{\varepsilon_c}{\varepsilon_c^*} - b \left(\frac{\varepsilon_c - \varepsilon_c^{\lim}}{\varepsilon_c^* - \varepsilon_c^{\lim}} \right)^c \right] & \text{for } \varepsilon_c > \varepsilon_c^{\lim}
\end{aligned}
\tag{22}
$$

where $\varepsilon_c^* = a\varepsilon_{co}$ represents the compressive axial strain at zero volumetric strain, which for

normal strength concrete commonly occurs at strains of 0.002 to 0.0035; The parameters a, b

and c are a function of both concrete type (such as normal strength, high strength or rubberised

concrete) and level of confinement; b can be used to reflect the degree of passive confinement

and a value of 1 is used for unconfined concrete under uniaxial compressive load, while its

value decreases with increasing confinement level. Pantazopoulou and Mills suggested the use

of $a = 1$. The value of c can be used to modify the descending part of the curves, a higher value

describes a more brittle behaviour, whilst a lower value describes a more ductile behaviour (e.g.

fibre reinforced concrete and rubberised concrete).

In order to comply with the mechanical model of generalised springs and abovementioned

differently confined regions, the model has been modified to relate the volumetric strain to axial

stress (see Eq. (23)).

$$
\begin{aligned}
\varepsilon_V &= -\frac{(1-2v)}{E_c} f_c & \text{for } f_c \leq f_{cr} \\
\varepsilon_V &= -\frac{(1-2v)}{E_c} f_c^* \left[\frac{f_c}{f_c^*} - b \left(\frac{f_c - f_{cr}}{f_c^* - f_{cr}} \right)^c \right] & \text{for } f > f_{cr}
\end{aligned}
\tag{23}
$$

where f_{cr} is the critical stress, which RuC can be determined using the equation proposed by

Raffoul et al. [19] ($f_{cr} = f_{co}(-6.5 \times 10^{-6} K_j^2 + 5.8 \times 10^{-3} K_j + 0.8)$) and for RC can be considered

equal to the unconfined strength; f_c^* indicates the axial stress at which the volumetric strain

becomes zero, which is 1.2 and 1.5 times the unconfined strength of RC and RuC, respectively.

Based on the regression analysis of experimental data presented in Chapter 3, the parameters b and c can be determined by Eq. (24). Parameter b is a function of confinement stiffness. The value of c = 2 is used for RC, as recommend by Pantazopoulou and Mills, whilst the value of 1.5 is adopted for RuC, as RuC has lower strength than RC with a more ductile post-peak behaviour.

$$
\begin{aligned}
b &= 3.05 Ln\left(K_j\right) - 18.9; c = 1.5 \quad \text{for RuC} \quad (R^2 = 84\%) \\
b &= -1.98 Ln\left(K_j\right) + 6.2; c = 2 \quad \text{for RC} \quad (R^2 = 93\%)
\end{aligned}
\tag{24}
$$

5.4.4 Strain reduction factor $k_{\varepsilon f}$

The hoop rupture strain ($\varepsilon_{h,rup}$) of an FRP jacket has been shown to be smaller than the ultimate tensile strain (ε_{fu}) and these two strains can be related by using a strain reduction factor ($k_{\varepsilon f}$) [20, 21]. Lim and Ozbakkaloglu [20] suggested an equation for $k_{\varepsilon f}$ for FRP-confined cylinders as a function of the elastic modulus of FRP composite (E_f) and unconfined concrete strength (f_{co}). According to the experimental results presented in Chapter 4 and collected from [1, 22], the value of $k_{\varepsilon f}$ has been found to be affected by the properties of FRP jacket (such as the elastic modulus (E_f) and number of layers (n_f)), unconfined concrete strength (f_{co}) and section characteristics (circular and non-circular, size of corner and aspect ratio of cross-section). Based on regression analysis of experimental results, the following equation is proposed to determine the value of $k_{\varepsilon f}$:

$$
k_{\varepsilon f} = \frac{\varepsilon_{h,rup}}{\varepsilon_{fu}} = \left(0.7 \cdot K_j^{0.06}\right)^{a/2r}
\tag{25}
$$

where K_j is the ratio of FRP jacket stiffness to concrete strength, r is the radius of the corner and a is the side length of the square or the long side length of the rectangular cross-section.
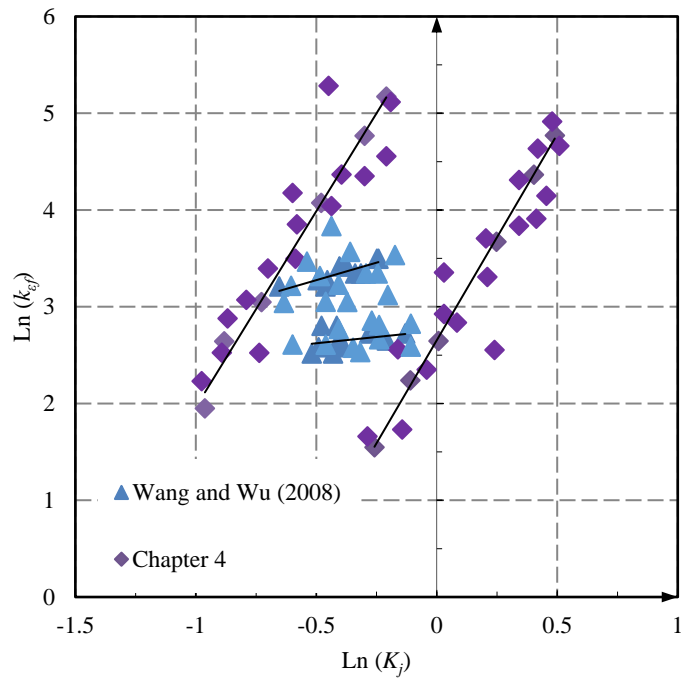
Fig. 5 - 15. Regression analysis of experimental results.
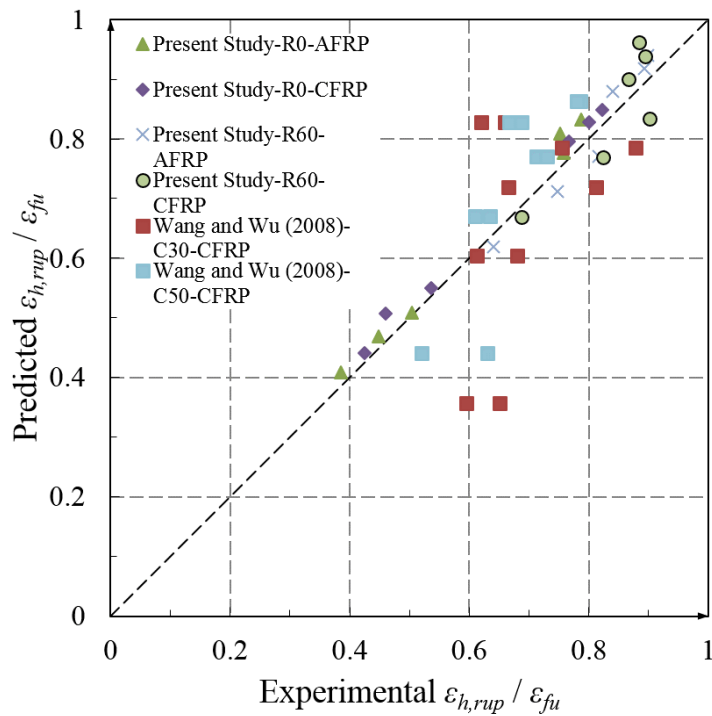
Fig. 5 - 16. Performance of Eq. (25) against experimental data.

5.4.5   Biaxial compressive stress-strain relationship

Test results [23-25] indicate that the strength of concrete under biaxial compression is dependent on the ratio of principal stresses. The stress-strain relation for concrete under biaxial compression suggested by [26] is adopted in this study (see Eq. (26)).

$$\sigma_{c\_biaxial} = \frac{\varepsilon_c E_c}{(1-v\lambda)\left[1+\left(\frac{1}{1-v\lambda}\frac{E_c}{E_s}-\frac{2}{\varepsilon_p}\right)\varepsilon_c+\left(\frac{\varepsilon_c}{\varepsilon_p}\right)^2\right]} \tag{26}$$

where $\sigma_{c\_biaxial}$ and ε_c are the stress and strain under biaxial loading, respectively; E_c is the modulus of elasticity of concrete under uniaxial loading; v is the Poisson's ratio under uniaxial loading; ε_p is the strain at maximum stress of concrete under biaxial compression (for RC, $\varepsilon_p = 0.0025$; for RuC, $\varepsilon_p = 0.0015$); λ is the ratio of the two principal stresses; E_s is the secant modulus at maximum stress and f_{cb} is the ultimate strength of concrete under biaxial compression and can be determined by Eq. (27).

$$\begin{aligned} \lambda < 0.2 \quad & f_{cb} = \left(1+\frac{\lambda}{1.2-\lambda}\right)\cdot f_{co} \\ \lambda \geq 0.2 \quad & f_{cb} = 1.2 f_{co} \end{aligned} \tag{27}$$

5.4.6   Multiaxial compressive stress-strain relationship

5.4.6.1 Strength under multiaxial states of stress

The maximum compressive strength (f_{cc}) at a given confining pressures can be determined from the failure criterion (Eq. (28)) recommended by Mode Code 2010 [27].

$$\alpha\frac{J_2}{f_{co}^2}+\lambda\frac{\sqrt{J_2}}{f_{co}}+\beta\frac{I_1}{f_{co}}-1=0 \tag{28}$$

where the invariants of the stress tensor (I_1) and the stress deviators (J_2 and J_3) can be calculated according to Eq. (29).

$$I_1 = \sigma_1 + \sigma_2 + \sigma_3$$

$$J_2 = \frac{1}{6}\left[(\sigma_1 - \sigma_2)^2 + (\sigma_2 - \sigma_3)^2 + (\sigma_3 - \sigma_1)^2\right]$$

$$J_3 = (\sigma_1 - \sigma_m) \cdot (\sigma_2 - \sigma_m) \cdot (\sigma_3 - \sigma_m)$$

$$\sigma_m = (\sigma_1 + \sigma_2 + \sigma_3)/3$$

$$(29)$$

and

$$\lambda = c_1 \cdot \cos\left[\frac{1}{3}\arccos(c_2 \cdot \cos 3\theta)\right] \qquad \cos 3\theta \geq 0$$

$$\lambda = c_1 \cdot \cos\left[\frac{\pi}{3} - \frac{1}{3}\arccos(-c_2 \cdot \cos 3\theta)\right] \quad \cos 3\theta \leq 0$$

$$\cos 3\theta = \frac{3\sqrt{3}}{2}\frac{J_2}{J_2^{3/2}}$$

$$(30)$$

The coefficients α, β, c_1 and c_2 in Eq. (30) are material parameters that depend on the uniaxial compressive strength, the biaxial compressive strength (f_{cb}) and the triaxial compressive strength at one point on the compressive meridian ($\sigma_1 = \sigma_2 \geq \sigma_3$). Those parameters value have been studied in detail study by Ottosen [28] for different ratios of $k = f_{ct}/f_{co}$. In this study, the ratio of k is 0.12. Therefore, the following values are adopted:

$$\alpha = 0.9218; \beta = 2.5969; c_1 = 9.9110 \text{ and } c_2 = 0.9647$$

5.4.6.2 Strain under multiaxial states of stress

As suggested by Mirmiran and Shahawy [29], the ultimate compressive strain (ε_{cu}) is obtained from the analysis of the dilation rate (Eq. (31)), which defines the ratio of ultimate area strain (ε_{Au}) to axial strain ratio (ε_{cu}) and can be determined experimentally. The theoretical ultimate area strain (ε_{Au}) can be determined by the ultimate lateral hoop strain ($\varepsilon_{h,rup}$) through Eq. (11).

$$\eta = -\frac{\varepsilon_{Au}}{\varepsilon_{cu}}$$

$$(31)$$

The parameter η depends on the normalised effective confining stiffness (K_j) and given by:

$$\eta = C_1 K_j^{-C_2}$$

$$(32)$$

where C_1 and C_2 are experimental constants. Values of $C_1 = 2.8$ and $C_2 = 0.26$ are used in this study and for the tests conducted as part of this research and others [1, 3] provide $R^2 = 94$.
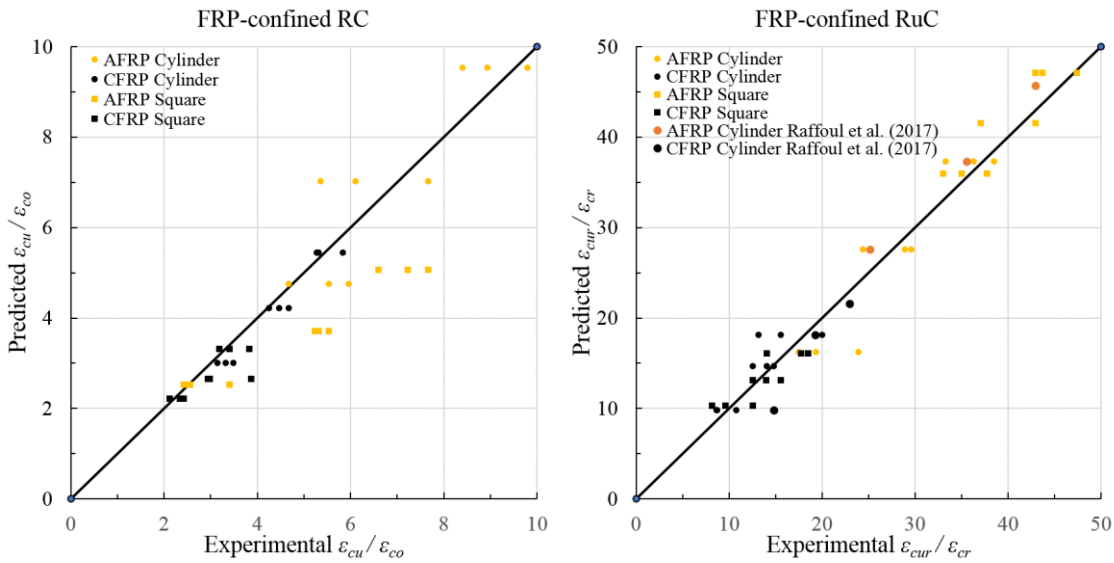
Fig. 5 - 17. Performance of Eq. (32) against experimental data.

5.4.6.3 Stress-strain relation under multiaxial states of stress

The stress-strain curve of concrete under multiaxial stress state is described using the model proposed by Mander et al. [30], as shown below:

$$f_{c\_triaxial} = \frac{f_{cc} x r}{r - 1 + x^r}$$

(33)

where

$$x = \frac{\varepsilon_c}{\varepsilon_{cc}}; \ r = \frac{E_{co}}{E_{co} - E_{sec}} \text{ and } E_{sec} = \frac{f_{cc}}{\varepsilon_{cc}}$$

(34)

5.4.7   Proposed Model – General procedure

The proposed analytical model assumes that at a given confinement ratio, concrete with passive or active confinement exhibits similar axial stress and strain values [31, 32]. A full-range stress-strain curve for non-circular sections FRP-confined concrete can be obtained using the incremental procedure shown below:

1. An initial increment of axial strain (ε_c) is imposed (for example, $\varepsilon_c = 500\mu\varepsilon$). The axial strain is increased incrementally by ε_c for each iteration.

2. Set an assumed value to target compressive stress (σ_{c_target}).

3. Calculate volumetric strain (ε_V), then area strain (ε_A) and equivalent lateral strain ($\varepsilon_{a,eq}$). If $\varepsilon_{a,eq} > k_s\varepsilon_{fu}$, the specimen failed; if $\varepsilon_{a,eq} < k_s\varepsilon_{fu}$, go to step 4.

4. Calculate confining pressures for each region (f_1, f_2, f_3 and f_4).

5. Calculate ultimate compressive stress (f_{cc1} and f_{cc2}) for Region 1 and 2 using corresponding confining pressures (f_1 and f_2).

6. Corresponding to the specific stress-strain relationship, compressive stresses (σ_{c1}, σ_{c2}, σ_{c3} and σ_{c4}) for each region are calculated. The average compressive stress (σ_c) is determined.

7. If the average compressive stress (σ_c) coincides with the target compressive stress (σ_{c_target}). applied in step 2, update target compressive stress and go back to step 1. Otherwise, steps 2-6 are repeated until the two stresses converge.
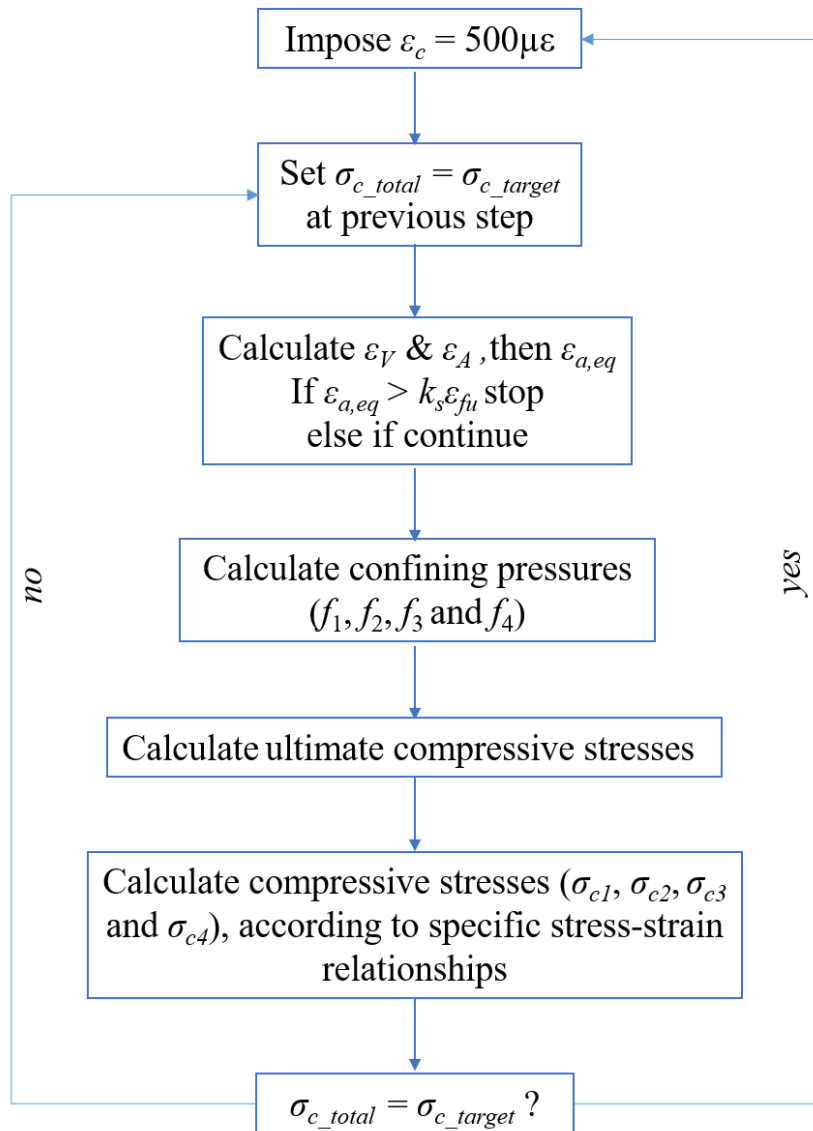
Fig. 5 - 18. Iterative procedure.

5.5   PROPOSED MODEL VS EXPERIMENTAL RESULTS

The stress-strain curves predicted by the proposed model are compared with the experimental results presented in Chapter 4. The performance of the proposed model in predicting the behaviour of FRP-confined rectangular RC columns and with different corner radii are validated by comparing with test data obtained from [1, 2, 33].

Fig. 5 - 19 and 5 - 20 compare the curves predicted by the proposed model and the average experimental results for FRP-confined RC and RuC, respectively. As can be seen, the overall

results show a good correlation for the different confinement level and concrete type. In general, the model predicts well in terms of the average initial stiffness, critical stress and strain, gradient of the curve and the ultimate stress and strain values of the tested specimens. In Fig. 5 - 19, it can be seen that the behaviour of poorly confined RC specimens is correctly reproduced by the proposed model. Fig. 5 - 20 indicates that the model can capture well the unique behaviour of FRP-confined RuC, including the increasing stiffness observed in the case of AFRP CRuC.

Fig. 5 - 21 compares the predicted curves against the experimental results of a series of FRP-confined square RC sections with different corner radii tested by Wang and Wu [11]. This test was chosen for comparison as the stress-strain curves were clearly reported in the original paper. It can be seen that the predictions agree reasonably well with experimental results. However, a degree of overestimation is shown in the case of C50, which was confined with one-layer of CFRP. Fig. 5 - 22 illustrates the predicted and experimental stress-strain curves of FRP-confined rectangular RC section with two different corner radii tested by Lam and Teng [5]. The initial slope of the stress-strain curve and ultimate axial strain is correctly predicted by the proposed model, but the second portion of the curve is only approximately predicted.
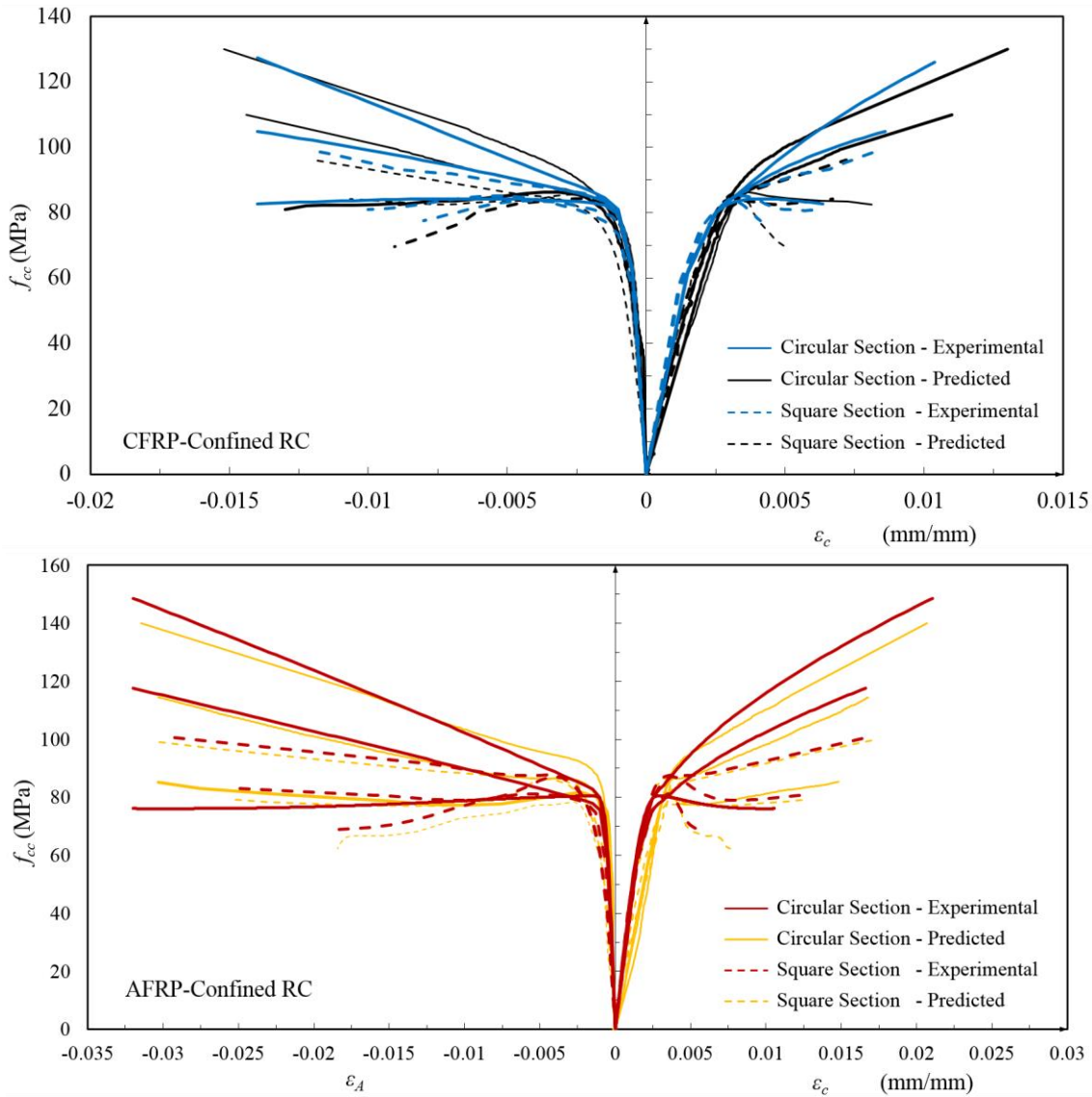
Fig. 5 - 19. Experimental stress-strain curves and model predictions for FRP-confined RC
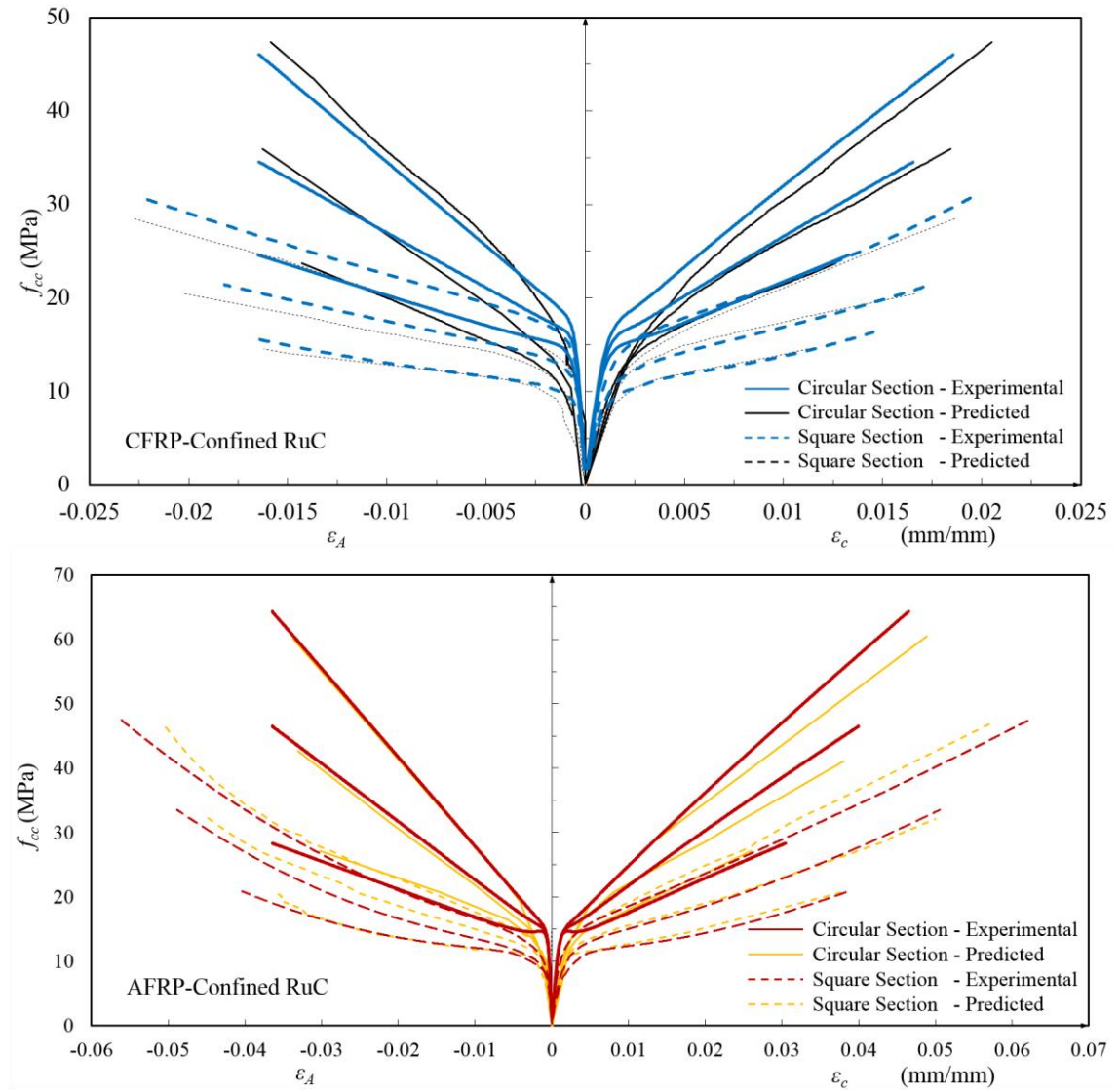
Fig. 5 - 20. Experimental stress-strain curves and model predictions for FRP-confined RuC
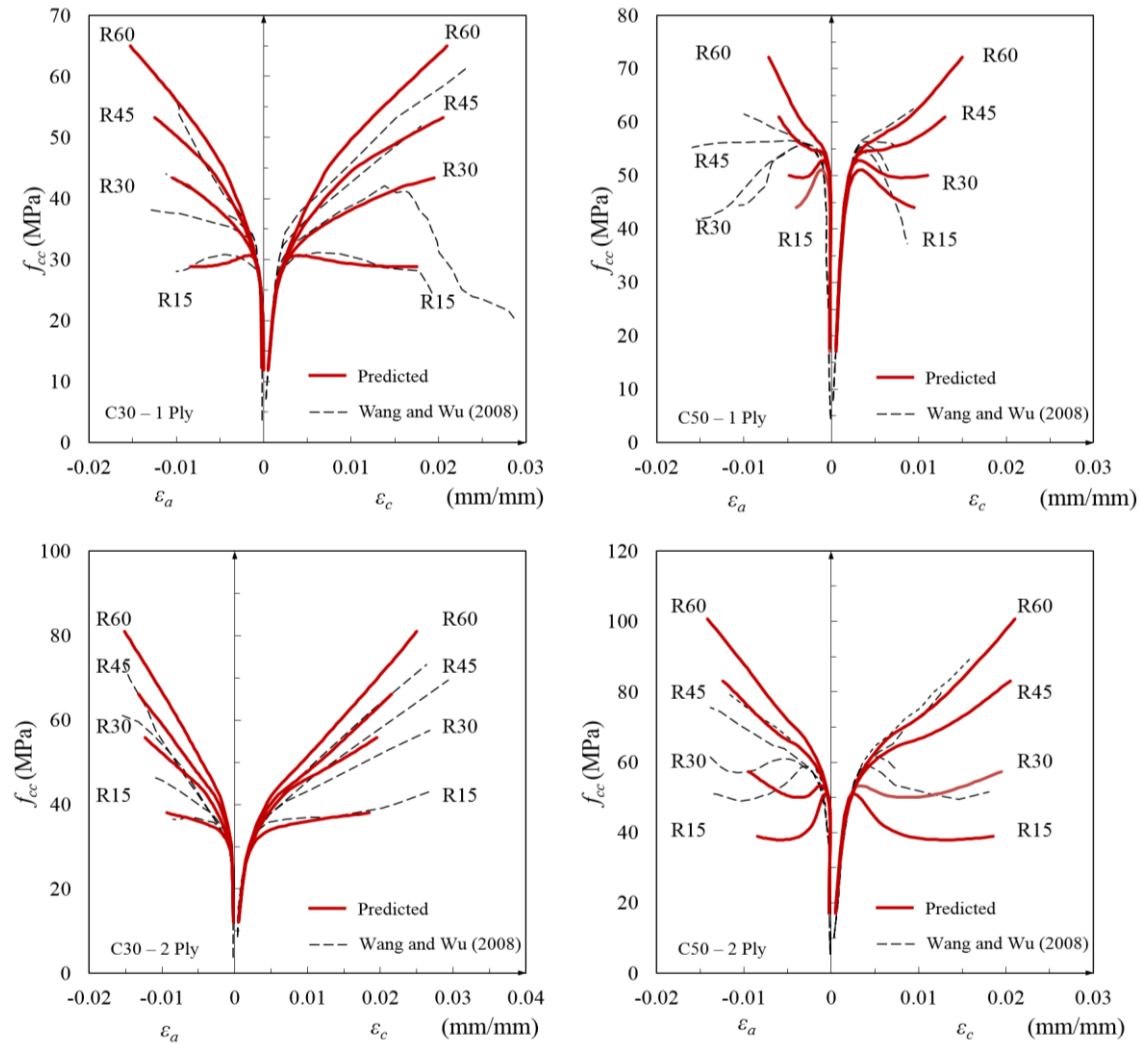
Fig. 5 - 21. Comparison of experimental stress-strain curves of FRP-confined RC in the square section with various corner radius tested by Wang and Wu (2008) with analytical predictions.
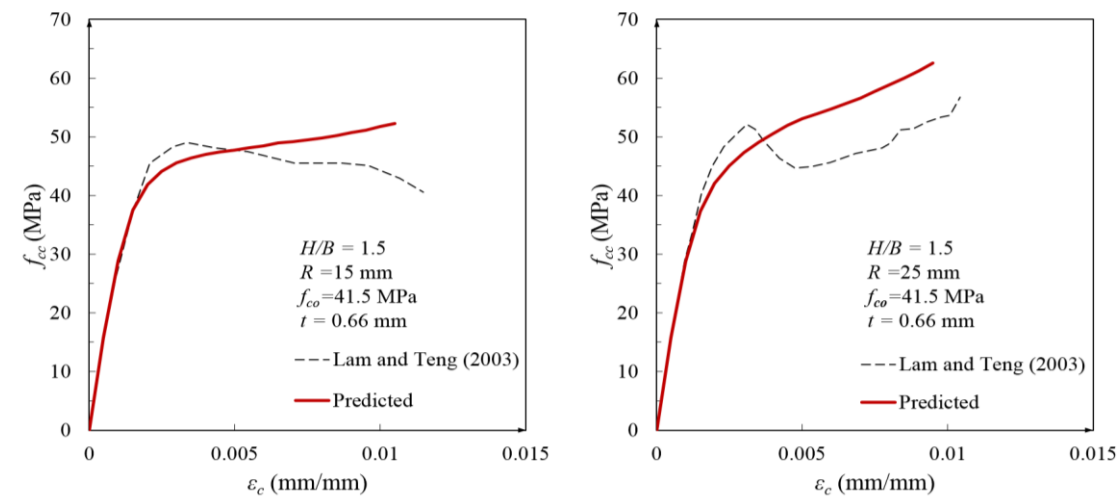
Fig. 5 - 22. Comparison of experimental stress-strain curves of FRP-confined RC in the rectangular section with various corner radius tested by Lam and Teng (2003) with analytical predictions.

5.6 CONCLUSIONS

In this Chapter, the existing design-oriented model and CDPM have been assessed using the test results obtained in Chapter 3. It has been found that they cannot predict the behaviour of FRP-confined rubberised concrete. A rational model for FRP-confined concrete columns is presented based on the new understanding of the confinement mechanism in non-circular sections. The distribution of axial stress and the interaction between the FRP jacket and the concrete are explicitly considered in the proposed model. An axial stress-to-volumetric strain relationship has been developed to reflect the influence of confinement stiffness on the volumetric behaviour of FRP-confined concrete columns. The specific volumetric contraction behaviour of FRP-confined RuC are particularly considered. By using the equivalent hoop strain as characteristic hoop strain, the ultimate point of the stress-strain model is defined. Comparisons of the predictions of the proposed stress-strain model with test results have shown the model provides a close prediction of the experimental stress-strain responses. However, further research should validate the accuracy of this model for the rectangular columns with different aspect cross-section ratio or confined by different types of FRP (e.g. glass or basalt sheets).

5.7 REFERENCES

1. Wang, L.-M. and Y.-F. Wu, *Effect of corner radius on the performance of CFRP-confined square concrete columns: Test.* Engineering structures, 2008. **30**(2): p. 493-505.
2. Lam, L. and J. Teng, *Design-oriented stress-strain model for FRP-confined concrete in rectangular columns.* Journal of Reinforced Plastics and Composites, 2003. **22**(13): p. 1149-1186.
3. Raffoul, S., et al., *Constitutive model for rubberized concrete passively confined with FRP laminates.* Journal of Composites for Construction, 2019. **accepted for publication**.
4. Raffoul, S., et al., *Behaviour of unconfined and FRP-confined rubberised concrete in axial compression.* Construction and Building Materials, 2017. **147**: p. 388-397.
5. Systèmes, D., *Abaqus Analysis User's Guide.* Solid (Continuum) Elements, 2014. **6**.
6. Tao, Z., Z.-B. Wang, and Q. Yu, *Finite element modelling of concrete-filled steel stub columns under axial compression.* Journal of Constructional Steel Research, 2013. **89**: p. 121-131.
7. Yu, T., et al., *Finite element modeling of confined concrete-I: Drucker–Prager type plasticity model.* Engineering structures, 2010. **32**(3): p. 665-679.
8. Hany, N.F., E.G. Hantouche, and M.H. Harajli, *Finite element modeling of FRP-confined concrete using modified concrete damaged plasticity.* Engineering structures, 2016. **125**: p. 1-14.
9. Teng, J., et al., *Theoretical model for fiber-reinforced polymer-confined concrete.* Journal of Composites for Construction, 2007. **11**(2): p. 201-210.
10. Papanikolaou, V.K. and A.J. Kappos, *Confinement-sensitive plasticity constitutive model for concrete in triaxial compression.* International Journal of solids and structures, 2007. **44**(21): p. 7021-7048.
11. Yu, T., et al., *Finite element modeling of confined concrete-II: Plastic-damage model.* Engineering structures, 2010. **32**(3): p. 680-691.
12. Rousakis, T.C., et al., *Analytical modelling of plastic behaviour of uniformly FRP confined concrete members.* Composites Part B: Engineering, 2008. **39**(7-8): p. 1104-1113.
13. Karabinis, A. and T. Rousakis, *Concrete confined by FRP material: a plasticity approach.* Engineering structures, 2002. **24**(7): p. 923-932.
14. Bompa, D., et al., *Experimental assessment and constitutive modelling of rubberised concrete materials.* Construction and Building Materials, 2017. **137**: p. 246-260.
15. Wang, Z., et al., *Tensile Stress-Strain Characteristics of Rubberised Concrete from Flexural Tests.* Submitted for publication, 2019.
16. Mirmiran, A., et al., *Effect of column parameters on FRP-confined concrete.* Journal of Composites for Construction, 1998. **2**(4): p. 175-185.
17. Al-Salloum, Y.A., *Influence of edge sharpness on the strength of square concrete columns confined with FRP composite laminates.* Composites Part B: Engineering, 2007. **38**(5-6): p. 640-650.
18. Pantazopoulou, S. and R. Mills, *Microstructural aspects of the mechanical response of plain concrete.* Materials Journal, 1995. **92**(6): p. 605-616.
19. Raffoul, S., Escolano-Margarit, D., Garcia, R., Guadagnini, M., Pilakoutas, K., *Constitutive model for rubberized concrete passively confined with FRP laminates.* Journal of Composites for Construction, 2019. **- accepted for publication**.
20. Lim, J.C. and T. Ozbakkaloglu, *Lateral strain-to-axial strain relationship of confined concrete.* Journal of Structural Engineering, 2014. **141**(5): p. 04014141.
21. Pessiki, S., et al., *Axial behavior of reinforced concrete columns confined with FRP jackets.* Journal of Composites for Construction, 2001. **5**(4): p. 237-245.

22.   Wu, Y.-F. and Y.-Y. Wei, *Effect of cross-sectional aspect ratio on the strength of CFRP-confined rectangular concrete columns.* Engineering structures, 2010. **32**(1): p. 32-45.

23.   Kupfer, H., H.K. Hilsdorf, and H. Rusch. *Behavior of concrete under biaxial stresses.* in *Journal Proceedings*. 1969.

24.   Darwin, D. and D.A. Pecknold, *Nonlinear biaxial stress-strain law for concrete.* Journal of the Engineering Mechanics Division, 1977. **103**(2): p. 229-241.

25.   Tasuji, M.E. and A.H. Nilson. *Stress-strain response and fracture of concrete in biaxial loading.* in *Journal Proceedings*. 1978.

26.   Liu, T.C., A.H. Nilson, and F.O.S. Floyd. *Stress-strain response and fracture of concrete in uniaxial and biaxial compression.* in *Journal Proceedings*. 1972.

27.   Walraven, J., *fib Model Code for Concrete Structures 2010: mastering challenges and encountering new ones.* Structural Concrete, 2013. **14**(1): p. 3-9.

28.   Ottosen, N.S., *A failure criterion for concrete.* American Society of Civil Engineers. Engineering Mechanics Division. Journal, 1977. **103**(4): p. 527-535.

29.   Mirmiran, A. and M. Shahawy, *Behavior of concrete columns confined by fiber composites.* Journal of Structural Engineering, 1997. **123**(5): p. 583-590.

30.   Mander, J.B., M.J. Priestley, and R. Park, *Theoretical stress-strain model for confined concrete.* Journal of Structural Engineering, 1988. **114**(8): p. 1804-1826.

31.   Jiang, T. and J. Teng, *Analysis-oriented stress–strain models for FRP–confined concrete.* Engineering structures, 2007. **29**(11): p. 2968-2986.

32.   Papastergiou, P., *A confinement model for concrete wrapped of pretensioned with frp.* 2010, The University of Sheffield.

33.   Rochette, P. and P. Labossiere, *Axial testing of rectangular column models confined with composites.* Journal of Composites for Construction, 2000. **4**(3): p. 129-136.

Chapter 6

Shear Behaviour Model for FRP-Confined and Unconfined Rubberised Concrete

6.1 INTRODUCTION

This paper presents experimental and numerical results of an ongoing investigation aiming to develop high-strength high-deformability fibre reinforced polymer (FRP) confined rubberized concrete (CRuC) suitable for structural applications. The rubberized concrete (RuC) utilises recycled rubber particles as a replacement for both fine and coarse aggregates. Rubber aggregates reduce the compressive strength and stiffness of RuC thus limiting its application for structural purposes. Confining RuC with FRP jackets recovers strength and enables the development of high deformability, ductility and energy dissipation capacity. Recent research mainly focuses on axial performance of RuC and CRuC, but there is little work on the shear behaviour of this flexible concrete. This paper adopts a nonlinear numerical approach for the practical implementation of the smeared, fixed-angle crack approach in finite element analysis to predict the shear response of RuC and CRuC. Constitutive models are proposed on the basis of fundamental test results. The model is validated through a simulation of a series of shear tests on RuC and CRuC with different shear span-to-depth ratios (a/d). The predictions of the model are then compared against experimental results and a good agreement is found.

The primary objective of this chapter is to assess if the Fixed-Angle Softened Truss Model for RC proposed by Pang and Hsu [1] can be used in the case of RuC and CRuC and modify it if necessary. The work is presented in four parts: The first part describes the original FA-STM and introduces a modification considering the properties of RuC and CRuC. The second part discusses the required constitutive models for the implementation of the modified FA-STM and how they are determined, including: 1) concrete in compression; 2) concrete in tension; 3) concrete in shear; and 4) FRP in tension. In the third part, a UMAT is developed to enable the implementation of the proposed model in ABAQUS. Finally, an experimental program on 18 prismatic samples is described and the accuracy of the proposed model is assessed. This work will lead to the development of numerical tools that will enable a deeper understanding of the behaviour of RuC and CRuC and will assist in developing applications for highly deformable elements. The results presented in this study are part of the FP7 EU-funded project Anagennisi

which aims to develop solutions to reuse all tire components in high value innovative concrete applications.

6.2   APPLICATION OF FA-STM IN RUC AND CRUC

The FA-STM theory is based on six equations derived from two-dimensional equilibrium and Mohr compatibility conditions. These theoretical equations, along with constitutive material laws, can be used in numerical analysis to predict the performance of structures subjected to external loading [1]. When dealing with RC 2-D elements subjected to in-plane shear and normal stresses (τ_{lt} and σ_l, σ_t), the FA-STM defines three coordinate systems (see Fig. 6 - 1a). a) *l-t*: the directions of longitudinal and transverse steel bars, respectively; b) *2-1*: the directions of the principal stresses of RC element; c) *d-r* coordinates: the directions of principal stresses in the concrete alone. The governing equations are derived by assuming that cracks in concrete are oriented at a fixed angle α_2, which is the angle between the *2*-axis and the *l*-axis. The angle between the *d*-axis and the *l*-axis is the rotating angle α, which continues to rotate away from the fixed angle α_2 as load increases. The angle between α_2 and α is defined as the deviating angle $\beta = \alpha_2 - \alpha$.

In order to apply FA-STM for unreinforced RuC and CRuC, the coordinate systems have to be redefined (see Fig. 6 - 1b) as follows: a) *l-t*: the directions of the longitudinal and transverse beam, respectively; b) *2-1*: the directions of the principal stresses of RuC or CRuC element. The angle between the *2*-axis and *l*-axis is called the principal angle θ_p; c) *n-m*: the parallel and perpendicular directions of the crack plane. Fixed angle α_2 is replaced by the angle of inclined strut; d) the principal directions in concrete at any stage are still represented by *d-r* coordinates, resulting in a rotating angle θ_c. The deviating angle β is redesignated as the difference between θ_f and θ_c. In RuC, the *2-1* coordinate coincides with the *d-r* coordinate.
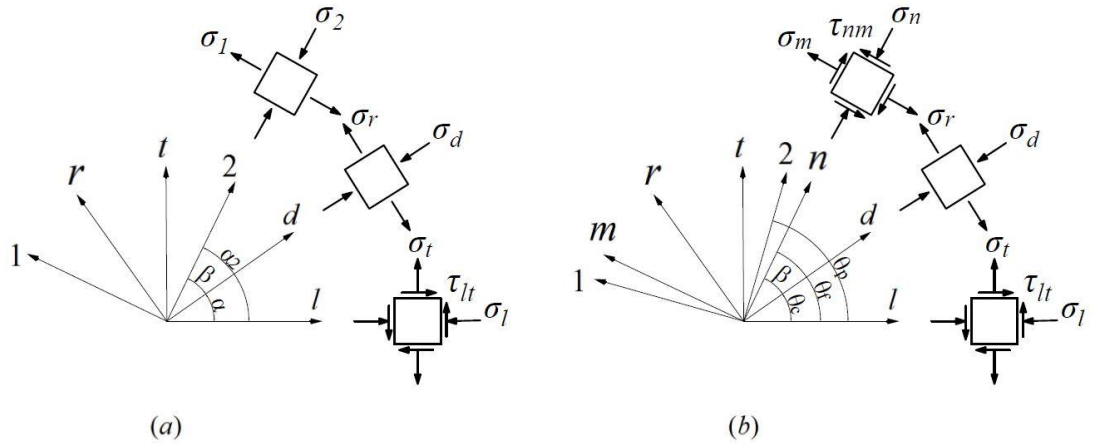
Fig. 6 - 1. Coordinate systems in the FA-STM (a) and proposed model (b).

6.2.1 The angle of the inclined strut

For members with a shear span-to-depth ratio (*a/d*) less than 2.5 to 2, a significant portion of the applied shear force can be transferred directly to the support through an inclined strut. This load-carrying mechanism is normally referred to as direct strut (one-panel model) [2, 3]. Experimental observations [4] indicate that a direct strut is the primary load mechanism for specimens with *a/d* of 1.85. ACI 318 [5] recommends using a one-panel strut when *a/d* is less than or equal to 2.1. The model presented here is based on this loading mechanism and developed for the D-Region (Deep beam shear region). The governing equations of the proposed model are derived by the angle of the inclined concrete strut (θ_f), which is defined by:

$$\theta_f = \frac{\pi}{2} - arctan\frac{a}{d} \tag{1}$$

where *a* is the distance between the applied load and support, *d* is the depth of specimen.

6.2.2 Governing equations

Fig. 6 - 1b shows the coordinate systems in a RuC element subjected to applied stresses σ_l, σ_t and τ_{lt}. Fig. 6 - 2a presents the stress state of a CRuC element under in-plane pure shear stress τ_{lt}. The stress in concrete and FRP are shown in Fig. 6 - 2b and Fig. 6 - 2c. It is assumed that the FRP can only resist the tensile stress, $\rho_t f_{frp}$, and the concrete is subjected to a set of in-

plane stresses $-\rho_t f_{frp}$ and τ_{lt} Stresses σ_n^c, σ_m^c and τ_{nm}^c are the average normal stresses and average shear stress of the concrete strut in the n and m directions. Equilibrium and compatibility equations for the RuC ($\rho_t=0$) and CRuC elements are derived by transforming the stresses and strains from the n-m to the l-t coordinate (Eq. (2) to (7)).
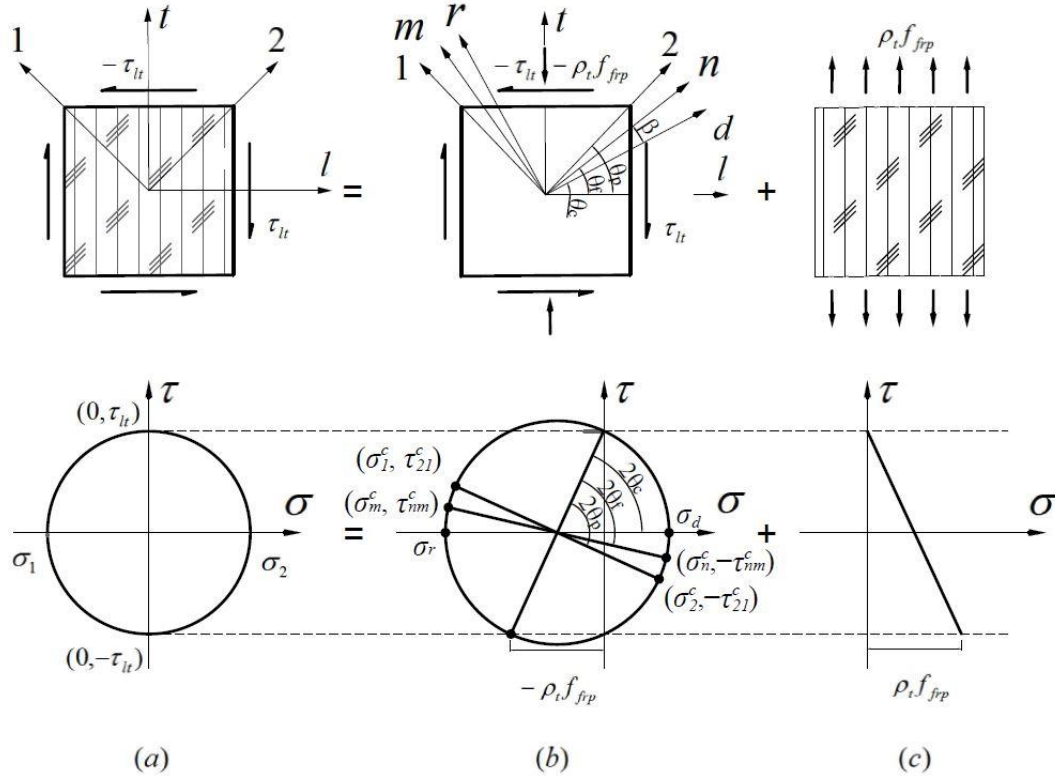
Fig. 6 - 2. The stress state in CRuC element under pure shear.

Stress equilibrium equations

$$\sigma_l = \sigma_n^c cos^2\theta_f + \sigma_m^c sin^2\theta_f + 2\tau_{nm}^c sin\theta_f cos\theta_f \tag{2}$$

$$\sigma_t = \sigma_n^c sin^2\theta_f + \sigma_m^c cos^2\theta_f - 2\tau_{nm}^c sin\theta_f cos\theta_f + \rho_t f_{frp} \tag{3}$$

$$\tau_{lt} = \left(-\sigma_n^c + \sigma_m^c\right) sin\theta_f cos\theta_f + \tau_{nm}^c \left(cos^2\theta_f - sin^2\theta_f\right) \tag{4}$$

Strain compatibility equations

$$\varepsilon_l = \varepsilon_n cos^2\theta_f + \varepsilon_m sin^2\theta_f + \gamma_{nm} sin\theta_f cos\theta_f \tag{5}$$

$$\varepsilon_t = \varepsilon_n sin^2\theta_f + \varepsilon_m cos^2\theta_f - \gamma_{nm} sin\theta_f cos\theta_f \tag{6}$$

$$\frac{\gamma_{lt}}{2} = (-\varepsilon_n + \varepsilon_m)sin\theta_f cos\theta_f + \frac{\gamma_{nm}}{2}\left(cos^2\theta_f - sin^2\theta_f\right) \tag{7}$$

To solve Eqs. (2)-(7), four constitutive laws are required: 1) concrete in compression, relating the average concrete stress σ_n^c and average strain ε_n in *n*-direction, 2) concrete in tension, relating the average concrete stress σ_m^c and average strain ε_m in *m*-direction, 3) concrete in shear, relating the average concrete shear stress τ_{nm}^c and average shear strain γ_{nm} in the *n-m* coordinate, and 4) FRP in tension (*t*-direction).

For RuC, the assumption that the constitutive relation in the direction of the inclined strut (σ_n^c-ε_n , σ_m^c-ε_m relation) is identical to that in the principal direction of concrete (σ_d-ε_d , σ_r-ε_r relation) can be considered accurate when *a/d* is less than or equal to 2.1 (Pang, 1996). However, the deviating angle *β* in CRuC will increase as the confining stress increases, which will lead to an increase in the difference between σ_n^c and σ_d as well as σ_m^c and σ_r . Therefore, the constitutive relation of cracked concrete in the direction of the inclined strut (σ_n^c-ε_n , σ_m^c-ε_m) cannot be replaced with the constitutive relation in the principal direction (σ_d-ε_r , σ_r-ε_r). The stresses σ_n^c, σ_m^c of concrete in the *n-m* coordinate and corresponding strains $\varepsilon_n, \varepsilon_m$ should be calculated by stress and strain transformation from the principal *d-r* coordinate using the equation shown below:

$$\begin{Bmatrix} \sigma_m^c \\ \sigma_n^c \\ \tau_{nm}^c \end{Bmatrix} = \begin{bmatrix} c^2 & s^2 & 2cs \\ s^2 & c^2 & -2cs \\ -cs & cs & c^2-s^2 \end{bmatrix} \begin{Bmatrix} \sigma_r \\ \sigma_d \\ 0 \end{Bmatrix}; \begin{Bmatrix} \varepsilon_m \\ \varepsilon_n \\ \gamma_{nm} \end{Bmatrix} = \begin{bmatrix} c^2 & s^2 & cs \\ s^2 & c^2 & -cs \\ -2cs & 2cs & c^2-s^2 \end{bmatrix} \begin{Bmatrix} \varepsilon_r \\ \varepsilon_d \\ 0 \end{Bmatrix} \tag{8}$$

where *c*=cos*β* and *s*=sin*β*.

6.3   CONSTITUTIVE LAWS

All tested specimens (cylinders and prisms) were manufactured using rubberized concrete with rubber particles replacing 60% of both fine and coarse mineral aggregates by volume. This 'optimized' mix was chosen from a detailed study on 40 mixes carried out by Raffoul et al. [6], which achieved the best balance between strength retention and deformability. Table 6 - 1 shows the properties of this particular mix.

Table 6 - 1. Summary of material properties

RuC		Basalt bars		Carbon fibres		
f_c' (MPa)	ε_{co} ($\times 10^{-3}$)	Elastic modulus (GPa)	Rupture strain (%)	Elastic modulus (GPa)	Ultimate strain (%)	Thickness of 1-layer (mm)
7.5	1.307	39 (5*)	2.81 (0.08*)	227 (17*)	0.9 (0.05*)	0.185 (0.01*)

*Standard Deviation

6.3.1   Compressive constitutive law

The uniaxial compressive stress-strain relations of RuC and CRuC can be obtained from compression tests. The details of the test setup and instrumentation have been discussed in chapter 4, section 4.2.3.
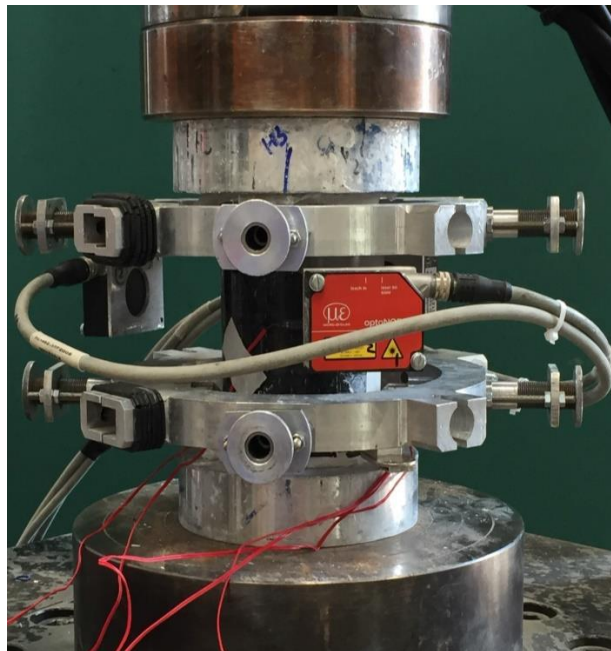
Fig. 6 - 3. Set-up overview of cylinder compression.

6.3.1.1 RuC

Up to the peak load, the experimental data matches well the modified stress-strain model (Eq. (9)) (see Fig. 6 - 4), which was initially proposed for FRP-confined concrete by Lam and Teng [6] (with $E_2 = 0$, see Eq. (19)). In order to capture the principal compressive behaviour of RuC under biaxial compression-tension, the model has been modified by introducing parameter ζ (a compressive capacity reduction factor).

$$\sigma_c = E_c \varepsilon_c - \frac{E_c^2}{4\zeta f_{co}'} \varepsilon_c^2 \tag{9}$$

The descending portion of the stress-strain model is based on Guo's model (Guo, 2014). It is represented as follows:

$$y = \frac{x}{\alpha(x-1)^\beta + x} (x > 1) \tag{10}$$

where $y = \dfrac{\sigma_c}{\zeta f_{co}'}$ and $x = \dfrac{\varepsilon_c}{\zeta \varepsilon_{co}}$.
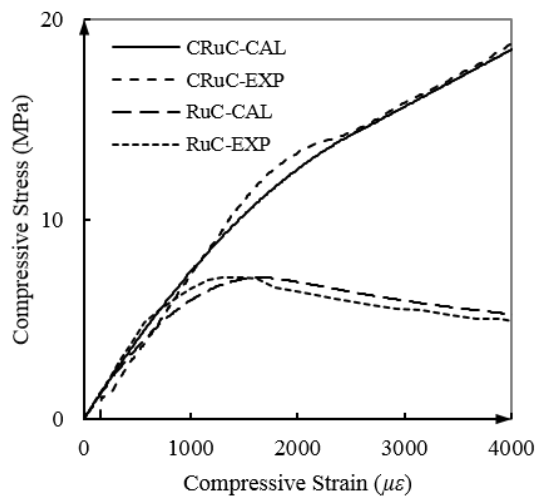
Fig. 6 - 4. Compressive constitutive laws of RuC and CRuC.

The parameters α, β can be calibrated using experimental data. For the concrete tested in this study, these parameters were found to be $\alpha=1$ and $\beta=1.55$ as shown in Eq. (11).

$$\frac{\sigma_c}{\zeta f_{co}'} = \frac{\dfrac{\varepsilon_c}{\zeta \varepsilon_{co}}}{\left(\dfrac{\varepsilon_c}{\zeta \varepsilon_{co}} - 1\right)^{1.55} + \dfrac{\varepsilon_c}{\zeta \varepsilon_{co}}} \tag{11}$$

The following equations, proposed by Bompa et al. [7], are used to determine the modulus of elasticity and crushing strain of RuC.

$$E_c = 12\left(\frac{f_{co}'}{10}\right)^{2/3} \; ; \; \varepsilon_{co} = 0.7 f_{co}'^{0.31} \tag{12}$$

6.3.1.2 Compressive capacity reduction factor

Since there is a biaxial stress state in the beam shear span, the resistance of the diagonal compression struts developed in that region is governed by the failure criterion in the compression-tension branch (see Fig. 6 - 5). Hence, the strength of the inclined strut $\left(f_{c,max}'\right)$ is lower than the uniaxial concrete compressive strength due to the existence of lateral tensile strain. A compressive capacity reduction factor ζ is used to account for this effect, which is defined as the ratio of maximum principal compressive stress to the uniaxial compressive stress of concrete $\left(\zeta = f_{c,max}' / f_{co}'\right)$. The biaxial failure criterion for concrete and ζ can be determined by testing square concrete panels subjected to various in-plane loading stress ratios σ_2 / σ_1. The general Drucker-Prager failure criterion is adopted here, as it captures well the interaction between tension and compression, and it can reflect the fact that the shear strength of concrete is higher than its tensile strength Eq. (13).

$$F = \alpha I_1 + \sqrt{J_2} - \tau_0 = 0 \tag{13}$$

where α and τ_0 are determined from the experiment, I_1 is the first invariant and J_2 is the second deviatoric.
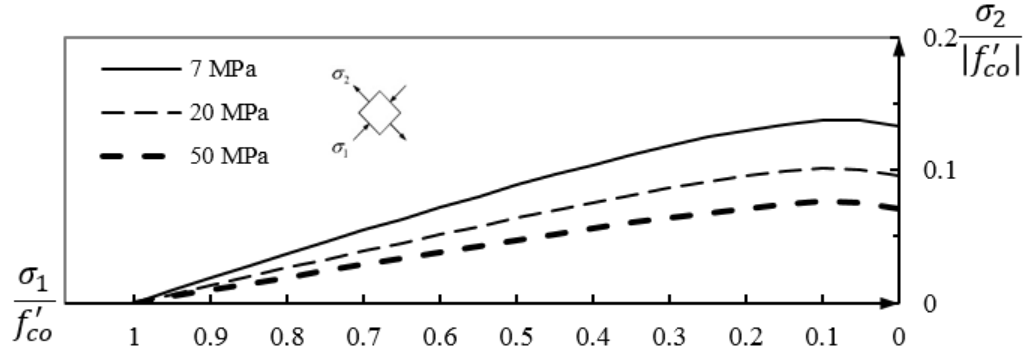
Fig. 6 - 5. Biaxial strength envelopes for concrete under combined tension and compression.

The parameters α and τ_0 for the failure surface in tension-compression quadrants are obtained by solving the stress states in uniaxial compression and tension, given as:

$$\alpha = \frac{1}{\sqrt{3}} \frac{f_{co}^{'} - f_{ct}}{f_{co}^{'} + f_{ct}} \; ; \tau_0 = \frac{2}{\sqrt{3}} \frac{f_{co}^{'} f_{ct}}{f_{co}^{'} + f_{ct}} \tag{14}$$

For plane stress conditions ($\sigma_3 = 0$), Eq. (13) can be written as:

$$\left(1 - 3\alpha^2\right)\left(\sigma_1^2 + \sigma_2^2\right) - \left(1 + 6\alpha^2\right)\sigma_1\sigma_2 + 6\tau_0\alpha\left(\sigma_1 + \sigma_2\right) - 3\tau_0 = 0 \tag{15}$$

Eq. (15) can be rewritten in the form:

$$A\left(\sigma_1^2 + \sigma_2^2\right) + B\sigma_1\sigma_2 + C\left(\sigma_1 + \sigma_2\right) + D = 0 \tag{16}$$

where $A = 1 - 3\alpha^2$, $B = -\left(1 + 6\alpha^2\right)$, $C = 6\tau_0\alpha$ and $D = -3\tau_0$

Substituting loading stress ratio $\varphi = \sigma_2 / \sigma_1$ and $\sigma_1 = \zeta f_{co}^{'}$ into Eq. (16) yields,

$$A\left(1 + \varphi^2\right) + B\varphi + C\left(1 + \varphi\right)\frac{1}{\zeta f_{co}^{'}} + \frac{D}{\left(\zeta f_{co}^{'}\right)^2} = 0 \tag{17}$$

where φ is the loading stress ratio. The principal tensile stress σ_1 and principal compressive stress σ_2 can be calculated by the corresponding principal strains ε_1 and ε_2 through relative constitutive laws, then the loading stress ratio φ is obtained. Solving Eq. (17) leads to:

$$\zeta = \frac{-\dfrac{2D}{f_{co}^{'\,2}}}{\dfrac{C(1+\varphi)}{f_{co}^{'}} - \sqrt{\left(\dfrac{C(1+\varphi)}{f_{co}^{'}}\right)^2 - 4\dfrac{\left[A\left(1+\varphi^2\right)+B\varphi\right]D}{f_{co}^{'\,2}}}} \quad (0<\zeta<1) \qquad (18)$$

With Eq. (18), the softening compressive stress-strain curve of RuC under different biaxial

loading stress ratios (tension and compression) can be obtained (see. Fig. 6 - 6).
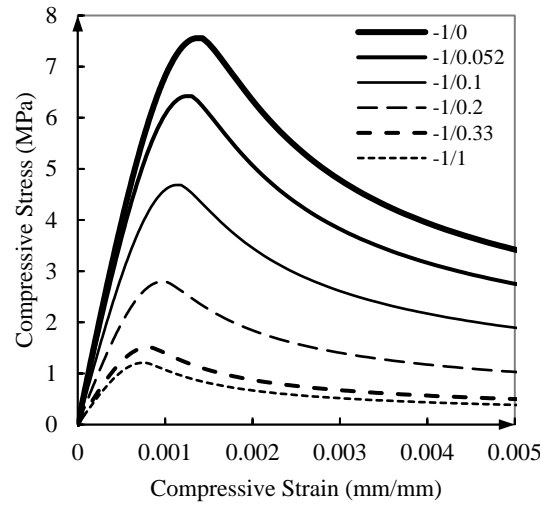
Fig. 6 - 6. Softening compressive stress-strain curve of RuC under different loading stress ratios.

6.3.1.3 CRuC

The model proposed by Lam and Teng [6] can also capture well the uniaxial compressive

behaviour of CRuC (see Fig. 6 - 4).

$$\sigma_c = E_c \varepsilon_c - \frac{\left(E_c - E_2\right)^2}{4\zeta f_{co}^{'}} \varepsilon_c^2 \quad \text{for } 0 \le \varepsilon_c \le \varepsilon_{tr} \qquad (19)$$

$$\sigma_c = \zeta f_{co}^{'} + E_2 \varepsilon_c \qquad \text{for } \varepsilon_{tr} \le \varepsilon_c \le \varepsilon_{cu} \qquad (20)$$

where σ_c and ε_c are the compressive stress and strain of CRuC, respectively, E_c is the elastic

modulus of RuC, ε_{tr} is the axial strain at the transition point, E_2 is the slope of the straight

second portion, and $f_{co}^{'}$ is the compressive strength of RuC. In order to capture the principal

compressive behaviour of CRuC under biaxial compression-tension, the model has been modified by introducing parameter ζ. The parameters ε_{tr} and E_2 are given by

$$\varepsilon_{tr} = \frac{2\zeta f_{co}^{'}}{\left(E_c - E_2\right)} \;;\; E_2 = \frac{f_{cc}^{'} - \zeta f_{co}^{'}}{\varepsilon_{cu}} \tag{21}$$

where ε_{cu} is the ultimate strain (Eq. (22)) and $f_{cc}^{'}$ is the compressive strength of CRuC (Eq. (23)), respectively.

$$\frac{\varepsilon_{cu}}{\zeta \varepsilon_{co}} = 1.75 + 12 k_{s2} \left(\frac{f_{l,a}}{\zeta f_{co}^{'}}\right)\left(\frac{\varepsilon_{h,rup}}{\zeta \varepsilon_{co}}\right)^{0.45} \tag{22}$$

$$\frac{f_{cc}^{'}}{\zeta f_{co}^{'}} = 1 + 3.3 k_{s1} \frac{f_{l,a}}{\zeta f_{co}^{'}} \tag{23}$$

where $\varepsilon_{h,rup}$ is the actual hoop rupture strain of FRP jacket, ε_{co} is the axial strain at compressive strength of RuC, $f_{l,a}$ is the actual maximum confining pressure, k_{s1} and k_{s2} are the shape factor for strength and strain enhancement, respectively, and defined as follows:

$$k_{s1} = \left(\frac{b}{h}\right)^2 \frac{A_e}{A_c} \;;\; k_{s2} = \left(\frac{b}{h}\right)^{0.5} \frac{A_e}{A_c} \tag{24}$$

where h and b are the depth and width of the rectangular section, respectively. A_e/A_c is the effective confinement area ratio (Eq. (26)).

6.3.1.4 FRP jacket

Substantial research [8-12] shows that FRP confinement can lead to an enhancement of the compressive strength and deformability of concrete. These enhancements rely mainly on: 1) the characteristics of FRP material; 2) section shape (circular or square); and 3) fibre orientation.

According to experimental results [6, 13, 14], FRP jackets rarely fail at the ultimate tensile strain obtained from direct tensile coupon tests. Hence, Lam and Teng [6] use the actual hoop rupture strain $\varepsilon_{h,rup}$ in their model, which relates to the ultimate tensile strain ε_{frp} through an

efficiency factor k_ε [13]. An average value of 0.586 for k_ε is recommended by Lam and Teng [6].

$$\varepsilon_{h,rup} = k_\varepsilon \varepsilon_f \tag{25}$$

It is commonly accepted that the concrete is uniformly confined in a circular section ($A_e = A_c$), while in a rectangular section, only part of the concrete is effectively confined by the FRP ($A_e < A_c$). The effective confinement area ratio (A_e/A_c) is given by Lam and Teng (2003):

$$\frac{A_e}{A_c} = \frac{1 - \left[\left(\frac{b}{h}\right)(h - 2R_c)^2 + \left(\frac{h}{b}\right)(h - 2R_c)^2\right]/3A_g - \rho_{sc}}{1 - \rho_{sc}} \tag{26}$$

where R_c is the size of round corner. ρ_{sc} refers to the ratio of vertical reinforcement, if implemented.

When FRP ruptures, the confining pressure reaches its maximum value given by

$$f_{l,a} = \frac{2E_f n_f t_f \varepsilon_{h,rup}}{D_{eq}} \tag{27}$$

where D_{eq} is the diameter of the equivalent circular section, which circumscribes the rectangular section. n_f and t_f are the number of layers and thickness of FRP jacket, respectively.

$$D_{eq} = \sqrt{h^2 + b^2} \tag{28}$$

When FRP with fibre oriented at an angle from the loading direction, the maximum confining pressure is modified as:

$$f_{l,a} = \frac{2E_f n_f t_f \varepsilon_{h,rup}}{D_{eq}} cos^2\theta_f \tag{29}$$

6.3.2 Tensile constitutive law

There are three main methods for determining the tensile characteristic of concrete experimentally: 1) direct tensile test; 2) Brazilian-split cylinder test; 3) three-point bending test. The direct tension test, theoretically, should yield the stress-strain relationship $(\sigma\text{-}\varepsilon)$ or stress-

crack width relationship $(\sigma\text{-}w)$ of concrete under pure uniaxial tension. However, this test is difficult to carry out, due to multiaxial stress at the boundary conditions, load eccentricity and uncertain crack location. The Brazilian-split cylinder test is the simplest method to obtain tensile strength, but it can provide neither the stress-strain nor the stress-displacement relation. However, this method was used by Bompa et al. [7] to predict the direct tensile strength of RuC (see Eq. (30)).

$$f_{ct} = 0.26 f_{co}^{'\ 2/3} \tag{30}$$

Cracking strain of RuC can be calculated as:

$$\varepsilon_{cr} = f_{ct} / E_c \tag{31}$$

The three-point bending test (see Fig. 6 - 7) is easier to perform and able to produce a stable load-deflection curve. Therefore, an inverse Finite Element Analysis (FEA) method is proposed to obtain the tensile stress-strain relation by taking advantage of data obtained from both Brazilian tests and three-point bending tests, as described below.

Fig. 6 - 7. Set-up overview of three-point bending test.

1. Calculation of fracture energy. The fracture energy of concrete G_F can be determined by energy U_s dissipated by fracturing in the specimens over the fracture surface area $(G_F = U_s / A_0)$. In the Crack Band theory [15], which used the "smeared crack" approach, assumes that cracks are distributed along a defined width of the fracture process zone. Bažant and Oh [15] assumed that the width (w_{cb}) of the fracture process

zone is equal to 3 times the nominal maximum aggregate size. The balance of energy

requires that the toughness $\left(W_s = \int_0^{\varepsilon_{ult}} \sigma(\varepsilon_{ct}) d\varepsilon_{ct}\right)$ can be calculated by dividing G_F by

w_{cb}.

$$W_s = \frac{G_F}{w_{cb}} \tag{32}$$

2. Calculation of ultimate tensile strain. The ultimate tensile strain of concrete can be

   determined by dividing the ultimate crack mouth opening by w_{cb}

$$\varepsilon_{ult} = \frac{w_{ult}}{2w_{cb}} \tag{33}$$

3. Determination of σ-ε curves. The general form of the tensile stress-strain model

   proposed by Guo [16] is adopted in this work as it has been known to simulate the

   tensile behaviour of concrete reasonably well.

$$y = \frac{x}{\phi(x-1)^{1.7} + x}(x > 1) \tag{34a}$$

where $x = \dfrac{\varepsilon_{ct}}{\varepsilon_{cr}}$, $y = \dfrac{\sigma_{ct}}{f_{ct}}$.

4. The damage variable d_t represents the portion of normalized energy dissipation for

   damage. The value of d_t is determined using Eq. (34b), where a value of 0 indicates no

   damage, while a value of 1 indicates that the material is fully damaged.

$$d_t = \int_0^{\varepsilon_{ct}} \sigma_{ct} d\varepsilon_{ct} / W_s \quad (0 \le d_t \le 1) \tag{34b}$$

Using fracture energy values determined from load-deflection curves from flexural tests on

RuC, the parameter "ϕ" was determined to be 0.036. The resulting σ-ε curve is shown in Fig. 6

- 8. The three-point bending tests have been modelled in Abaqus/Standard finite element

software package. The Concrete Damage Plasticity (CDP) model, utilizing the proposed tensile stress-strain curve of RuC and relative damage factor, was used to predict the load-deflection curve of the tested prisms. The load was applied experimentally via a steel roller in displacement control. In the numerical study, the steel roller was modelled as a rigid body and a displacement was applied to its reference point (see Fig. 6 - 9). A frictionless surface-to-surface interaction was assigned to the steel roller-concrete interface. The concrete was modelled using 2D 4-node linear plane stress (CPS4) elements with a mesh size of 5 mm within the fracture zone. Fig. 6 - 9 indicates the distribution of the tensile damage variable at failure (higher damage corresponds to red coloured area), whilst Fig. 6 - 10 shows a comparison between numerical and experimental results in terms of a typical load-displacement behaviour of RuC.
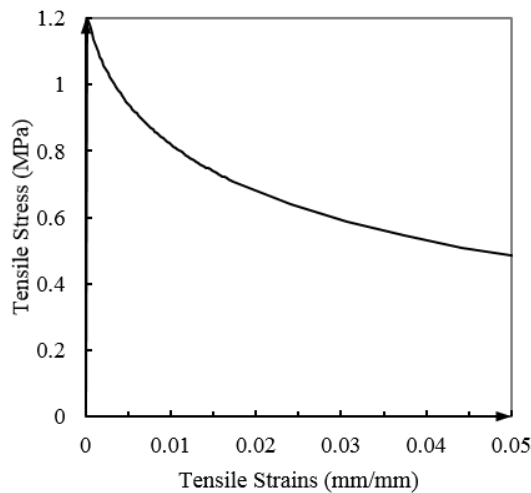
Fig. 6 - 8. Tensile stress-strain curve of RuC.
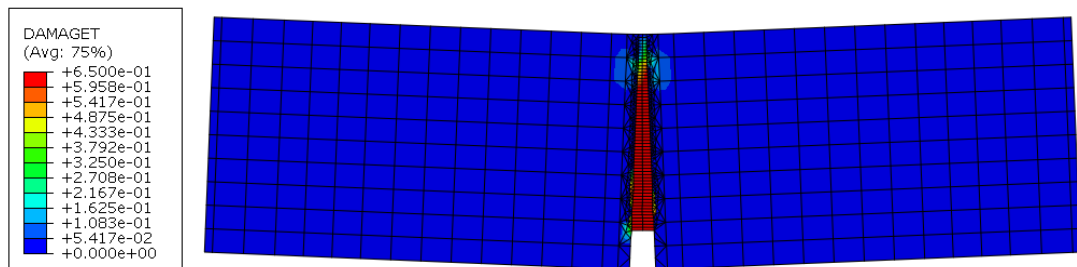
Fig. 6 - 9. The distribution of damage d_t at final state of the three-point bending tests. The red coloured area represents highly damage.
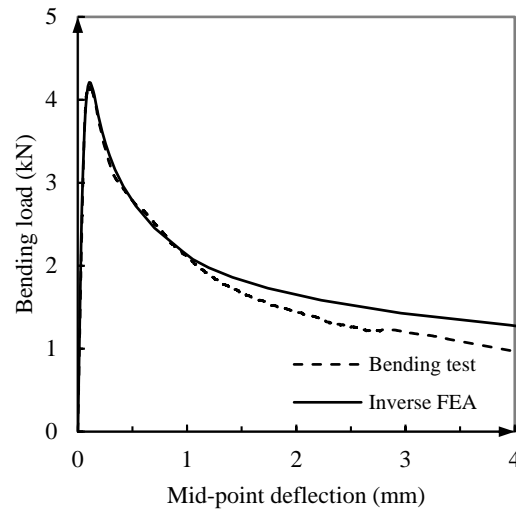
Fig. 6 - 10. Comparison of the load-deflection curves between inverse FEA and test ($\phi = 0.036$).

6.3.3 Shear constitutive law

Variables τ_{nm}^c and γ_{nm} (introduced in Eq. (2) through Eq. (7)) can be obtained from shear tests.

6.3.3.1 Shear stress τ_{nm}^c and shear strain γ_{nm} in RuC

By substituting Eq. (3) – Eq. (2) into Eq. (4) with pure shear state ($\sigma_l = 0, \sigma_t = 0$):

$$\tau_{nm}^c = \tau_{lt}\left(cos^2\theta_f - sin^2\theta_f\right) \tag{35}$$

By substituting Eq. (6) – Eq. (5) into Eq. (7) with pure shear state ($\varepsilon_l = 0, \varepsilon_t = 0$):

$$\gamma_{nm} = \gamma_{lt}\left(cos^2\theta_f - sin^2\theta_f\right) \tag{36}$$

$$G = \frac{\tau_{nm}^c}{\gamma_{nm}} = \frac{\tau_{lt}}{\gamma_{lt}} \tag{37}$$

As Eq. (37) does not include the angle θ_f, the shear modulus of smeared crack concrete should

be the same in any coordinate system. The shear stress-strain curve $\left(\tau_{lt}\text{-}\gamma_{lt}\right)$ can be obtained

from an asymmetric shear test as discussed in the next section.

6.3.3.2 Shear stress τ_{nm}^c and shear strain γ_{nm} in CRuC

The average concrete shear stress τ_{nm}^c can be obtained by writing the equilibrium condition along the *n*-direction of the triangular free body in Fig. 6 - 11 (Eq. (38)).

$$\tau_{nm}^c = \frac{1}{2}\rho_t f_t sin2\theta_f + \tau_{lt}cos2\theta_f \tag{38}$$
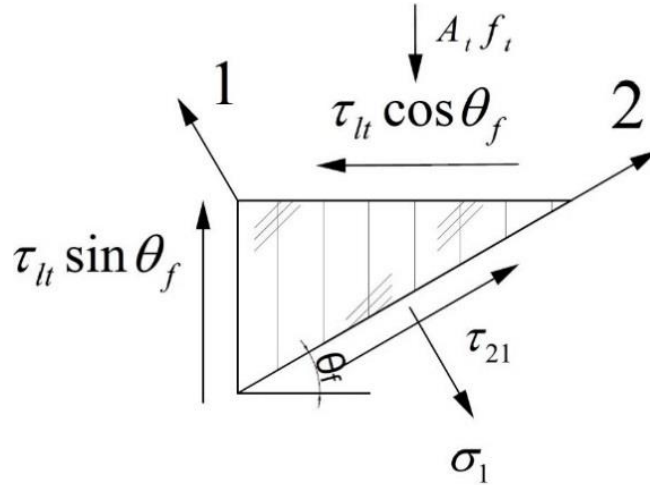
Fig. 6 - 11. Triangular free body.

The average shear strain γ_{nm} can be obtained from the compatibility relation and the measured four-average strain (ε_m, ε_n, ε_l and ε_t) along the m, n, l and t directions. This compatibility relation is derived by subtracting Eq. (6) from Eq. (5).

$$\gamma_{nm} = (\varepsilon_l - \varepsilon_t)csc2\theta_f + (\varepsilon_m - \varepsilon_n)cot2\theta_f \tag{39}$$

When $\theta_f = 45°$, Eq. (38) and Eq. (39) simplify to $\tau_{nm}^c = \frac{1}{2}\rho_t f_f$ and $\gamma_{nm} = -\varepsilon_t$, respectively. The shear modulus of CRuC beam is given by:

$$G = \frac{\tau_{nm}^c}{\gamma_{nm}} = \frac{\frac{1}{2}\rho_t E_f(-\varepsilon_t)}{-\varepsilon_t} = \frac{1}{2}\rho_t E_f \tag{40}$$

6.3.3.3 Asymmetric shear test

The τ_{lt}-γ_{lt} relation is obtained from the asymmetric shear test (see Fig. 6 - 12). The test was conducted on rectangular concrete prisms in which the central part (where the maximum shear forces are expected) was cast using RuC and had a reduced section of 70 mm, whereas the sides were cast with regular concrete and were reinforced with $\varnothing$ 6 mm steel bars (see Fig.5 - 12). The tests were carried out in an electromagnetic universal testing machine applying load monotonically in displacement control at a rate of 0.1 mm/min until failure. The measurement set-up is shown in Fig. 6 - 13. LVDTs and potentiometers (POT) were used to measure the deflections during the tests: LVDT 1 and 2 were situated on an aluminium yoke (fixed at the middle height of the prism) to measure the relative deflection at the mid-span of each side of the prism. Four potentiometers were used to measure absolute deflection. POT 1 measures the deflection at the free end of the prism. POT 2 and 4 measure the deformations at the supports. POT 3 measures the deflection at the mid-span externally. Two 10 mm 120 ohms strain gauges were placed at mid-span and oriented 45 degrees to the centreline of the prisms to measure the shear strains.
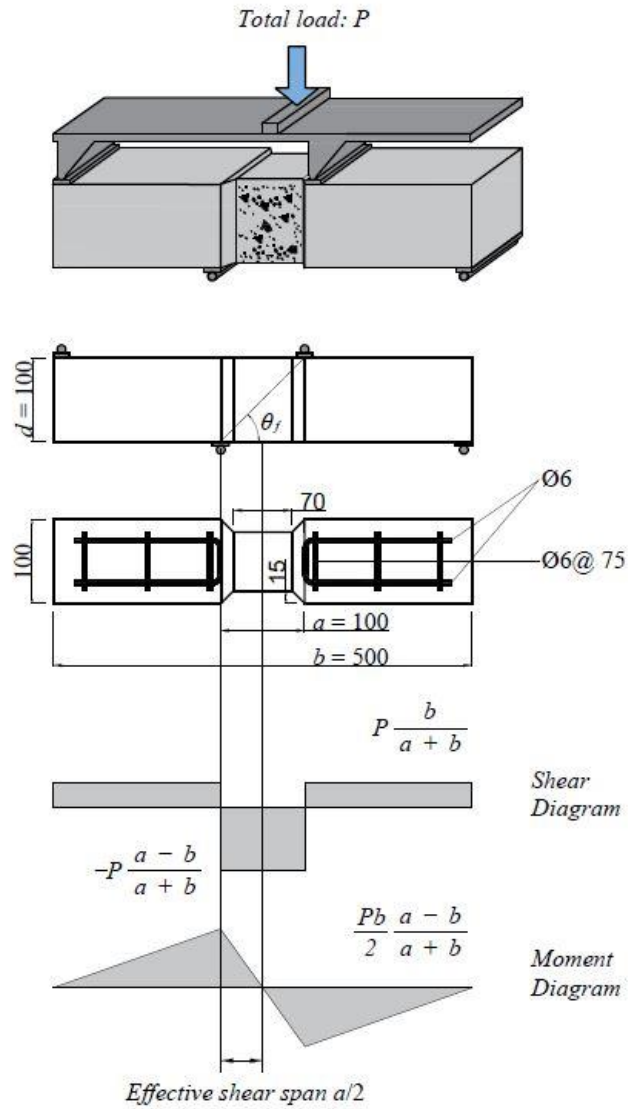
Fig. 6 - 12. Schematic of test set-up, angle of inclined strut, reinforcement details, and shear and bending moment diagrams (dimensions in mm).
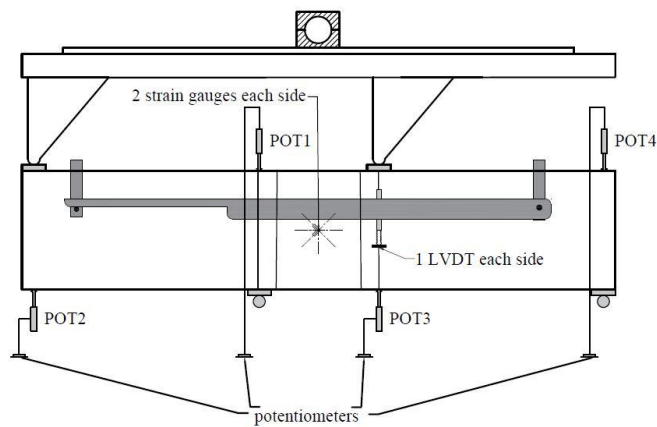
Fig. 6 - 13. Set-up overview of asymmetric shear test.

Using data from tests undertaken in this study (Fig. 6 - 14), Eq. (41) is suggested for predicting the shear strength of RuC with 60% rubber replacement as a function of the compressive strength. Eq. (41) has an average test-to-prediction strength ratio of 1.02 and COV of 4.3%

$$\tau_p = 0.36 f_{co}^{'\,0.57} \tag{41}$$

The relation between the value of shear strain γ_p at peak and shear strength τ_p (N/mm^2) of RuC with 60% rubber replacement can be represented by a regression equation (Eq. 42). Eq. (42) has an average test-to-prediction ratio of 1.08 and COV of 16.5%.

$$\gamma_p = \varepsilon_{1p} - \varepsilon_{2p} = \left(2160\tau_p - 766.6\right) \times 10^{-6} \,(\tau_p \text{ in MPa}) \tag{42}$$

The initial shear modulus of RuC is determined from the secant modulus at $0.3\,\tau_p$. The average value obtained is 2.687 GPa with a standard deviation at 0.25 GPa. The ratio between initial modulus G_0 and secant modulus at peak stress $\left(G_p = \tau_p / \gamma_p\right)$ varies from 2.3 to 2.7 and an average value of 2.51 is adopted (standard deviation is 0.064).
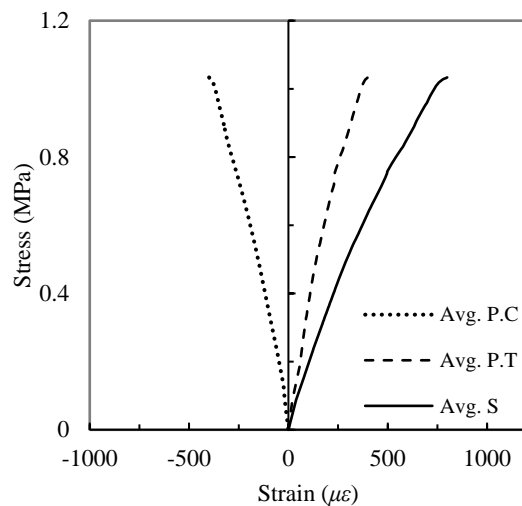
Fig. 6 - 14. The average principal compressive/tensile and shear strain versus corresponding stress (PC is the principal compressive strain, PT is the principal tensile strain and S is the shear strain).

6.3.3.4 Complete shear stress-strain curve

The complete stress-strain curve of RuC in shear comprises of two parts, as shown in Fig. 6 - 15a and Fig. 6 - 15b, representing the ascending and descending branches, respectively.

6.3.3.5 Ascending branch

Using the known boundary conditions, the ascending branch can be represented by a cubic equation of Eq. (43). The four boundary conditions are: 1) $x = 0, y = 0$; 2) $x = 0, \dfrac{dy}{dx} = \dfrac{G_0}{G_p}$; 3)

$x = 1, y = 1$; and 4) $x = 1, \dfrac{dy}{dx} = 0$ (where $x = \dfrac{\gamma}{\gamma_p}$, $y = \dfrac{\tau}{\tau_p}$).

$$\frac{\tau}{\tau_p} = 2.5 \times \frac{\gamma}{\gamma_p} - 2 \times (\frac{\gamma}{\gamma_p})^2 + 0.5 \times (\frac{\gamma}{\gamma_p})^3 \tag{43}$$

The comparative assessment between predicted and experimental constitutive response (see Fig. 6 - 15a) shows good agreement. The tangent shear modulus can also be determined from Eq. (44):

$$G_t = \frac{d\tau}{d\gamma} = \frac{\tau_p}{\gamma_p} \left[2.5 - 4 \times \frac{\gamma}{\gamma_p} + 1.5 \times \left(\frac{\gamma}{\gamma_p} \right)^2 \right] \tag{44}$$
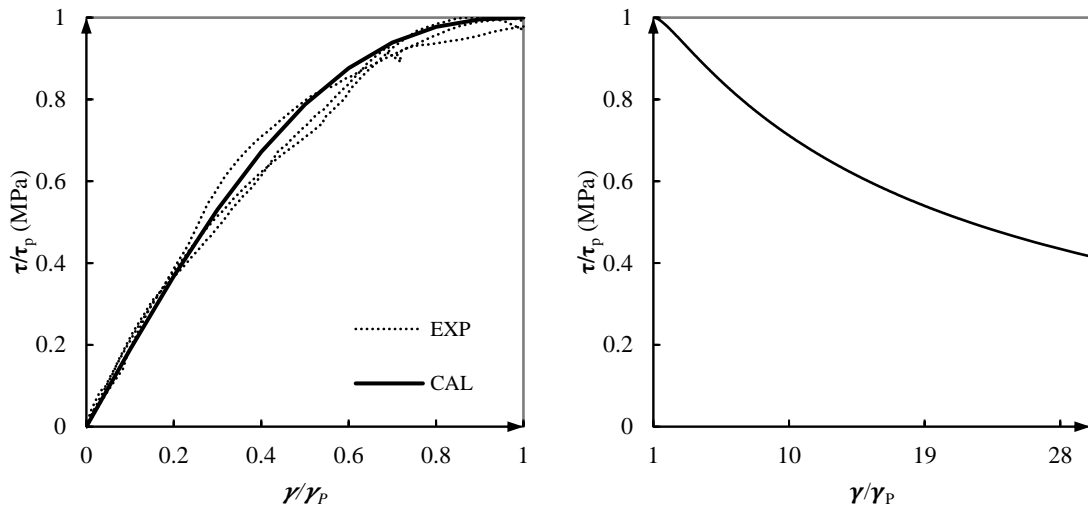
Fig. 6 - 15. Normalized shear stress-strain behaviour obtained from (a) axisymmetric shear test up to peak and (b) inverse FEA after peak.

6.3.3.6 Descending branch

An equation similar to that for concrete in tension is adopted,

$$y = \frac{x}{\eta(x-1)^{1.7} + x} \ (x > 1)$$

This equation again satisfies the four known boundary conditions: 1) $x = 1, y = 1$; 2) $x = 1, \dfrac{dy}{dx} = 0$; 3) $x \to \infty, y \to 0$; and 4) $x \to \infty, \dfrac{dy}{dx} \to 0$. Since strain gauges normally fail at or before peak load, the parameter η was determined to be 0.05 based on the numerical investigations in the present study (Fig. 6 - 16),

$$y = \frac{x}{0.05(x-1)^{1.7} + x} \quad (x > 1) \tag{45}$$
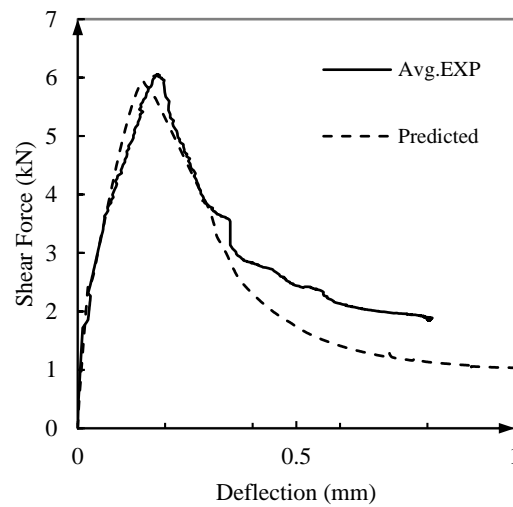
Fig. 6 - 16. Comparison of the load-deflection curves between inverse FEA and test ($\varphi = 0.05$).

6.4   NUMERICAL IMPLEMENTATION

The proposed shear behaviour model of CRuC and RuC has been implemented in Abaqus/Standard finite element software package using the user defined material subroutine (UMAT). The numerical integration algorithms update the Cauchy nominal stresses and solution dependent state variables, as well as the consistent tangent matrix, which ensures quadratic convergence rate of the Newton-Raphson method in the FEA. The solution scheme is based on the incremental form of strain. The loading history is discretized into a sequence of load steps $[F_i, F_{i+1}]$, $i \in 0,1,2,3 \dots n$. Each step is referred to as load increment. Driven by the strain increment $\Delta \varepsilon$, the discrete problem in the context of back Euler scheme can be stated as:

for a given variable set $\{\varepsilon_n, \sigma_n\}$ at the beginning of the (n+1)th increment, find the updated

variable set $\{\varepsilon_{n+1}, \sigma_{n+1}\}$ at the end of the (n+1)th increment. The updated stresses and solution-

dependent state variables are sorted at the end of the (n+1)th increment and are passed on to the

UMAT at the beginning of the next increment. The interactive procedure is summarized as in

Appendix.

6.5   EXPERIMENTAL PROGRAM

Eighteen prismatic samples (500 $\times$ 100 $\times$ 100 mm) were tested to assess the shear performance

of CRuC and RuC. Fig. 6 - 17 shows the geometry and reinforcement details of the prisms as

well as the loading and support conditions. The central parts of prisms were cast with RuC (with

a rubber content replacing 60% of aggregate by volume), whereas the sides were cast with

regular concrete. The prisms were reinforced with four basalt FRP bars ($\varnothing$ 4 mm) along the

length of the prism. Basalt-FRP bars were chosen for their low shear and axial stiffness, so as to

enable the development of expected higher deformations within shear span. Three different

shear span-to-depth ratios (*a/d* = 0.5, 0.75 and 1) were considered. For each ratio, tests were

conducted on three unconfined samples and three additional specimens confined with one layer

of Carbon-FRP by using a wet lay-up technique. The overlap length is 90 mm and located on

the top of the prism. Table 6 - 1 shows the material properties of the Basalt-FRP bars and

Carbon fabric used in this research as obtained from direct tensile coupon tests. The adopted test

setup was the same as described in Fig. 6 - 13 and used to obtain the shear stress-strain curve.
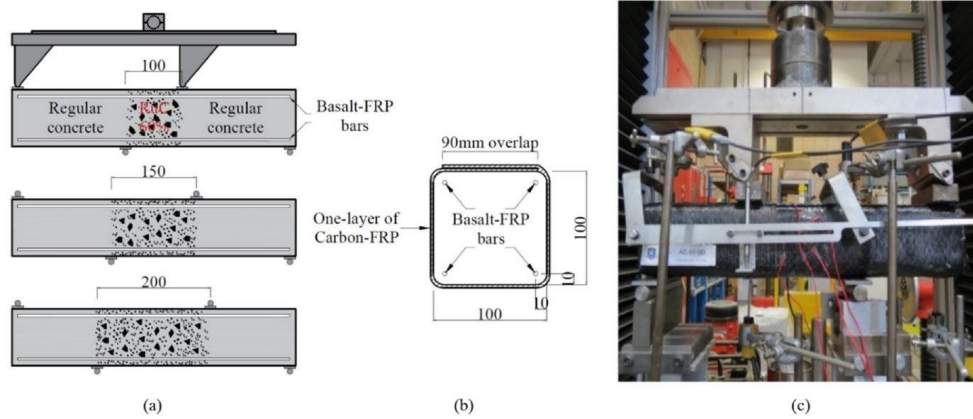
Fig. 6 - 17. Configuration of specimens (a), reinforcement detail (b) and experimental set-up overview (c) (dimensions in mm).

Fig. 6 - 18 and 19 show the average experimental shear stress-strain and shear force-deflection plots for various *a/d* ratios of RuC and CRuC, respectively. The shear stress τ was determined by normalizing the shear force with respect to the cross-sectional area at mid-span. The shear strain γ was measured by two strain gauges boned on the surface of the beam or the CFRP jacket and oriented ± 45 degrees to the centre line of the prisms. Due to the pure shear stress state at mid-span, it is assumed that the directions of ± 45 degrees are the principal directions of strain. Therefore, the shear strain can be determined by the two strain gauge readings, $\gamma = \varepsilon_{1p} - \varepsilon_{2p}$. The deflection was the average reading of LVDT 1 and 2 (see Fig. 6 - 13). The grey shaded area of the curve in Fig. 6 - 19 represents the range of experimental results. This variability can be attributed to the manufacturing quality of the FRP jackets and the inherent variability of concrete.
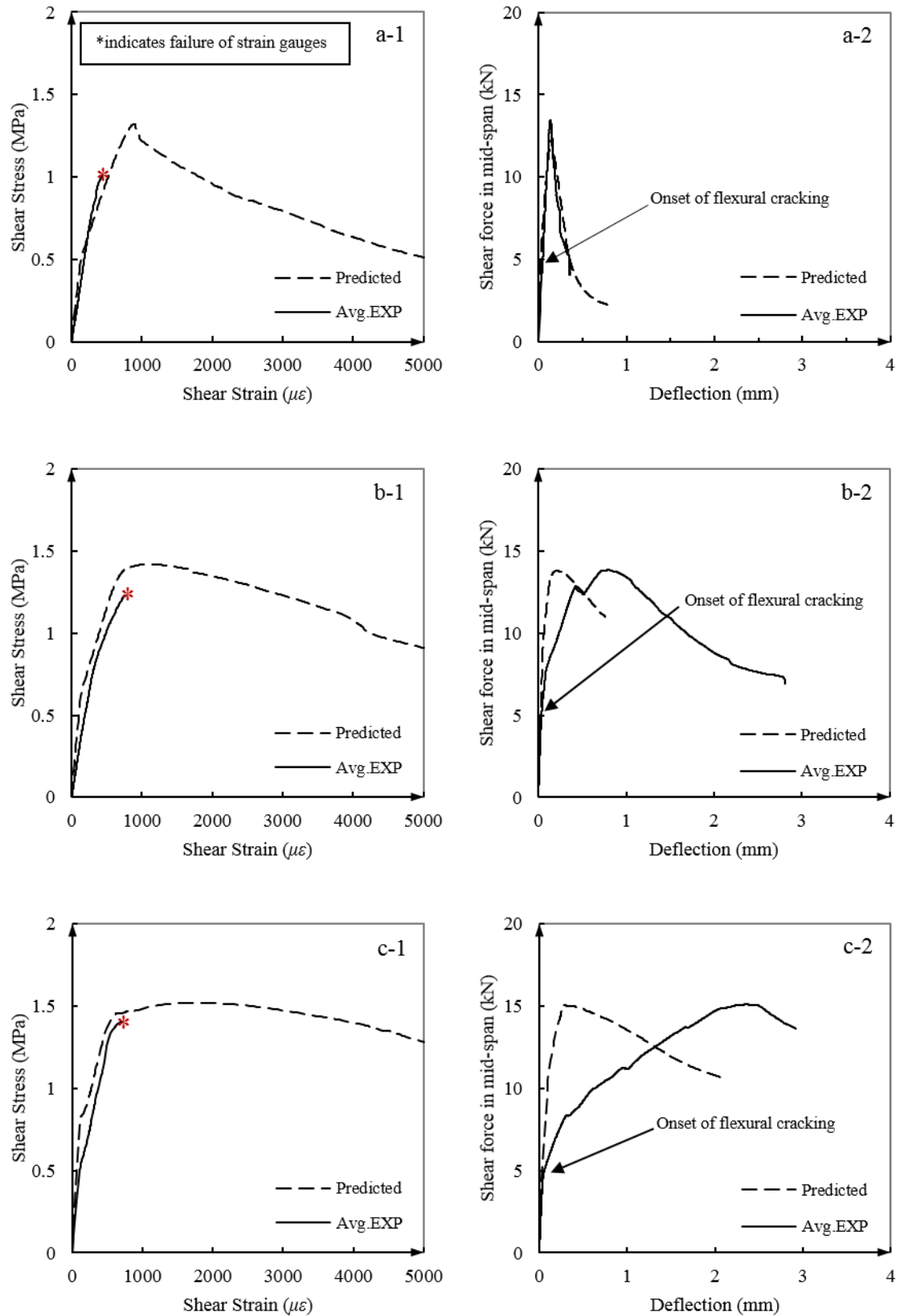
Fig. 6 - 18. Comparisons between numerical and experimental shear stress-strain curves (left) and load-deflection curves (right) of RuC specimens ((a) a/d =0.5; (b) a/d =0.75; (c) a/d =1).
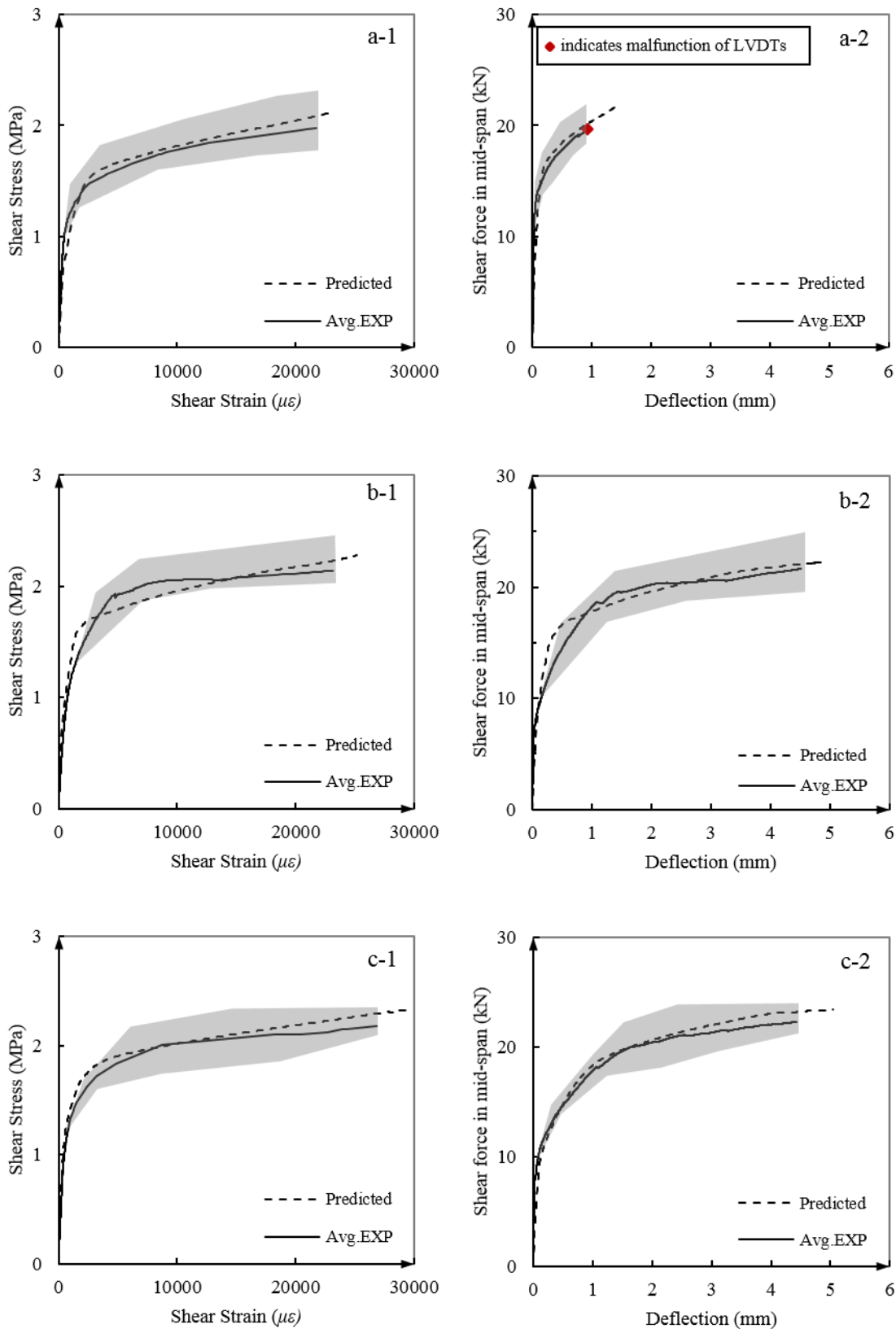
Fig. 6 - 19. Comparisons between numerical and experimental shear stress-strain curves (left) and load-deflection curves (right) of CRuC specimens ((a) a/d =0.5; (b) a/d =0.75; (c) a/d =1).

By comparing the results shown in Fig. 6 - 18 and 19, it can be seen that both stress and strain at failure for confined specimens are higher than for unconfined specimens, clearly indicating that CFRP confinement enhances the load-carrying capacity and deformability. The hardening behaviour of CRuC can be explained by the fact that the confinement pressure provided by the CFRP jacket maintains the integrity of the concrete and enhances its ability to carry load. Although the load-deflection curves of unconfined specimens are heavily influenced by their *a/d* ratio (i.e. increasing *a/d* increases the moment in the flexural region), the *a/d* ratio does not have a significant influence on the shear stress-strain curves. The shear deformation of confined specimens increases with increasing *a/d* ratio and results in both higher ultimate shear strain and deflection. Table 6 - 2 summarizes the average experimental data for both RuC and CRuC. In comparison to RuC, $G_{0,CRuC}$ is similar to $G_{0,RuC}$ (without considering the abnormal value $G_{0,RuC} = 4407$ in the case of *a/d*=1.0). An estimated value 1200 $\mu\varepsilon$ for the peak shear strain of RuC (γ_p) was obtained from numerical analysis as the strain gauges crossing the shear cracks failed prematurely and no experimental results were available. The ultimate shear strain of CRuC (γ_{cu}) is enhanced by more than 20 times compared to γ_p, whilst the ultimate shear stress of CRuC (τ_{cc}) is increased by 35%. This enhancement enables the CRuC specimens to dissipate about 12 times more energy than their respective RuC specimens (see Fig. 6 - 20). Since a complete stress-strain relationship could not be obtained, Γ_{RuC} is calculated by integrating Eq. (43) and (45), and is found to be 0.006 N/mm^3.

Table 6 - 2. Comparison between numerical and average experimental result of parameters used in Fig. 6 - 21.

		$G_{0,RuC}$	$G_{0,CRuC}$	G_2	$\tau_{cr,RuC}$	$\tau_{cr,CRuC}$	τ_p	τ_t	τ_{cc}	$\gamma_{cr,RuC}$	$\gamma_{cr,CRuC}$	γ_t	γ_{cu}	Γ_{CRuC}
		N/mm^2					MPa					$\mu\varepsilon$		N/mm^2
a/d=0.5	Avg.Exp	2782	2873	22	0.7	0.5	1.4	1.75	2	247	174	9086	21751	0.058
	Numerical	3547	2600	28	0.5	0.65	1.3	1.56	2.1	129	250	6212	22808	0.067
a/d=0.75	Avg.Exp	2492	2100	21	0.8	0.7	1.3	1.82	2.1	305	330	6968	23163	0.069
	Numerical	4703	2458	24	0.6	0.74	1.4	1.79	2.2	129	301	5317	25057	0.072
a/d=1.0	Avg.Exp	4407	2216	16	0.5	0.86	1.4	1.94	2.2	118	388	8773	26689	0.082
	Numerical	5833	2693	17	0.8	0.94	1.5	1.88	2.3	132	349	4332	29453	0.095

The shear stress-strain responses of RuC and CRuC are characterized by three phases: I) an elastic phase up to the cracking shear stress (τ_{cr}). τ_{cr} defines the shear stress at which onset of microcracking occurs; II) a hardening response up to the maximum shear capacity of RuC (τ_p) or the transition point of CRuC (τ_t); and III) this phase is a function of confinement level and that is characterized by a softening branch for RuC and a linear hardening branch for CRuC up to failure. In Phase I, the initial slope of CRuC is the same as the initial shear modulus of RuC. The responses of RuC and CRuC in Phase II and III are affected by the presence of an FRP jacket. The linear hardening behaviour of CRuC can be explained by the fact that the confinement pressure provided by the CFRP jacket maintains the integrity of the concrete and enhances its ability to carry load. The slope (G_2) of this hardening portion is affected by the number of layers or type of FRP jacket. Based on this experimental observation, the assumptions proposed by Lam and Teng (2003b) for the behaviour of FRP-confined concrete under compression are used for shear response of CRuC, that is, the τ-γ model consists of a parabolic first portion and a straight line second portion (see Fig. 6 - 21). The parabolic first portion intersects the linear second portion smoothly.
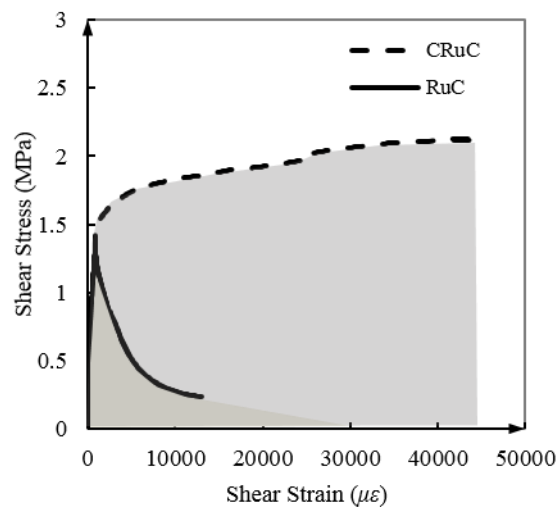
Fig. 6 - 20. Comparison of energy dissipation between RuC and CRuC.
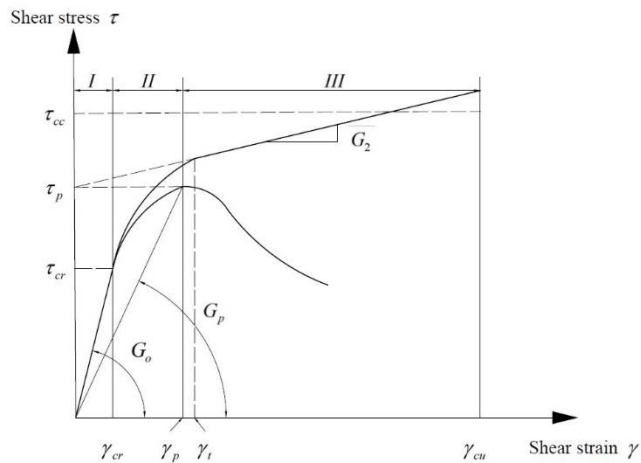
Fig. 6 - 21. Shear stress (τ)-strain (γ) model for RuC and CRuC.

6.6   VERIFICATION OF THE MATERIAL MODEL

The finite element mesh used to perform the simulation of the beams failing in shear is illustrated in Fig. 6 - 22. In the experiment, the load was applied via a loading beam in displacement control and was transferred to the specimen by two steel rollers (see Fig .5 - 17b). In the numerical study, a displacement was applied at a reference point, which was coupled with two nodal points on the beam (see Fig. 6 - 22). Four-node quadrilateral elements were used to model the concrete, while two-node truss elements were used to model the basalt bars. The perfect bond between the concrete and the basalt bars was assumed. The total mesh consists of 130 plane stress quadrilateral elements for concrete, 25 linear truss elements for basalt bars.
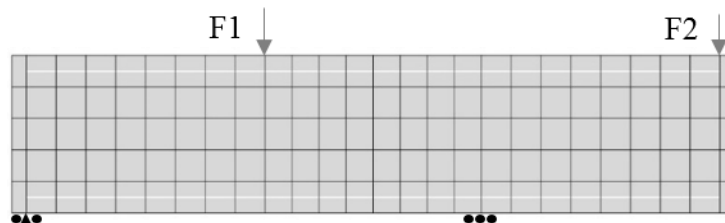
Fig. 6 - 22. Finite element mesh used in the numerical modelling of asymmetric shear test.

Fig. 6 - 18 and Fig. 6 - 19 compare the curves predicted by the proposed model and the average experimental shear stress-strain and load-deflection curves for RuC and CRuC, respectively. For

the case of RuC, the comparative assessment indicates that numerical modelling predicts reasonably well the ascending branch of the stress-strain curves. However, the initial stiffnesses of predicted curves are generally higher than that observed experimentally. Furthermore, the numerical model fails to predict the load-deflection behaviour of the specimens (*a/d* =0.75 and 1.0) beyond the load causing extensive flexural cracking (see Fig. 6 - 18), due to the low amount of flexural reinforcement provided. For the case of CRuC, the comparative assessment between predicted and average experimental curves shows well agreement.

Table 6 - 2 compares the critical material parameters, which are obtained from experimental data and numerical modelling. For the case of RuC, the numerical values of initial shear modulus ($G_{0,RuC}$) are higher than the experimental ones, while cracking shear stress and shear strength ($\tau_{cr,RuC}$ and τ_p) are similar to the experimental observations. For the case of CRuC, the predicted $G_{0,CRuC}$ and G_2 agrees well with the experimental values. The tendency of G_2 to decrease with increasing *a/d* is also demonstrated. The cracking shear stress $\tau_{cr,CRuC}$ is higher than $\tau_{cr,RuC}$ because the FRP helps may control cracking in the concrete. The transition between nonlinear and linear behaviour (τ_t, γ_t) in the numerical model occurs earlier than that in the experiment. This may be attributed to the fact that no gap between the jacket and concrete is allowed in the numerical model, thus the jacket is mobilized earlier. The numerical ultimate stress/strain values (τ_{cc} and γ_{cu}) are higher than the corresponding experimental values. This may be attributed to the fact that the effectiveness of FRP in confining concrete subjected to a combination of moment and shear is substantially different from the case of concrete under compression only. Hence, this aspect requires further investigation.

6.7   CONCLUSIONS

This paper presents the development and implementation of constitutive material models for RuC and CRuC into nonlinear FEA using a smeared, fixed crack approach. The material

constitutive laws were determined by combining the experimental methods (uniaxial compression test, three-point bending test and asymmetric four-point bend test) with inverse FEA. The experimental work used to calibrate and validate the model is also discussed in detail. On the basis of the results presented here, the following conclusions can be drawn:

- CRuC made with high rubber volumes (60% of aggregate replacement) and confined with one layer of carbon fibres shows ductile and stable performance that allows the development of high shear deformations (up to 40 times of RuC) at shear strength values are up to two times higher than for RuC. This innovative concrete can be used to develop highly deformable RC components for structures.

- By modifying the FA-STM, a new material model was developed, which can be used to provide a reasonable characterization of the shear behaviour of RuC and CRuC. The abilities of the model to portray the load-displacement relation and the shear stress-strain relation are verified.

- The model can be used to examine the shear performance of highly deformable CRuC elements, such as bridge bearings, shear wall coupling beams or base isolation columns.

6.8 APPENDIX

Step 1: Provide material properties of concrete ($f_{co}^{'}$) and FRP (E_f , n_f , t_f and $\varepsilon_{h,rup}$).

Eqs. (12)(29)(30)(31)(41)(42) are used to solve 7 unknown material properties: elastic modulus, E_c , crushing strain, ε_{co} , FRP-confinement pressure, $f_{l,a}$, tensile strength, f_{ct} , cracking strain, ε_{cr} , shear strength, τ_p , and corresponding shear strain, γ_p .

Step 2: Extract strain and strain increment in current load step.

$$\varepsilon_n = \varepsilon_{n\text{-}1} + \Delta\varepsilon$$

Step 3: Transform the strain $[\varepsilon_x, \varepsilon_y, \gamma_{xy}]^T$ to the strain $[\varepsilon_1, \varepsilon_2, \gamma_{12}]^T$ on the crack plane.

$$\begin{Bmatrix} \varepsilon_1 \\ \varepsilon_2 \\ \gamma_{12} \end{Bmatrix} = \begin{bmatrix} c^2 & s^2 & 2cs \\ s^2 & c^2 & -2cs \\ -cs & cs & c^2 - s^2 \end{bmatrix} \begin{Bmatrix} \varepsilon_x \\ \varepsilon_y \\ \gamma_{xy} \end{Bmatrix}$$

where $c = \cos\varphi, s = \sin\varphi$ and $\varphi = 180° - \theta_f$.

Step 4: Select stress state from seven cases.

Case	Stress states
Uncracked tension - Uncracked tension	$\varepsilon_1 < \varepsilon_{cr}, \varepsilon_2 < \varepsilon_{cr}$
Uncracked tension - Uncrushed compression	$\varepsilon_1 < \varepsilon_{cr}, \varepsilon_{cu} < \varepsilon_2 < 0$
Uncrushed compression - Uncrushed compression	$\varepsilon_{co} < \varepsilon_1 < 0, \varepsilon_{cu} < \varepsilon_2 < 0$
Cracked tension - Cracked tension	$\varepsilon_1 \geq \varepsilon_{cr}, \varepsilon_2 \geq \varepsilon_{cr}$
Cracked tension - Uncracked tension	$\varepsilon_1 \geq \varepsilon_{cr}, \varepsilon_2 < \varepsilon_{cr}$
Cracked tension - Uncrushed compression	$\varepsilon_1 \geq \varepsilon_{cr}, \varepsilon_{cu} < \varepsilon_2 < 0$
Crushed compression - Crushed compression	$\varepsilon_1 < \varepsilon_{co}, \varepsilon_2 < \varepsilon_{cu}$

The components of tangential stiffness matrix can be determined by corresponding constitutive

laws (Eqs. (9)(11)(18)(19)(20)(34)(40)(44)(45)).

$$\begin{Bmatrix} \sigma_1 \\ \sigma_2 \\ \tau_{12} \end{Bmatrix} = \begin{bmatrix} E_1 & \mu E_1 & 0 \\ \mu E_2 & E_2 & 0 \\ 0 & 0 & G_{12} \end{bmatrix} \begin{Bmatrix} \varepsilon_1 \\ \varepsilon_2 \\ \gamma_{12} \end{Bmatrix}$$

Step 5: Transfer the stiffness matrix in *1-2* coordinate back to *x-y* coordinate.

$$\left[E_{xy}^c \right] = \left[T^{-1} \right]\left[E_{12} \right]\left[T \right]$$

$$[T] = \begin{bmatrix} cos^2\theta & sin^2\theta & cos\theta sin\theta \\ sin^2\theta & cos^2\theta & -cos\theta sin\theta \\ -2cos\theta sin\theta & 2cos\theta sin\theta & cos^2\theta - sin^2\theta \end{bmatrix}$$

Step 6: Determine the Jacobian for FRP-confined concrete in *x,y* direction

$$\left[E_{xy} \right] = \left[E_{xy}^c \right] + \left[E_{yy}^{frp} \right] = \begin{bmatrix} E_{xx}^c & E_{xy}^c & E_{x\gamma}^c \\ E_{yx}^c & E_{yy}^c + E_{yy}^{frp} & E_{y\gamma}^c \\ E_{\tau x}^c & E_{\tau y}^c & E_{\tau\gamma}^c \end{bmatrix}$$

Step 7: Update stress and strain.

$$\sigma_{i+1} = \sigma_i + E_{xy}d\varepsilon_i$$

Step 8: Check the convergence at the current load step. If it is satisfied, go to the next load step. Otherwise, go to step 2. If loading completed or the limit state criteria are reached, stop the computation.

6.9   ACKNOWLEDGEMENTS

6.10 REFERENCES

1.   Pang, X.-B. and T.T. Hsu, *Fixed angle softened truss model for reinforced concrete.* ACI Structural Journal, 1996. **93**(2): p. 197-207.
2.   Kani, G.N., *On shear in reinforced concrete*. 1979: Department of Civil Engineering, University of Toronto.
3.   Collins, M.P., *Torque-twist characteristics of reinforced concrete beams.* Inelasticity and non-linearity in structural concrete, 1973: p. 211-231.
4.   Birrcher, D., et al., *Strength and serviceability design of reinforced concrete deep beams.* 2009.
5.   Committee, A., A.C. Institute, and I.O.f. Standardization. *Building code requirements for structural concrete (ACI 318-08) and commentary.* 2008. American Concrete Institute.
6.   Lam, L. and J. Teng, *Design-oriented stress–strain model for FRP-confined concrete.* Construction and Building Materials, 2003. **17**(6): p. 471-489.
7.   Bompa, D., et al., *Experimental assessment and constitutive modelling of rubberised concrete materials.* Construction and Building Materials, 2017. **137**: p. 246-260.
8.   Teng, J., et al., *Refinement of a design-oriented stress–strain model for FRP-confined concrete.* Journal of Composites for Construction, 2009. **13**(4): p. 269-278.
9.   Saadatmanesh, H., M.R. Ehsani, and M.-W. Li, *Strength and ductility of concrete columns externally reinforced with fiber composite straps.* Structural Journal, 1994. **91**(4): p. 434-447.
10.   Raffoul, S., et al., *Behaviour of unconfined and FRP-confined rubberised concrete in axial compression.* Construction and Building Materials, 2017. **147**: p. 388-397.
11.   Ozbakkaloglu, T. and E. Akin, *Behavior of FRP-confined normal-and high-strength concrete under cyclic axial compression.* Journal of Composites for Construction, 2011. **16**(4): p. 451-463.
12.   Lam, L., et al., *FRP-confined concrete under axial cyclic compression.* Cement and Concrete Composites, 2006. **28**(10): p. 949-958.
13.   Pessiki, S., et al., *Axial behavior of reinforced concrete columns confined with FRP jackets.* Journal of Composites for Construction, 2001. **5**(4): p. 237-245.
14.   Li, G., et al., *Effect of fiber orientation on the structural behavior of FRP wrapped concrete cylinders.* Composite structures, 2006. **74**(4): p. 475-483.
15.   Bažant, Z.P. and B.H. Oh, *Crack band theory for fracture of concrete.* Matériaux et construction, 1983. **16**(3): p. 155-177.
16.   Guo, Z., *Principles of reinforced concrete*. 2014: Butterworth-Heinemann.

Chapter 7

Summary, conclusions and recommendations for future research

7.1   SUMMARY AND CONCLUSIONS

The aim of this research was to understand the behaviour of FRP-confined and unconfined RuC and to develop stress-strain models that can be used for finite element modelling of CRuC in structural applications. This aim was achieved through extensive experimental and numerical work on the behaviour of RuC externally confined with FRP under various loading conditions.

This chapter summarises the main conclusions from this thesis and recommends future research in the field. All of the research objectives set out in Chapter 1 were achieved.

7.1.1   Tensile behaviour of RuC

The tensile behaviour of RuC was examined by three-point bending tests and splitting tests to develop an understanding of the effect of rubber contents on the flexural behaviour of concrete. The following conclusions are drawn:

➢ Replacing mineral aggregates with rubber particles leads to an apparent reduction in strength (compressive, tensile and flexural) and elastic modulus. A less severe reduction is observed in the tensile and flexural compared to the compressive properties.

➢ Replacing mineral aggregates with rubber particles enhances the fracture energy and energy absorption capacity and leads to a more ductile post-cracking behaviour.

➢ A tensile stress-crack opening relation for rubberised concrete is proposed, which can provide significantly more accurate predictions compared to the *σ-w* model derived using the Model Code 2010 in terms of the peak load, energy absorption capacity and load-deflection response over the loading range.

7.1.2   Compressive behaviour of CRuC and RuC

128 circular and square columns were tested under axial compression to investigate their stress-strain response.

Experimental conclusions:

> ➤ Replacing mineral aggregates with high volume rubber aggregates can significantly reduce concrete strength, whilst dramatically enhance deformability. By utilising the advantages of rubber inclusions, a large amount of strength can be recovered if FRP-confinement provided as well as improving the effectiveness of FRP confinement. As a result, CRuC specimens exhibit significantly higher deformability (ultimate axial strains up to 5.7%) and absorb more energy than CRC.

> ➤ CRuC exhibits volumetric contraction throughout the loading history, while CRC shows volumetric expansion. This is due to the flowable behaviour of rubber, and it can fill up the crack or voids in CRuC.

> ➤ The effect of the corner geometry on the effectiveness of confinement in CRuC is much less severe than in CRC due to the enhanced lateral strain. For the same FRP confinement level, the AFRP CRuC square sections show higher deformability (up to 19%) than the circular sections with an acceptable sacrifice in strength (less than 20%). This may imply the CRuC square column is preferable than the circular column,in where high deformation is needed.

> ➤ The secant dilation ratio of CRuC stabilises at around 0.4. This makes this material suitable for the development of high-strength highly-deformability elements under shear.

Modelling conclusions:

> ➤ The simple division of non-circular sections into two areas of confined and unconfined sections cannot reflect the actual stress distribution and leads to inaccurate results. Therefore, a new understanding of effective confinement area is proposed based on a more rational mechanism.

> ➤ The CDPM and existing stress-strain models for CRC are unable to predict the behaviour of FRP-confined rubberised concrete owing to the CRuC elements have completely different volumetric behaviour as that of CRC.

➢ A new σ-ε model is developed for CRC and CRuC, as well as circular and non-circular sections. It provides more accurate prediction as the model includes the microstructure properties of concrete through a series of relations established from experimental data and essential stress-strain response.

7.1.3 Shear Behaviour of CRuC and RuC

The axisymmetric four-point bending test was adopted to examine the shear performance of FRP-confined and unconfined RuC.

➢ The shear strength of RuC is close to its direct tensile strength.

➢ Replacing mineral aggregates with rubber particles can make shear failures of more ductile.

➢ CRuC made with high rubber volumes (60% of aggregate replacement) and confined with one layer of carbon fibres shows ductile and stable performance that allows the development of high shear deformations (up to 40 times of RuC) at shear strength values are up to two times higher than for RuC. This confirms that this innovative concrete can be used to develop highly deformable RC components for structures.

➢ By modifying the FA-STM, a new material model is developed for the characterisation of the shear behaviour of RuC and CRuC. The abilities of the model to portray the load-displacement relation and the shear stress-strain relation are verified.

7.2 RECOMMENDATIONS FOR FUTURE RESEARCH

This section presents recommendations for future research related to this study.

7.2.1 Tension

➢ The proposed model needs to be evaluated for other rubber contents. Due to time limits, only two rubber contents were examined and a limited number of specimens were tested. Additional experiments are necessary to cover a wide range of rubber contents.

- ➢ The relationship between the crack band width and rubber contents need to be further investigated.

- ➢ Errors caused by assuming a linear distributed crack can be reduced by adopting a nonlinear assumption.

- ➢ Despite spurious mesh sensitivity being eliminated by a simple mesh related modification of the material properties, local deformation is not reliably simulated. This defect could be addressed by utilising more advanced methods, such as non-local damage theory and the nonlinear strain-gradient softening and localization. Size effects also need to be taken into account.

7.2.2 Compression

- ➢ Due to time limits, only one rubber content and a single corner radius were examined. The knowledge in the behaviour of FRP-confined rubberised concrete in non-circular sections with various rubber contents, corner radius and cross-section aspect ratios is still limited or blank. More tests are needed to fill this gap.

- ➢ Due to the limited database, the performance of the proposed model has not been fully assessed. Future research should evaluate the applicability of the proposed model to other rubber contents and various cross-section shapes.

- ➢ There is little or no knowledge in the behaviour of rubberised concrete under biaxial or triaxial stress state. More tests are needed in this field.

- ➢ The axial behaviour of FRP-confined reinforced RuC needs to be examined in order to explore the potential use in structural applications.

- ➢ Some parameters in the proposed model are obtained by curve-fitting of the database of experimental stress-strain results. However, a more rational model should recognise and incorporates the physical properties of material microstructure, such as water-cement ratio, age, the volume fraction of mineral or rubber aggregates, paste porosity and paste-aggregates interface properties.

➢ The reasons for the premature FRP rupture and a rational explanation of why the performance of the concrete columns confined by different types of FRP sheets with identical stiffness differs, remains uncertain.

➢ Experimental work is needed to compare the behaviour of confined and unconfined rubberised concrete with conventional concrete having a similar strength.

7.2.3 Shear

➢ Due to time limits only small scale shear tests were carried out. Full-scaled shear tests are also needed.

➢ The shear performance of RuC confined by different types of FRP (e.g. aramid and glass) and various confinement stiffness needs to be examined.

➢ More experimental work needs to be done on FRP-confined RuC beam of different sizes and a wide range of shear span to depth ratios or effective depths in order to investigate the shear behaviour in a more systematic manner.

➢ The proposed model relies on the angle of an inclined struct which limits the application of the model to deep shear beams. Therefore, a more advanced definition of crack angle needs to be determined.

Appendices

Appendix A   **Experimental results (Asymmetric shear tests; Flexural Tests and Compressive Test)**

Appendix B   **Finite Element Models (Asymmetric shear tests; Flexural Tests and Compressive Test)**

Appendix C   **Program Code (Shear behaviour model and Analytical model)**

Appendix A. Experimental results

A1. Asymmetric shear tests on FRP-confined and unconfined rubberised concrete

AN1   AN2
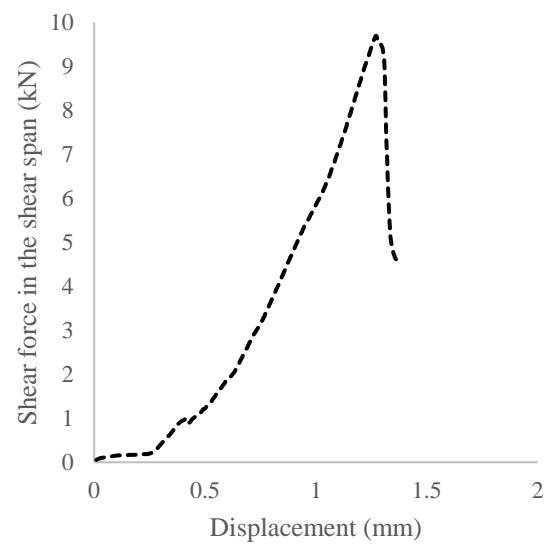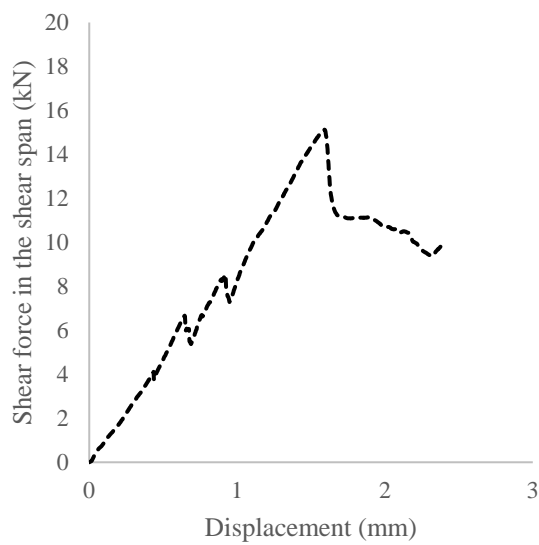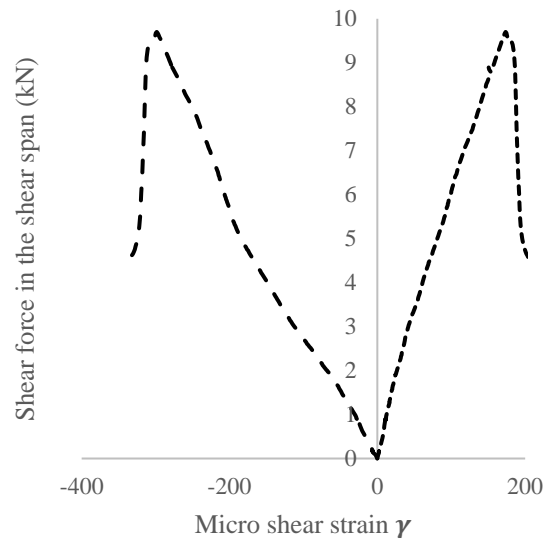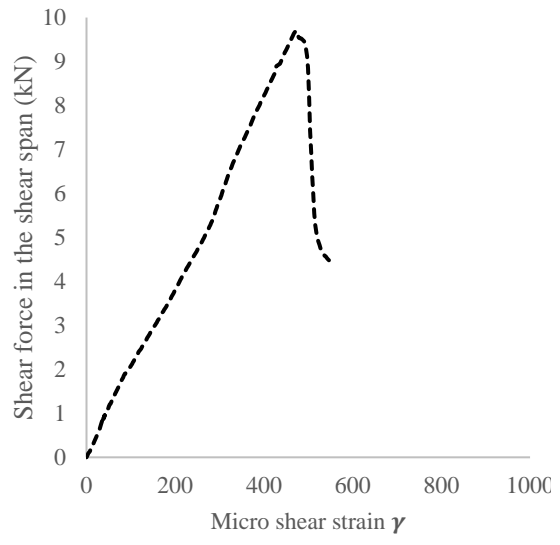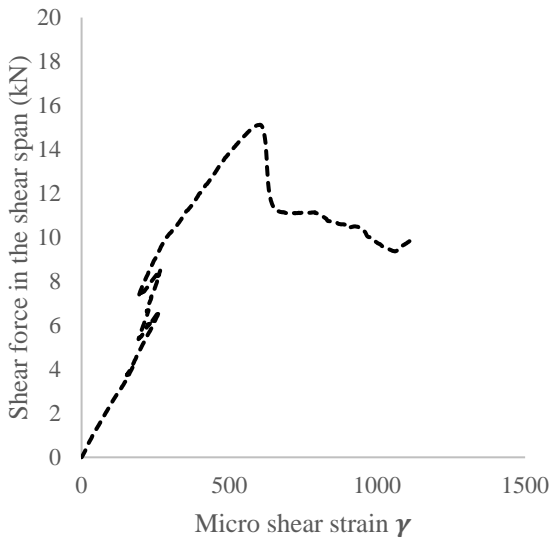
RBU-1
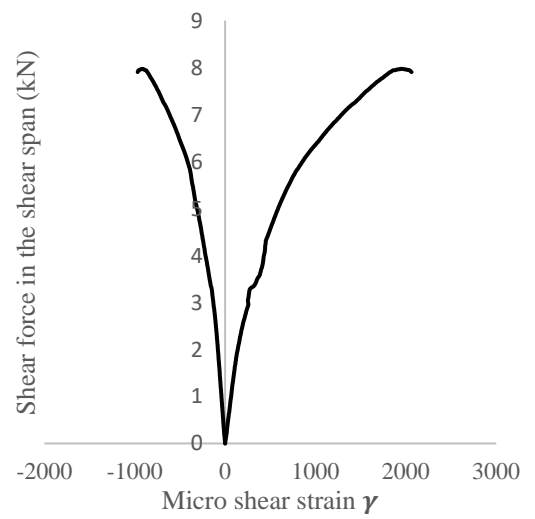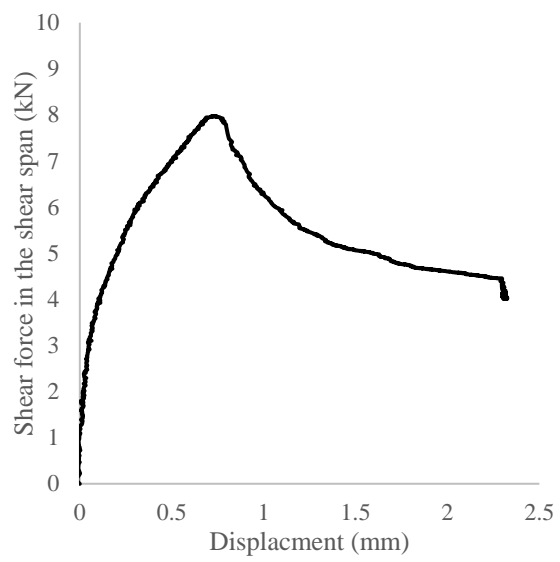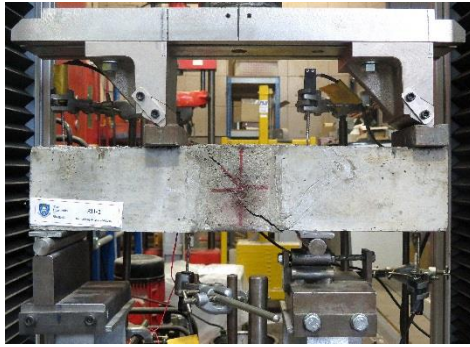
RBU-2
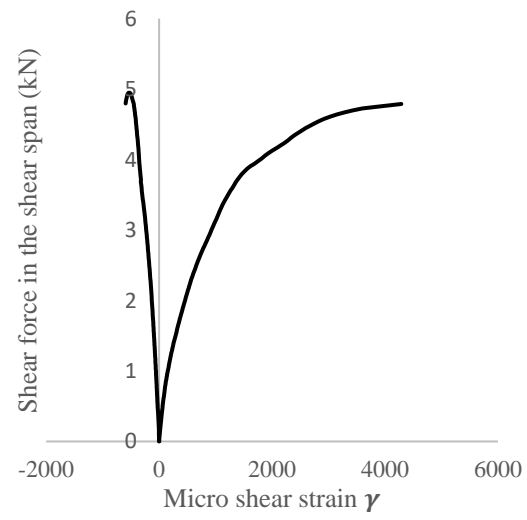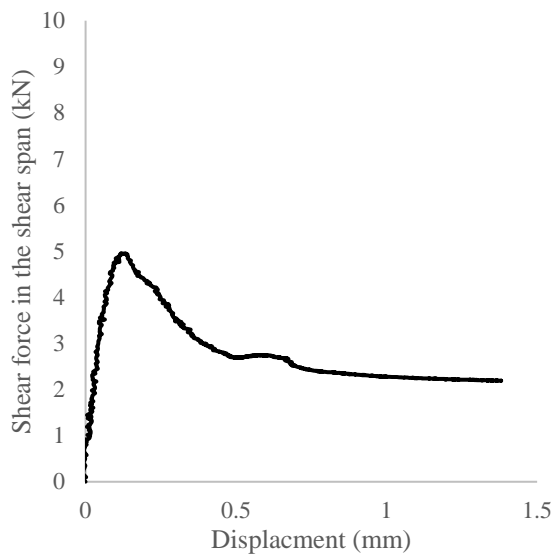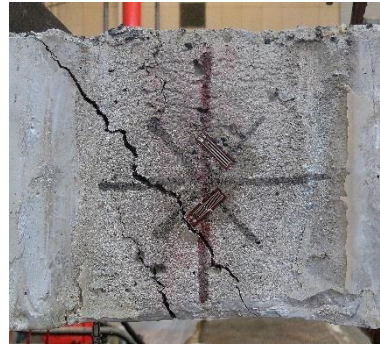
RU-2
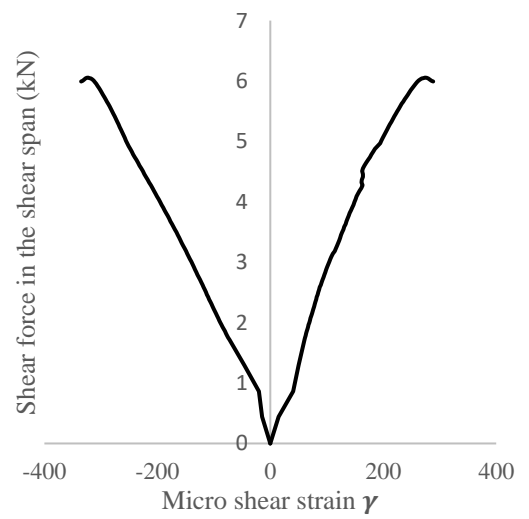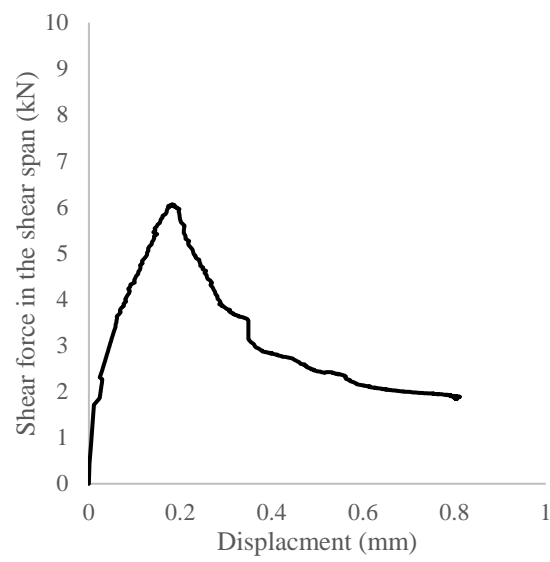
AD1.0U-1
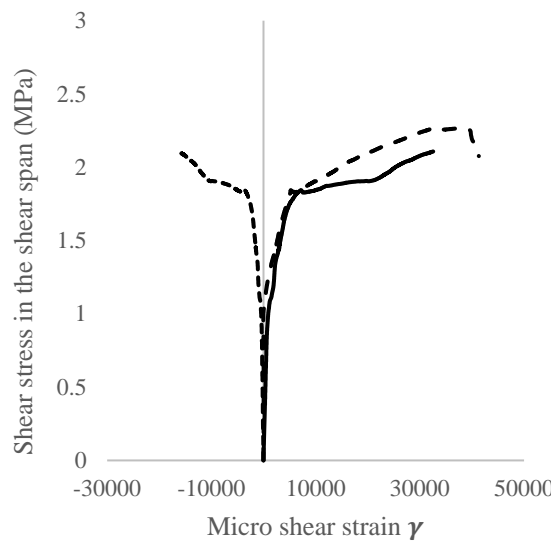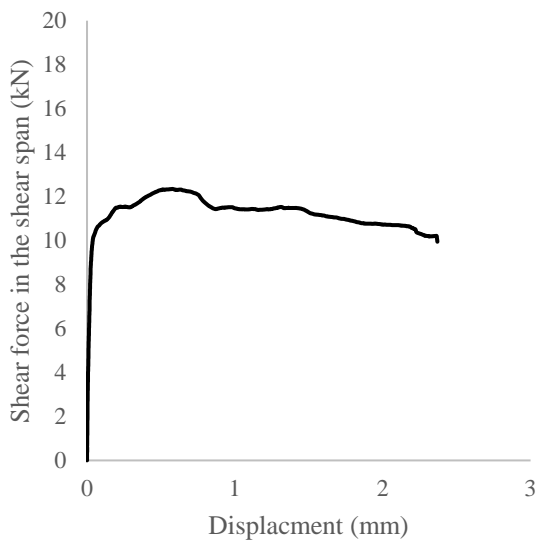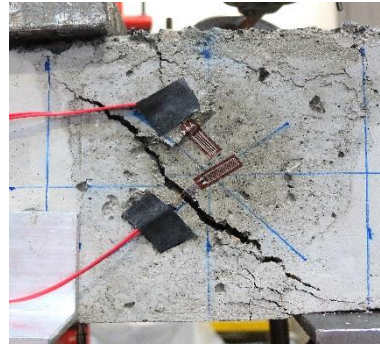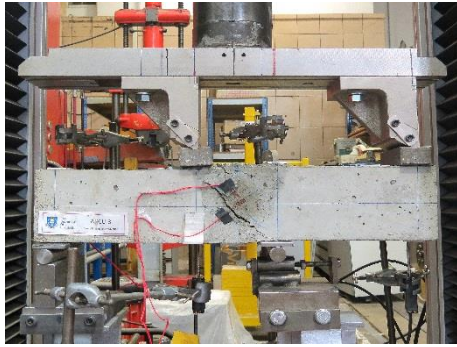
AD1.0U-2
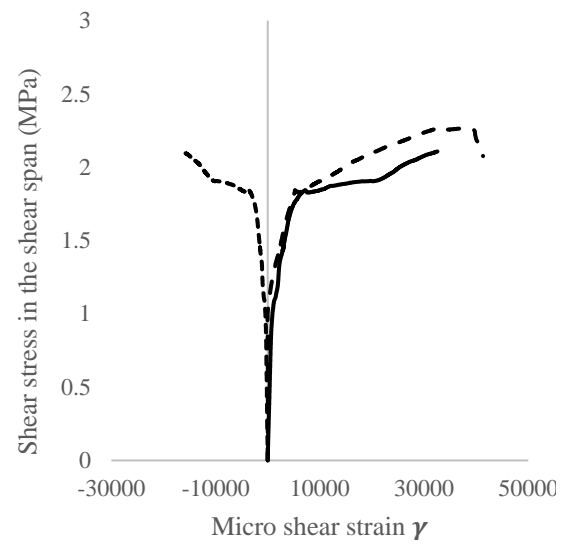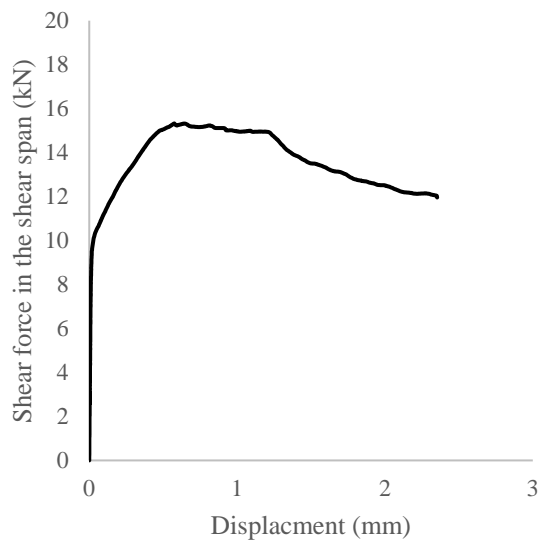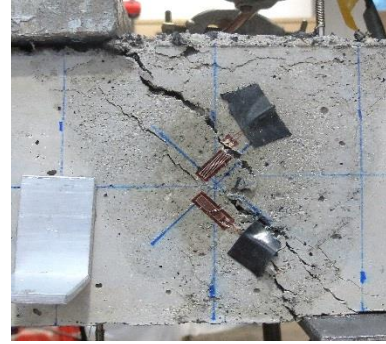
AD1.5U-1
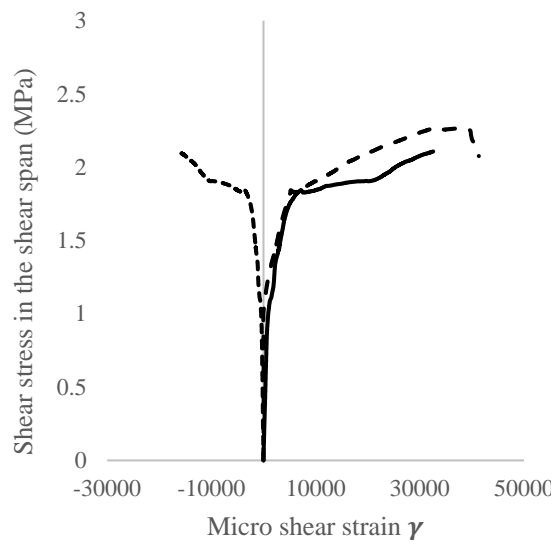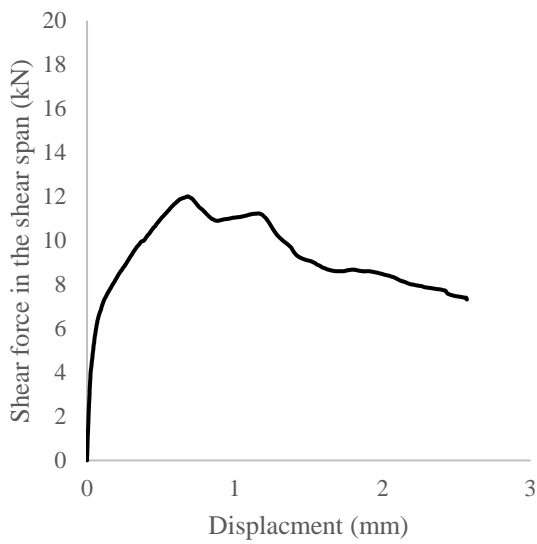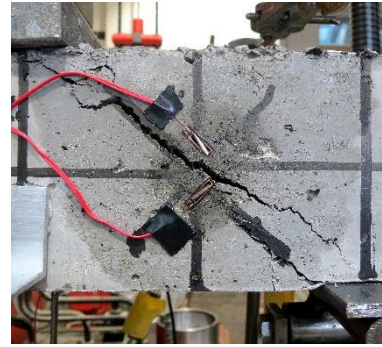
AD1.5U-2
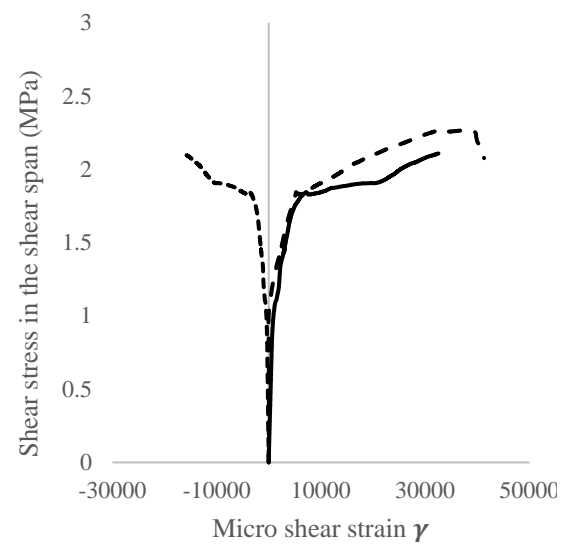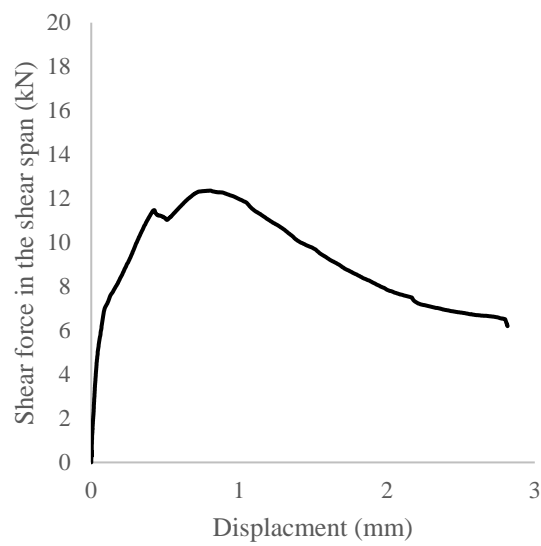
AD2.0U-1
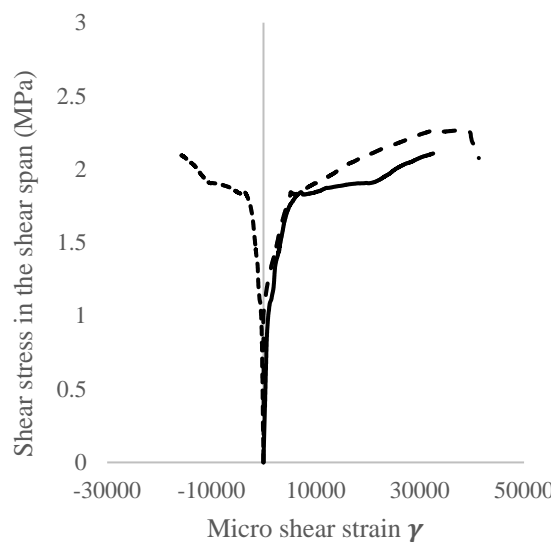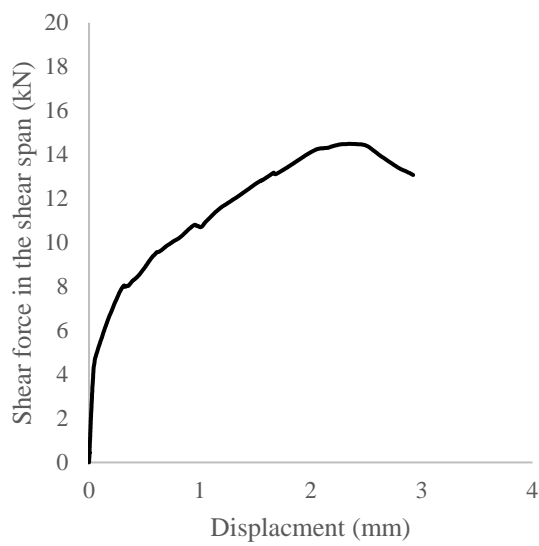
AD2.0U-2
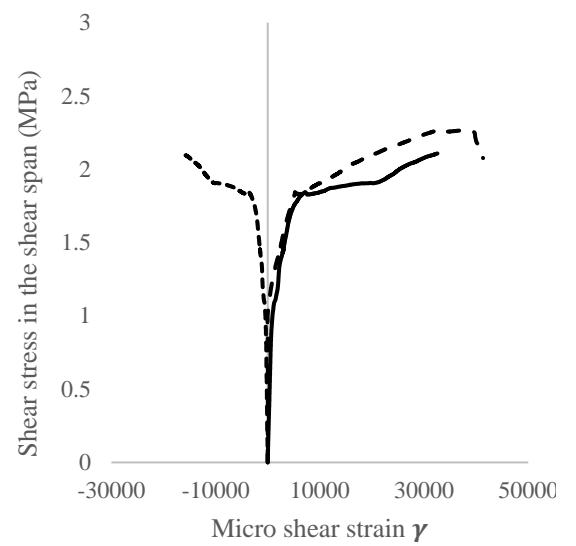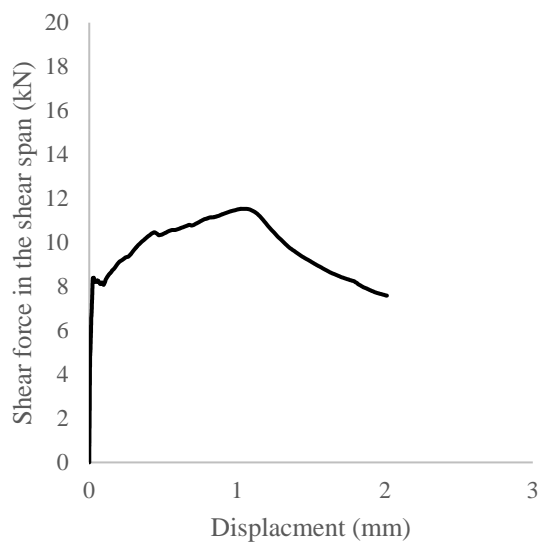
RC-1
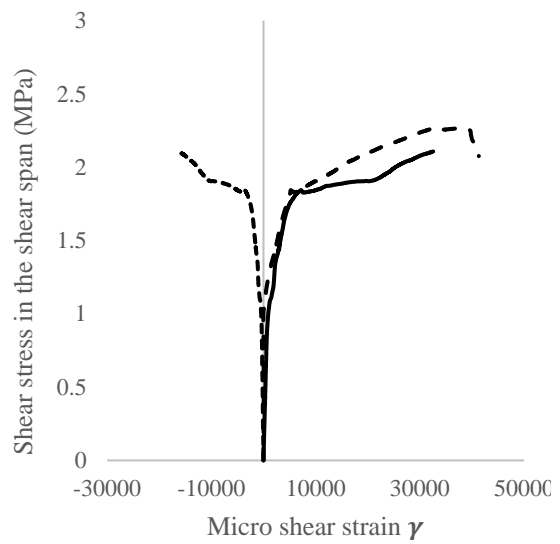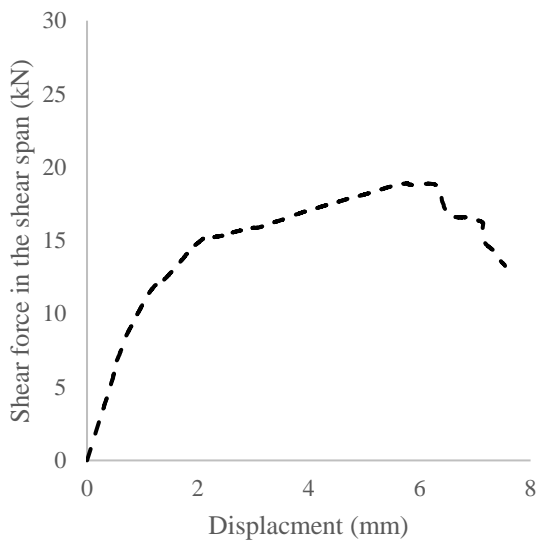
RC-2
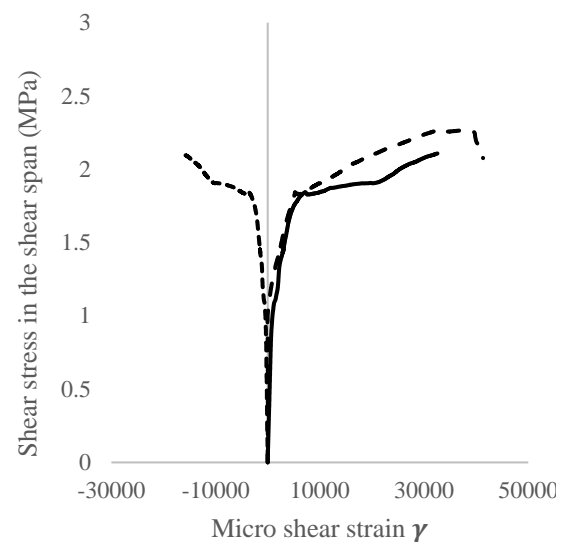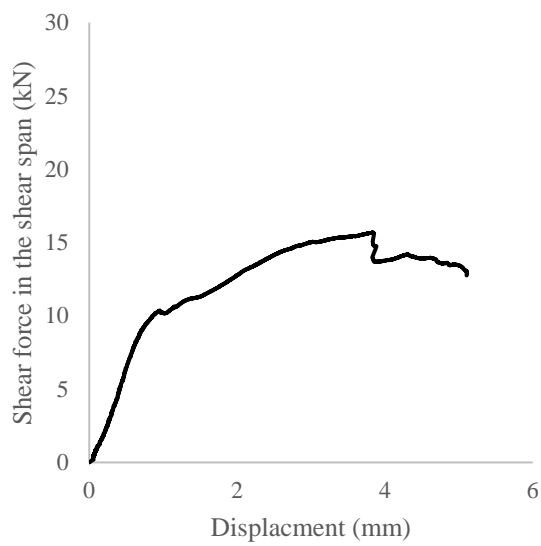
AD1.0C-1
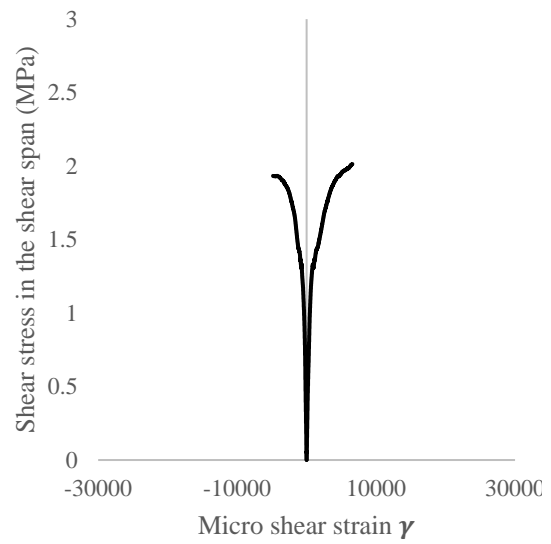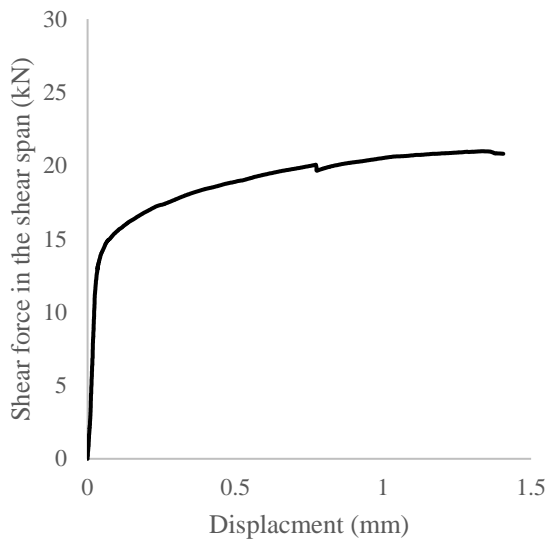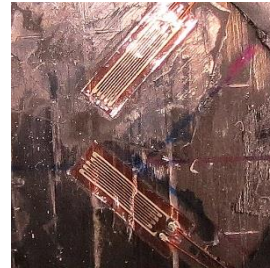
AD1.0C-2
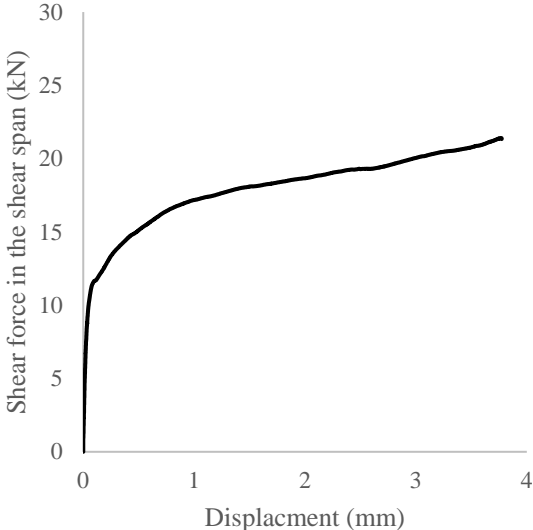
AD1.5C-1
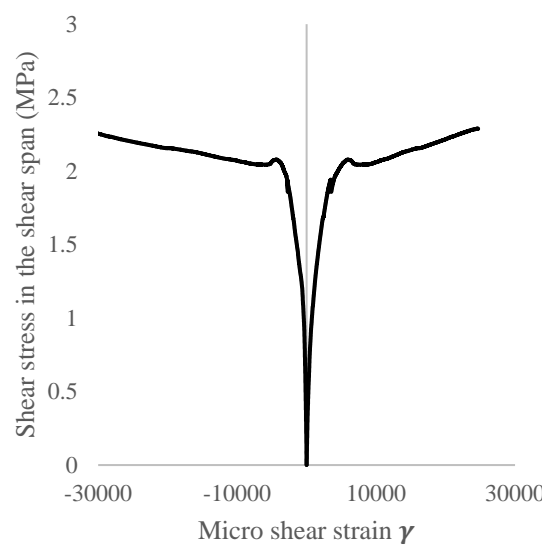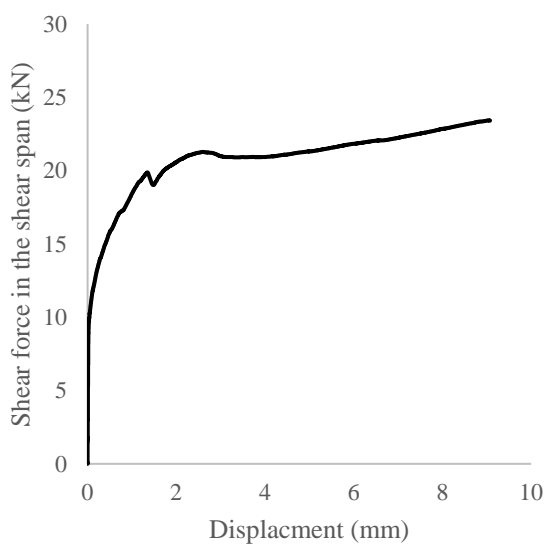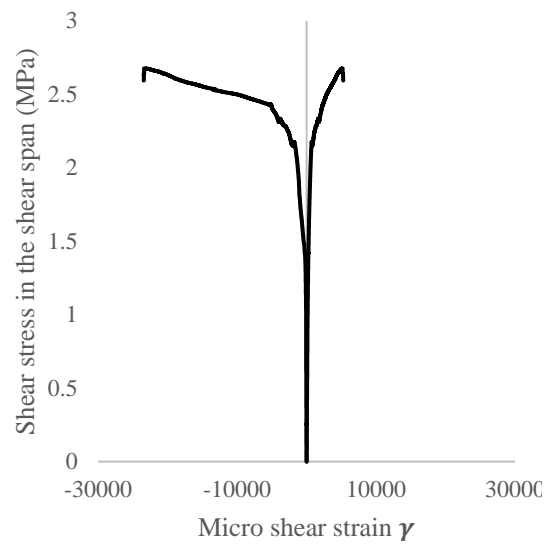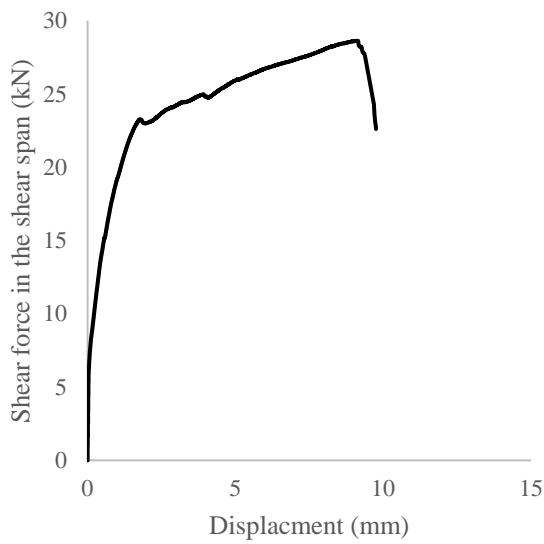
AD2.0C-1
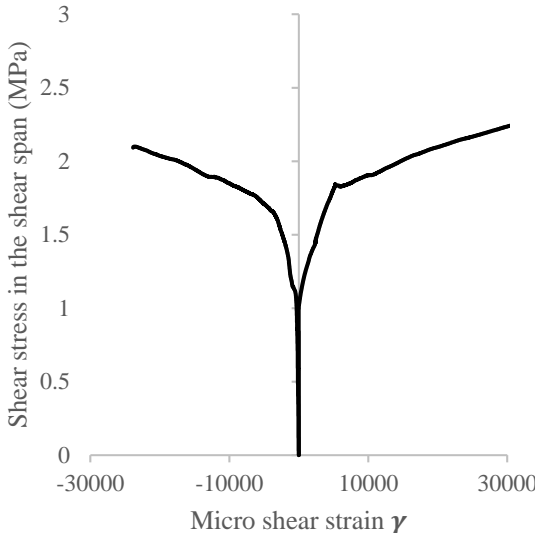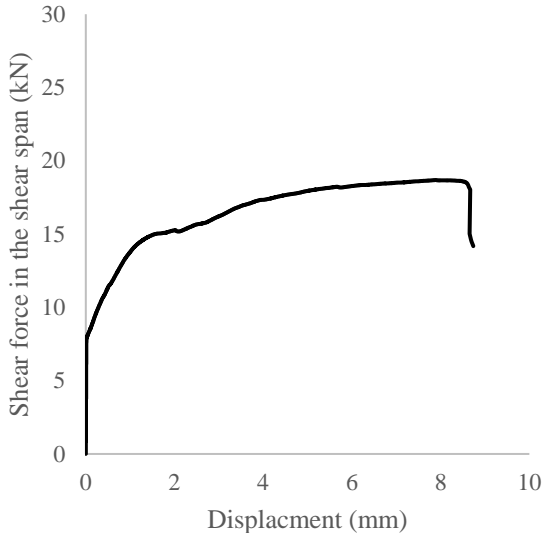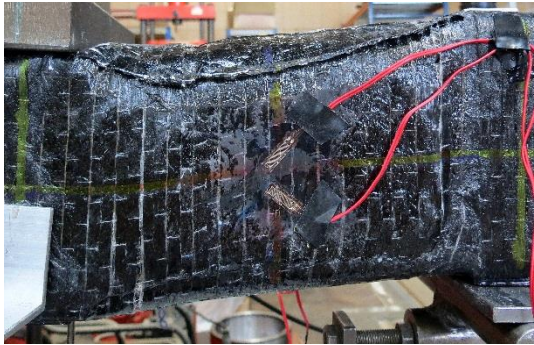
AD2.0C-2
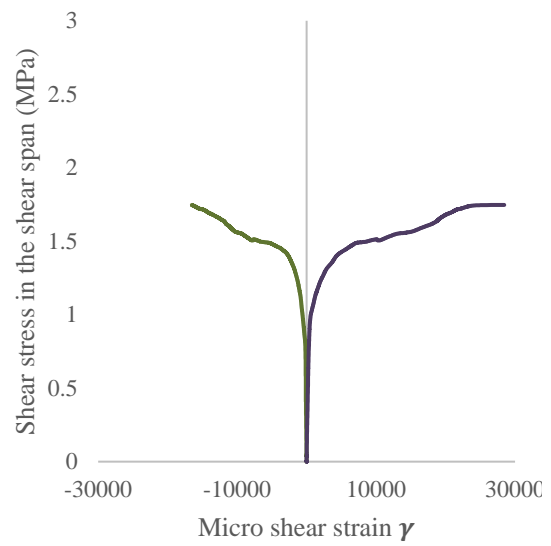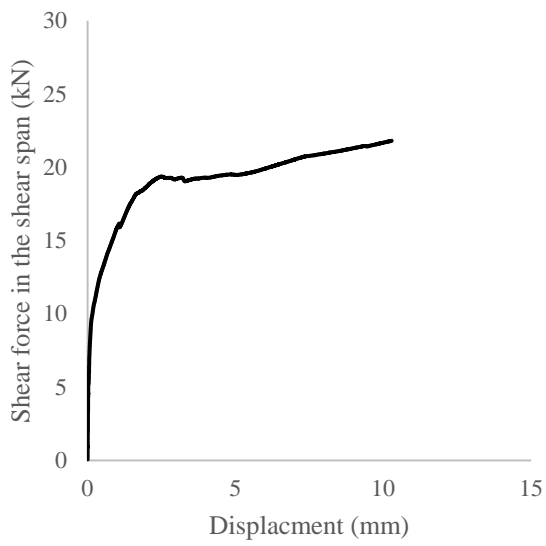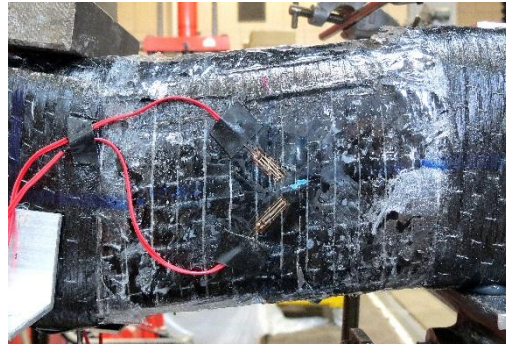
RBC-1
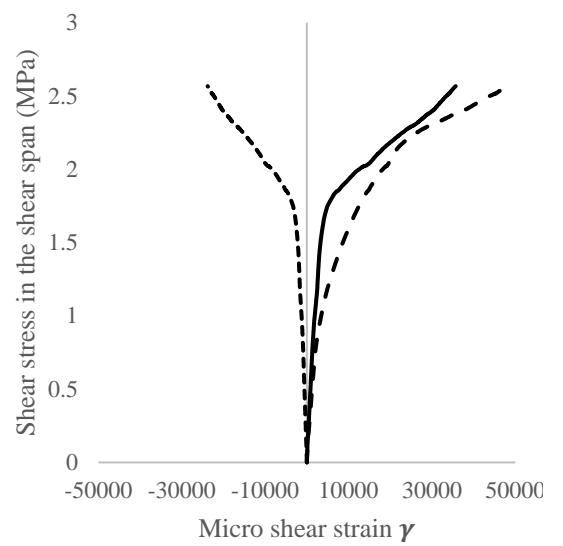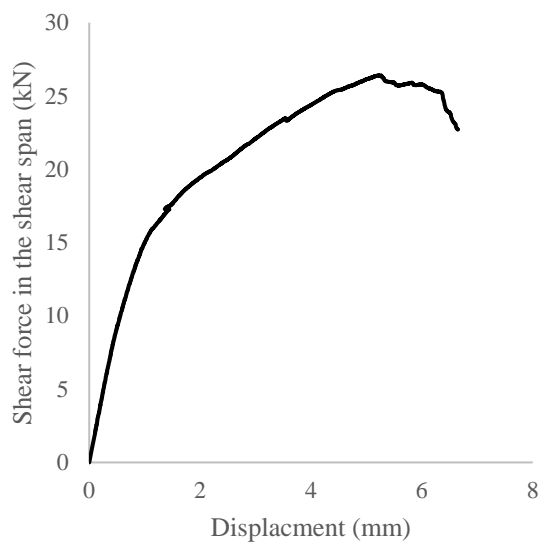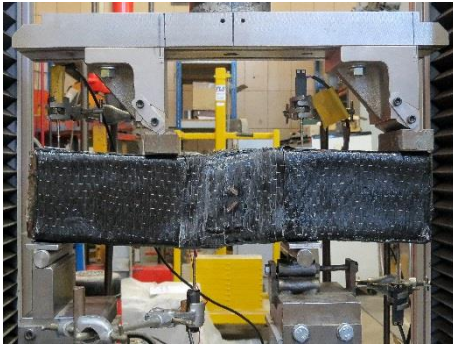
AC60SD
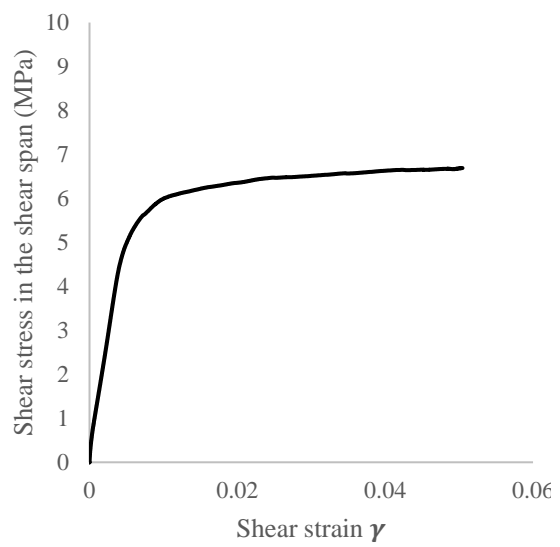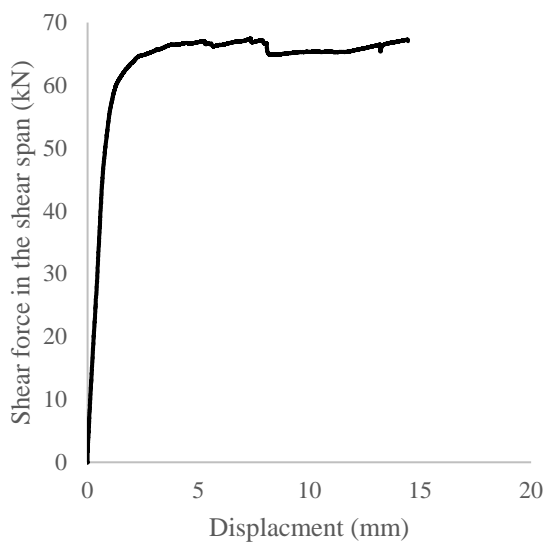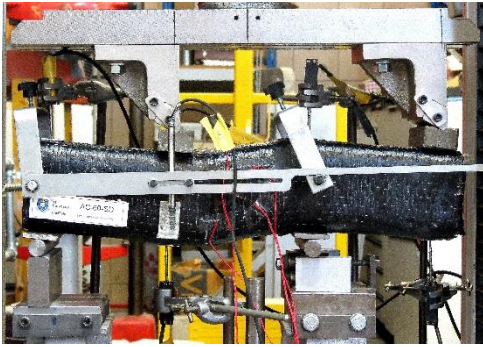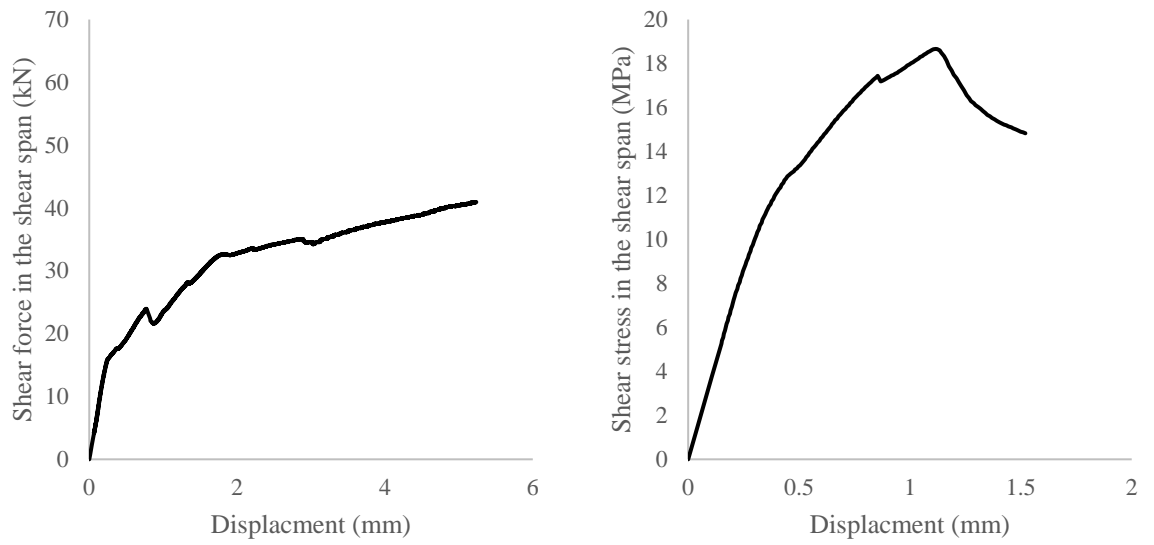
Figure. A1 – 1. Experimental results of asymmetric shear tests.

Table A1 – 1. Main results of asymmetric shear tests.

Specimen	Shear Capacity (kN)	Height (mm)	Width (mm)	Ultimate shear stress (MPa)
RC-1	15.67	101.5	73.2	2.11
RC-2	18.90	104.7	74.7	2.41
AD1C-1	20.97	101.2	100.0	2.07
AD1C-2	21.40	101.9	100.1	2.10
AD1.5C-1	28.62	106.9	100.0	2.68
AD1.5C-2	23.43	102.3	100.3	2.29
AD2C-1	18.68	100.8	100.0	1.85
AD2C-2	21.80	104.1	100.0	2.09
RU-3	4.95	100.1	68.2	0.73
RU-4	6.05	102.2	70.7	0.83
AD1U-3	12.34	104.4	100.1	1.18
AD1U-4	15.33	107.1	100.1	1.42
AD1.5U-3	12.00	103.6	100.0	1.16
AD1.5U-4	12.36	104.1	100.3	1.19
AD2U-3	14.49	106.5	100.0	1.36
AD2U-4	11.53	101.4	100.0	1.14

*Note: R = reduced width in mid-span, AD = the shear-span-to-depth ratio, C = FRP-confined specimen, U= unconfined specimen

Table A1 – 2. Properties of rubberised concrete

	Cube compressive strength	Cylinder compressive strength	Splitting tensile strength	Average shear stress (RuC)	Average shear stress (CRuC)
	MPa				
Average Value	11.5	7.2	1.3	1.12	2.2
Standard deviation	1.05	1.21	0.18	0.93	1.06
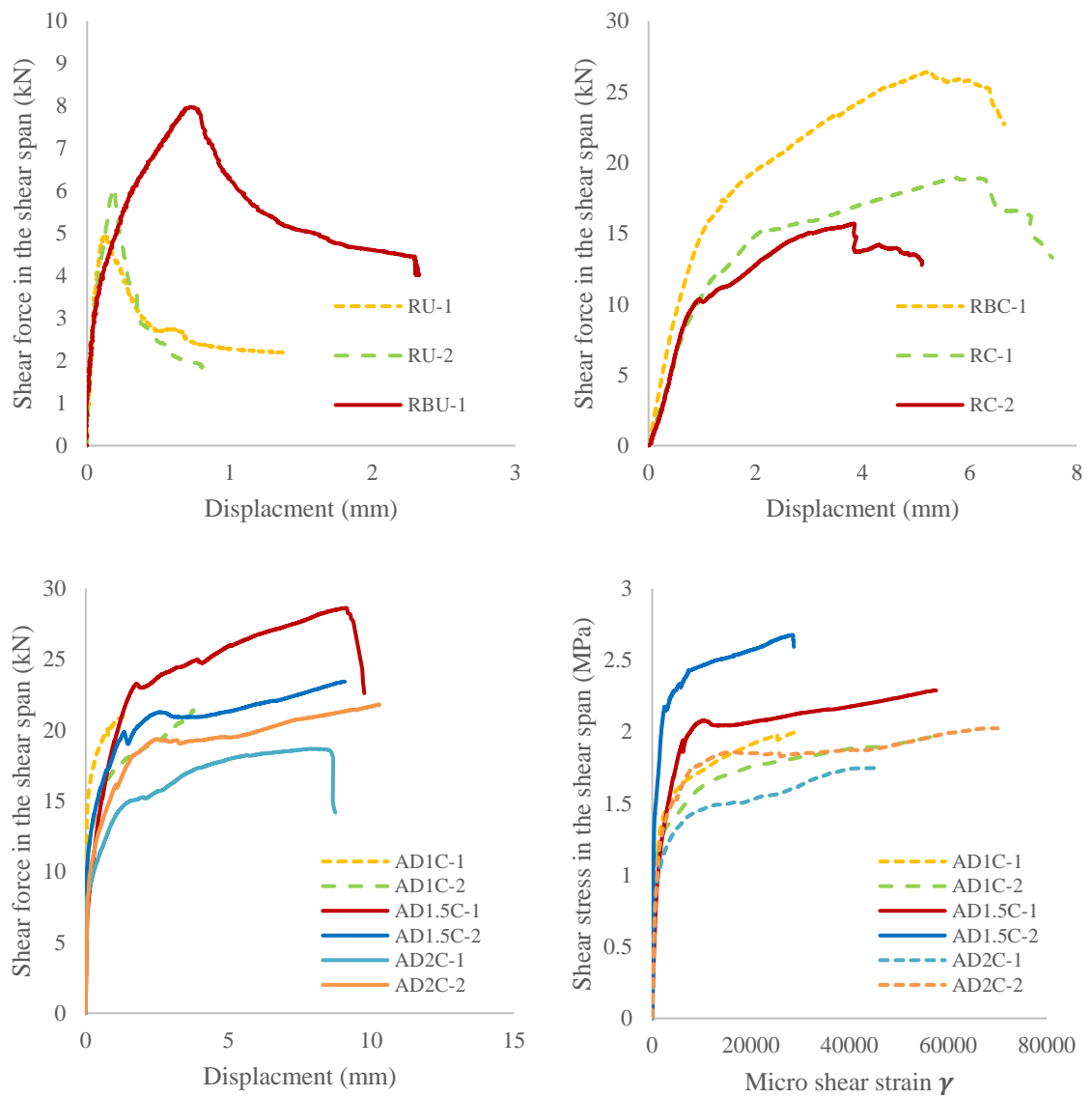
Figure. A1 – 2. Summary of asymmetric shear tests.

A2. Three-Point Bending Tests on Rubberised Concrete
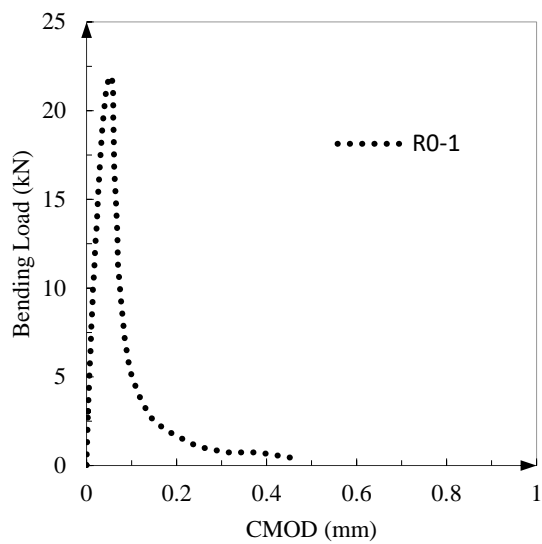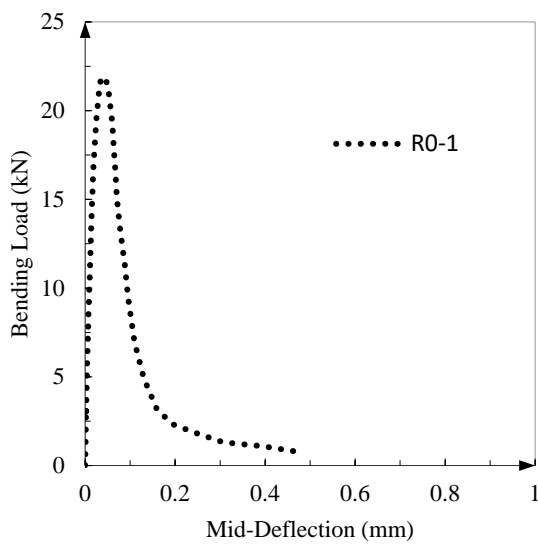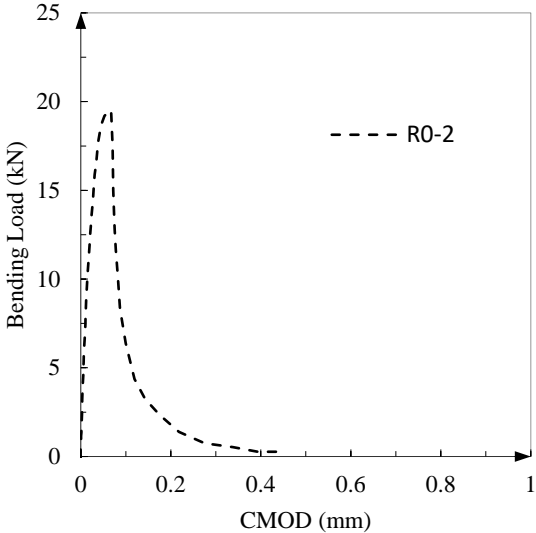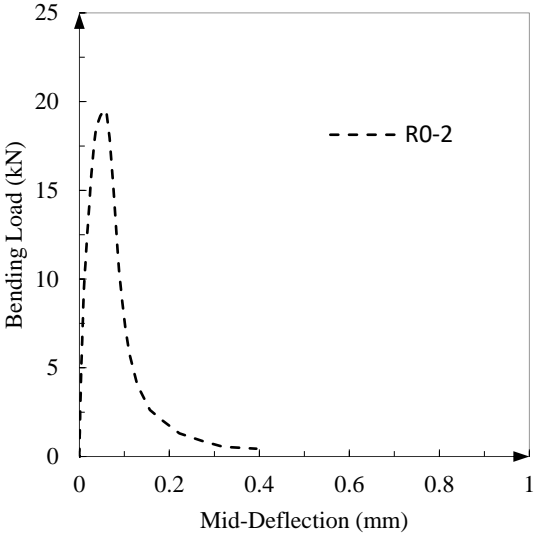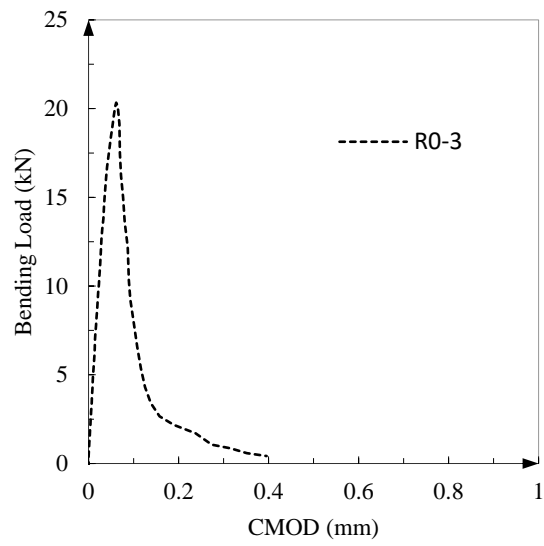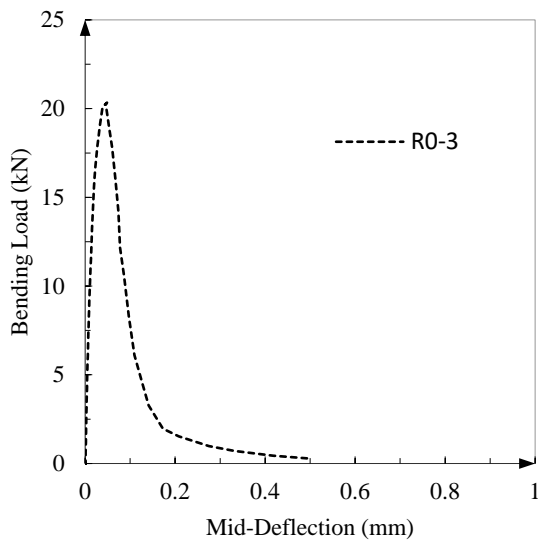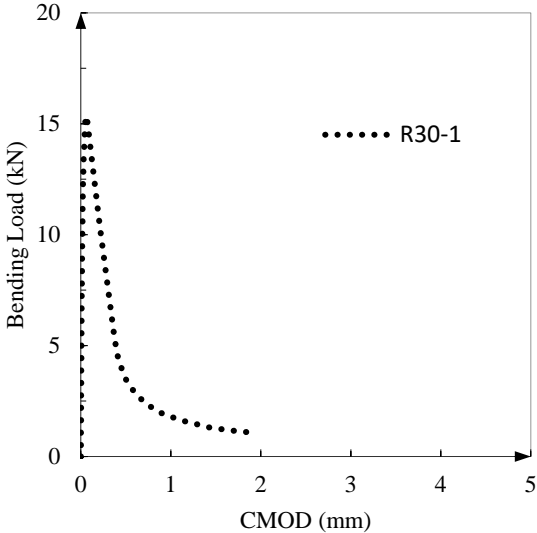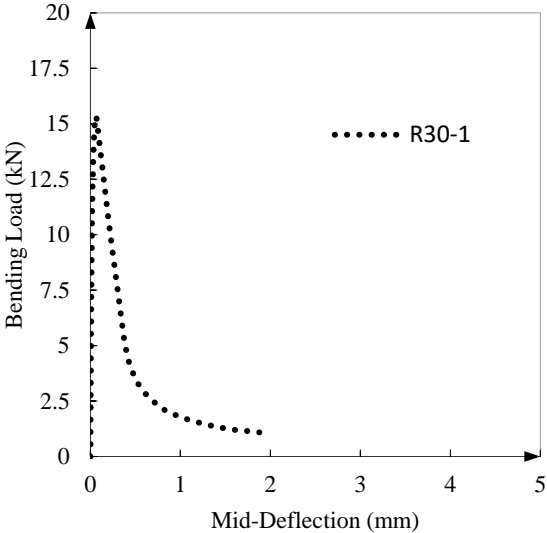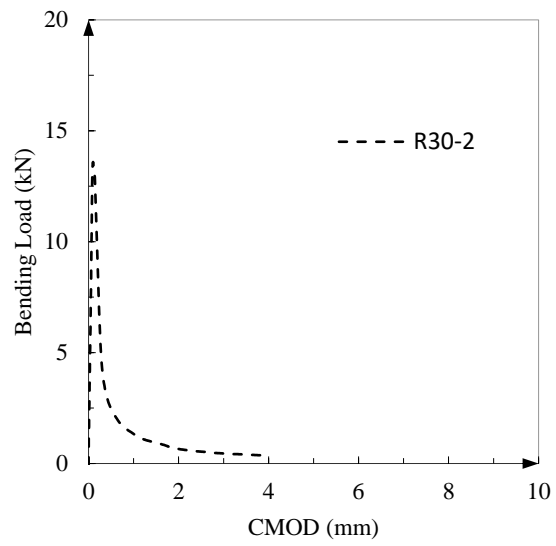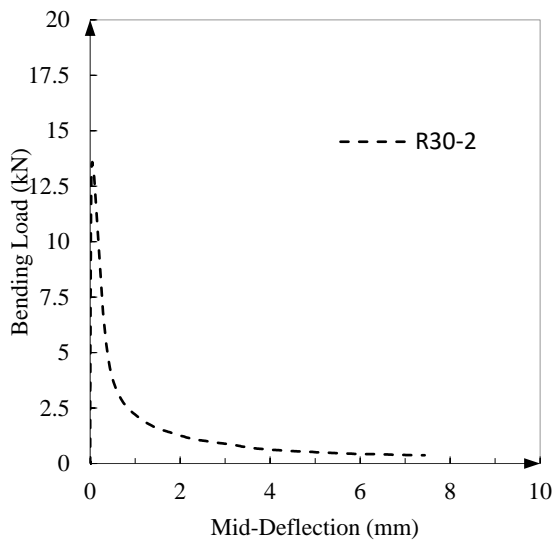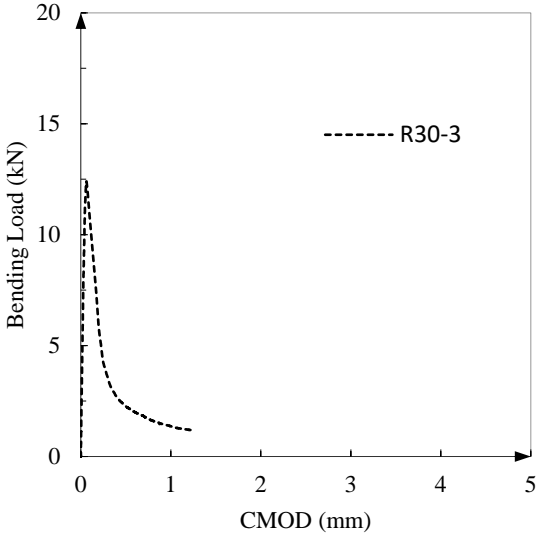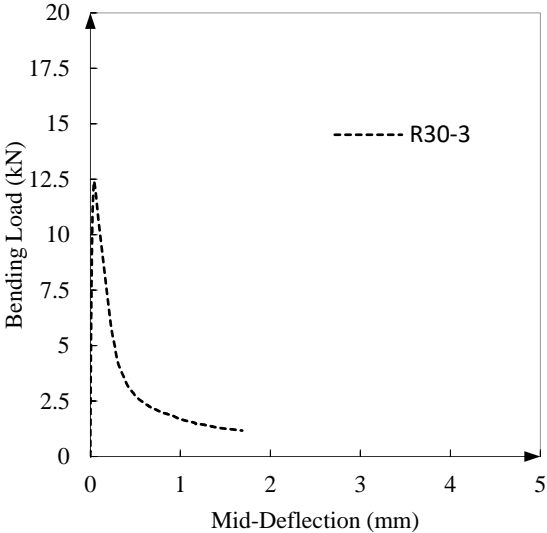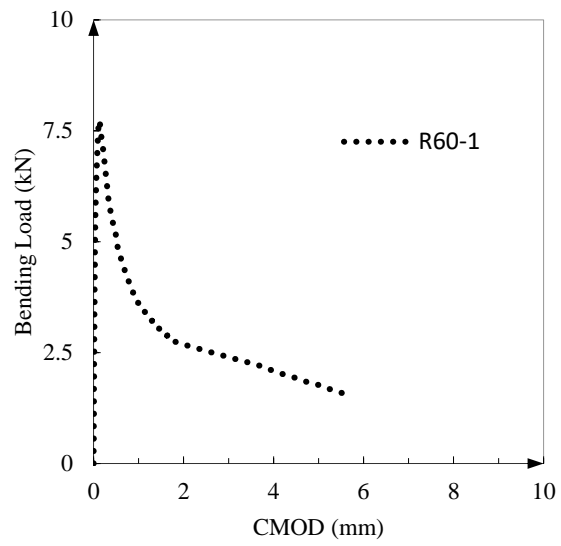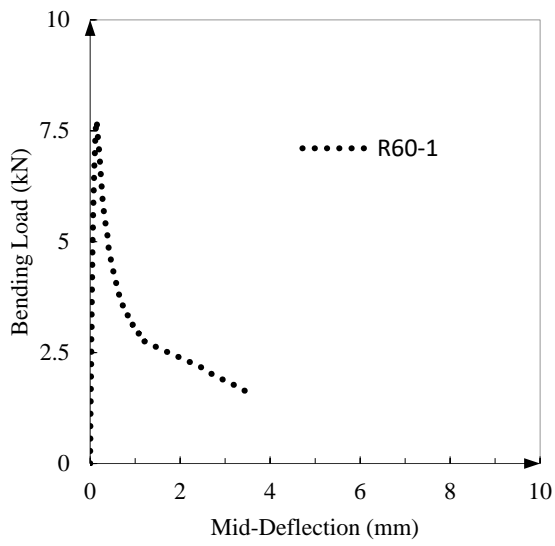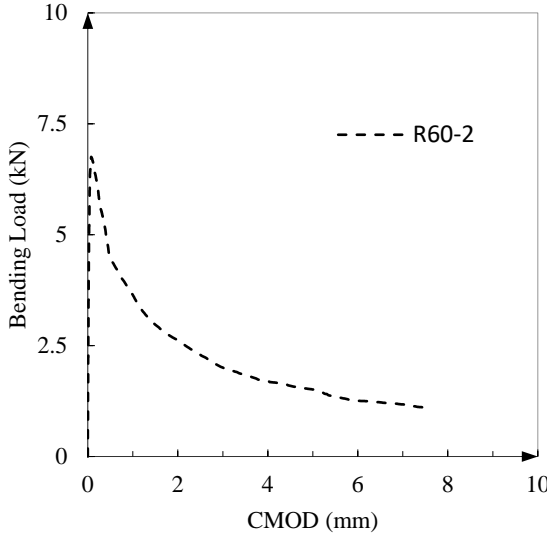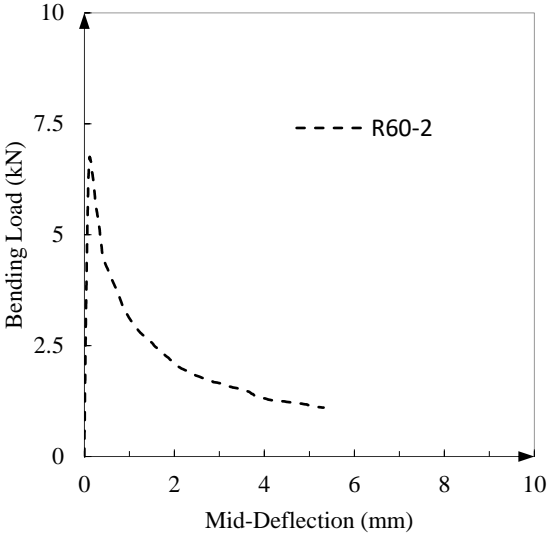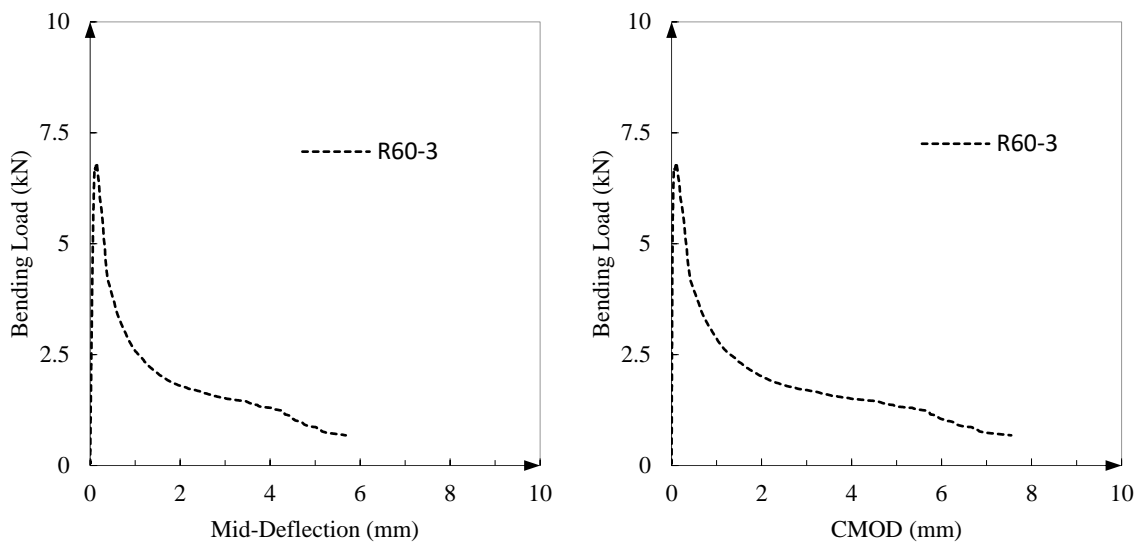
Figure. A2 – 1. Experimental results of three-point bending tests.

A3. Axial compression tests on FRP-confined Rubberised Concrete

0LA-S1-R0   1LA-SL-R60   2LA-SL-R60   3LA-SL-R60

1LA-S1-R60-1 1LA-S1-R60-2 1LA-S1-R60-3 1LC-S1-R60-1 1LC-S1-R60-2 1LC-S1-R60-3

2LA-S1-R60-1 2LA-S1-R60-2 2LA-S1-R60-3 2LC-S1-R60-1 2LC-S1-R60-2 2LC-S1-R60-3

3LA-S1-R60-1 3LA-S1-R60-2 3LA-S1-R60-3 3LC-S1-R60-1 3LC-S1-R60-2 3LC-S1-R60-3

1LA-S1-R0-1   1LA-S1-R0-2   1LA-S1-R0-3   1LC-S1-R0-1   1LC-S1-R0-2   1LC-S1-R0-3

2LA-S1-R0-1   2LA-S1-R0-2   2LA-S1-R0-3   2LC-S1-R0-1   2LC-S1-R0-2   2LC-S1-R0-3

3LA-S1-R0-2   3LA-S1-R0-3

3LA-S1-R0-1   3LC-S1-R0-1   3LC-S1-R0-2   3LC-S1-R0-3

3LA-C-R0

1LA-C-R60   2LA-C-R60   3LA-C-R60   1LA-C-R0   2LA-C-R0

Figure. A3 – 1. Failure mode of FRP-confined concrete.

Carbon-FRP confined regular concrete in circular section
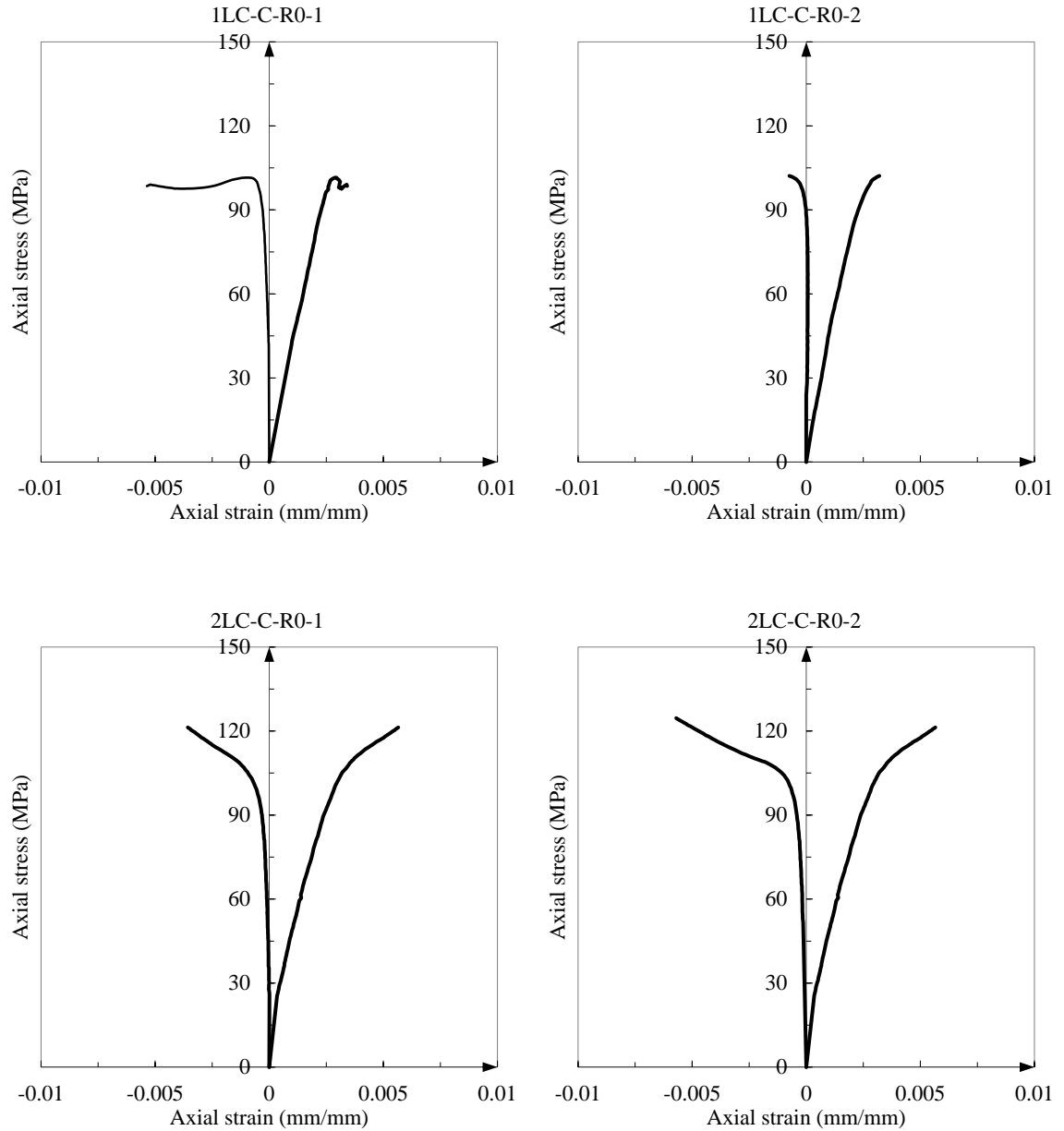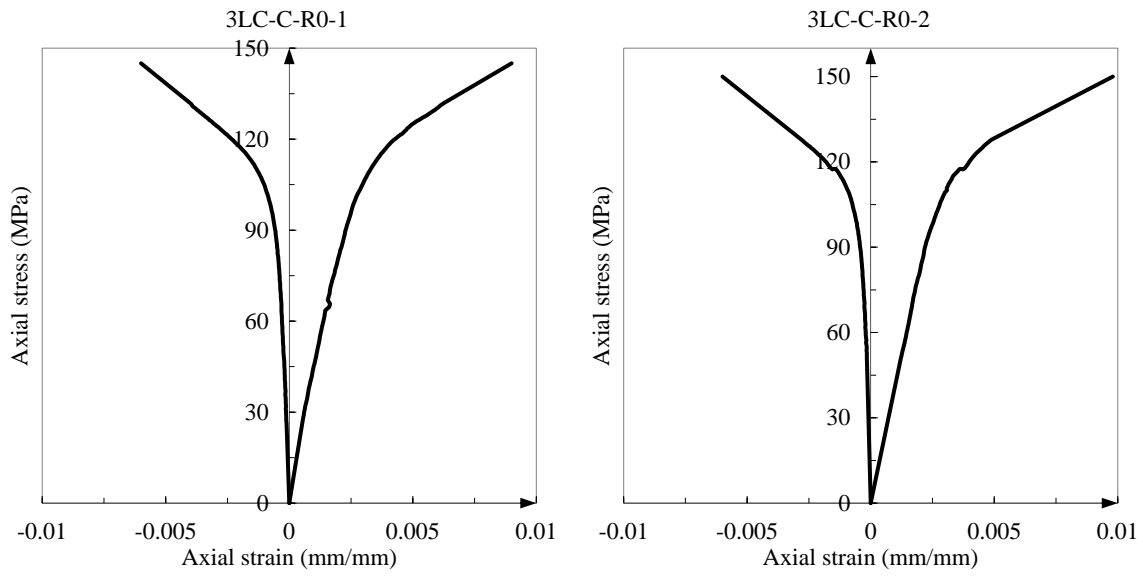
1LC-C-R0-1

1LC-C-R0-2

2LC-C-R0-1

2LC-C-R0-2

3LC-C-R0-1

3LC-C-R0-2

Aramid-FRP confined regular concrete in circular section

1LA-C-R0-1

1LA-C-R0-1

2LA-C-R0-1

2LA-C-R0-2

3LA-C-R0-1

3LA-C-R0-2

Carbon-FRP confined rubberised concrete in circular section

1LC-C-R60-1

1LC-C-R60-2

2LC-C-R60-1

2LC-C-R60-2

3LC-C-R60-1

3LC-C-R60-2

Aramid-FRP confined rubberised concrete in circular section

1LA-C-R60-1

1LA-C-R60-2

2LA-C-R60-1

2LA-C-R60-2

3LA-C-R60-1

3LA-C-R60-2

4LA-C-R60-1

4LA-C-R60-2

Carbon-FRP confined regular concrete in square section

1LC-S-R0-1

1LC-S-R0-2

2LC-S-R0-1

2LC-S-R0-2

3LC-S-R0-1

3LC-S-R0-2

Aramid-FRP confined regular concrete in square section

1LA-S-R0-1

1LA-S-R0-2

2LA-S-R0-1

2LA-S-R0-2

3LA-S-R0-1

3LA-S-R0-2

Carbon-FRP confined rubberised concrete in square section

1LC-S-R60-1

1LC-S-R60-2

2LC-S-R60-1

2LC-S-R60-2

3LC-S-R60-1

3LC-S-R60-2

1LC-S2-R60

2LC-S2-R60

3LC-S2-R60

Aramid-FRP confined rubberised concrete in square section

1LA-S-R60-1

1LA-S-R60-2

2LA-S-R60-1

2LA-S-R60-2

2LA-S-R60-3

3LA-S-R60-1

3LA-S-R60-2

3LA-S-R60-3

3LA-S-R60-4
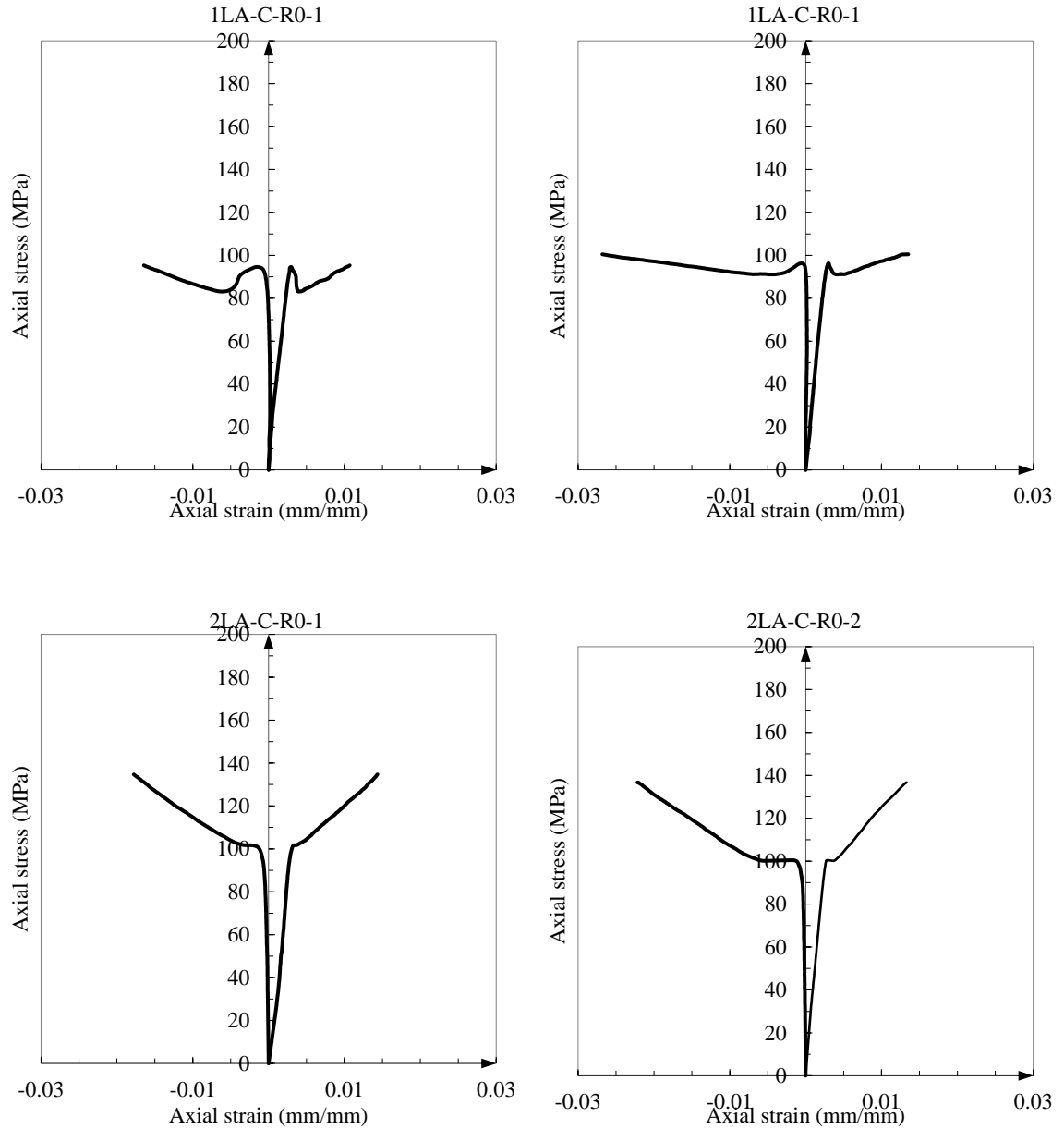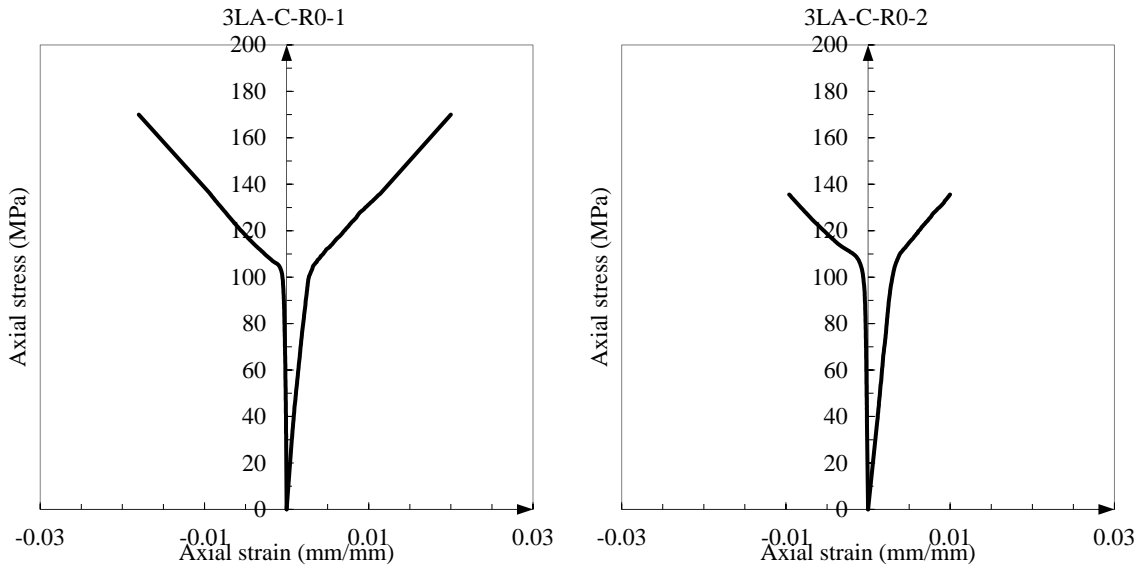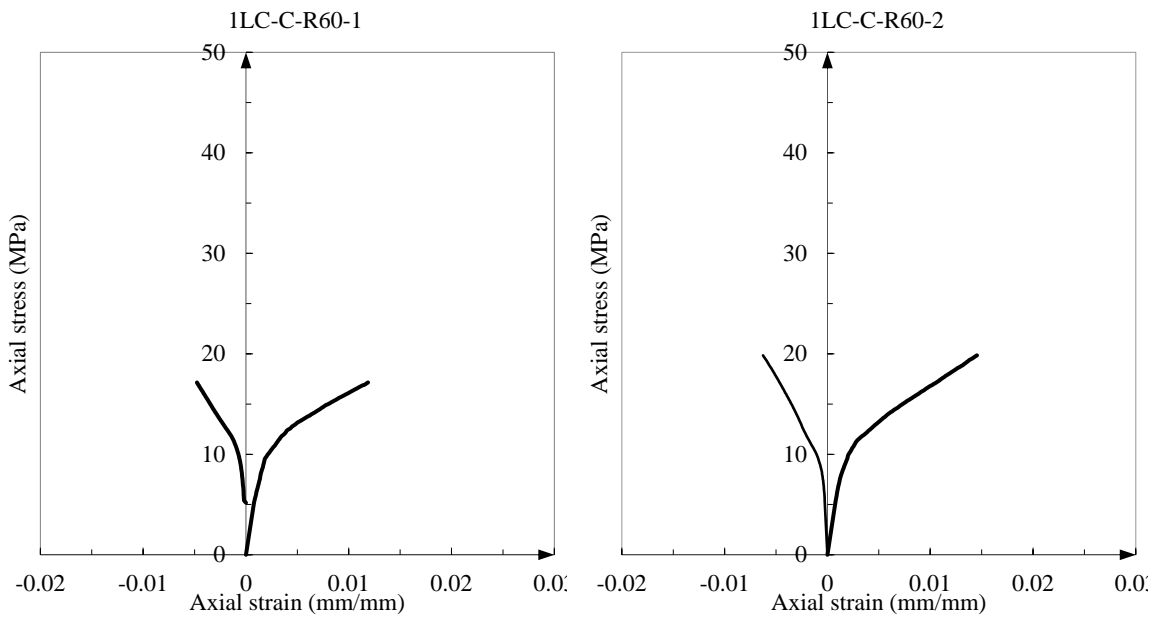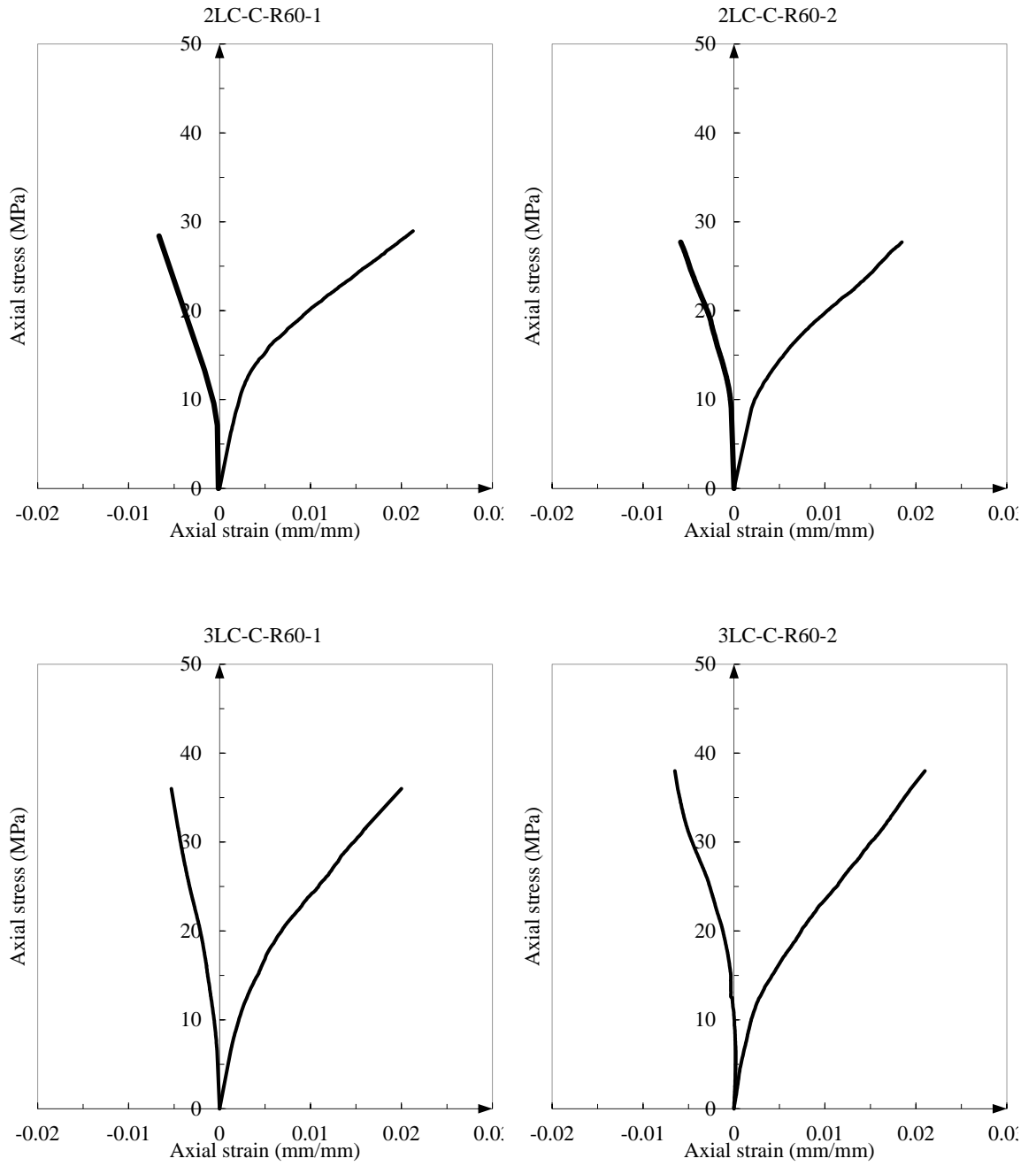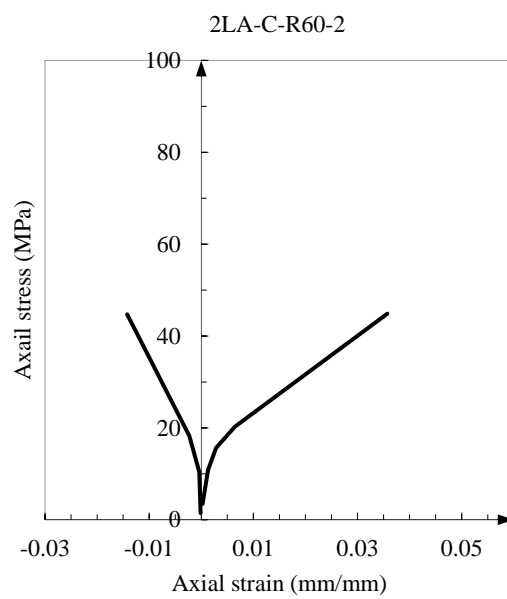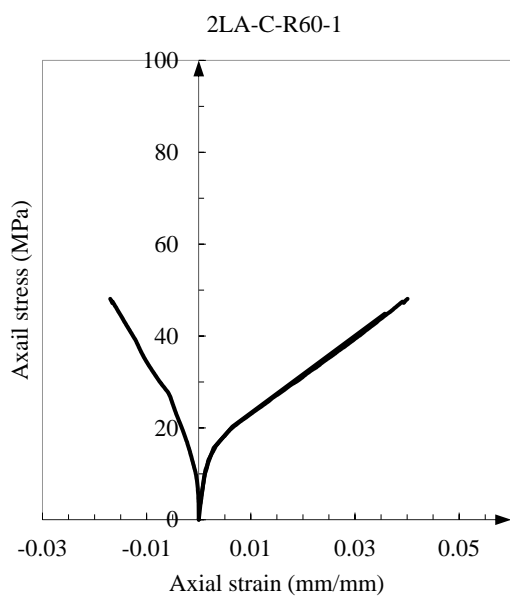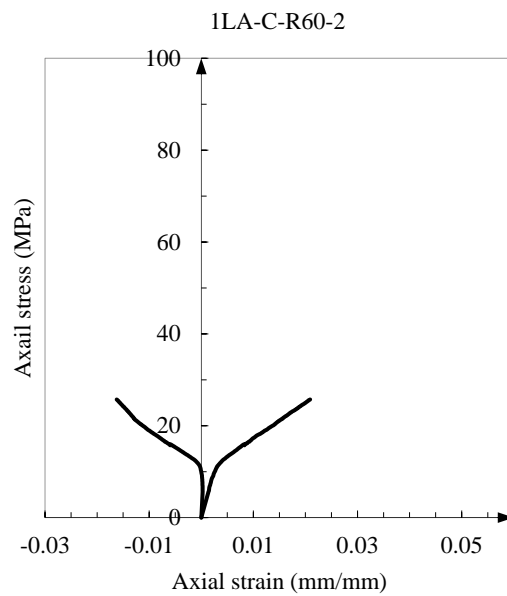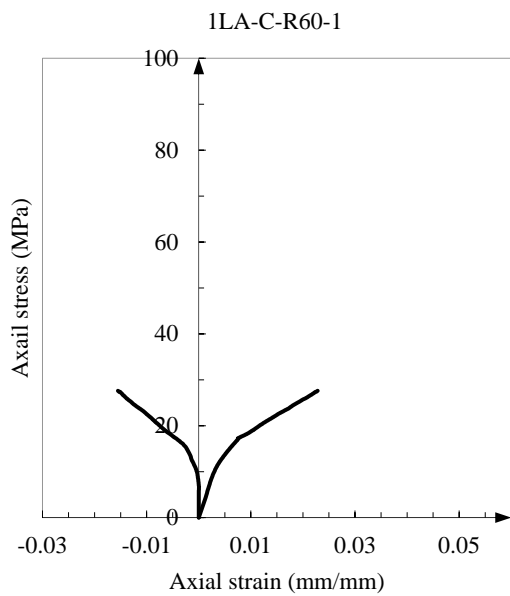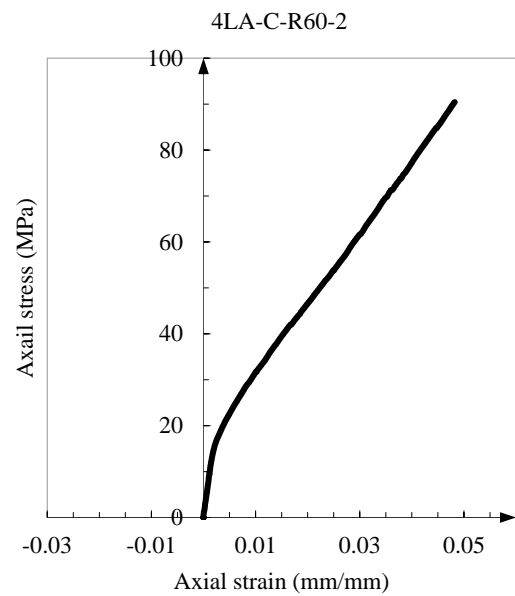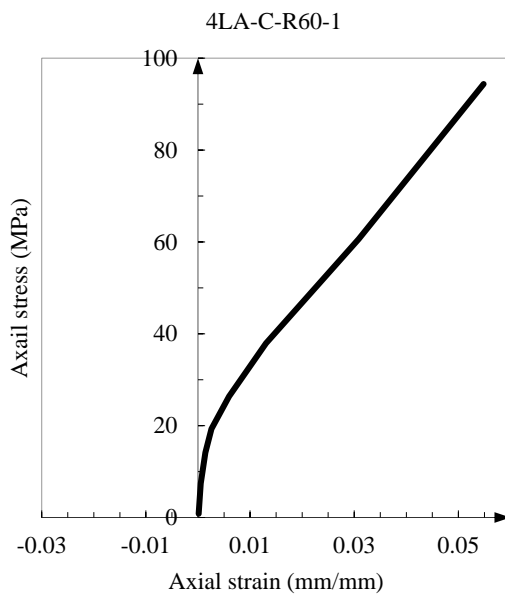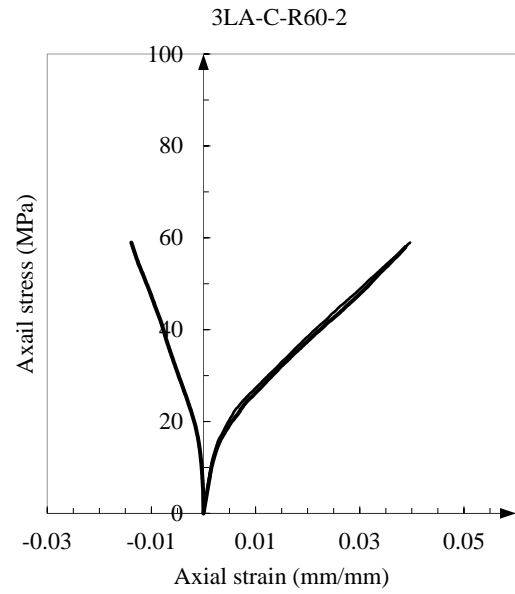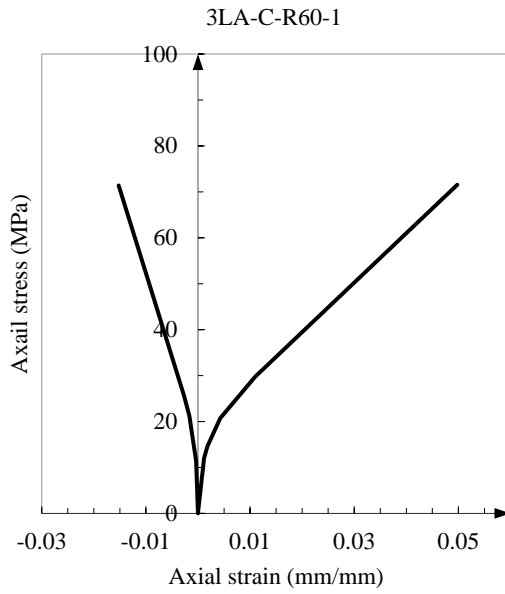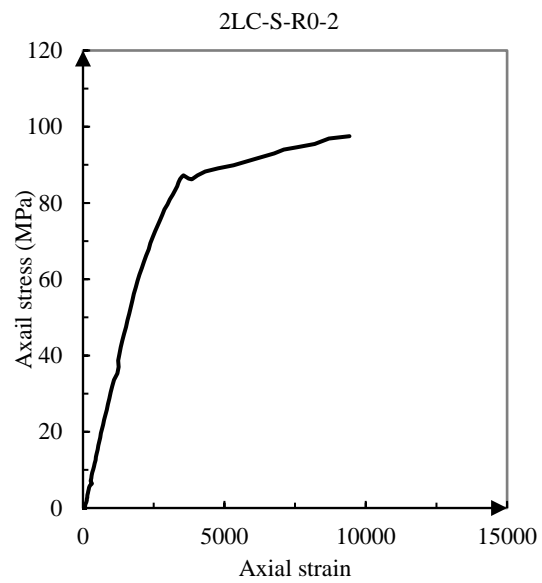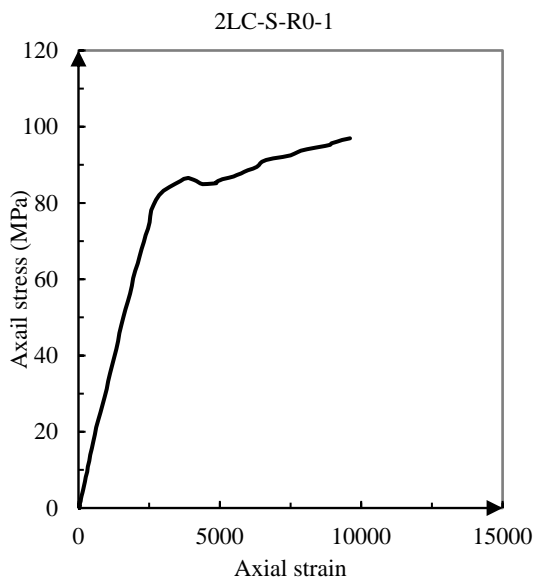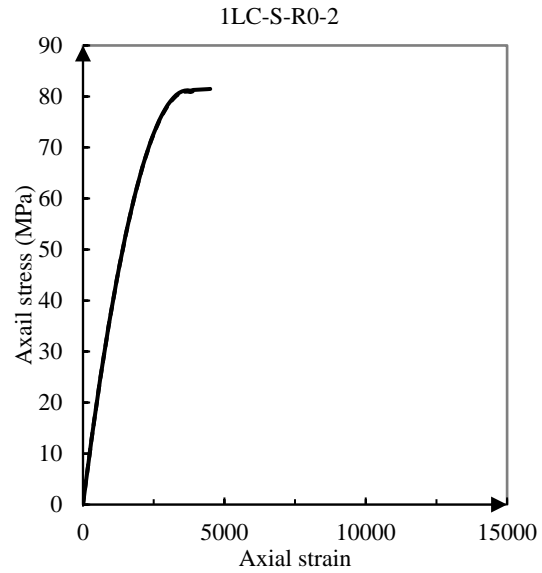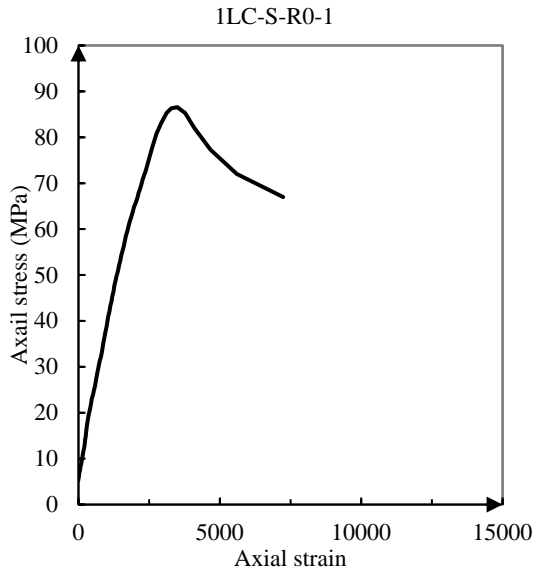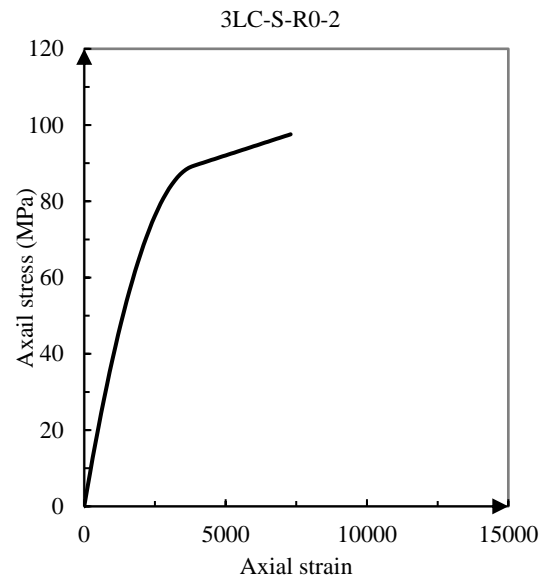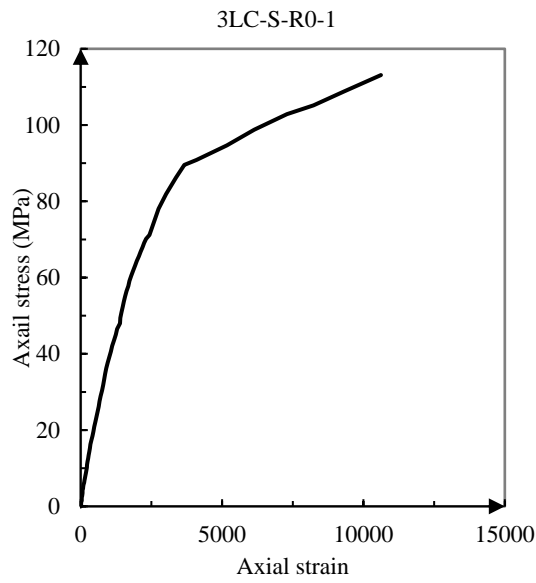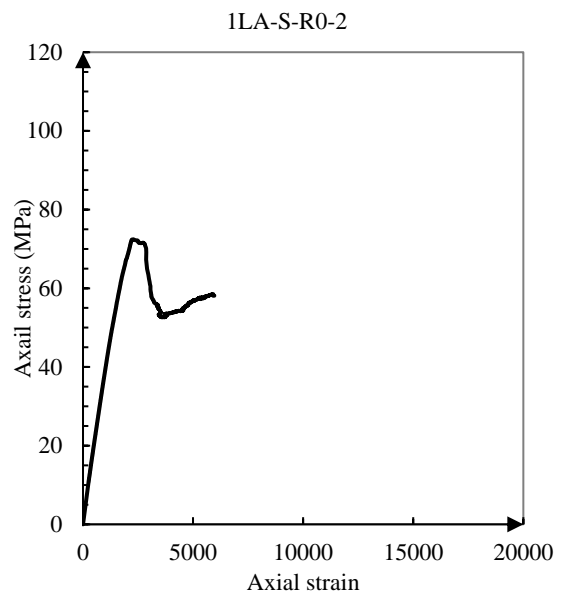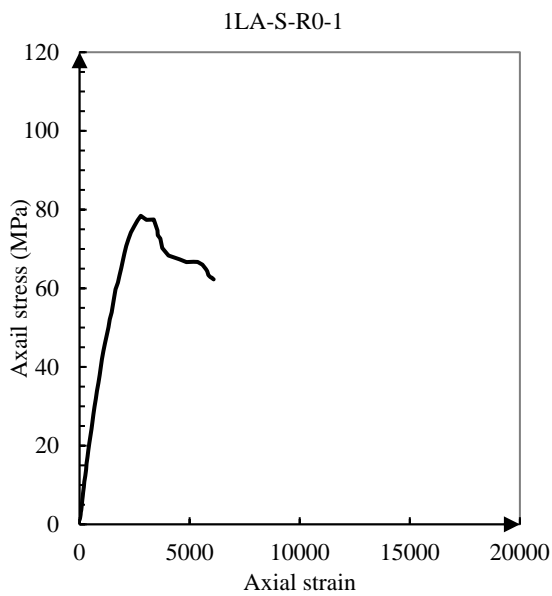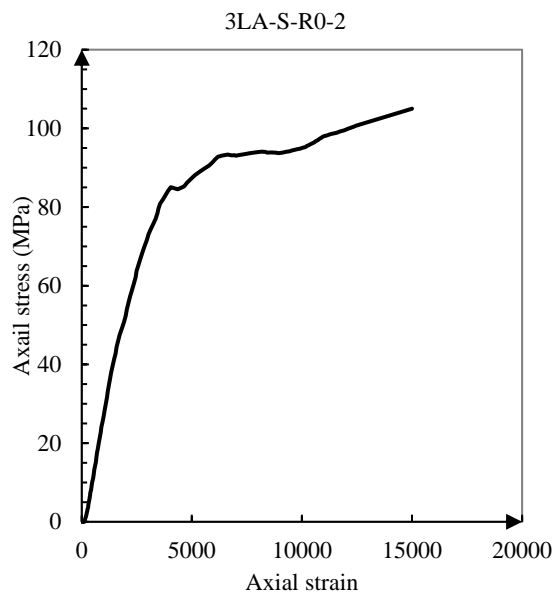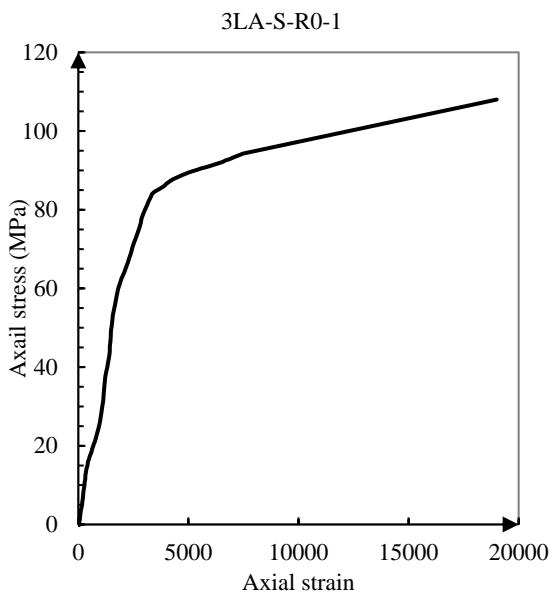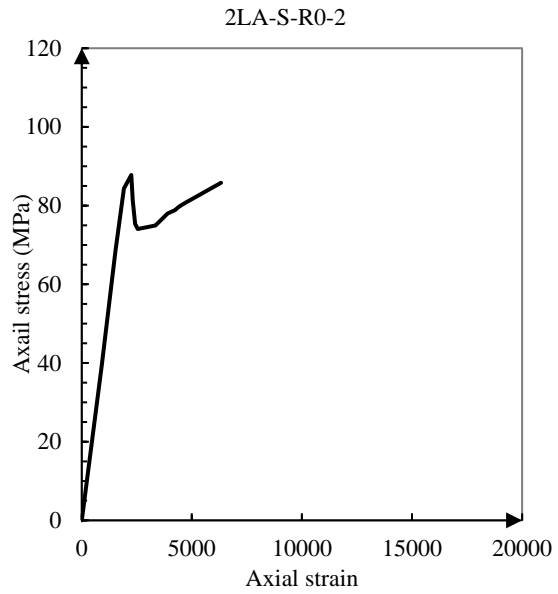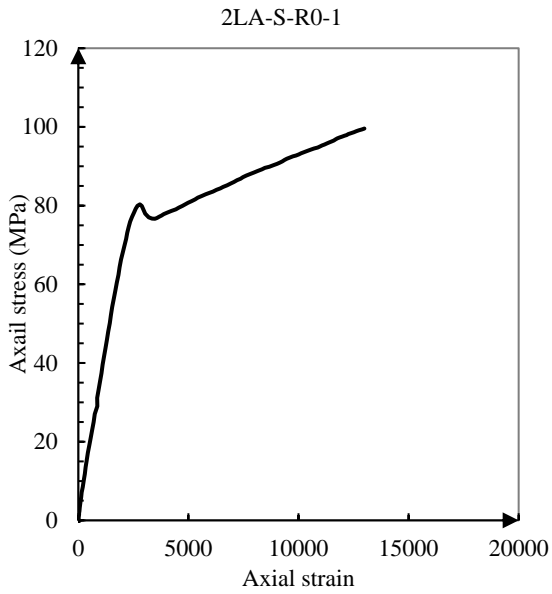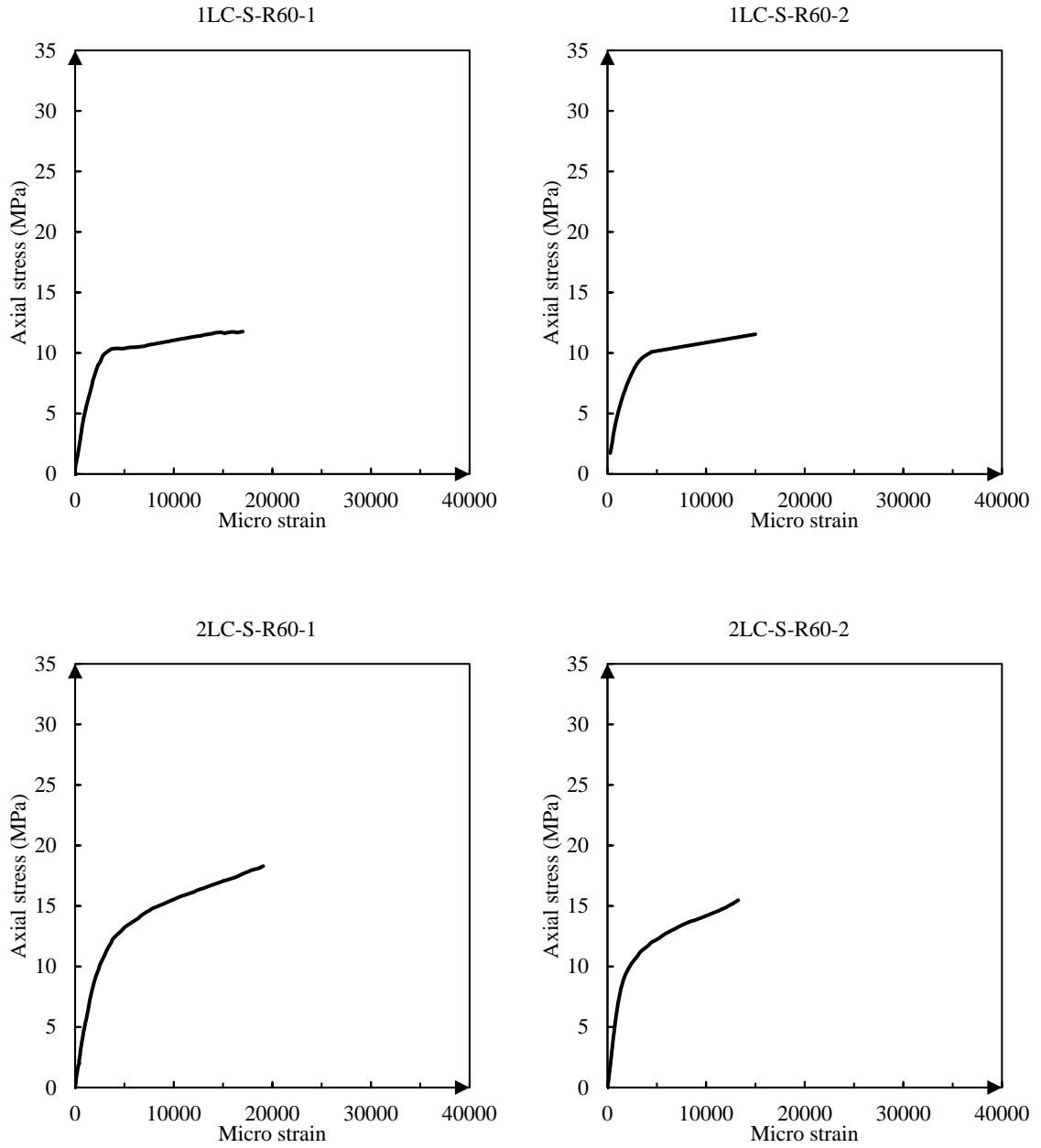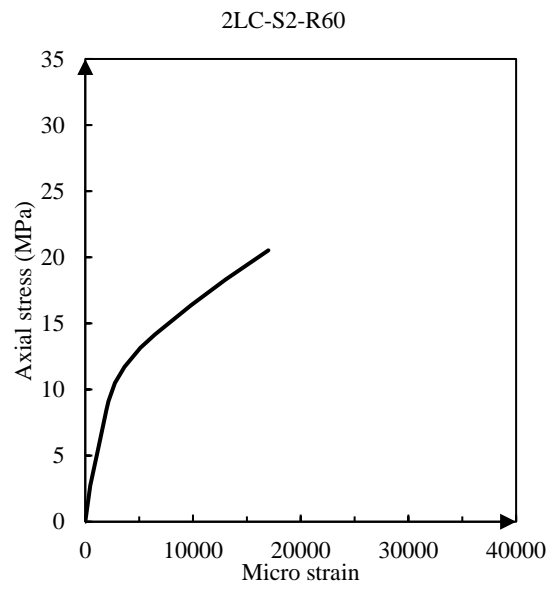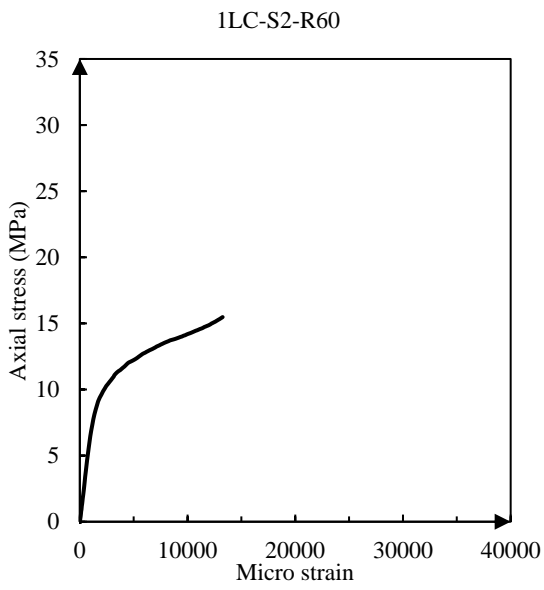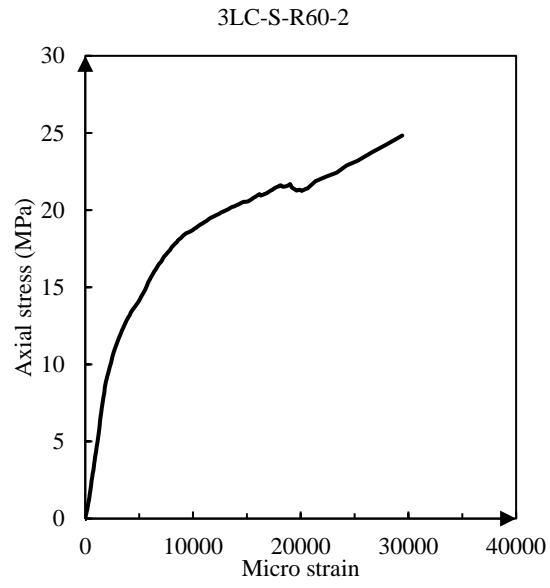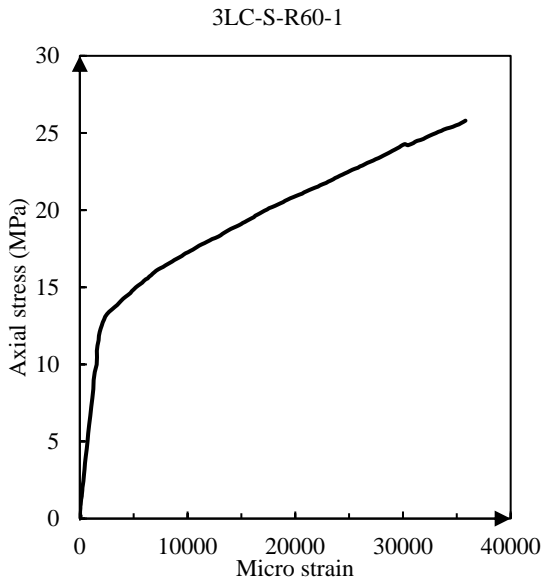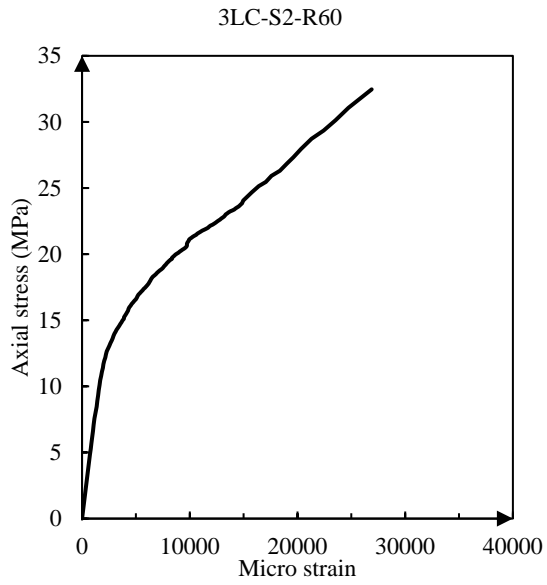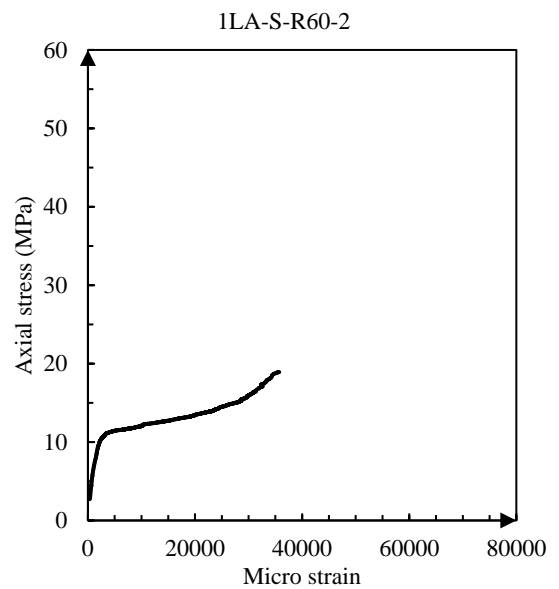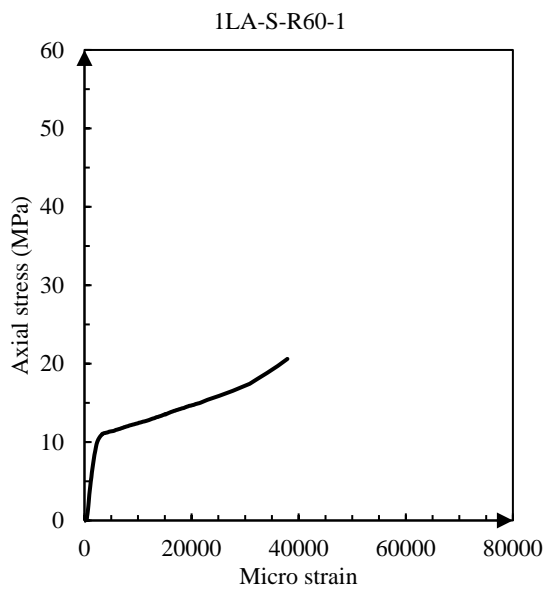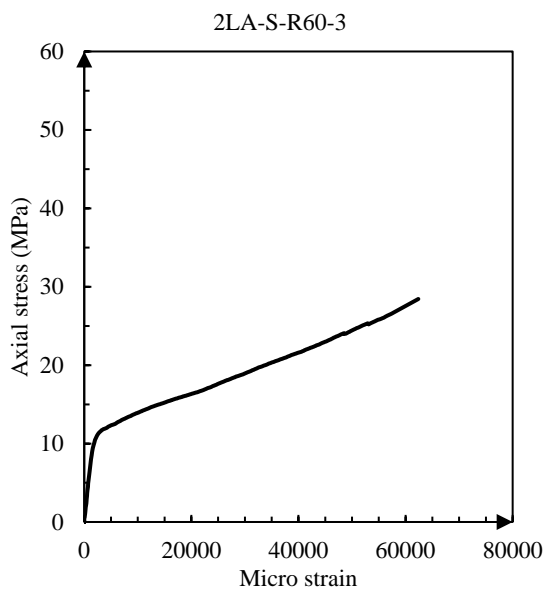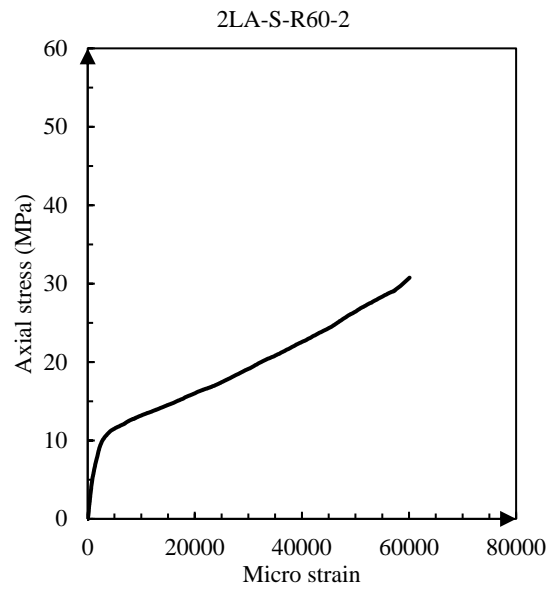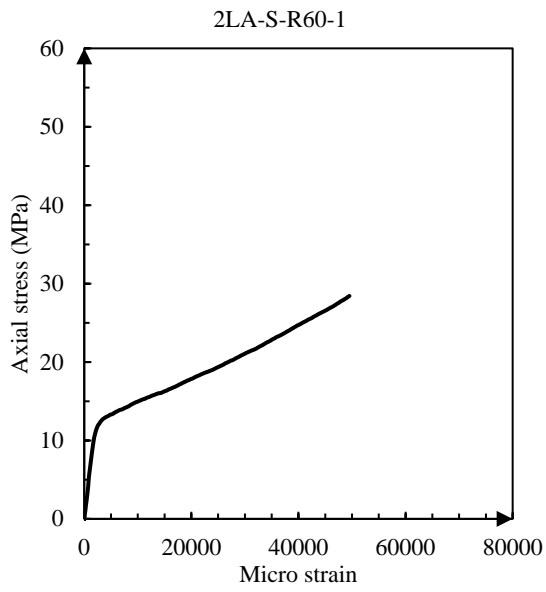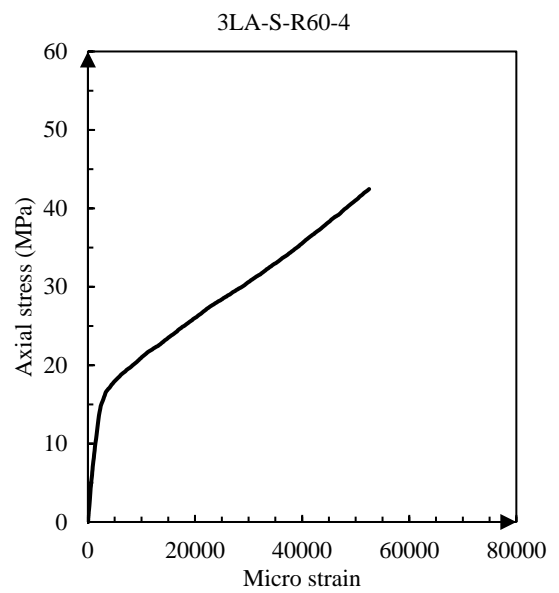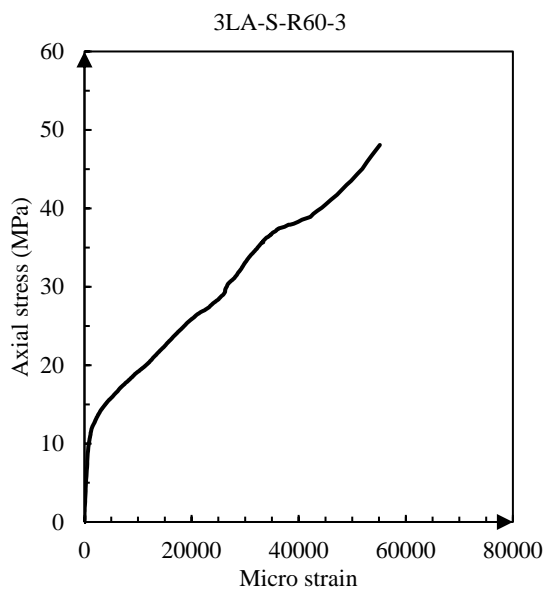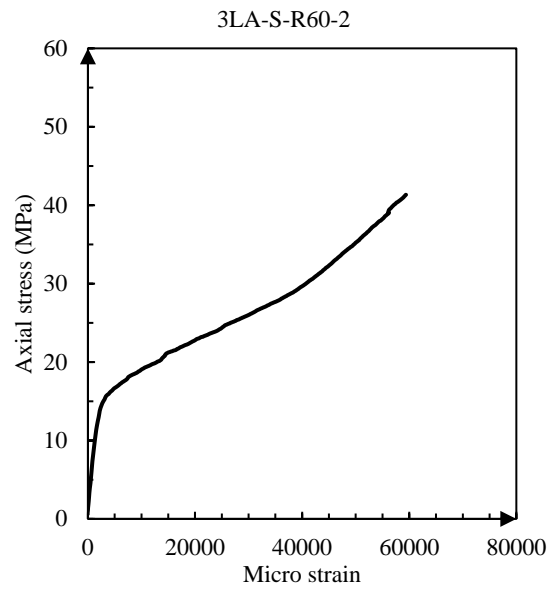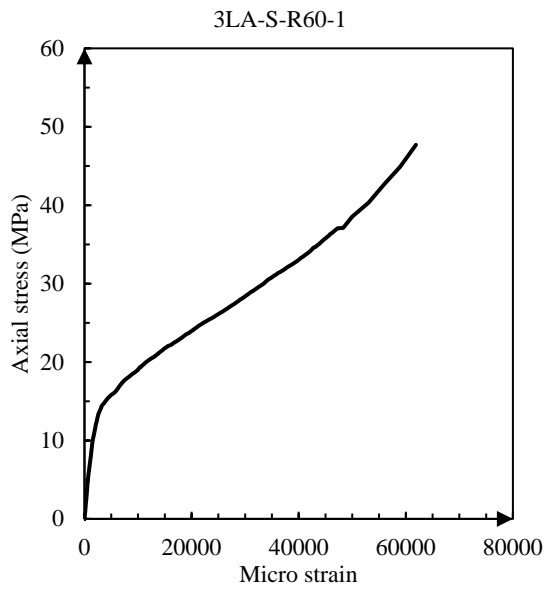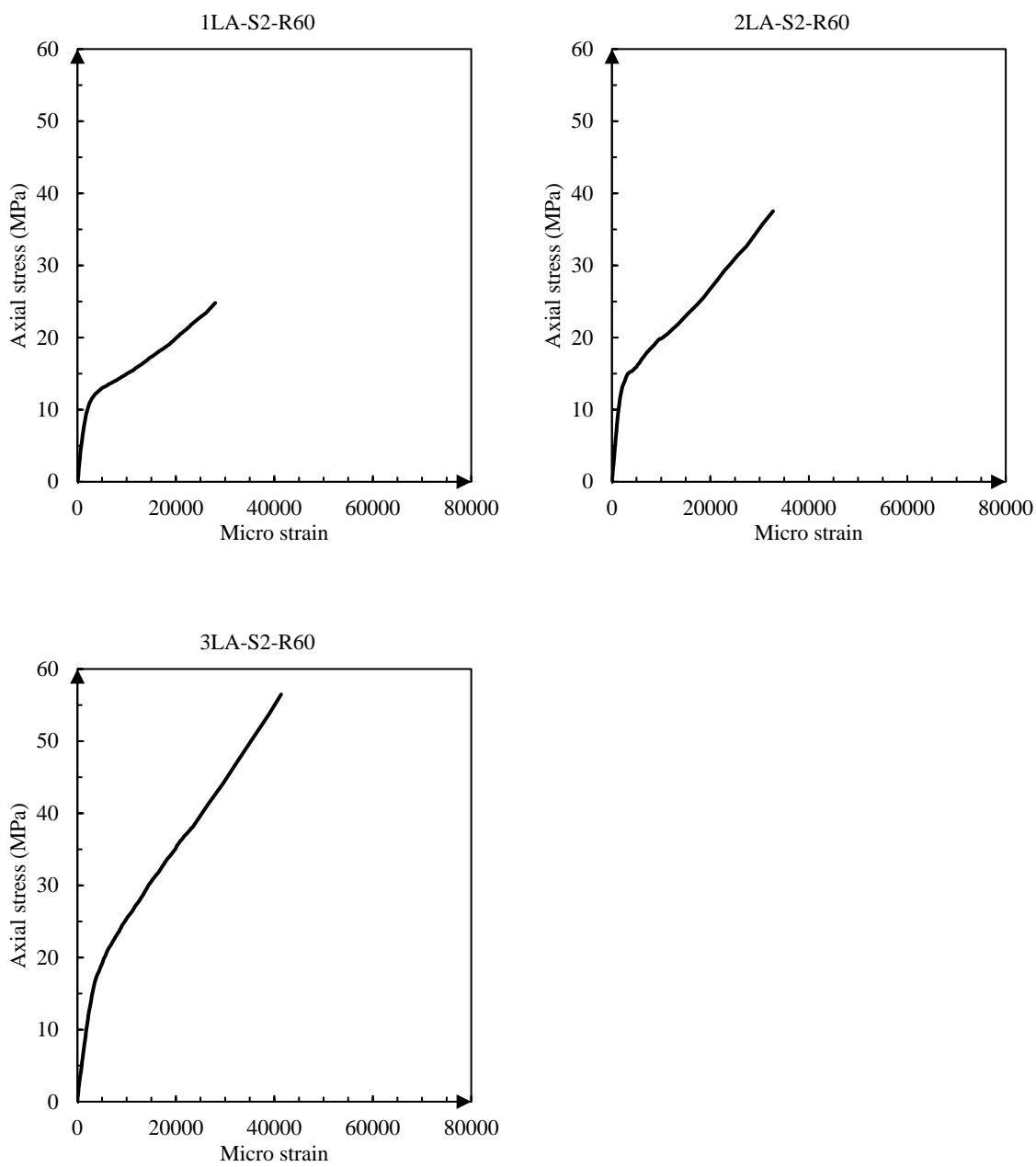
Figure. A3 – 2. Experimental results of FRP-confined concrete under axial compression.

Appendix B. FE models

B1. THREE-POINT BENDING TEST
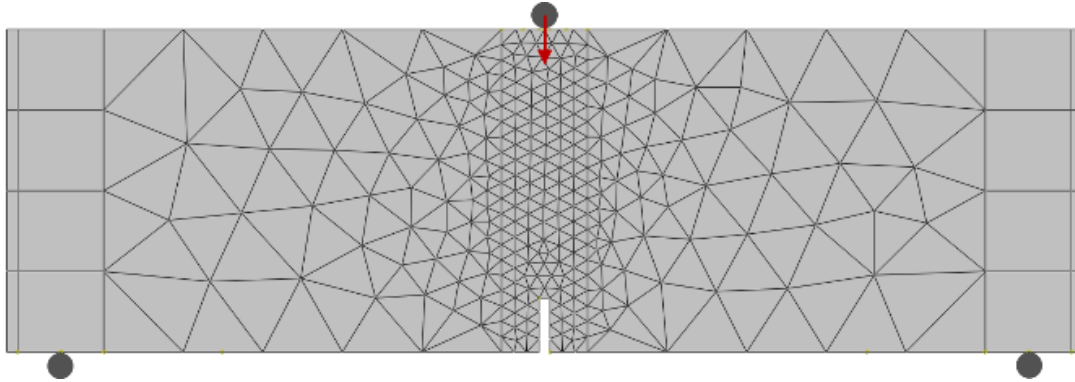
*Heading

** Job name: r0-5-model Model name: R0-5-mode

** Generated by: Abaqus/CAE 6.14-2

*Preprint, echo=NO, model=NO, history=NO, contact=NO

**

** PARTS

**

*Part, name=TPB

*Element, type=CPS4R

** Section: concrete

*Solid Section, elset=Set-77, material=RuC

*End Part

**

**

** ASSEMBLY

**

*Assembly, name=Assembly

**

*Instance, name=beam-1, part= TPB

*End Instance

**

** Constraint: Constraint-1

*Coupling, constraint name=Constraint-1

*Kinematic

2, 2

*End Assembly

**

** MATERIALS

**

*Material, name= RuC

*Elastic

*Concrete Damaged Plasticity

*Concrete Compression Hardening

*Concrete Tension Stiffening

**

** INTERACTION PROPERTIES

**

*Surface Interaction, name=IntProp-1

1.,

*Frictionless

*Surface Behavior, pressure-overclosure=HARD

**

** BOUNDARY CONDITIONS

**

** Type: Displacement/Rotation

**

** INTERACTIONS

**

** Interaction: Int-1

*Contact Pair, interaction=IntProp-1, type=SURFACE TO SURFACE

** --

**

** STEP: Step-1

**

*Step, name=Step-1, nlgeom=YES, inc=10000

*Static

0.01, 1., 1e-7, 0.1

```
**
** BOUNDARY CONDITIONS
**
** Type: Displacement/Rotation
*Boundary
**
** OUTPUT REQUESTS
**
*Restart, write, frequency=0
**
** FIELD OUTPUT: F-Output-1
**
*Output, field
*Node Output
CF, RF, U
*Element Output, directions=YES
DAMAGEC, DAMAGET, ELEDEN, ELEN, ENER, EVOL, IVOL, LE, PE, PEEQ,
PEMAG, S
*Contact Output
CDISP, CSTRESS
**
** HISTORY OUTPUT: H-Output-1
**
*Output, history, variable=PRESELECT
*End Step
```

B2. COMPRESSION TESTS
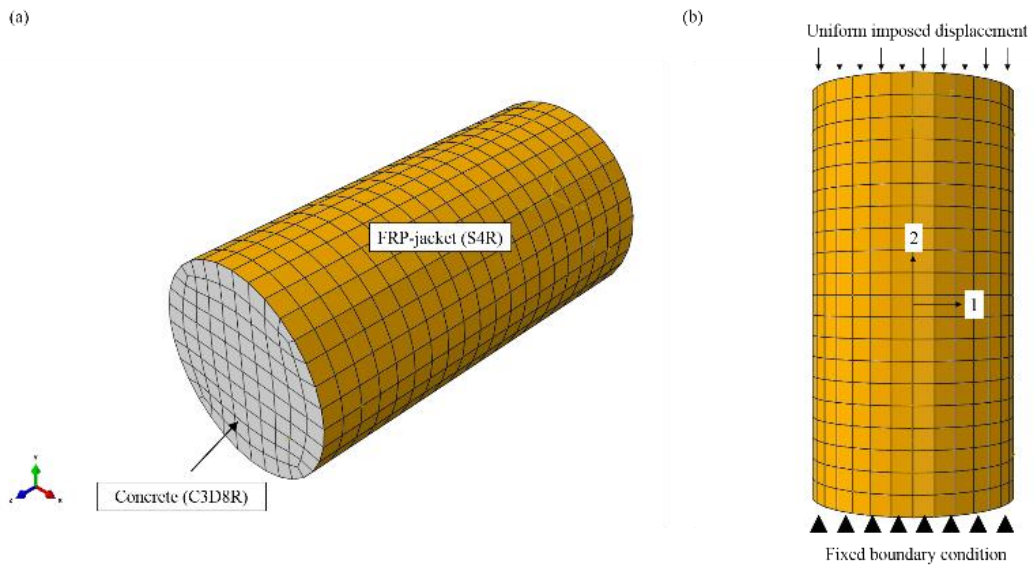
*Heading

** Job name: cyy Model name: Cylinder compression tests

** Generated by: Abaqus/CAE 6.14-2

*Preprint, echo=NO, model=NO, history=NO, contact=NO

**

** PARTS

**

*Part, name=FRP

** Section: FRP

*Shell Section, elset=Set-1, material=aramid/carbon

*End Part

**

*Part, name=Concrete

** Section: RuC

*Solid Section, elset=Set-4, material=RuC

*End Part

**

**

** ASSEMBLY

**

** Constraint: Constraint-1

*Coupling, constraint name=Ref to Concrete

*Kinematic

** Constraint: Constraint-2

*Tie, name=FRP to Concrete

*End Assembly

**

** MATERIALS

**

*Material, name=aramid/carbon

*Material, name="RuC"

*Concrete Damaged Plasticity

*Concrete Compression Hardening

*Concrete Tension Stiffening

**

** BOUNDARY CONDITIONS

**

** Name: BC-2 Type: Displacement/Rotation

*Boundary

** --

**

** STEP: Step-1

**

*Step, name=Step-1, nlgeom=YES, inc=10000

*Static

0.01, 1., 1e-07, 0.1

**

** OUTPUT REQUESTS

**

*Restart, write, frequency=0

**

** FIELD OUTPUT: F-Output-1

**

*Output, field

*Node Output

CF, RF, U

*Element Output, directions=YES

DAMAGEC, LE, PE, PEEQ, PEMAG, S

*Contact Output

CDISP, CSTRESS

**

** HISTORY OUTPUT: H-Output-1

**

*Output, history, variable=PRESELECT

*End Step

B3. ASYMMETRIC SHEAR MODEL
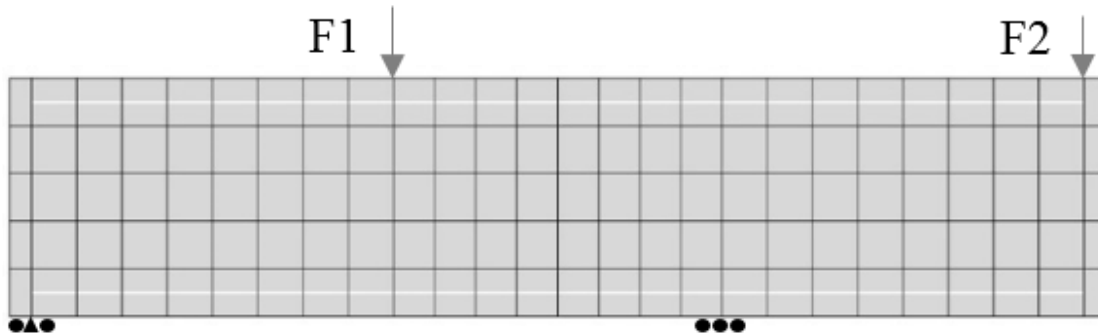
*Heading

** Job name: Asymmetric shear model

** Generated by: Abaqus/CAE 6.14-2

*Preprint, echo=NO, model=NO, history=NO, contact=NO

**

** PARTS

**

*Part, name= Reinforcement

*Node

*Element, type=T2D2

** Section: Reinforcement

*Solid Section, elset=Set-1, material=basalt

*Part, name=Concrete

*Node

*Element, type=CPS4

** Section: RuC

*Solid Section, elset=Set-26, material= UMAT

,

*End Part

**

**

** ASSEMBLY

**

*Assembly, name=Assembly

**

*Instance, name

*End Instance

** Constraint: Constraint-1

*Coupling, constraint name=Constraint-1

*Kinematic

** Constraint: Constraint-2

*Embedded Element

*End Assembly

**

** MATERIALS

**

*Material, name=UMAT

*Depvar

*User Material, constants

*Material, name=basalt

*Material, name=RuC

**

** INTERACTION PROPERTIES

**

*Surface Interaction, name=IntProp-1

1.,

*Friction

0.,

*Surface Behaviour, pressure-overclosure=HARD

**

** BOUNDARY CONDITIONS

**

** Name: BC-2 Type: Displacement/Rotation

*Boundary

** Name: BC-3 Type: Displacement/Rotation

** --

**

** STEP: Step-1

**

*Step, name=Step-1, nlgeom=YES, inc=10000

*Static, stabilize, factor=0.0002, allsdtol=0, continue=NO

0.001, 1., 1e-15, 0.001

**

** OUTPUT REQUESTS

**

*Restart, write, frequency=0

**

** FIELD OUTPUT: F-Output-1

**

*Output, field

*Node Output

CF, RF, U

*Element Output, directions=YES

E, LE, PE, PEEQ, PEMAG, S, SDV, STATUS, UVARM

*Contact Output

CDISP, CSTRESS

**

** HISTORY OUTPUT: H-Output-1

**

*Output, history, variable=PRESELECT

*End Step

Appendix C. Program Code

C1. UMAT FOR SHEAR BEAHVIOUR MODEL OF FRP-CONFINED AND

UNCONFINED RUBBERISED CONCRETE

```
      SUBROUTINE UMAT(STRESS,STATEV,DDSDDE,SSE,SPD,SCD,RPL,DDSDDT,
1 DRPLDE,DRPLDT,STRAN,DSTRAN,TIME,DTIME,TEMP,DTEMP,PREDEF,DPRED,
2 CMNAME,NDI,NSHR,NTENS,NSTATV,PROPS,NPROPS,COORDS,DROT,
3 PNEWDT,CELENT,DFGRDO,DFGRDl,NOEL,NPT,LAYER,KSPT,KSTEP,KINC)

  include 'aba_param.inc'
   CHARACTER*8 CMNAME
    DIMENSION STRESS(NTENS),STATEV(NSTATV),DDSDDE(NTENS,NTENS),
1 DDSDDT(NTENS),DRPLDE(NTENS),STRAN(NTENS),DSTRAN(NTENS),
2 TIME(2),PREDEF(1),DPRED(1),PROPS(NPROPS),COORDS(3),DROT(3,3)
    DIMENSION DFGRD0(3,3),DFGRDl(3,3),PEPS(3),PSIGC(2),TRM(3,3),
1 SIGC(3),TM(3,3),TTM(3,3),D(3,3),E(3,3),DD(3,3),STRANT(3)
    PARAMETER (ZERO=0.D0, ONE=1.D0, TWO=2.D0, THREE=3.D0, FOUR=4.D0,
1 SIX=6.D0,PI=3.14159265359)
    INTEGER*4 NTENS,NDI,K1,K2
    REAL*8 EMOD,ENU,ELAM,EG,EC,ET,ES,FC,FT,FS,A1T,A1C,A2C,A1S,PHI,
1 KF,E11,E12,E13,E21,E22,E23,E31,E32,E33,TR1,CR1,CR2,SR,SS,
2 SPAN,HH,A2S,CP,TP,SP,DT1,DC1,DT2,DC2,CC,FCC,ECC,ECS,FCS,YEF,T,N,
3 EF,S,SEMOD,AF,f2

C UMAT FOR ISOTROPIC ELASTICITY

C
C STATE VARIABLES
C
    STATEV(16)=DSTRAN(1)
    STATEV(17)=DSTRAN(2)
    STATEV(18)=DSTRAN(3)
C
    STATEV(19)=STRAN(1)
    STATEV(20)=STRAN(2)
    STATEV(21)=STRAN(3)


C    PROPS(1) - UNIAXIAL COMPRESION STRENGTH
    FC=PROPS(1)
C    PROPS(2) - BETA_C
    A2C=PROPS(2)
C    PROPS(3) - RHO_C
    CP=PROPS(3)
C    PROPS(4) - BETA_T
    A1T=PROPS(4)
C    PROPS(5) - RHO_T
    TP=PROPS(5)
C    PROPS(6) - ALPHA_S
    A1S=PROPS(6)
C    PROPS(7) - BETA_S
    A2S=PROPS(7)
C    PROPS(8) - RHO_S
    SP=PROPS(8)
C    PROPS(9) - FRP LAYERS
    N=PROPS(9)
C    PROPS(10) - FRP MODULUS
```

```
      YEF=PROPS(10)
C   PROPS(11) - FRP ULTIMATE STRAIN
      EF=PROPS(11)
C        PROPS(12) - HEIGHT OF SPECIMEN
      HH=PROPS(12)
C        PROPS(13) - SHEAR SPAN OF SPECIMEN
      SS=PROPS(13)
C   PROPS(14) - FRP EFFICIENCY FACTOR
      KF=PROPS(14)
C   PROPS(15) - SHAPEFACTOR
      S=PROPS(15)
C   PROPS(16) - THICKNESS OF FRP
      T=PROPS(16)

C
C ELASTIC PROPERTIES
C
C   YOUNG'S MODULUS
      EMOD = 12*(PROPS(1)/10)**0.67*1000

C   CRUSHING STRAIN
      EC = -0.7*PROPS(1)**0.31/1000

C   TENSILE STRENGTH
      FT= 0.26*PROPS(1)**0.67

C   CRACKING STRAIN        0.0001
      ET=FT/EMOD

C   SHEAR STRENGTH
      FS= 0.36*PROPS(1)**0.57

C   SHEAR STRAIN
      ES=(2160*FS-766)/1000000

C   INITIAL SHEAR MODULUS
      YEG=2.5*FS/ES

C   TOTAL STRAIN
      DO K1=1,NTENS
        STRANT(K1)=STRAN(K1)+DSTRAN(K1)
      ENDDO

C
C ELASTIC STIFFNESS
C
      CALL ASET(DDSDDE,ZERO,NTENS*NTENS)

      DO K1=1,NDI
        DO K2=1,2
          DDSDDE(K2,K1)=ELAM
        END DO
        DDSDDE(K1,K1)=EG2+ELAM
      END DO

      DO K1=NDI+1, NTENS
        DDSDDE(K1,K1)=YEG
      END DO
```

```
 IF (STRANT(1).EQ.ZERO.AND.STRANT(2).EQ.ZERO.AND.
1 STRANT(3).EQ.ZERO) THEN

      GOTO 10
 ELSE
 IF (STRANT(1).EQ.ZERO.AND.STRANT(2).EQ.ZERO) THEN
   PEPS(1)=0.5*STRANT(3)
   PEPS(2)=-0.5*STRANT(3)
   PHI=45.0*PI/180.0
 ELSE
   A1=(STRANT(1)+STRANT(2))/2
   B1=-STRANT(1)*STRANT(2)+(STRANT(3)/2)**2
   IF(STRANT(1).EQ.STRANT(2)) THEN
     PHI=45.0*PI/180.0
   ELSE
     C1=STRANT(3)/(STRANT(1)-STRANT(2))
     PHI=ATAN(C1)/TWO
   ENDIF
   IF (B1.LE.ZERO) THEN
     WRITE(6,*)'B1=NEG.',A1**TWO+B1
      PEPS(1)=A1
      PEPS(2)=A1
   END IF
   IF (STRANT(2).GT.STRANT(1)) THEN
       PEPS(1)=A1-SQRT(A1**2+B1)
       PEPS(2)=A1+SQRT(A1**2+B1)
   ELSE
       PEPS(1)=A1+SQRT(A1**2+B1)
       PEPS(2)=A1-SQRT(A1**2+B1)
   ENDIF
 ENDIF
 IF(PEPS(1).LE.ZERO) THEN
   CR1=PEPS(1)/EC
   IF(CR1.GT.ZERO.AND.CR1.LE.ONE) THEN
     PSIGC(1)=(A1C*CR1+(3-2*A1C)*CR1**2+(A1C-2)
1 *CR1**3)*FC
   ELSE
     PSIGC(1)=(CR1/(A2C*(CR1-1)**2+CR1))*FC
   ENDIF
 ENDIF

 IF(PEPS(2).LE.ZERO) THEN
   CR2=PEPS(2)/EC
   IF(CR2.GT.ZERO.AND.CR2.LE.ONE) THEN
     PSIGC(2)=(A1C*CR2+(3-2*A1C)*CR2**2+(A1C-2)
1 *CR2**3)*FC
   ELSE
     PSIGC(2)=(CR2/(A2C*(CR2-1)**2+CR2))*FC
   ENDIF
 ENDIF

 IF(PEPS(1).GT.ZERO) THEN
   TR1=PEPS(1)/ET
   IF(TR1.LE.ONE.AND.TR1.GE.ZERO) THEN
     PSIGC(1)=EMOD*PEPS(1)
   ELSE
     PSIGC(1)=TR1/(A1T*(TR1-1)**TWO+TR1)*FT
```

233

```
          ENDIF
       ENDIF

      IF(PEPS(2).GT.ZERO) THEN
        TR2=PEPS(2)/ET
        IF(TR2.LE.ONE.AND.TR2.GE.ZERO) THEN
          PSIGC(2)=EMOD*PEPS(2)
        ELSE
          PSIGC(2)=TR2/(A1T*(TR2-1)**TWO+TR2)*FT
        ENDIF
      ENDIF
c   Fix angle
      FA=ATAN(SS/HH)

c   Principal strain
      PEPS(1)=STRANT(1)*COS(FA)**2+STRANT(2)*SIN(FA)**2
     1 +STRANT(3)*SIN(FA)*COS(FA)
      PEPS(2)=STRANT(1)*SIN(FA)**2+STRANT(2)*COS(FA)**2
     1 -STRANT(3)*SIN(FA)*COS(FA)
      PEPS(3)=2*(STRANT(2)-STRANT(1))*SIN(FA)*COS(FA)
     1 +STRANT(3)*(COS(FA)**2-SIN(FA)**2)

C
C SOFTEN COEFFCIENT
C

      IF(PEPS(1).LT.ZERO.AND.PEPS(2).GT.ZERO) THEN

            IF (PEPS(2).LT.ET) THEN
        R=PEPS(2)/ET
      ELSE
                  R=1
      END IF
      END IF
      IF(PEPS(2).LT.ZERO.AND.PEPS(1).GT.ZERO) THEN

            IF (PEPS(1).LT.ET) THEN
                  R=PEPS(1)/ET
      ELSE
                  R=1
      END IF
      END IF
                  SCO=(0.1*R-0.95*R**2)+1
                  SKF=SCO*KF
      IF (PEPS(2).GE.ZERO.AND.PEPS(1).GE.ZERO) THEN

                  SCO=1
                  SKF=KF
      ELSE IF (PEPS(2).LE.ZERO.AND.PEPS(1).LT.ZERO) THEN
                  SCO=1
                  SKF=KF
      END IF

      AF=ATAN(HH/SS)
      WRITE(6,*) AF*180/PI
C  FRP
      IF (N.GT.O) THEN
      FCS=-SCO*FC
            SEMOD = 12*(-FCS/10)**0.67*1000
```

```
    ECS = -(0.7*(-FCS)**0.31/1000          )
         ED=0.5*HH/COS(AF)
         CC=2*YEF*N*T*EF*KF*COS(AF)**2/ED
         ECC=(1.75+5.53*0.58*(CC/-FCS)*(EF*KF/-ECS)**0.45)*ECS
         FCC=-(-FCS+3.3*0.58*CC)
         YE2=((-FCC+FCS)/-ECC)/2
         E2=2*FCS/(SEMOD-YE2)

    ELSE
         CC=0
    ECC=0
    FCC=0
    YE2=0
         E2=0
    END IF

C
C 1 COMPRESSION AND COMPRESSION
C

    IF (PEPS(1).LT.ZERO.AND.PEPS(2).LT.ZERO) THEN

      CR1=PEPS(1)/EC
      CR2=PEPS(2)/EC
      F1=A2C*(CR1-1)**CP+CR1
      F2=A2C*(CR2-1)**CP+CR2

    IF (CR1.GT.ZERO.AND.CR1.LE.ONE) THEN
      E11=EMOD-EMOD**2/(2*FC)*PEPS(1)
    ELSE
      E11=-FC/EC*(1/F1-(CR1*(A2C*CP*(CR1-1)**(CP-1)+1))/F1**2)
    END IF
    IF (CR2.GT.ZERO.AND.CR2.LE.ONE) THEN
      E22=EMOD-EMOD**2/(2*FC)*PEPS(2)
    ELSE
      E22=-FC/EC*(1/F2-(CR2*(A2C*CP*(CR2-1)**(CP-1)+1))/F2**2)
    END IF
      E12=0.0D0
      E13=0.0D0
      E21=0.0D0
      E23=0.0D0
    END IF
C
C 2A  UNCRACK TENSION AND COMPRESSION
C

    IF (PEPS(1).GT.ZERO.AND.PEPS(2).LT.ZERO.AND.PEPS(1).LT.ET) THEN

      E11=SEMOD
      CR2=PEPS(2)/ECS
      F2=A2C*(CR2-1)**CP+CR2

      IF (N.NE.ZERO) THEN
        IF (PEPS(2).LT.ZERO.AND.PEPS(2).GT.E2) THEN
          E22=SEMOD-(SEMOD-YE2)**2/(2*-FCS)*PEPS(2)
        ELSE IF (PEPS(2).LT.E2) THEN
          E22=YE2
        END IF
```

```
      ELSE
        IF (CR2.GT.ZERO.AND.CR2.LE.ONE) THEN
          E22=SEMOD-SEMOD**2/(2*-FCS)*PEPS(2)
        ELSE
          E22=FCS/ECS*(1/F2-(CR2*(A2C*CP*(CR2-1)**(CP-1)+1))/F2**2)
        END IF
      END IF
        E12=0.0D0
        E13=0.0D0
        E21=0.0D0
        E23=0.0D0
      END IF
C
C 2B COMPRESSION AND UNCRACKED TENSION
C

    IF(PEPS(1).LT.ZERO.AND.PEPS(2).LT.ET.AND.PEPS(2).GT.ZERO) THEN

                CR1=PEPS(1)/ECS
      F1=A2C*(CR1-1)**CP+CR1
      IF (N.NE.ZERO) THEN
        IF (PEPS(1).LT.ZERO.AND.PEPS(1).GT.E2) THEN
          E11=SEMOD-(SEMOD-YE2)**2/(2*-FCS)*PEPS(1)
        ELSE IF (PEPS(1).LT.E2) THEN
          E11=YE2
        END IF
      ELSE
        IF (CR1.GT.ZERO.AND.CR1.LE.ONE) THEN
          E11=SEMOD-SEMOD**2/(2*-FCS)*PEPS(1)
        ELSE
          E11=FCS/ECS*(1/F1-(CR1*(A2C*CP*(CR1-1)**(CP-1)+1))/F1**2)
        END IF
      END IF

        E22=SEMOD
        E12=0.0D0
        E13=0.0D0
        E21=0.0D0
        E23=0.0D0

    END IF
C
C 3A CRACKED TENSION AND COMPRESSION
C

    IF(PEPS(1).GE.ET.AND.PEPS(2).LT.ZERO) THEN

                TR1=PEPS(1)/ET
      CR2=PEPS(2)/ECS

      F1=A1T*(TR1-1)**TP+TR1
      F2=A2C*(CR2-1)**CP+CR2
      IF (N.NE.ZERO) THEN
          E11=SEMOD*(1/F1-(TR1*(A1T*TP*(TR1-1)**(TP-1)+1))/F1**2)
      ELSE
          E11=SEMOD*(1/F1-(TR1*(A1T*TP*(TR1-1)**(TP-1)+1))/F1**2)
      END IF

      IF (N.NE.ZERO) THEN
```

```
      IF (PEPS(2).LT.ZERO.AND.PEPS(2).GT.E2) THEN
        E22=SEMOD-(SEMOD-YE2)**2/(2*-FCS)*PEPS(2)
      ELSE IF (PEPS(2).LT.E2) THEN
        E22=YE2
      END IF
    ELSE
      IF (CR2.GT.ZERO.AND.CR2.LE.ONE) THEN
        E22=SEMOD-SEMOD**2/(2*-FCS)*PEPS(2)
      ELSE
        E22=FCS/ECS*(1/F2-(CR2*(A2C*CP*(CR2-1)**(CP-1)+1))/F2**2)
      END IF
    END IF
      E12=0.0D0
      E13=0.0D0
      E21=0.0D0
      E23=0.0D0

    END IF
C
C 3B COMPRESSION AND CRACKED TENSION
C

    IF(PEPS(1).LT.ZERO.AND.PEPS(2).GE.ET) THEN

                  CR1=PEPS(1)/ECS
      F1=A2C*(CR1-1)**CP+CR1
      TR2=PEPS(2)/ET
      F2=A1T*(TR2-1)**TP+TR2
      IF (N.NE.ZERO) THEN
        IF (PEPS(1).LT.ZERO.AND.PEPS(1).GT.E2) THEN
          E11=SEMOD-(SEMOD-YE2)**2/(2*-FCS)*PEPS(1)
        ELSE IF (PEPS(1).LT.E2) THEN
          E11=YE2
        END IF
      ELSE
        IF (CR1.GT.ZERO.AND.CR1.LE.ONE) THEN
          E11=SEMOD-SEMOD**2/(2*-FCS)*PEPS(1)
        ELSE
          E11=FCS/ECS*(1/F1-(CR1*(A2C*CPS*(CR1-1)**(CPS-1)+1))/F1**2)
        END IF
      END IF
      IF (N.NE.ZERO) THEN
          E22=SEMOD*(1/F2-(TR2*(A1T*TP*(TR2-1)**(TP-1)+1))/F2**2)
      ELSE
          E22=SEMOD*(1/F2-(TR2*(A1T*TP*(TR2-1)**(TP-1)+1))/F2**2)
      END IF

        E12=0.0D0
        E13=0.0D0
        E21=0.0D0
        E23=0.0D0
    END IF
C
C 4 UNCRACKED TENSION AND UNCRACKED TENSION
C

    IF (PEPS(1).GT.ZERO.AND.PEPS(2).GT.ZERO.AND.PEPS(1).LT.ET
   1 .AND.PEPS(2).LT.ET) THEN
```

```
                    E11=SEMOD
                    E22=SEMOD
                    E12=0.0D0
                    E13=0.0D0
                    E21=0.0D0
                    E23=0.0D0

            END IF
C
C 5A CRACKED TENSION AND UNCRACKED TENSION
C

        IF (PEPS(2).GT.ZERO.AND.PEPS(1).GE.ET.AND.PEPS(2).LT.ET) THEN

                TR1=PEPS(1)/ET
                F1=A1T*(TR1-1)**TP+TR1
              IF (N.NE.ZERO) THEN
                    E11=SEMOD*(1/F1-(TR1*(A1T*TP*(TR1-1)**(TP-1)+1))/F1**2)
              ELSE
                    E11=SEMOD*(1/F1-(TR1*(A1T*TP*(TR1-1)**(TP-1)+1))/F1**2)
              END IF

                E22=SEMOD
                E12=0.0D0
                E13=0.0D0
                E21=0.0D0
                E23=0.0D0
            END IF
C
C 5B UNCRACKED TENSION AND CRACKED TENSION
C

        IF (PEPS(1).GT.ZERO.AND.PEPS(2).GE.ET.AND.PEPS(1).LT.ET) THEN

                E11=SEMOD
                TR2=PEPS(2)/ET
                F2=A1T*(TR2-1)**TP+TR2
              IF (N.NE.ZERO) THEN
                    E22=SEMOD*(1/F2-(TR2*(A1T*TP*(TR2-1)**(TP-1)+1))/F2**2)
              ELSE
                    E22=SEMOD*(1/F2-(TR2*(A1T*TP*(TR2-1)**(TP-1)+1))/F2**2)
              END IF

                E12=0.0D0
                E13=0.0D0
                E21=0.0D0
                E23=0.0D0
            END IF
C
C 6  CRACKED TENSION AND CRACKED TENSION
C

        IF (PEPS(1).GE.ET.AND.PEPS(2).GE.ET) THEN

                TR1=PEPS(1)/ET
                F1=A1T*(TR1-1)**TP+TR1
                TR2=PEPS(2)/ET
                F2=A1T*(TR2-1)**TP+TR2
                E22=SEMOD*(1/F2-(TR2*(A1T*TP*(TR2-1)**(TP-1)+1))/F2**2)
```

```
                    E11=SEMOD*(1/F1-(TR1*(A1T*TP*(TR1-1)**(TP-1)+1))/F1**2)
       E12=0.0D0
       E13=0.0D0
       E21=0.0D0
       E23=0.0D0
    END IF


    IF (STRANT(2).LT.SKF*KF*EF) THEN
       E31=0.0
       E32=0.0
       E33=425*SCO*3
    END IF



    DO K1=1,3
      DO K2=1,3
         DDSDDE(K1,K2)=ZERO
      END DO
    ENDDO
C Stiffness matrix in Prin-D
    DDSDDE(1,1)=E11
    DDSDDE(1,2)=E12
    DDSDDE(1,3)=E13
    DDSDDE(2,1)=E21
    DDSDDE(2,2)=E22
    DDSDDE(2,3)=E23
    DDSDDE(3,1)=E31
    DDSDDE(3,2)=E32
    DDSDDE(3,3)=E33


C Stiffness matrix in xy-D
    PHI=FA
    TM(1,1)=COS(PHI)**2
    TM(1,2)=SIN(PHI)**2
    TM(1,3)=COS(PHI)*SIN(PHI)
    TM(2,1)=SIN(PHI)**2
    TM(2,2)=COS(PHI)**2
    TM(2,3)=-COS(PHI)*SIN(PHI)
    TM(3,1)=-2*COS(PHI)*SIN(PHI)
    TM(3,2)=2*COS(PHI)*SIN(PHI)
    TM(3,3)=COS(PHI)**2-SIN(PHI)**2

    TTM(1,1)=COS(PHI)**2
    TTM(1,2)=SIN(PHI)**2
    TTM(1,3)=-2*COS(PHI)*SIN(PHI)
    TTM(2,1)=SIN(PHI)**2
    TTM(2,2)=COS(PHI)**2
    TTM(2,3)=2*COS(PHI)*SIN(PHI)
    TTM(3,1)=COS(PHI)*SIN(PHI)
    TTM(3,2)=-COS(PHI)*SIN(PHI)
    TTM(3,3)=COS(PHI)**2-SIN(PHI)**2


    DO K1=1,3
      DO K2=1,3
        D(K1,K2)=ZERO
        DO K3=1,3
           D(K1,K2)=D(K1,K2)+TTM(K1,K3)*DDSDDE(K3,K2)
        END DO
```

```
      END DO
    END DO

    DO K1=1,3
      DO K2=1,3
        DD(K1,K2)=ZERO
        DO K3=1,3
          DD(K1,K2)=DD(K1,K2)+D(K1,K3)*TM(K3,K2)
        END DO
      END DO
    END DO

    DO K1=1,3
      DO K2=1,3
        DDSDDE(K1,K2)=DD(K1,K2)
      END DO
    END DO

    IF (STRANT(2).LT.SKF*KF*EF) THEN
      DDSDDE(2,2)=DDSDDE(2,2)+800
    END IF
    END IF
    DO K1=1,NTENS
      DO K2=1,NTENS
        STRESS(K2)=STRESS(K2)+DDSDDE(K2,K1)*DSTRAN(K1)
      END DO
    END DO

10  RETURN
    END SUBROUTINE
```

C2. ANALYTICAL-ORIENTED MODEL FOR FRP-CONFINED COLUMNS

```matlab
clear all
clc
close all
%Section type Sqaure-1;Rctangular-2;Circular-3
H=150;
W=150;
R=30;
    if H == W && R ~= 0
    Section = 1
    elseif H ~= W && R ~= 0
    Section = 2
    elseif H == W && R == 0
    Section = 3
    end

pvr = 0;
%concrete property 1-RC;2-RuC
if pvr == 0;
c_type = 1;
else
c_type = 2;
end

%concrete compressive strength fc
fco=30;
if pvr ~= 0
fc=(1/(1+2*(8.7*pvr/2)^(3/2)))*fco
else
fc=fco
end
%concrete tensile strength ft
ft=0.26*fc^(2/3);
%Poisson ratio v
if pvr ~= 0
    v = 0.35;
else
    v = 8e-6*(fc)^2+0.0002*fc+0.138
end
%Elastic modulus
Ec=12000*(0.1*fc)^(2/3);
%peak compresive strain
eco1=0.7*fc^0.31/1000;
eco=(1-pvr)*eco1;
%FRP property
nf=1;
Ef=222000;
tf=0.165*nf;
```

```matlab
efu=0.02;
if Section == 1 || Section == 2
    Di = sqrt(H^2+W^2)
elseif Section == 3
    Di = H
end
%confining stiffness
kj=2*Ef*tf/Di;
%strain reduction factor ke
if pvr ~= 0
    ke = (1-2.3*fc*10^-3-0.75*Ef*10^-6)*(4*R/H)^0.288
else
    ke = (1-2.3*fc*10^-3-0.75*Ef*10^-6)*(2*R/H)^0.288
end
step=0.0005;
assumption=1;

%Area partion
if Section == 3
    A=(H/2)^2*3.14;
elseif Section == 1 || Section == 2
    A=3.14*R^2+2*(H-2*R)*R+2*(W-2*R)*R+(H-2*R)*(W-2*R);
end
if Section == 1
    A1=1.14*R^2;
    A2=3.14*H^2/16;
    A4=((H-2*R)^2+(W-2*R)^2)/3;
    A3=A-A1-A2-A4;
elseif Section == 2
    A1=1.14*R^2;
    A2=3.14*H*W/16;
    A4=((H-2*R)^2+(W-2*R)^2)/3;
    A3=A-A1-A2-A4;
end

fc0=assumption;
P=zeros(5000,16);
tic
a=0.7;
if pvr ~= 0
    b=1.2;
    c=2;
    DC=-1.98*log(kj)+6.2;
    fcr=fc;
else
    b=1.5;
    c=1.5;
    DC=3.05*log(kj)-18.9;
    fcr=fc*(-6.5*10e-6*kj^2+5.8e-3*kj+0.8;
end
```

```matlab
fcr=fc*(-6.5*10e-6*kj^2+5.8e-3*kj+0.8;
for r=1:2000
    ec=r*step
    fc_initial=fc0;
    if fc_initial<=fcr
        eV=-(1-2*v)/Ec*10^-4*fc_initial;
    elseif fc_initial>fcr
        eV=-(1-2*v)/Ec*10^-4*b*fc*((fc_initial/(b*fc))-
DC*((fc_initial-fcr)/(b*fc-fcr))^c);
    end
    eA=eV+ec;
    el=sqrt(eA+1)-1;

    if el>ke*efu
        break
    end

    Fl=Ef*el*tf*sqrt(2);
    %confining pressure circular
    fcc = Fl*2/Di;
    %confining pressure f1
    fl_1triaxial=Fl/R*sqrt(2);
    %confining pressure f2
    if Section == 1
        R2 = H/2;
        fl_2triaxial = Fl/R2;
        fl_3triaxial = Fl/R2;
    elseif Section == 2
        R2 = H/2;
        R3 = W/2;
        fl_2triaxial = Fl/R2;
        fl_3triaxial = Fl/R3;
    end
    %confining pressure f3
    f1_biaxial=Fl/2/R;
    %confining pressure f4
    fan=(H-2*R)*(1+el);
    if pvr ~= 0
        fan2=110*eA;
    elseif pvr == 0
        fan2=10*eA;
    end
    AFAN=4*fan*fan2*0.7;
    R4=(fan^2+4*fan2^2)/8/fan2;
    f2_biaxial=Fl/R4/sqrt(2);

%ultimate fcc for A1 and A2
fcc_1triaxial=ottosen(-fc,ft,-fl_1triaxial,-fl_1triaxial);
fcc_2triaxial=ottosen(-fc,ft,-fl_2triaxial,-fl_3triaxial);
fcc_ctriaxial=ottosen(-fc,ft,-fcc,-fcc);
```

```
%compressive stress
fc_1triaxial=mander(Ec,fc,ec,eco,-fcc_1triaxial);
fc_2triaxial=mander(Ec,fc,ec,eco,-fcc_2triaxial);
fc_1biaxial=liu(Ec,ec,fc,v,f1_biaxial);
fc_2biaxial=liu(Ec,ec,fc,v,f2_biaxial);
fccc=mander(Ec,fc,ec,eco,-fcc_ctriaxial);
%unconfined
%fc_uniaxial=uni(fc,ec,eco);
%total

if Section == 1 || Section == 2

fc_total=fc_1triaxial*A1/A+fc_2triaxial*A2/A+fc_1biaxial*A3
/A+fc_2biaxial*(A4)/A;
elseif Section ==3
   fc_total=fccc;
end
fc0=fc_total;
while abs(fc_total-fc_initial)>0.01

    fc_initial=fc0;
    if fc_initial<=a*fc
       eV=-(1-3*v)*10^-4*fc_initial;
    elseif fc_initial>a*fc
       eV=-(1-3*v)*10^-4*b*fc*((fc_initial/(b*fc))-
((fc_initial-a*fc)/(b*fc-a*fc))^c);
    end
    eA=eV+ec;
    el=sqrt(eA+1)-1;

    if el>ke*efu
        break
    end

    Fl=Ef*el*tf*sqrt(2);
    %confining pressure circular
    fcc = Fl*2/Di;
    %confining pressure f1
    fl_1triaxial=Fl/R*sqrt(2);
    %confining pressure f2
    if Section == 1
       R2 = H/2;
       fl_2triaxial = Fl/R2;
       fl_3triaxial = Fl/R2;
    elseif Section == 2
       R2 = H/2;
       R3 = W/2;
       fl_2triaxial = Fl/R2;
       fl_3triaxial = Fl/R3;
    end
```

```matlab
        %confining pressure f3
        f1_biaxial=Fl/2/R;
        %confining pressure f4
        fan=(H-2*R)*(1+el);
        if pvr ~= 0
            fan2=110*eA;
        elseif pvr == 0
            fan2=10*eA;
        end
        AFAN=4*fan*fan2*0.7;
        R4=(fan^2+4*fan2^2)/8/fan2;
        f2_biaxial=Fl/R4/sqrt(2);

%ultimate fcc for A1 and A2
fcc_1triaxial=ottosen(-fc,ft,-fl_1triaxial,-fl_1triaxial);
fcc_2triaxial=ottosen(-fc,ft,-fl_2triaxial,-fl_3triaxial);
fcc_ctriaxial=ottosen(-fc,ft,-fcc,-fcc);
%compressive stress
fc_1triaxial=mander(Ec,fc,ec,eco,-fcc_1triaxial);
fc_2triaxial=mander(Ec,fc,ec,eco,-fcc_2triaxial);
fc_1biaxial=liu(Ec,ec,fc,v,f1_biaxial);
fc_2biaxial=liu(Ec,ec,fc,v,f2_biaxial);
fccc=mander(Ec,fc,ec,eco,-fcc_ctriaxial);
%unconfined
%fc_uniaxial=uni(fc,ec,eco);
%total

if Section == 1 || Section == 2

fc_total=fc_1triaxial*A1/A+fc_2triaxial*A2/A+fc_1biaxial*A3
/A+fc_2biaxial*(A4)/A;
elseif Section ==3
  fc_total=fccc;
end

end
fc0=fc_total;
P(r,1)=-eA;
P(r,2)=-el;
P(r,3)=ec;
P(r,4)=fc_total;
P(r,5)=f1_biaxial;
P(r,6)=f2_biaxial;
P(r,7)=fc_1biaxial;
P(r,8)=fc_2biaxial;
P(r,9)=fl_1triaxial;
P(r,10)=fl_2triaxial;
P(r,11)=fl_3triaxial;
P(r,12)=-fcc_1triaxial;
P(r,13)=-fcc_2triaxial;
```

```
P(r,14)=fc_1triaxial;
P(r,15)=fc_2triaxial;
P(r,16)=Fl;
if el>efu
    break
end
end
m=1;
while P(m,1)>0
    m=m+1;
end
k=m-1;
K=P(1:k,:);
Vertical_Strain=[0 ; K(:,3)];
Lateral_Strain=[0 ; K(:,2)];
Vertical_Stress=[0; K(:,5)];
Biaxial_Lateral_stress1=[0; K(:,6)];
Biaxial_Lateral_stress2=[0; K(:,7)];
Biaxial_Vertical_stress1=[0 ; K(:,8)];
Biaxial_Vertical_stress2=[0 ; K(:,9)];
Triaxial_one_Lateral_stress1=[0 ; K(:,10)];
Triaxial_two_Lateral_stress=[0 ; K(:,11)];
Triaxial_Maximum_Vertical_stress_fcc1=[0 ; K(:,12)];
Triaxial_Maximum_Vertical_stress_fcc2=[0 ; K(:,13)];
Traxial_Vertical_stress1=[0 ; K(:,14)];
Traxial_Vertical_stress2=[0 ; K(:,15)];
if
max(Vertical_Stress)>Vertical_Stress(length(Vertical_Stress
))
    Maximum_Vertical_Stress=max(Vertical_Stress);

Ultimate_Vertical_Stress=Vertical_Stress(length(Vertical_St
ress));
end
if
max(Vertical_Stress)==Vertical_Stress(length(Vertical_Stres
s))

Maximum_Vertical_Stress=Vertical_Stress(length(Vertical_Str
ess));
end
Maximum_Lateral_Strain=Lateral_Strain(length(Lateral_Strain
));
q=1;
if
max(Vertical_Stress)>Vertical_Stress(length(Vertical_Stress
))
    while K(q+1,5)>K(q,5)
     q=q+1;
    end
```

```matlab
    Strain_at_Peak_Stress=K(q,1);

Ultimate_Vertical_Strain=Vertical_Strain(length(Vertical_St
rain));
end
if
max(Vertical_Stress)==Vertical_Stress(length(Vertical_Stres
s))

Maximum_Vertical_Strain=Vertical_Strain(length(Vertical_Str
ain));
end
plot(Vertical_Strain,Vertical_Stress,-
Lateral_Strain,Vertical_Stress);
grid
xlabel('Axial Strain (+),Lateral Strain (-)');
ylabel('Axial Stress (MPa)');
title('Stress-Strain');
toc;



function fc_biaxial=liu(Ec,ec,fc,v,s2)
q=1;
a0=0.00001;
a=a0;

if a<0.2
fcp=(1+a/(1.2-a))*fc;
end
if a>=0.2 && a<=1
  fcp=1.2*fc;
end
if a<=1
ecp=0.0025;
end
x=s2/a;
fc_biaxial=(ec*Ec)/((1-v*a)*(1+(Ec/(fcp*(1-v*a))-
2/(ecp))*ec+(ec/(ecp))^2));
if a>1
    break
end
end



function fc_triaxial=mander(Ec,fc,ec,eco,fcc)
ecc=eco*(1+5*(fcc/fc-1));
x=ec/ecc;
Esec=fcc/ecc;
r=Ec/(Ec-Esec);
```

```
fc_triaxial=(fcc*x*r)/(r-1+x^r);
```